REINITIATION MODE STUDY OF HIGHLY IRREGULAR DETONATION

by

NANDAKUMAR VIJAYAKUMAR

Presented to the Faculty of the Graduate School of

The University of Texas at Arlington in Partial Fulfillment

of the Requirements

for the Degree of

DOCTOR OF PHILOSOPHY

THE UNIVERSITY OF TEXAS AT ARLINGTON

May 2020

Abstract

REINITIATION MODE STUDY OF HIGHLY IRREGULAR DETONATION

Nandakumar Vijayakumar, MS

The University of Texas at Arlington, 2020

Advisors: Dr. Donald Wilson & Dr. Ramakanth Munipalli

The propagation of detonation waves is governed by their stability characteristics. Interest in highly unstable detonation grew when early experiments revealed limits of operation to be directly proportional to the stability of detonation. This research focuses on reinitiation pathways of highly irregular self-sustaining detonation. This is an important aspect of stability which is not yet fully understood, while many possible mechanisms have been proposed in the literature. First, a one-dimensional instability model simulation was performed using a global one-step chemistry mechanism to understand the different unstable modes by increasing the activation energy of a mixture of hydrogen and oxygen. The reinitiation mode of a regular detonation was studied using a highly diluted hydrogen-oxygen mixture at 6.67 kPa. A comparative study was made with three models of reacting gas dynamics: (a) inviscid flow with a global one-step chemistry, (b) inviscid flow with multistep chemistry, and (c) viscous flow with a global one-step chemistry. Reinitiation mechanism with shock-induced combustion played a major role in the survival of a regular detonation. The drawbacks of using global one-step chemistry for a highly diluted reactant mixture were noted. The ability of a two-dimensional, inviscid CFD code with a simple ad-hoc one-step chemistry model to capture successful reinitiation of a marginal and ordinary highly irregular self-sustaining detonation was tested. Two types of reinitiation modes were categorized as triple point reinitiation and Mach reflection reinitiation. Flow features such as curved slip line and hotspot interaction were found to be the major mechanisms for a Mach reflection-based reinitiation. Inviscid numerical simulation was observed to be acceptable for regular detonations since the primary combustion mechanism is shock heating. Due to the presence of reactant jets and pockets, effects of including transport terms on the flame velocity at the unburnt reactant interface were investigated with a two-dimensional viscous oxymethane detonation simulation using a spatially fourth-order accurate WENO scheme. With the reduction in artificial diffusion using fine grid resolution, the

number of minor triple points was found to reduce. Most of the numerical study in similar works regarding the reinitiation of methane-oxygen detonation has been obtained from a single step chemistry model. An inviscid multistep chemistry model was used to simulate the highly irregular detonation using a reduced chemistry mechanism which was derived from the GRI-1.2 detailed mechanism. Two types of transverse wave structures categories based on their strength and evolution which was not captured using a single-step chemistry model were observed. The evolution of the strong transverse wave structure was addressed by studying the feedback mechanism of the Mach reflection reinitiation. Finally, the presence of transverse detonation in the highly irregular detonation has been identified and studied in detail.

Acknowledgements

I would like to first thank my supervisors, Dr. Donald Wilson, and Dr. Ramakanth Munipalli for their guidance, encouragement, and patience without which this research would not have been possible. I feel fortunate and could not imagine better advisors to provide me with their valuable time and support. Secondly, my sincere gratitude to Dr. Ralf Deiterding for providing us with the CFD code AMROC for this academic research. A special thanks to Dr. Brian Dennis, Dr. Zhen Han, Dr. Guojun Liao, and Dr. Kamesh Subbarao for serving in my dissertation committee and providing valuable insights. I would also like to thank Dr. Dora Musielak for her interest, support, and encouragement for my thesis. A note of thanks to the TACC supercomputing center for providing me with the computational resource.

Immense and continuous support from family and friends for accomplishing any work out of a person's circle of competence is implicit. It would have been impossible to persist through my Ph.D. thesis without the love and support of my wife Monisha Mohan. I am truly indebted to the trust I received from my parents and my brother on this journey when they were tested with hardships. I appreciate the motivation provided by my friends Karthikeyan Manimaran, Ajay C.K., Pengkai Ru, Siddarth Chinthamani, Umang Dighe, and Vijay Gopal who never failed to lift me during my tough times. Last but not the least, the adventure in every new day was taught to me by my furry friend Kikki.

May 29, 2020

Table of Contents

Nomenclature

A	Preexponential Factor
c_p	Specific heat at constant pressure
c_v	Specific heat at constant volume
D	Mass diffusivity
D	Detonation Velocity
D_a	Damkohler number
E_a	Activation Energy
e	Specific internal energy
f	Overdriven Factor
H	Domain Height
h	Specific enthalpy
Le	Lewis number
p	Pressure
Pr	Prandtl number
R	Gas Constant
T	Temperature
u	X component of velocity vector
v	Y component of velocity vector
V	Species diffusion velocity
Q	Nondimensionalized Heat of Formation
Y	Species mass fraction
Z	Reaction progress variable
λ	Detonation cell width
Δ	Thickness length

γ	Specific heat ratio
ν	Dynamic viscosity
κ	Thermal diffusivity
ω	Vorticity
$\dot{\omega}$	Reaction rate
ρ	Density
θ_{VN}	Nondimensionalized Activation Energy
σ	Stress tensor
τ	Shear stress term
χ	Stability Parameter

Acronyms

AMR	Adaptive mesh refinement
CD	Centered Difference
CJ	Chapman-Jouguet
DDT	Deflagration to Detonation
DNS	Direct numerical simulation
HRL	Half reaction length
KH	Kelvin Helmholtz
LES	Large eddy simulation
RDE	Rotating Detonation Engine
RM	Richtmyer Meshkov
RMS	Root mean square
SAMR	Structured adaptive mesh refinement
SWACER	Shockwave amplification by coherent energy release
WENO	Weighted Essential Non Oscillatory
ZND	Zeldovich-Neumann-Doring

	Subscript
i	Induction zone
e	Exothermic zone
u	Universal Gas Constant
VN	Von-Neumann
	Superscript
$\rightarrow$	Vector

List of Illustrations

List of Tables

Chapter-1 Introduction

Most gaseous detonations are laterally and longitudinally oscillating since a planar detonation is unstable to transverse oscillations with an amplitude greater than one to two half reaction zone thickness [1] [2] [3, 4]. Reinitiation in detonation is the process responsible for the coupling of the shock front and the reaction zone when it separates locally or substantially indicated by the velocity of the detonation complex falling below Chapman-Jouguet (CJ) detonation velocity. It is an essential process in the formation of a new Mach stem by producing a localized explosion [5, 3]. The limitations of obtaining details of the flow field from experiments, advancement in numerical methods towards predictive simulations, and expanding computational resources have created interest in studying detonation in detail using computational fluid dynamics (CFD). A reinitiation mode study focuses to understand gas dynamic response to an explosive energy addition in a localized region. This research is particularly focused on studying the reinitiation mode of methane-oxygen detonation operating at low pressures using numerical analysis. This chapter aims to provide a brief introduction to different categories of detonation and the corresponding reinitiation mechanism that was observed.

1.1 Motivation & Application

The role played by coupling between events occurring at different scales and the issues faced when ignoring smaller scales specifically in a reactive flow has been explained in detail by Powers [6]. The performance of a detonation-based engine may be predicted well using an analysis with an overall scale of the engine in the order of meters which captures the right pressure and velocity profile. But the key phenomenon such as transverse wave dynamics, reinitiation of cells, transport of flame, etc. occurs at length and time scale at orders of magnitude smaller than engineering scale. It is at this scale which the propagation sequence of a detonation takes place and varies significantly with thermodynamic conditions. In the series of events supporting the propagation of a detonation wave, reinitiation plays a key self-sustaining role and is often composed of triple point reflections with the additional influence of mixing layers and vortices. The knowledge gained from a detonation physics research can potentially contribute towards the design and performance of detonation engines. For example, Lu et al. [7] question if the hotspots at

the vicinity of triple points can destabilize a detonation in a Rotating Detonation Engine (RDE). The mechanism of the production of hotspots is also questioned in the same paper. Hotspot is one of the pathways through which reinitiation of highly unstable detonation occurs and events leading to a hotspot are studied in this thesis. On the other hand, the role of understanding of propagation mechanism in avoiding the failure of detonation and subsequent reinitiation of the detonation in such events can be necessary. The critical diameter for a successful transition from the pre-detonator to the combustion chamber depends on the detonation propagation mechanism as explained in section 1.5 and in ref [8, 9]. It is well known that detonation initiation can be achieved by a deflagration to detonation transition (DDT) process involving flame acceleration or direct initiation process involving a powerful ignition [2]. A decoupled shock-flame complex also reinitiates a new Mach stem either through DDT or a local explosion center via triple point collision. This thesis contributes to the existing state of knowledge of the mechanism of detonation operating in low pressures by breaking down the physics involved in those events through a systematic analysis.

1.2 Detonation Stability Limit

When a one-dimensional Zel'dovich-von Neumann-Doring (ZND) detonation is perturbed, the detonation begins oscillating laterally creating a pressure profile with harmonic oscillations. If this perturbation dies within a short period it is a neutrally stable detonation. The limit until which this perturbation dampens is the stability limit of detonation for the respective Mach number. If this perturbation grows and reaches a steady oscillation cycle (also called a limit cycle [10]) it is a weakly unstable detonation. Weakly unstable detonation contains single and a regular prominent mode of oscillation. The characteristics of this single unstable mode can be measured with its growth rate, amplitude, and frequency. A single unstable mode means it contains only one peak pressure value in the limit cycle of the detonation [11]. The transition in the stability of detonation can be predicted using a stability parameter relating to the chemical properties of the detonation. The global activation energy behaves like a stability parameter since the increase in activation energy increased instability in detonation [12] and was chosen through experimental visualization, power spectral analysis, computational analysis and stability analysis [12] [13] [4] [14]. The

following diagram shows the influence of reduced activation energy on the degree of irregularity by deviating from the neutral longitudinal stability curve [12] [13].

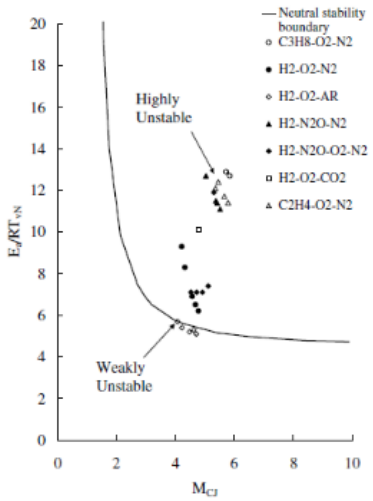

Figure 1-1 Comparison of Degree of Instability for Different Mixtures (taken from [12])

Erpenbeck [15] used $Q, E_a \; and \; f$ to determine stability boundaries in one dimension. Short and Sharpe recognized the role of ratio of induction to reaction zone through chain branching cross over temperature parameter using a using two-step induction parameter model [16]. Later using a similar two-step induction parameter chemistry model, Ng developed a stability parameter model through one-dimensional instability analysis by correlating the induction and reaction zone length scales along with activation energy [11]. This parameter was validated for the stability of detonation with a wide range of mixtures by Radulescu [17] and found a good agreement.

$$Stability\ Parameter = \chi = \frac{t_i}{t_e}\left(\frac{E_a}{RT}\right)\left(\frac{Q}{RT}\right) \qquad 1\text{-}1$$

The stability parameter (eq 1-1) accounts for the three most important parameters which can be chosen to describe the nature of detonation as well as to measure from a one-dimensional analysis. The first parameter is the ratio of the induction zone to the reaction zone. This accounts for the time scale of the feedback pressure pulses from the reaction zone before reaching the front. The second term is the non-dimensional activation energy which is a measure of the energy required by the reactants to reach the exothermic phase. The third parameter is the non-dimensional heat of formation which provides for the

change in sensible enthalpy depending on the mixture. With the increase in this stability parameter, additional modes start to appear in the pressure evolution graph through periodic doubling slowly deviating from regular harmonic oscillations until reaching a highly unstable state. When the stability parameter for the chosen Mach number is too far from the neutrally stable limit, multiple unstable modes in irregular patterns (aperiodic) are produced by the shock pressure history graph which is categorized as highly unstable detonation. The numerical resolution of the grid required to capture the unstable modes with lower wavelength creates a constraint on simulating highly unstable detonation [11, 18]. Further increase in stability parameter pushes the system to become chaotic. The relationship between the stability parameter to the propagation of detonation is detailed in [19].

In weakly unstable detonation, the energy released by particles with different ignition time results in compression waves which was found to be in coherence with each other giving a global structure appeal [20]. This was because of the reduced sensitivity to temperature fluctuations on the induction zone and reaction zone time scale being of the same order as the induction zone time scale. Whereas in the case of highly unstable detonation, the length scale of the induction zone is at least an order of magnitude larger than the reaction zone thickness and the rate of reaction is highly sensitive to temperature fluctuation. The timescale between the compression pulses varies significantly, because of its temperature sensitivity, missing the coherence and to cause an irregular detonation front. It has been proven that the natural inclination for a mixture with high stability parameter results in a strong accelerating blast wave from hot spot ignitions due to the gradient in reactivity and coupling between reaction time scale and acoustic time scale [19]. In a different isolated study of inducing heat through the wall in a tube, it was clarified that, when the reaction rate is fast, the energy release was determined to result in shock waves propagating away from the source [21]. To give a brief introduction to the hot spot, shock-induced ignition can occur in two different modes depending upon the pressure and temperature of the heated reactants [22]. For a very strong shock wave like a blast wave, the ignition is sharp and abrupt. For a weak shock wave, the ignitions occur mildly with the formation of spots of reacted materials. A hotspot is an ignition center with temperature and the rate of reaction higher than the surrounding reactants processed by a shockwave [22]. Local hotspots or reaction centers are common in a compressed and heated unreacted material behind the shock

or unreacted peninsulas behind the turbulent flame front [2] [23]. The reason for the formation of a hot spot has been analyzed and credited to the inhomogeneous initial state causing the chemical activity to proceed at different times [24]. The difference in the strength/timing of the pressure pulse, incident shock strength or hydrodynamic instabilities cause this inhomogeneity [19, 25, 24]. A weak blast wave from hotspot merges with the precursor shock to form an overdriven detonation [2]. Lee has proposed a mechanism in which a compression wave, which travels faster than the flame, amplifies into a reactive detonation wave rapidly due to the shockwave amplification by coherent energy release (SWACER) mechanism if the environment surrounding the compression wave is preconditioned for chemical energy release to synchronize with the wave [2]. Oran et al., confirms the SWACER mechanism in multiple numerical studies of experimental setups [26] [23]. The waves from the hot spot travel in both directions, interacting with both the flame and the precursor shock. It was observed that stronger precursor shock with intense turbulence produced hot spots closer to the flame [23]. Detailed work on the hot spot by mathematically analyzing its initiation, structure, and development can be found in more detail in the research by Jackson et al. [24].

1.3 Evolution of the Cell Cycle

The onset of linear instability or perturbation is due to the amplification of acoustic waves which is bounded by the hydrodynamic thickness, high sensitivity of chemical reaction rate to post-shock temperature, and hydrodynamic instabilities [27]. Hydrodynamic thickness is the distance between the precursor shock and the unsteady sonic plane of a three-dimensional detonation [1]. In computational studies formation of transverse wave [4] where a ZND overdriven detonation transitions to a planar steady-state CJ detonation can also arise due to numerical perturbations from the shock front caused by smearing of the shock. When the growth of this linear perturbation is sufficiently large it gives rise to coupled longitudinal and transverse instability [12]. The presence of transverse waves was not suspected until experimental studies performed in the late 1950s [27]. The cellular structure of a detonation wave is three dimensional with transverse waves reflecting from the bounded walls. The propagation direction of the transverse wave in a round tube is circumferential and radial whereas in a rectangular tube it is orthogonal [12].

A triple point or a Mach reflection is an intersection of incident shock, Mach stem, and transverse wave and the oscillation of the triple point along the lead shock creates a reproducible cell structure. A tangential discontinuity usually called a slip line is a contact discontinuity that arises from the triple point in a Mach reflection forming an interface between gas behind Mach stem and gas behind the incident shock. The flow properties on either side of the slip line except for the static pressure and normal component of velocity are different [28, 29]. For a Mach reflection, the shape of the slip line depends on several factors such as the Mach number of the incident shock, the deflection angle, and the specific heat ratio of the gas. For gases with low specific heat, this slip line tends to curve forward towards the Mach stem resulting in a forward jet [30]. In several environments such as the flow field observed in RDE, this slip line becomes unstable and results in a Kelvin-Helmholtz (KH) instability [31]. The role of an unstable slip line from the transverse waves was questioned if it leads to the decoupling (by transporting unreacted material) or aids the recoupling process (increasing the reaction rate) [12]. The inflection point in this slip line leads to vortex rollup eventually causing a mixing layer through KH instabilities [32]. The differential kinetic energy of the two steams is the source for the KH instabilities and these instabilities diffuse the gradient between the two fields [33]. The mixing layer is fully turbulent and causes mixing between two adjacent flows in which one region moves faster. The triple points are formed by several mechanisms in a detonation: (a) when shock front comes in contact with a solid surface (boundary layer shock interaction or with an incident angle), (b) when the incoming shockwaves interact with the lead shock front in detonation [34], (c) when detonation enters a diverging area [3] and (d) when the inflection point is formed in the Mach stem which straightens instead of being concave [35]. When a non-reactive shock interacts with a solid surface it either forms a reflected shock or a Mach reflection [30]. More analysis of nonreactive Mach reflections can be found in the book by Ben-Dor [36].

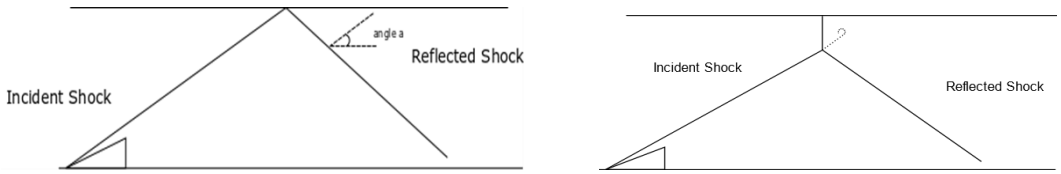

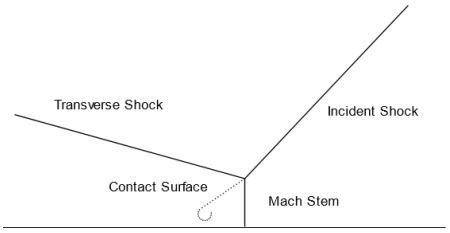

Figure 1-2 Illustration showing the formation of Mach Reflection

Sometimes a few triple points moving in the same direction coalesce whereas other triple points diminish with the average number staying the same after reaching quasi-steady-state [4]. A detailed study behind the reason for the formation of the triple point due to inflection points in the flow behind detonation when there is a local decoupling of reaction zone from the shock front was studied by Oran et al. [35]. Two types of triple point structures namely weak structure and strong structure have been documented. Weak structure triple point has a single Mach transverse configuration and the strong structure configuration has a double Mach transverse wave configuration [37, 38]. The following sketch shows a strong triple point configuration with a second transverse wave.

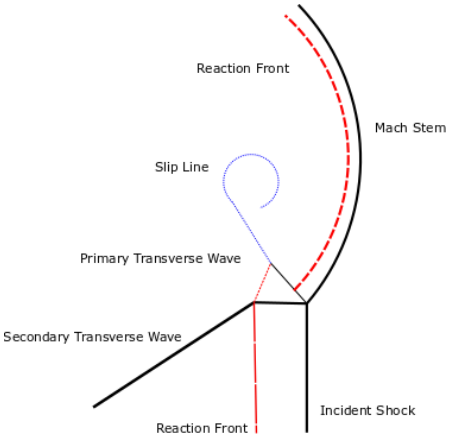

Figure 1-3 Schematic of Strong Triple Point Configuration

The induction zone length is shorter behind the Mach stem and longer behind the incident shock. A contact surface (commonly referred to as slip line) is formed between the products of the primary transverse wave and Mach stem. Transverse shock waves interact with shockwaves of the opposite family and create a local increase in pressure and temperature forming a bounded region and increase the velocity of the lead shock enclosing this region. As the shock travels faster, the gas enclosed within this region

expands decaying the shock strength forming a cell cycle [12]. This longitudinal instability gives the multifront appearance of the lead shock. The transverse wave propagates into the reaction zone at a local acoustic velocity relative to the shock front. Depending upon the regularity of the cell structure created by the triple points, a freely propagating developed detonation is categorized into regular detonation (regular spacing of transverse waves) and irregular detonation (irregular spacing of transverse waves). The more irregular a detonation is, the higher the pressure created by the triple point structures [4].

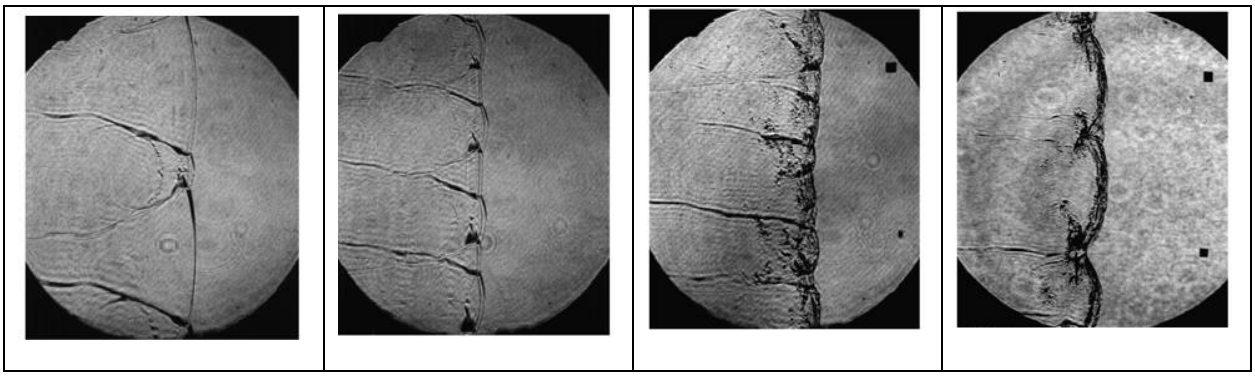

Figure 1-4 Stability decreasing from left to right (taken from [12])

The above diagram shows the influence of the increasing irregularity of the structure with activation energy. Theoretically, this can be illustrated by showing the sensitivity of the reaction rate to temperature with a simple derivation. The change in product mass fraction of a global one-step reaction (Z) is given by

$$\frac{DZ}{Dt} = k(1 - Z)\exp\left(-\frac{E_a}{RT}\right) \qquad 1\text{-}2$$

After a small perturbation in post-shock temperature, the change in product mass fraction is given by [12],

$$\frac{DZ'}{Dt} \approx k(1 - Z)\exp\left(-\theta\frac{T'}{T_{VN}}\right) \qquad 1\text{-}3$$

We can see that the distribution of perturbation of product mass fraction has reduced activation energy by a multiplication factor. The linear stability theory predicts when fixing all parameters but increasing just the reduced activation energy makes the detonation more unstable to small perturbations [27]. A schematic diagram of one complete cell cycle of an ordinary regular detonation is shown in the diagram below (Figure 1-5). A detonation cell is formed when the products behind the Mach stem expands resulting in movement of triple points away from each other. After the triple points bounce from a wall, they

approach each other. The final 25% of the cell cycle is the reinitiation phase. During this reinitiation phase, a substantial amount of energy is imparted into the mixture in a very short time. A clear comparison of the reinitiation sequence with a direct initiation sequence is made in the work of Lee [5].

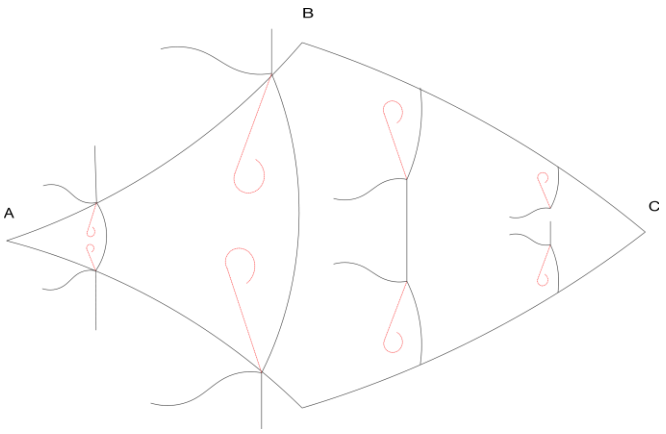

Figure 1-5 Schematic of a Single Cell Cycle

Few categories of detonation are essential to be briefed to understand the reason why different reinitiation mechanism are proposed for irregular detonation.

1.4 Marginal and Ordinary Detonations

Depending upon the velocity profile of the detonation front, detonation can be categorized to be a marginal detonation or an ordinary detonation. The instantaneous velocity can be found to vary in the range of $1.25 - 0.85\ D_{CJ}$ for ordinary detonation and $1.4 - 0.7\ D_{CJ}$ for marginal detonation [12]. The experimental average velocity of a self-sustained ordinary detonation wave is reported to be close to CJ velocity whereas for a marginal detonation it is $0.8 - 0.9\ D_{CJ}$ [3]. A marginal detonation represents a detonation very close to its detonation limit and may fail if the initial pressure is reduced further, more diluent is added, or if the operating chamber size is made narrower [35, 37]. The more marginal the detonation is, the stronger the transverse waves are for the same mixture, creating a possibility for transverse detonation [35]. From the literature study of experimental and numerical works, secondary cells are found to appear for reactants with high activation energy $(E_a/RT_{ZND} > 6.5)$ operating marginal limits [39, 40]. By adding diluents in the reactant mixture, the value of the Von-Neuman temperature is increased by increasing the shock strength due to the greater value of polytropic exponent (γ) [4]. Change in the flow behind a shockwave by just

changing γ was also investigated in [41]. Further discussion regarding the marginal detonations can be found elsewhere [42, 37, 4] The difference between both types of detonation can also be found in a detailed numerical analysis of Taylor et al. [43].

When considering the stationary detonation case, the computational domain is a function of detonation velocity D. And, for a given mixture and fixed initial temperature, the exothermic time scale reduces with an increase in initial pressure demanding smaller time steps, especially with explicit CFD codes. Marginal detonations give an advantage in this scenario since both their half-reaction length is thicker compared to ordinary detonations due to weak shock front and their average detonation front velocity is less in lower pressures. Considering this reason, the methane-oxygen detonation at 3500 Pa and 6000 Pa was chosen in this study to take advantage of the computational economy.

1.5 Regularity and Instability in Detonations

The relationship between instability and irregularity is straight forward. In section 1.2, it was explained that for highly unstable detonation, the amplitude and frequency of the pressure pulses from the reaction zone were high. This causes the appearance of the detonation front as well as the cell structures on a soot foil to be very irregular. Few reported properties for varying instability in literature are stated in this section before discussing respective reinitiation mechanisms. For weakly stable detonations the ratio $\frac{\Delta_i}{\Delta_e}$ ranges from1 to 10 [27]. But for a highly unstable detonation, this ratio has been measured from 20 up to 60 [44] [27]. One dimensional detonation simulation reveals that with the increase in activation energy and induction length to the energy release ratio, the lead shock amplitude oscillation increases until the detonation ceases and decays [27].

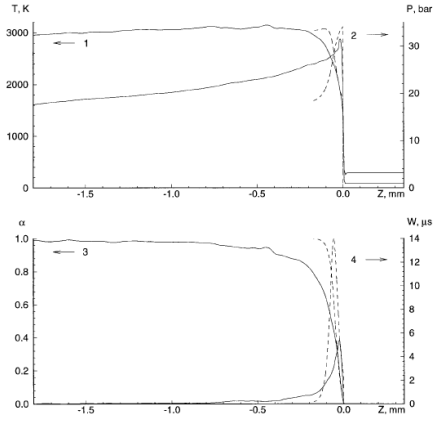

Figure 1-6 Comparison of profiles of moderately unstable detonation (continuous line) with a steady ZND solution (dashed line) (taken from [4])

The transverse waves are weak in strength and travel with acoustic velocity in weakly unstable waves but travel with a velocity higher than acoustic velocity and are stronger in highly unstable waves [4]. The longitudinal instability increases with irregularity which can be shown from the graph of average detonation velocity along the x-axis below [4]. We can see that the highly unstable detonation has oscillations leading to higher amplitudes well above and below CJ detonation velocity.

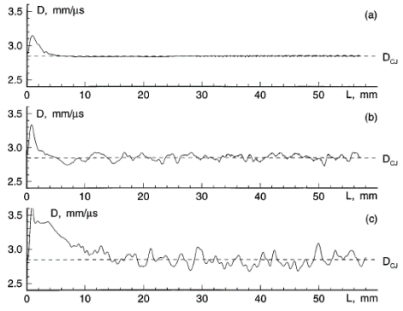

Figure 1-7 Shock Velocity as a Function of Distance a) $\theta_* = 2.1$ b) $\theta_* = 4.9$ c) $\theta_* = 7.4$ (taken from [4])

A study by Radulescu gave a correlation of failure of detonation waves on porous walls [9]. An argon diluted hydrocarbon detonation wave survived for 100 λ in a porous wall and died due to loss of mass and momentum of the expanding gas were as in undiluted hydrocarbon mixture the cancellation of transverse waves leads to failure at 3-7λ. The scaling factor of critical diameter to cell width for a transition of a detonation successfully from a tube to unconfined space has the irregularity of the mixture as a factor

(irregular mixture $D_c = 13\lambda$ & 40λ for regular mixtures) [12]. Further study about the role played by the mixture composition for DDT resulted in a faster transition length for highly unstable detonation (7 λ) compared to weakly unstable detonation (40λ) [27]. Higher frequency of appearance and disappearance of triple points and large variation of shock intensity amplitude were two possible theories for the insensitivity of the highly unstable detonation to perturbations due to external boundary which are less in amplitude relatively [4]. The size, penetration distance, and consumption mechanism of unreacted pockets increase with activation energy [4]. Statistical analysis of two cases by Liang et al. [45] gives a comparison from experimental measurements of stable (case 1) and unstable (case 2) detonation. The diagram to the left compares the relative frequency of traveling detonation velocity for the two cases for which the highly unstable case travels with velocity below CJ velocity most often initiating decoupling of reaction front. In the diagram to the right we can compare the Joint Distribution Function (JDF) of unstable detonation with iso-volume CJ combustion model representing ideal detonation which shows that, except for values close to CJ velocity, the reaction zone thickness varies widely.

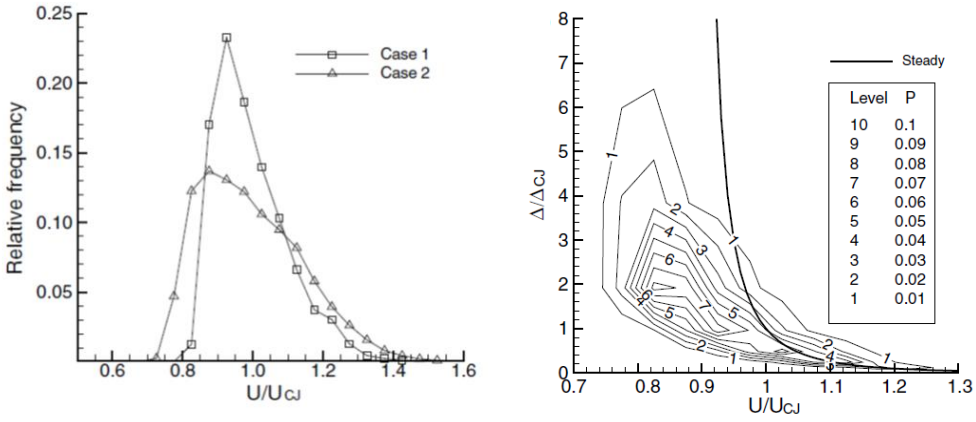

Figure 1-8: a) Relative Frequency of Case 1 & 2 b) Joint Probability Distribution of reaction length ratio of Case 2 (taken from [45])

A method to determine the deviation of the detonation mechanism from the usual shock heating mechanism proposed by analytical methods such as ZND theory is to determine the average sonic plane location in the products of the detonation. Two important processes influencing this location are chemical

exothermicity and production and destruction of mechanical and thermal fluctuations in reaction zone [44]. Gamezo et al. discusses three different mechanisms for the unburnt reactant pockets for varying reactant activation energies [4]. For low activation energy, the reactant auto ignites from the shock and transverse waves (hydrogen-oxygen detonation diluted with argon). For moderately unstable cases, molecular diffusion is expected to play a vital role. For highly unstable detonation, the hydrodynamic instabilities aid by breaking the pockets into smaller fragments [4]. To date, it is believed that the methane-oxygen detonation falls under the third category [46].

1.5.1 Weakly Unstable Detonation

The weakly unstable detonation is classified with one prominent transverse wavelength with $\theta \sim 5$ [27] [47]. For weakly unstable waves, the transverse waves tend to be a reactive shockwave that consumes the unburnt reactants [12] [27]. A weakly unstable detonation with regular cell pattern has only one transverse wavelength and a smooth wave front [34]. In a narrow channel, weakly unstable detonation is seen to have a weak triple point configuration [12]. The keystone features (explained in detail in Chapter-4) which appear due to the spatial instability of the shock front with shear layer separating burnt and unburnt gases is present in weakly unstable detonation [12] [47]. More details regarding weakly unstable detonation are presented in Chapter-4 along with the analysis of its reinitiation method.

1.5.2 Moderate Unstable Detonation

Austin et al. mentions a moderate unstable detonation category ($\theta \sim 7$). The cell structures recorded in the soot foils are less regular when compared to the weakly unstable detonation with a system of secondary transverse waves that are observed throughout the cell [47]. In the same study, a closer look at the keystone features shows an incident wave surrounded by several KH shear layers segregating reacted and unreacted gases. Above observations were also observed in experimental as well as numerical studies by Gamezo et al. [48, 40] where detonation waves moving in transverse waves (primary instability), overdriven parts of shock front and instabilities of transverse detonations were found to be influencing the propagation of acetylene-oxygen detonation in marginal conditions.

1.5.3 Highly Unstable Detonation

Since the structure of highly unstable detonation is the focus of the study in this thesis it is elaborated in this section based on previous experimental and numerical analysis [41] [44] [2]. After the planar detonation becomes cellular due to instabilities at some point in time, the cellular detonation front develop stronger and weaker part. The shock ignition in the high activation energy mixture is inefficient and decays from the beginning of a cell cycle. This is also seen when a one-dimensional unsteady hydrocarbon detonation is performed [34] where the decaying shock does not survive with the absence of triple points. The reaction front is influenced at different ranges of length scale and has a larger critical ignition delay resulting in decoupling between lead shock and reaction zone in different regions [12]. The triple point which oscillates along the front adjoins the stronger and weaker detonation. A large part of the lead shock is non-reactive creating an atmosphere for the post-shock conditions to have an interface between reacted and non-reacted gases [1]. The triple point gives rise to non-reactive transverse shock and strong shear layer separating reacted and unreacted gas. The movement of triple point pinches the unreacted gas which forms the pockets of gas drifting downstream. This forms the primary cell cycle. A sub-cycle or secondary cycle in highly unstable detonation has been reported often though both experimental and numerical studies. Two prominent length scales for the cellular structures on soot foil and in numerical studies have been reported along with the absence of a distinct keystone structure [47]. For highly unstable cases, a localized explosion is also observed in several experimental and numerical cases [12] [47] [35]. Two different reasons are reported for these minor explosions. The first proposed reason is the hot spots created by the collision of transverse waves before the collision of triple points [49]. The second proposed reason is the action of hydrodynamic instabilities on unburnt reactant pockets creating reaction waves [2]. The transverse shock wave interacts with unburnt reactant pockets and breaks them down into smaller fragments through compressible vortices. Both methods are expected to experience a hot spot ignition pathway. A large spectrum of transverse waves is interacting both parallel and perpendicular to the mainshock front [34]. In a highly unstable detonation, the lead shock is highly irregular with structures of varying length scales being visible [47]. Less OH concentration in regions appears for a highly unstable detonation showing less reactivity and a bright OH concentration in the regions where transverse waves collide recording minor

explosive events [12]. These secondary cell structures hint the possibility of overlapping cells leading to a corrugated shock front [47]. During the lower limit of the lead shock velocity, approximately, $M{\sim}0.8M_{CJ}$, a local decoupling of the reaction zone and the lead shock is observed [12] [47]. A notable event in highly unstable detonation is “clipping” was the VN pressure drops below the global maximum pressure [38] [50].

1.6 Reinitiation Phase in Cell Cycle

The structure of a detonation is highly transient in multidimensions, making it difficult to derive a unique and meaningful average. Reinitiation occurs at the beginning of a cell cycle with a sudden outburst of energy resulting in an overdriven detonation that relaxes to a CJ detonation with time. For a regular detonation, reinitiation can be from the phase where the transverse wave of the opposite family has started to interact and end when the new Mach stem with two triple points emerges.

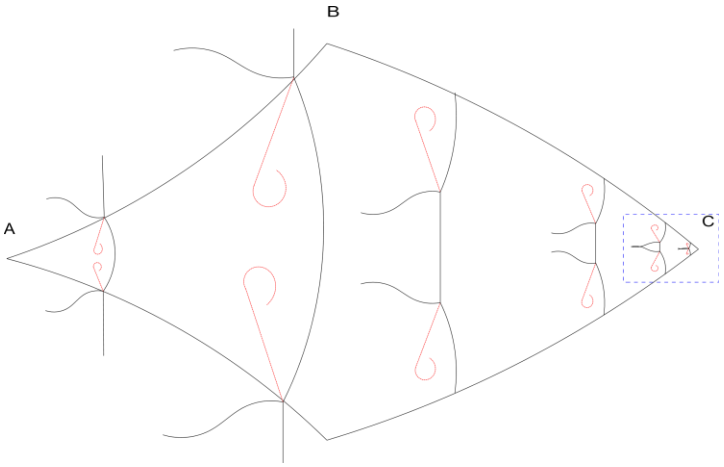

Figure 1-9 Reinitiation Phase Highlighted in Cell Cycle

Depending on the operating mode of detonation, the reinitiation mechanism varies for marginal/ordinary and regular/irregular mixtures. In this thesis, we focus on two cases: regular-ordinary detonation and irregular-marginal detonation. One major factor permitting different mechanisms for reinitiation in regular and irregular detonations is the shock front decay time [10]. It is shown that the induction time increases more than an order of magnitude for irregular detonation when compared to regular detonation for the same level of reduction in shock front velocity [12]. An analytical experiment was performed by Eckett et al. [51], wherein one cell cycle frame of reference when the time taken for the decay

of the shock was less than a critical value $t_{d,c}$ predicted by an one-dimensional model called critical decay rate (CDR) model, local decoupling occurs and was demonstrated for several mixtures from experiments [12, 51]. This CDR model takes chemical heat release, curvature, and hydrodynamic unsteadiness into account using single-step chemistry, temperature reaction zone structure equation. To understand the change in the physics of detonation when regularity is varied for ordinary detonations, a good initial point would be from the work of Gamezo et al. [4] in which detonation in a heat release profile equivalent to the stoichiometric hydrogen-oxygen mixture is investigated by varying the reduced activation energy using a global one-step chemistry model. The operating pressure, temperature, and computational domain are chosen to ensure an ordinary detonation. Similarly, an experimental work of comparison of ordinary detonations with varying regularity can be found in the work of Austin [47]. A stoichiometric methane air-based irregular ordinary detonation study can so be found in Kessler et al. [39] operating at atmospheric pressure with multiple cells. The transformation from irregular marginal detonation to the irregular ordinary detonation of a methane-oxygen detonation can be seen in the experimental work of Bhattacharjee [52] where transverse detonation waves were seen at 12 kPa forming secondary cell patterns.

1.6.1 Regular Ordinary Detonation

Reinitiation in regular ordinary detonation using argon diluted hydrogen-oxygen has been studied both experimentally and numerically for varying percentages of the diluent. Experimental analysis of 70 % diluted hydrogen-oxygen mixture at 6.67 kPa was performed by Dormal et al. [53], Libouton et al. [54] Lefebvre [55] and Eckett [10]. Numerical analysis performed by Lefebvre et al. [56] with a two-step induction parameter model concluded that the mass density behind triple points was quite high which explains the reason for dense energy release. Since the Mach structure converted from single Mach structure to double Mach structure, this detonation was categorized to be marginal in that work. The reinitiation process for a new detonation cell was shown to be due to interacting transverse waves forming a rectangular high energy region when triple points collide. This rapid energy release leads to a new locally overdriven shock front with two new triple points diverging with time and resulting in relaxation of the high energy-dense region. Oran et al. [42] studied the reinitiation mode further using a detailed chemistry model and gave a further description of the reinitiation mode based on the energy release density and its percentage length in a cell.

In addition to the high energy release of transverse wave collisions, the triple points collision created a circular high energy region that ends in an explosion that reignites the detonation when transverse waves collide. Eckett [10] also obtained a similar energy release profile. The reinitiation was further verified in the work of Deiterding [38] in both 2D and 3D by using detailed chemistry and in-depth grid resolution with a minimum of 0.031 mm. A numerical study with detailed chemistry and a grid resolution of 0.025 mm was performed by Hu et.al. [37], to study the reinitiation phase in-depth. It was stated that the reinitiation phase is a three-step process. More recent work on the comparison of both experimental and numerical work for argon diluted hydrogen-oxygen mixture was performed by Gallier et al. [57] to study the diffraction and re-initiation of the detonation.

The process of reinitiation of detonation for this scenario is explained based on the database available in the literature stated above using a schematic illustration. The origin of a new triple point from the inflection region is discussed elsewhere [35]. Let us consider the following scenario of two strong triple points A and B approaching each other in the following schematic sketched in chronological order from left to right. The triple point oscillates longitudinally along with the shock front. The induction length behind the Mach stem is less than the induction length behind the incident shock since Mach stem is stronger. We can see that the secondary transverse waves have met already at C in the frame (a). When the triple points also collide at D (frame (b)), a high pressure and temperature region is formed which is enclosed by heated, unreacted reactants. The transverse wave bounces off each other almost perpendicular to this unreacted gas and triple point collision forms a very high temperature zone than the rectangular region (frame (c)). Point D forms a kink often known as a key like a zone as a result of the new Mach stem. Combustion caused reflected transverse wave creates a pressure wave at D which merges with the shock front. The reflecting transverse waves merge with the new Mach stem forming triple points that move away from each other (frame (d)).

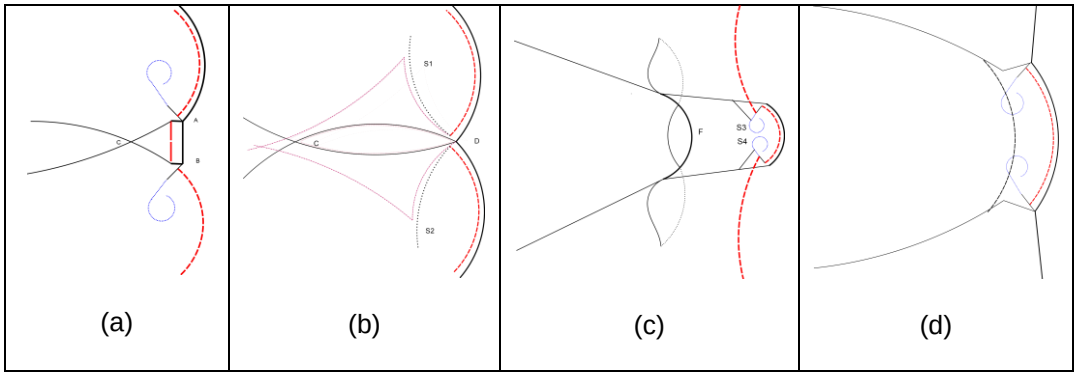

Figure 1-10 Schematic of Reinitiation Phase for Regular Ordinary Detonation

We can see that shockwave heating is the dominant mechanism of combustion in regular detonations. A more detailed version of this reinitiation process based on our numerical simulations is analyzed explained in chapter 4. It was briefly explained in this section to understand the contrast in the reinitiation process when compared to highly irregular detonation explained in the next section.

1.6.2 Irregular Marginal Detonation

The following description is an effort to explain the reinitiation of methane-oxygen detonation based on experimental and numerical studies at low pressures. Since it is an ongoing research and an important part of this research, definitive conclusions are still to be derived. Reinitiation of a decoupled shock-flame complex in an irregular detonation has been proposed to occur by either one or a combination of five different mechanisms namely [52]; fast reaction rate behind Mach stem (which applies to both regular and irregular detonation), KH instability, RM instability, transverse wave detonation, and strong jet formation during transverse shock reflection. Experimental results from the work of Kiyanda et al. [58] on single-headed methane-oxygen detonation using high speed self-emitted light photography give visual evidence of the reinitiation in irregular detonation to take a deeper look into this sequence. Reinitiation of Mach stems was observed by two pathways. First through triple point reflection and second through a hydrodynamically-generated Mach stem. With the occurrence of two different methods to generate Mach stems, irregular detonation does not operate based on one single mechanism as a regular detonation does. It is interesting to point out that just by observing the structure, a prominent difference in the irregular detonation is the tongue like reactants forming behind the triple point in the place of slip lines in a regular detonation as shown below.

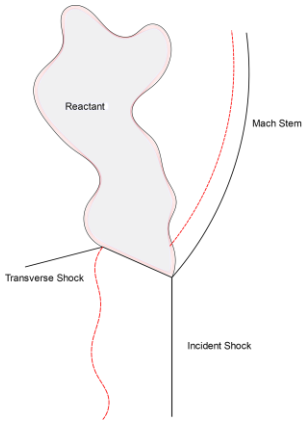

Figure 1-11 Schematic of Triple point in Irregular Detonation

It can be recognized that the edge of this tongue is formed by a contact surface and since it is exposed to a reacting environment, a flame. Intense luminosity in the experiment [59] confirms it. As shown in the schematic, the transverse wave processes the unburnt material in the induction zone but fails to burn it. The triple point collision with the wall reinitiates the Mach stem. This mode of reinitiation will be addressed as a *triple point reinitiation* in this thesis. When the transverse wave hits the boundary and is reflected normally into this heated reactant tongue, rapid combustion occurs, and a localized explosion is recorded along with the formation of new Mach cells. Burning of unburnt pockets due to repeated shockwave interaction demonstrates similarity with the first pathway to achieve DDT as discussed earlier if not only through direct shock wave autoignition.

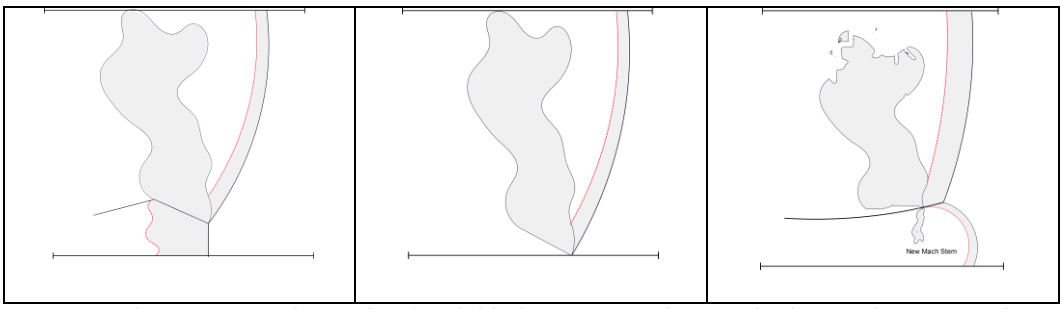

Figure 1-12 Schematic of Reinitiation Process in Marginal Irregular Detonation

The second method of reinitiation that was reported from the same experiment was by generating a new transverse wave because of a self-generated explosion center. Self-generated triple points for a regular detonation by inflection point has been mentioned in the literature before [35, 38]. This new triple point collided with another triple point which was already present to create a new Mach stem. The sudden

energy release due to the fast reaction of unburnt heated gas was recognized but the reason for this formation of explosion centers near the walls was not further investigated. Another study of the reinitiation mechanism of highly irregular detonation [60] investigated methane oxygen detonation through numerical and experimental work clarified the self-generated explosion from a sequence of images of density gradients obtained from schlieren images. It was proposed that the shear layer between the unreacted gas in the tongue structure and the reacted gas from Mach stem is a KH instability. This instantly mixes and entrains the reactants and products through the roll-ups it produces creating a bed of “hot spots”. This second mode of reinitiation will be referred to as *weak reflection reinitiation* in this thesis. Apart from the weak reflection reinitiation mode, the author [60] also reports local explosions in the reaction zone. The cause of these explosions was speculated to be due to the interaction of transverse waves on separated reaction front causing an instantaneous increase in reaction rate either due to RM instability or SWACER mechanism. The hotspot reinitiation was also suspected for weak reflection reinitiation mode in another experimental study of methane oxygen detonation where the grid induced gases behind the shock front reacted and released a strong pressure pulse which accelerated the lead shock [60]. The numerical counterpart of the same experiment where a two-dimensional, Euler equations with one step chemistry to omit the instability and turbulence effects resulted in the failure of detonation. In a different work, the weak reflection reinitiation was observed and discussed from the standpoint of a possibility of shockwave amplification by coherent energy release (SWACER) mechanism due to localized mixing resulting in the explosion [61]. To further clarify the mechanism, a single-headed shock was passed through a grid plate. Results from this experiment indicated that intense energy release was correlated with the grid induced oblique shocklets and turbulent reaction zone interaction. Hence weightage was provided on turbulent mixing of hot and cold reactants either through KH instability or RM instability and the pressure wave arising from this sudden exothermicity is correlated to the feedback provided by the reaction zone to decaying shock front to be responsible for weak reflection reinitiation.

A separate reinitiation study was performed for oxy-methane detonation by Bhattacharjee in a thin rectangular channel to investigate the reignition mechanism at different initial pressures and several finds were stated [62] [52]. The reaction zone of a traveling detonation wave was artificially separated by placing

an obstacle in its path to isolate and study the reignition mechanisms responsible for both triple point reignition and weak reflection reignition. The variation in reinitiation modes was showcased with varying initiation pressures. For initiation pressure below 5.5 kPa, the detonation quenched after passing through the obstacle. For weak reflection reinitiation at around 10 kPa, the primary role of bringing the burnt products in the vicinity of unburnt reactants behind the grown Mach reflection is credited to the forward jet. The first event in this sequence is the curving of the slip line in forwarding direction due to the pressure profile behind the transverse wave and the wall boundary. This creates an environment of hot unreacted gases and products to mix.

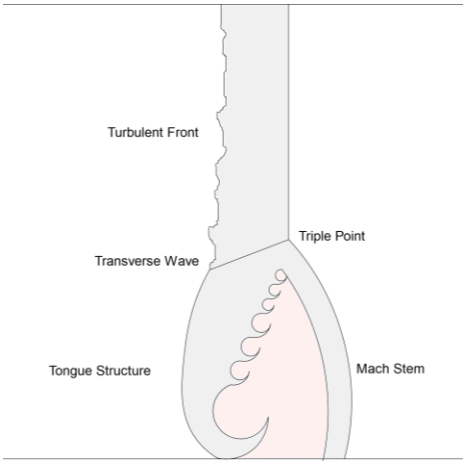

Figure 1-13 Schematic of Reinitiation Observed in Marginal Oxymethane Detonation

Following the formation of a mixed burnt/unburnt region as shown in the diagram above, a sudden increase in reaction lead to the reinitiation. From ignition time delay studies, this sudden increase in the reaction was credited to hot spot formation and not the influence of Mach stem. The hot spot theory was also confirmed by performing a rough plate wall experimental test and calculating its induction time in the same work [62]. Hot spots formed behind transverse waves also resulted in transverse detonation for the initial pressure of 12.5 kPa. The setup and mixture conditions in [62] were simulated numerically by using two dimensional Euler equations with one step and two-step chemistry to study the reinitiation mechanism of highly irregular detonation further by Lau-Chapdelaine [63]. The decaying detonation quenched immediately for a pressure of 5.5 kPa and eventually died for 10.3 kPa. Successful reinitiation through weak

reflection reinitiation for both a one-step and two-step chemistry model was observed for an initial pressure of 11.9 kPa. In the sequence of events where the weak reflection has led the non-reacting triple point to move upwards, the reinitiation proceeded via hot spot formation along the wall where the triple point reflected. The role of the forward jet was clarified to be transporting the flame pocket formed by hot spot when the separation between the shock and the reaction zone is large enough to inject the flame behind Mach stem. For the 12.5 kPa case, the forward jet was strong enough to carry the flame from the reaction front to increase the speed of the Mach stem. In addition to it, more hot spots were found behind the main triple point. The triple point reinitiation mode was observed at 17.6 kPa. Though the experiments observed transverse detonation, the chemistry solved by the two-step model was not enough to predict a sustaining transverse detonation. The role of KH instability and RM instability was sorted to be non-influential in the perspective of the reinitiation of detonation. A notable feature of irregular detonation apart from the reinitiation mechanics is the unburnt reactant pockets which travel detached from the shock front. This is formed when the triple point hits a solid surface and pinches off the attached reactant zone. The consumption mechanism of these pockets is of interest in many works in the literature since it is consumed within the average sonic plane [49, 52, 12, 47, 64]. The rate of consumption of unburnt reactant pockets in methane-oxygen detonation is orders of magnitude less than theoretical shock-induced combustion. This has been analyzed by Maxwell [46] [65] using compressible LES simulations using one equation chemistry model. Two proposed theories are transverse wave interaction with unburnt pockets and vorticity produced by KH instability leading to mixing between burnt and unburnt gases [44]. A recent study based on reactive Euler equations and global one-step reaction for a low-pressure methane-oxygen detonation prove the consumption of unburnt pockets is still possible at fast rates without solving for turbulence with very fine grid points by Kiyanda et. al [66]. A detailed resolution of 320 grid points per ZND half-reaction zone length was used. It is acknowledged that the consumption mechanism of these drifting pockets is an open problem, but it does not seem to influence the rapid dynamics of the shock front and it is of secondary importance in this thesis. A direct comparison of the numerical setup from this research can be made with the research published by Radulescu et.al [44] where a self-sustained highly irregular detonation had been investigated for global structure and behavior. In that work, where the chemistry was calibrated for a stoichiometric

oxymethane detonation at an initial pressure of 3400 kPa, both the triple point reinitiation and weak reflection reinitiation modes have been confirmed through a two-dimensional Euler based global one-step simulation.

1.7 Research Problem & Dissertation Outline

The experimental database suggests that with increasing irregularity, the more a mixture is detonable [17]. Cell cycle analysis of regular detonation shows a prominent reinitiation phase with shock-induced combustion playing a major role. The role of transverse wave collision and hydrodynamic instabilities are suspected to take over the lead shock in propagation mechanism as the irregularity of detonation increases. Though previous researchers have addressed the reinitiation mechanisms of highly irregular detonation, it was based on artificially separated shock flame complex for a limited period. Bhattacharjee [62] mentions that the incident shock is stronger in a self-sustained detonation than the one obtained through the obstacle method. Survival of the self-sustained detonation in initial pressure below 6kPa and failure of the detonation which passes through the obstacles provide evidence for the same. The foremost objective of this study is to determine and contribute to the understanding of reinitiation of a self-sustained highly unstable marginal detonation, specifically methane-oxygen detonation at low operating pressure. The reactive Euler simulation was used to study the methane-oxygen detonation at 3500 Pa and 6000 Pa in the absence of diffusion and viscosity with global one-step chemistry. If the turbulent activity is mandatory, the detonation is expected to fail and result in a decoupled shock flame complex. The absence of physical diffusion for contact surfaces has been found to result in high temperature in non-reacting flows since the pressure on both sides is the same but the density jump is stronger than the actual scenario [30]. This might result in an artificial acceleration of reaction. Diffusion relaxes this jump by increasing the thickness of the slip line. The two-dimensional KH instabilities responsible for accelerated mixing in contact discontinuities are reported to be highly damped in second-order numerical simulations [60]. Also using very fine grids for detonation problems without proper diffusion mechanisms may result in activating instability modes that are not active in nature. Hence a higher-order viscous study with a global one-step reaction is performed to determine the modes of reinitiation of detonation for highly irregular detonation. Finally, though a two-step induction parameter model is an attractive option for irregular detonation, failure

to capture sustaining transverse detonation mode reinitiation in experiments questions the scope of the model [63]. A further investigation on the role of chemistry is made by deriving and using a multistep chemistry model after verifying that the artificial temperature increase along the contact surface does not occur in a substantial amount from the viscous study.

1.8 Assumptions in Problem Setup

The description of various events occurring in a detonation that has been briefed until now can be applied to understand the approximations made in this study. This research is performed to aid a part of the systematic breakdown of sequential events occurring in the reinitiation of irregular detonation widely. Oran [26] states why simulations with advanced numerical models such as three-dimensional, reactive Navier Stokes solution are challenging even now. With the limited amount of computational resources available, approximations are essential. The set of equations to be solved, domain, and the dimensions are decided upon observing the experimental results and prioritizing the global features observed in the results.

Two-Dimensional Flow Features – Assumption I

The fluid motion of a fluid parcel at any instant can be split into three categories, translational motion, motion due to dilatation (compressibility), and rotational motion around its axis. This rotational motion can be addressed using the vorticity vector that is twice the angular velocity of the fluid particle about its axis. The vorticity vector is stated as

$$\vec{\omega} = \omega_i \hat{\imath} + \omega_j \hat{\jmath} + \omega_k \hat{k}$$

$$\omega_i = \frac{\partial w}{\partial y} - \frac{\partial v}{\partial z}$$

$$\omega_j = \frac{\partial u}{\partial z} - \frac{\partial w}{\partial x}$$

$$\omega_k = \frac{\partial v}{\partial x} - \frac{\partial u}{\partial y}$$

The transport equation of vorticity is given by [67]

$$\frac{D\vec{\omega}}{Dt} = -\vec{\omega}\left(\nabla . \vec{V}\right) + \frac{(\nabla\rho \times \nabla p)}{\rho^2} + (\vec{\omega} . \nabla)\vec{V} + \nu(\nabla^2 \vec{\omega}) \qquad 1\text{-}4$$

In general, there are three categories of vorticity production based on its mechanism; shear flow without shocks, flows with shocks, and flows without shock and turbulence production [68]. Turbulence

(eddies) originates from vortices (which become unstable) produced by instabilities in the mean shear as observed in KH instability. if the turbulence enters in an environment where there is no shear or any other maintenance mechanism, it decays [69]. Two-Dimensional simulation ignores the three-dimensional mechanisms generating vortices. But if the event of interest occurs in time scales much faster than the time scale of vortices produced, then the two-dimensional approximation is reasonable. In Chapter-3, we explain that the reaction should occur at acoustic timescales to have an impact on the detonation front. Consider the diagram below where a blob of heated reactants is surrounded by the combusted products in the box. When vortices of different scales can interact with the blob, it breaks it into small pieces of blobs increasing the surface area in contact with the products.

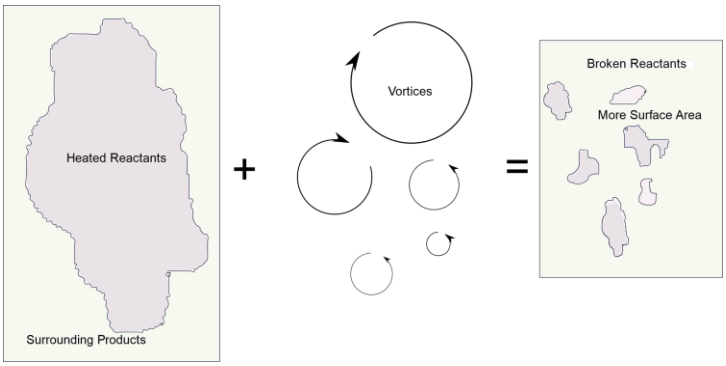

Figure 1-14 Schematic of Flame – Vortices Interaction

Depending upon the flow Damkohler number ($Da = \tau_f / t_c$) the effect of these vortices on the reactant blob and its reacting interface can be predicted. If Da is greater than one, then the chemical time scale is lesser than the integral turbulence time scale. In that scenario, the vortices can either wrinkle the flame interface or corrugate the flame interface depending upon the characteristic eddy velocity, both of which increase the flame surface area. On the other hand, when Da is less than one then the overall reaction rate is controlled by chemistry. Overall, either the coherent structures from instabilities or the turbulent structure interact with the flame interface in the forward jet or unburnt pockets and increase the flame surface area which in turn increases the reaction rate. *But does the turbulent transport occur at the rate at which it provides feedback to the front in highly irregular detonations during reinitiation?* The answer to this question is not direct since the pockets are already compressed by the detonation front and must contain radicals ready to react in high pressure and temperature zone with the flame interface. A direct

method to calculate Da requires reliable turbulent parameters (RMS of velocity) for highly irregular detonation from experiments or three-dimensional DNS simulations and reliable reaction rate parameters. Since this data is not available in the open literature, the vitality of turbulence is investigated in chapter-5 of this thesis by instead performing an inviscid two-dimensional simulation to check for the self-sustaining detonations.

Two-Dimensional Detonation Propagation – Assumption - II

The experiments which have been chosen for study are thin rectangular chamber setup with a high aspect ratio to avoid the influence of the movement of a triple point in the third direction (planar mode). This is achieved by reducing the third dimension below the natural transverse wave spacing (cell height) [3]. A detonation is planar when the flow variables are independent of the z-axis and is confirmed by the absence of slapping waves in the top and bottom walls of the rectangular chamber. The influence of the third dimension is suppressed by having a dimension ratio of $\frac{\lambda}{h} \approx 6 - 10$ [70, 2]. The diagonal/rectangular mode which demands the presence of the third dimension is not considered in the simulation.

Transport Property Models – Assumption - III

Transport properties for combustion applications require proper treatment since instabilities related to premixed flames are related to the competition between the diffusion rates [71]. Since the thermodynamic properties are modeled not to vary with temperature, the ratio of the transport properties can be treated the same way. The dimensionless variables connecting the different diffusivities are used to close the unknown transport coefficients in reactive Navier-Stokes equations are shown below.

$$Le = \frac{Thermal\ Diffusivity}{Mass\ Diffusivity} = \frac{\kappa}{D_Y}$$

$$Pr = \frac{Momentum\ Diffusivity}{Thermal\ \ Diffusivity} = \frac{\nu}{\kappa}$$

The Prandtl number and Lewis numbers are assumed to be constant. Since we use constant specific heat assumption, once the viscosity is known, the thermal conductivity can be obtained. The transport properties dynamic viscosity, thermal diffusivity and mass diffusivities in this research are modeled using the power law in the following form

$$\nu = \nu_{ref}\left(\frac{T}{T_{ref}}\right)^{\frac{3}{2}}\left(\frac{P_{ref}}{P}\right) \quad \text{1-5}$$

$$\kappa = \kappa_{ref}\left(\frac{T}{T_{ref}}\right)^{\frac{3}{2}}\left(\frac{P_{ref}}{P}\right) \quad \text{1-6}$$

$$D_Y = D_{Yref}\left(\frac{T}{T_{ref}}\right)^{\frac{3}{2}}\left(\frac{P_{ref}}{P}\right) \quad \text{1-7}$$

The kinematic viscosity(μ) varies by an order of magnitude between the induction zone and reaction zone($(O)10^{-5}\left(\frac{m^2}{s}\right) - (O)10^{-4}\left(\frac{m^2}{s}\right) for\ stoichiometric\ oxymethane$) but the order of magnitude of thermodynamic parameters does not vary in the steady ZND solution. The $\nu_{ref}, \kappa_{ref}\ and\ D_{Yref}$ are constants. The power-law lets the value of diffusion coefficients be a value in between induction zone and sonic plane making the Reynolds number appropriate. Though the transport properties by themselves vary with pressure and temperature, the Prandtl number makes the interaction between c_p and thermal diffusivity consistent. The Lewis number is chosen according to the reactant mixture so that the ratio between the thermal diffusivity and mass diffusivity is consistent.

1.8.1 Summary

To summarize, a brief introduction about the categories of detonation and its propagation mechanism was provided in this chapter. The reinitiation mode of regular detonation is well established but the reinitiation mode of irregular detonation is unclear at the present time. Experimental investigation of marginal irregular detonation has been preferred over ordinary irregular detonations due to the advantage in its length and time scales. This thesis aims to study the reinitiation mode of marginal irregular detonation using numerical simulation. The following chapter gives a brief introduction to the numerical method used in this thesis followed by an introduction of the AMR framework used by the CFD code (chapter 2). Verification and validation of the inviscid CFD code are provided in Chapter-3. The reinitiation mechanism of regular-ordinary detonation has been described in Chapter-4 using the inviscid and viscous flow model. Chapter-5 analyzes the influence of three-dimensional effects by ignoring the third dimension along with transport terms in a self-sustaining oxy-methane detonation comparable with experiments at an initial pressure of 3.5 kPa and 6 kPa. After verifying the self-sustaining detonation in Chapter-5, the influence of

transport terms in the evolution of reinitiation is studied in Chapter-6 using a higher-order accurate viscous global one-step model. The validation of the derived reduced mechanism for premixed methane-oxygen detonation and the influence of accurate reaction rates on the reinitiation mechanism has been detailed in Chapter - 7. Chapter-8 concludes this thesis, discussing the reinitiation mechanism by considering all the results obtained and recommends a few approaches to extend this research to 3D simulations.

Chapter-2 Numerical Methods

2.1 Governing Equations

This chapter briefs on the numerical methods and algorithms of solvers used for the CFD simulations in this thesis. It also contains a description of the criteria for choosing the computational setup, boundary conditions and the artificial errors expected when solving solutions with discontinuities. The numerical scheme of the inviscid solver is explained in detail to provide an overall understanding of the flow-SAMR solver integration and the numerical scheme of the viscous solver is explained briefly.

All the numerical analysis in this thesis was performed using the AMROC (VTF) code by Dr. Ralf Deiterding and group [72]. Two different codes were used for this study. The finite volume based code was used for the inviscid study with and without chemistry. The higher-order finite difference based WENO-CD code was used for the viscous calculations. A simplified chemistry model, referred to as global one-step chemistry (in this thesis), was used along with both the inviscid and viscous model. The detailed chemistry model involving multistep chemistry mechanism was used only with the inviscid model. To understand the assumptions, the equations used in the inviscid and viscous models are derived from the reactive Navier Stokes equations in the following section.

2.2 Reactive Navier Stokes Equation

All the assumptions made in deriving a model are mentioned before stating the respective set of equations. As mentioned in the introduction chapter, only two-dimensional simulations are considered in this thesis.

A:1 The third-dimension z is neglected in all the governing equations

The balance equation for overall mass conservation for multispecies gas mixture is written in differential form as

$$\frac{\partial \rho}{\partial t} + \frac{\partial \rho u}{\partial x} + \frac{\partial \rho v}{\partial y} = 0 \qquad 2\text{-}1$$

The species conservation equation for multispecies gas mixture is given as

$$\frac{\partial \rho Y_i}{\partial t} + \frac{\partial \rho((u + V_i)Y_i)}{\partial x} + \frac{\partial \rho((v + V_i)Y_i)}{\partial y} = \dot{\omega}_\iota \qquad 2\text{-}2$$

where the pressure p and density ρ are mixture properties which are defined by

$$\rho = \sum \rho_i \quad (2\text{-}3)$$

$$p = \sum p_i \quad (2\text{-}4)$$

$$Y_i = \rho_i / \rho \quad (2\text{-}5)$$

Before heading into the momentum and energy equations, the definition of tensor quantities and flux quantities are explained below. The stress tensor σ is defined as

$$\sigma_{j,k} = \tau_{j,k} - p\delta_{j,k} \quad (2\text{-}6)$$

where $j\ and\ k = 1, 2$. The viscous stress term $\tau_{j,k}$ is expressed in terms of normal and shear stress.

A:2 The gas mixture behaves like a Newtonian fluid and accepts Stokes hypothesis for bulk viscosity.

The shear stresses are given by

$$\tau_{xy} = \tau_{yx} = \mu\left(\left(\frac{\partial u}{\partial y} + \frac{\partial v}{\partial x}\right)\right) \quad (2\text{-}7)$$

And the normal stresses are given by

$$\tau_{xx} = \mu\left(2\frac{\partial u}{\partial x} - \frac{2}{3}\left(\frac{\partial u}{\partial x} + \frac{\partial v}{\partial y}\right)\right) \quad (2\text{-}8)$$

$$\tau_{yy} = \mu\left(2\frac{\partial v}{\partial y} - \frac{2}{3}\left(\frac{\partial u}{\partial x} + \frac{\partial v}{\partial y}\right)\right) \quad (2\text{-}9)$$

Here μ is the kinematic viscosity of the gas mixture and is a function of temperature and mass fraction.

$$\mu = f(Y_i, T) \quad (2\text{-}10)$$

A:3 The energy flux due to thermal conduction accepts the approximation through Fourier's Law of heat conduction.

The energy flux due to thermal conduction and mass diffusion of species is given as

$$q_x = -k\left(\frac{\partial T}{\partial x}\right) + \rho\sum_{i=1}^{N} h_i Y_i V_{i,x} \quad (2\text{-}11)$$

$$q_y = -k\left(\frac{\partial T}{\partial x}\right) + \rho\sum_{i=1}^{N} h_i Y_i V_{i,y} \quad (2\text{-}12)$$

$$k = f(Y_i, T) \quad (2\text{-}13)$$

A:4 Each species is assumed to be behaving as a thermally perfect gas by ignoring intermolecular forces

$$c_{p_i} = f(T) \quad \text{2-14}$$

$$c_{v_i} = f(T) \quad \text{2-15}$$

And

$$dh_i = c_{p_i} dT \quad \text{2-16}$$

$$de_i = c_{v_i} dT \quad \text{2-17}$$

Integrating the above equation, we get the specific enthalpy of a single species. The specific heat constants at a constant pressure $c_{p_i}(T)$ and volume $c_{v_i}(T)$ are given by polynomial functions as a function of temperature only with limits. The specific enthalpy and specific internal energy of the species are given by

$$h_i(T) = \Delta h_i^0 + \int c_{p_i}(T)\,\mathrm{dT} \quad \text{2-18}$$

$$e_i(T) = \Delta h_i^0 + \int c_{v_i}(T)\,\mathrm{dT} - R_u T_0 / W_i \quad \text{2-19}$$

The $h_i(T)$ and $e_i(T)$ should remain positive and non-zero. The individual species gas constant and specific heat ratio can be determined using the following relation

$$R_i = c_{pi}(T) - c_{vi}(T) \quad \text{2-20}$$

$$\gamma_i(T) = \frac{c_{pi}(T)}{c_{vi}(T)} \quad \text{2-21}$$

The ideal gas law holds for each species, hence

$$p_i = \frac{\rho_i R_u T}{W_i} \quad \text{2-22}$$

The momentum conservation for x and y components are shown below

A:5 The body force terms in the momentum equation $\sum_{i=1}^{N} Y_i f_{x,i}$ *and* $\rho \sum_{i=1}^{N} Y_i f_{y,i}$ *are neglected*

$$\frac{\partial \rho u}{\partial t} + \frac{\partial \rho u^2}{\partial x} + \frac{\partial \rho u v}{\partial y} = -\frac{\partial p}{\partial x} + \frac{\partial \tau_{xx}}{\partial x} + \frac{\partial \tau_{yx}}{\partial y} \quad \text{2-23}$$

$$\frac{\partial \rho v}{\partial t} + \frac{\partial \rho u v}{\partial x} + \frac{\partial \rho v^2}{\partial y} = -\frac{\partial p}{\partial y} + \frac{\partial \tau_{xy}}{\partial x} + \frac{\partial \tau_{yy}}{\partial y} \quad \text{2-24}$$

The total energy conservation along with the assumptions of the above system is stated as

A:6 The power produced by body force terms in the energy equation $\rho \sum_{i=1}^{N} Y_i f_i \, (u + U_j)$ *and the heat source term* $\dot{Q}$ *are neglected*

$$\frac{\partial \rho E}{\partial t} + \frac{\partial \rho (E+p) u}{\partial x} + \frac{\partial \rho (E+p) v}{\partial y} \tag{2-25}$$

$$= \rho \dot{q} + \frac{\partial}{\partial x}\left(k\left(\frac{\partial T}{\partial x}\right)\right) + \frac{\partial}{\partial y}\left(k\left(\frac{\partial T}{\partial y}\right)\right) + \frac{\partial (u\tau_{xx})}{\partial x} + \frac{\partial (u\tau_{yx})}{\partial y}$$

$$+ \frac{\partial (v\tau_{xy})}{\partial x} + \frac{\partial (v\tau_{yy})}{\partial y} + \rho \sum_{i=1}^{N} h_i Y_i V_{i,x} + \rho \sum_{i=1}^{N} h_i Y_i V_{i,y}$$

The total energy is defined as

$$E = e + \frac{1}{2}(u^2 + v^2) \tag{2-26}$$

The specific internal energy of the mixture is given as

$$e = \sum_{i=1}^{N} Y_i \, e_i \tag{2-27}$$

2.3 Reactive Euler Equation

In the above set of reactive Navier Stokes equation, the normal stress terms τ_{xx}, τ_{yy} and shear stress terms $\tau_{xy} = \tau_{yx}$ are neglected in momentum and energy equation to obtain the reactive time-dependent multistep Euler equations an are shown below

$$\frac{\partial \rho}{\partial t} + \frac{\partial \rho u}{\partial x} + \frac{\partial \rho v}{\partial y} = 0 \tag{2-28}$$

$$\frac{\partial \rho Y_k}{\partial t} + \frac{\partial \rho u Y_k}{\partial x} + \frac{\partial \rho v Y_k}{\partial y} = \dot{\omega}_k \tag{2-29}$$

$$\frac{\partial \rho u}{\partial t} + \frac{\partial \rho u^2}{\partial x} + \frac{\partial \rho uv}{\partial y} = -\frac{\partial p}{\partial x} \tag{2-30}$$

$$\frac{\partial \rho v}{\partial t} + \frac{\partial \rho uv}{\partial x} + \frac{\partial \rho v^2}{\partial y} = -\frac{\partial p}{\partial y} \tag{2-31}$$

$$\frac{\partial \rho E}{\partial t} + \frac{\partial \rho (E+p) u}{\partial x} + \frac{\partial \rho (E+p) v}{\partial y} = 0 \tag{2-32}$$

Evaluation of Temperature

The ideal gas equation of the mixture is given by [73]

$$p = \rho RT \tag{2-33}$$

From the basic thermodynamic equation of state

$$p = \sum \rho h_i(T) - \rho e_t + \frac{\rho(u^2 + v^2)}{2} \tag{2-34}$$

Hence, an implicit equation with both the above equation is given as

$$p = \sum \rho_i h_i(T) - \rho e_t + \frac{\rho(u^2 + v^2)}{2} - \rho RT = 0 \tag{2-35}$$

The set of equations in this subsection is referred to as the inviscid Euler equations with a multistep chemistry model.

2.3.1 Inviscid Global One-Step Model

Determining the best simplified model depends on the purpose of the model. In this thesis, the purpose of this kinetic model is to capture the overall detonation features such as the velocity distribution in a cell cycle and reproduce the dynamics. The global one-step chemistry model assumes only a forward exothermic reaction such that $Reactants\ (A) \rightarrow Products\ (B)$ and both reactant and products are calorically perfect with same specific heat ratio $\gamma_A = \gamma_B = \gamma$ [3]. The value of specific heat constant is taken at VN state behind the lead shock and the value of the molecular weight of the mixture is kept constant as its initial condition [74] [46]. The rate of the reaction is given by

$$\dot{\omega}_A = k\rho_A exp\left(-\frac{E_A}{RT}\right) \tag{2-36}$$

The equation of the state is given by

$$P = (\gamma - 1)(\rho e - \rho(1 - Z)q_0) \tag{2-37}$$

where Z is the mass fraction of product B. The values of activation energy E_A, $preexponential\ factor\ A$ and enthalpy of formation q_o are the unknowns of this model and must be determined. The value of energy flux q_o added to the products through detonation is obtained from CJ theory. From the simplified model of detonation [3] to obtain parameters at the CJ state, we use the following equation

$$\left(M_{CJ}-\frac{1}{M_{CJ}}\right)=\left[\frac{2q(\gamma^2-1)}{\gamma}\right] \quad 2\text{-}38$$

The value of global heat release Q at the CJ state for an ideal gas equation is determined using the following equation [2].

$$q=\frac{Q}{RT_o}=\frac{\gamma}{2(\gamma^2-1)}\left[M_{CJ}-\frac{1}{M_{CJ}}\right]^2 \quad 2\text{-}39$$

$$q=\frac{\gamma RT_o}{2(\gamma^2-1)}\left[M_{CJ}-\frac{1}{M_{CJ}}\right]^2=\frac{c_o^2}{2(\gamma^2-1)}\left[M_{CJ}-\frac{1}{M_{CJ}}\right]^2 \quad 2\text{-}40$$

The nondimensional Q is then obtained using

$$Q=\left(\frac{\rho_o}{P_o}\right)\frac{c_o^2}{2(\gamma^2-1)}\left[M_{CJ}-\frac{1}{M_{CJ}}\right]^2 \quad 2\text{-}41$$

The above equation consists of one equation and two unknowns (γ & Q). To close the system, the deflagration branch of the same mixture is considered. The adiabatic flame temperature of the system is given as

$$T_B=T_u+\frac{q}{c_p}=T_u+\frac{qR(\gamma-1)}{\gamma} \quad 2\text{-}42$$

The system is now complete with two equations and two unknowns. The values of γ and Q are varied by fixing the M_{CJ},T_u,T_B and R for the specified initial conditions. The intersection of both curves provides the value of Q and γ [39].The value of activation energy is obtained by performing a constant volume ignition zero-dimensional model. The initial condition for this model is the post-shock condition of a non-reacting shock wave traveling at CJ velocity. The equations solved for constant ignition combustion are as follows [75]

$$\frac{d\rho}{dt}=0 \quad 2\text{-}43$$

$$\frac{dw}{dt}=0 \quad 2\text{-}44$$

$$\frac{dP}{dt}=-\rho a_f^2\dot{\sigma} \quad 2\text{-}45$$

$$\frac{dY_i}{dt}=\dot{\omega}_\iota \quad 2\text{-}46$$

The post-shock conditions $P_{VN}\ and\ T_{VN}$ for $(U_{CJ} \pm 0.01U_{CJ})$ is obtained and the respective ignition delay time for the constant volume combustion is determined from a detailed chemistry mechanism. Then the activation energy can be obtained from the following relationship

$$\frac{E_a}{R_{ideal}} = \frac{(\ln(\tau_+) - \ln(\tau_-))}{\left[\frac{1}{T_+} - \frac{1}{T_-}\right]} \quad \text{2-47}$$

By using the above equations, the governing equation for the global one-step chemistry, inviscid model is given below

$$\frac{\partial \rho}{\partial t} + \frac{\partial \rho u}{\partial x} + \frac{\partial \rho v}{\partial y} = 0 \quad \text{2-48}$$

$$\frac{\partial \rho u}{\partial t} + \frac{\partial \rho u^2}{\partial x} + \frac{\partial \rho uv}{\partial y} = -\frac{\partial p}{\partial x} \quad \text{2-49}$$

$$\frac{\partial \rho v}{\partial t} + \frac{\partial \rho uv}{\partial x} + \frac{\partial \rho v^2}{\partial y} = -\frac{\partial p}{\partial y} \quad \text{2-50}$$

$$\frac{\partial \rho E}{\partial t} + \frac{\partial \rho (E+p)u}{\partial x} + \frac{\partial \rho (E+p)v}{\partial y} = 0 \quad \text{2-51}$$

$$\frac{\partial \rho Z}{\partial t} + \frac{\partial \rho u \mathrm{Z}}{\partial x} + \frac{\partial \rho v \mathrm{Z}}{\partial y} = k(1-Z)exp\left(-\frac{E_A}{RT}\right) \quad \text{2-52}$$

2.3.2 Viscous Global One-Step Model

By adding the stress terms in the momentum equations and the work done/heat added by these stress terms on the fluid in the energy equation, the governing equation of the two-dimensional viscous model with global one-step reaction kinetics model which is used for viscous simulations is given below

$$\frac{\partial \rho}{\partial t} + \frac{\partial \rho u}{\partial x} + \frac{\partial \rho v}{\partial y} = 0 \quad \text{2-53}$$

$$\frac{\partial \rho u}{\partial t} + \frac{\partial \rho u^2}{\partial x} + \frac{\partial \rho uv}{\partial y} = -\frac{\partial p}{\partial x} + \frac{\partial \tau_{xx}}{\partial x} + \frac{\partial \tau_{yx}}{\partial y} \quad \text{2-54}$$

$$\frac{\partial \rho v}{\partial t} + \frac{\partial \rho uv}{\partial x} + \frac{\partial \rho v^2}{\partial y} = -\frac{\partial p}{\partial y} + \frac{\partial \tau_{xy}}{\partial x} + \frac{\partial \tau_{yy}}{\partial y} \quad \text{2-55}$$

$$\frac{\partial \rho E}{\partial t}+\frac{\partial \rho (E+p)u}{\partial x}+\frac{\partial \rho (E+p)v}{\partial y} \tag{2-56}$$

$$=\rho\dot{q}+\frac{\partial}{\partial \mathrm{x}}\left(k\left(\frac{\partial T}{\partial x}\right)\right)+\frac{\partial}{\partial \mathrm{y}}\left(k\left(\frac{\partial T}{\partial y}\right)\right)+\frac{\partial (u\tau_{xx})}{\partial x}+\frac{\partial (u\tau_{yx})}{\partial y}+\frac{\partial (v\tau_{xy})}{\partial x}$$

$$+\frac{\partial (v\tau_{yy})}{\partial y}$$

$$\frac{\partial \rho Z}{\partial t}+\frac{\partial \rho u\mathrm{Z}}{\partial x}+\frac{\partial \rho v\mathrm{Z}}{\partial y}=k(1-Z)exp\left(-\frac{E_A}{RT}\right)+D\rho\left(\frac{\partial Z}{\partial x}\right)+D\rho\left(\frac{\partial Z}{\partial y}\right) \tag{2-57}$$

With the stresses related to velocity gradients as follows

$$\tau_{xx}=\mu(T)\left(2\frac{\partial u}{\partial x}-\frac{2}{3}\left(\frac{\partial u}{\partial x}+\frac{\partial v}{\partial y}\right)\right) \tag{2-58}$$

$$\tau_{xy}=\tau_{yx}=\mu(T)\left(\left(\frac{\partial u}{\partial y}+\frac{\partial v}{\partial x}\right)\right) \tag{2-59}$$

$$\tau_{yy}=\mu(T)\left(2\frac{\partial v}{\partial y}-\frac{2}{3}\left(\frac{\partial u}{\partial x}+\frac{\partial v}{\partial y}\right)\right) \tag{2-60}$$

2.3.3 Normalization and Initiation

Nondimensionalization of the variables was performed according to the approach of Williams [74]

$$x^*=\frac{x}{L_\infty};p^*=\frac{p}{\rho_o a_o^2},v^*=\frac{v}{a_o},\rho^*=\frac{\rho}{\rho_o},u^*=\frac{u}{a_o},T^*=\frac{T}{\frac{c_{p_o}}{a_o^2}} \tag{2-61}$$

The length of the domain is scaled with a reference length of 1 mm. The source term is marched in time using an explicit fourth-order accurate Runge-Kutta (RK) method using the Fortran code “DVERK” [76].

2.4 Godunov’s Method

The notations of symbols were adopted from Randy Leveque [77] since the CFD code is built upon Clawpack. Finite difference methods where the derivatives are approximated with finite-difference stencils tend to break down near discontinuities [77]. The finite volume method is a method in which the spatial domain is divided into intervals and approximate total integral of state variables within these volumes. A cell-centered cell average formulation (Q_i^n) , which is to divide the integral value with volume of the cell, is

adopted for solving the governing equations. The cell averaged values are then marched in time after determining the fluxes through the edges of these cells.

The integral form of conservation law in one dimension is given as

$$\frac{d}{dt}\int_{x_{i-\frac{1}{2}}}^{x_{i+\frac{1}{2}}} q(x,t)dx = f\left(q\left(x_{i-\frac{1}{2}},t\right)\right) - f\left(q\left(x_{i+\frac{1}{2}},t\right)\right) \quad 2\text{-}62$$

By replacing $q(x,t)$ with its cell averaged form of Q_i^n and flux at a cell interface $f\left(q\left(x_{i-\frac{1}{2}},t\right)\right)$ with its average flux $F_{i-\frac{1}{2}}$ within a cell (x_i) we get

$$Q_i^n \approx \frac{1}{\Delta x}\int_{x_{i-\frac{1}{2}}}^{x_{i+\frac{1}{2}}} q(x,t_n)dx \quad 2\text{-}63$$

$$F_{i-\frac{1}{2}} \approx \frac{1}{\Delta t}\int_{t_n}^{t_{n+1}} f\left(q\left(x_{i-\frac{1}{2}},t\right)\right)dt \quad 2\text{-}64$$

This results in a time explicit conservative numerical form in one dimension as [78]

$$Q_i^{n+1} = Q_i^n - \frac{\Delta t}{\Delta x}\left[F_{i+\frac{1}{2}}^n - F_{i-\frac{1}{2}}^n\right] \quad 2\text{-}65$$

In a Godunov method, the average flux function is obtained by solving the Riemann problem at the cell interface given as

$$F_{i-\frac{1}{2}} \approx \frac{1}{\Delta t}\int_{t_n}^{t_{n+1}} f\left(q^{rp}\left(x_{i-\frac{1}{2}},t\right)\right)dt \quad 2\text{-}66$$

Care must be taken to make sure the numerical scheme developed from this discretization is convergent, consistent and stable. Stability can only be expected when the numerical domain of dependence matches with the physical domain of dependence. This criterion is kept in check, especially for explicit schemes, using the CFL condition given by

$$\nu \leq \frac{\Delta t}{\Delta x}\max_{\mathrm{p}}[\lambda^p] \quad 2\text{-}67$$

The numerical approach adopted in this study takes the wave propagation viewpoint following [77]. The advantage of this viewpoint lies in applying Godunov's method to hyperbolic systems in non-conservative forms. Let ℓ^p be the left eigen vector. A jump between two states defined by a Riemann problem (q_l, q_r) can be defined as

$$\alpha^p = \ell^p (q_r - q_l) \quad \text{2-68}$$

Based on the definition of α^p vector, then jump notation can be defined as

$$\mathcal{W}^p = \alpha^p r^p \quad \text{2-69}$$

2.5 Approximate Riemann Solver

Centered schemes gather information from both the sides of a computed point when updating a solution rather than giving weightage based on the propagation of information along characteristics since no distinction between upstream and downstream is made [79] [80]. Lack of physics in the numerical scheme gives rise to nonphysical oscillations. For a solution containing discontinuities, upwind schemes are a natural choice over space centered schemes since it takes the hyperbolic character of the system into account. When solving linear hyperbolic equations, the Riemann problem is typically a similarity solution as a function of x/t and consists of finite set of waves that propagate away from the origin with constant wave speeds [77]. Decomposition of data into waves traveling into finite volume including reflection and transmission gives the magnitude and direction of the numerical flux.

Broadly, hyperbolic PDE solvers are segregated into flux splitting upwind scheme and Godunov type scheme [80]. The flux splitting schemes use the directional discretization of the flux $F(Q)$ based on the sign of eigenvalue (λ) (direction of propagation of characteristic wave) of Jacobian matrix. The Godunov type schemes solves exact or appropriate local Riemann problem at the cell interfaces to obtain the flux, $F(Q)$ [80]. The derivation of exact solution-based Godunov scheme has been detailed in various references [78] [77] [38]. Since a Godunov scheme can be written in conservative form, it is valid over entire domain though the solution contains discontinuities.

The approximate solver of Roe proceeds by solving linear Riemann problem at the cell interfaces instead of the original non-linear Riemann problem. The actual non-linear conservation system is replaced by a linear conservation system with constant matrices but with same initial conditions. Assume the following system of nonlinear conservation laws

$$Q_t + F_t = 0 \quad \text{2-70}$$

By chain rule

$$Q_t + A(Q)\mathrm{Q_x} = 0 \qquad 2\text{-}71$$

According to Roe linearization the original matrix is replaced by constant matrix $\bar{A} = \bar{A}(U_L, U_R)$. Hence the modified system of conservation laws is given by

$$Q_t + \bar{A}Q_x = 0 \qquad 2\text{-}72$$

The constant Jacobian matrix must satisfy three properties to be acceptable. The matrix should contain real eigen values with linearly independent right Eigen value to be hyperbolic, should be consistent with the original Jacobian matrix and should maintain conservation across discontinuities. By defining $|A| = R|\Lambda|R^{-1}; A^{+} = R\Lambda^{+}R^{-1}; A^{-1} = R\Lambda^{-1}R^{-1}$, where R is the matrix of Eigen vectors, we get [77]

$$F_{i-\frac{1}{2}} \approx \frac{1}{\Delta t}\int_{t_n}^{t_{n+1}} f\left(q^{rp}\left(x_{i-\frac{1}{2}}, t\right)\right)dt = AQ_{i-1} + \sum_{p=1}^{m}(\lambda^p)^{-}\mathcal{W}^p_{i-\frac{1}{2}} \qquad 2\text{-}73$$

Or

$$F_{i-\frac{1}{2}} = AQ_i - \sum_{p=1}^{m}(\lambda^p)^{+}\mathcal{W}^p_{i+\frac{1}{2}} \qquad 2\text{-}74$$

2.5.1 Roe Linearization

The numerical flux in Roe's method is defined by taking the average of the above two equations

$$F_{i-\frac{1}{2}} = \frac{1}{2}(AQ_{i-1} + AQ_i) - \frac{1}{2}|A|(Q_{i-1} - Q_i) \qquad 2\text{-}75$$

Once the constant Jacobian matrix is determined the corresponding Eigen values $\bar{\lambda}(U_L, U_R)$ and right eigen vectors are derived $\bar{r}(U_L, U_R)$. The wave strengths can be determined as follows

$$\Delta Q = Q_R - Q_L = \sum \bar{\alpha}^i \bar{r}^i \qquad 2\text{-}76$$

The wave strength can be made as a function of average values, $\bar{\alpha}^i = \bar{\alpha}^i(U_L, U_R)$.The numerical flux at the interface is now determined using the final form

$$F_{i+\frac{1}{2}} = \frac{1}{2}(F_L + F_R) - \frac{1}{2}\sum_{i=1}^{m}\bar{\alpha}_i\left|\bar{\lambda}_i\right|\bar{r}^i \qquad 2\text{-}77$$

For linearizing this problem, a constant Jacobian matrix must be derived. The matrix is derived by integrating the Jacobian matrix over a suitable path in space state between $U_{i+\frac{1}{2}}$ and U_i. By this method, an

integral form of a matrix $\hat{A}$ is obtained. To overcome the issue of solving the integral of nonlinear equations, Roe' proposed an approach where a common parameter vector Q is introduced such that both the conserved variables U and the flux vector F are made function of it.

$$Q = Q(\mathcal{Z}) \quad \& \quad F = F(\mathcal{Z}) \tag{2-78}$$

The conservative variables and fluxes are replaced by Roe's average variables which satisfy all the three required criteria.

$$F_{i+\frac{1}{2}} = \hat{C}_{i+\frac{1}{2}}(Q_{i+1} - Q_i) \tag{2-79}$$

$$U_{i+\frac{1}{2}} = \hat{B}_{i+\frac{1}{2}}(Q_{i+1} - Q_i) \tag{2-80}$$

$$\hat{A}_{i+\frac{1}{2}} = \hat{C}_{i+\frac{1}{2}}/\hat{B}_{i+\frac{1}{2}} \tag{2-81}$$

2.5.2 Roe Solver

The algorithm of the Roe solver is provided briefly in the section for Euler equations [78] [77]. A generalization to multistep Euler equations is made in the derivation. The Roe solver approximates the Riemann problem at the cell interface using three discontinuities [78]. The algorithm followed by a Roe solver to obtain the intercell boundary is provided below

- First, the Roe averaged values for primitive variables such as $\tilde{u}$, $\tilde{v}$, $\tilde{\rho}$, $\tilde{c}$, $\tilde{H}$ are determined.
- Second the Eigenvalue $\tilde{\lambda_i}$ and the right Eigenvector $\tilde{r}$ of matrix $\tilde{A}$ are obtained using the averaged variables.
- The wave strength a_m is determined with which the wave jump criteria $\mathcal{W}_i$ is also calculated.
- With the above quantities, the flux at the interface $F^{roe}_{i+\frac{1}{2}}$ can be calculated.

2.5.3 Entropy Correction

2.5.4 Higher Resolution Extension

Demand for a higher-order solution with no nonphysical oscillation near shockwaves is conflicting [78]. A monotone scheme that avoids non-physical oscillations near gradients for a constant coefficient linear scheme is the first order inaccuracy. Total Variation Diminishing (TVD) methods provide a balance

between this conflicting requirement in nonlinear problems by deriving properties from exact scalar conservation law [78]. In this research, we choose the Monotone Upwind Schemes for Conservation Laws (MUSCL) variant MUSCL- Hancock approach which is a slope limiting TVD approach. The first order Godunov method can be extended to the MUSCL-Hancock higher-order scheme using the following three steps.

The data reconstruction is performed using the following formula

$$\tilde{Q}_i^L = Q_i^n - \frac{1}{2}\Delta_i \; ; \; \tilde{Q}_i^R = Q_i^n + \frac{1}{2}\Delta_i \qquad 2\text{-}82$$

With

$$\Delta_i = \frac{1}{2}(1+\omega)\Phi^+_{i-\frac{1}{2}}\Delta u_{i-\frac{1}{2}} + \frac{1}{2}(1-\omega)\Phi^-_{i+\frac{1}{2}}\Delta u_{i+\frac{1}{2}} \qquad 2\text{-}83$$

The high-resolution schemes are an extension of the first-order upwind scheme.

2.5.5 Dimensional and Time Operator Splitting

The two-dimensional reactive Euler system is an inhomogeneous, non-linear hyperbolic system of equations and can be written in differential form as

$$q_t + f(q)_x = s(q) \qquad 2\text{-}84$$

When the source terms depend only on $q(x,t)$ and not on its derivatives it is possible to do an operator splitting known as fractional step methods where the above method can be split into a homogenous system of equations governing hydrodynamics and ordinary differential equations governing the reaction. Analytical proof of the method of fractional steps can be found in Toro [78].

$$q_t + f(q)_x = 0 \qquad 2\text{-}85$$

$$q_t = s(q) \qquad 2\text{-}86$$

The fractional step procedure has the advantage of allowing us to use the high-resolution methods derived for homogenous equations. The fractional step method can be subdivided into Godunov Splitting and Strang Splitting [77]. From an algorithm standpoint, Godunov splitting can be derived as follows

$$Q_i^* = \mathcal{H}(Q) = Q_i^n - \frac{\Delta t}{\Delta x}\left[F^n_{i+\frac{1}{2}} - F^n_{i-\frac{1}{2}}\right] \qquad 2\text{-}87$$

$$Q_i^{n+1} = \mathcal{S}(\mathrm{Q}) = Q_i^* + \mathrm{S}(\mathrm{Q_i}) \qquad 2\text{-}88$$

Godunov splitting is only first-order accurate. Strang splitting, which is second-order accurate, is obtained by modifying the above algorithm by splitting the source term operator into two.

$$Q_i^{n+1} = \mathcal{S}^{\frac{1}{2}\Delta t}(\mathrm{Q})\mathcal{H}(Q)^{\Delta t}\mathcal{S}^{\frac{1}{2}\Delta t}(\mathrm{Q}) \qquad 2\text{-}89$$

Since a Riemann problem is inherently one-dimensional, the approach to solving the multidimensional problem depends upon the type of the grid chosen. If the finite volume is close to rectangular, then the dimensional splitting method offers a simple way to extend the one-dimensional high-resolution method to more dimensions [77]. This approach is possible only when the governing system of equations can be separated into individual scalar equations. As with the operator splitting method, the dimensional splitting method offers an advantage of using the preexisting high-resolution one-dimensional schemes. The limitations of dimensional splitting can be found elsewhere [77]. The algorithm of the Godunov dimensional splitting is defined below

x-sweep

$$Q_{ij}^{*} = \mathcal{X}(Q)^{\Delta t} = Q_{ij}^{n} - \frac{\Delta t}{\Delta x}\left[F^{n}_{i+\frac{1}{2},j} - F^{n}_{i-\frac{1}{2},j}\right] \qquad 2\text{-}90$$

y-sweep

$$Q_{i,j}^{n+1} = \mathcal{Y}(Q)^{\Delta t} = Q_{i,j}^{*} - \frac{\Delta t}{\Delta x}\left[G^{*}_{i,j+\frac{1}{2}} - G^{*}_{i,j-\frac{1}{2}}\right] \qquad 2\text{-}91$$

Hence along with the source term integration, the formula reads

$$Q_{i,j}^{n+1} = \mathcal{S}^{\frac{1}{2}\Delta t}(\mathrm{Q})\mathcal{X}(Q)^{\Delta t}\mathcal{Y}(Q)^{\Delta t}\mathcal{S}^{\frac{1}{2}\Delta t} \qquad 2\text{-}92$$

A comparative study was performed by Deiterding for unstable gaseous detonation to study the difference between Godunov operator splitting using second-order discretization schemes and overall second-order accurate wave propagation scheme [38]. The difference between both the schemes for the same initial conditions and setup was found to be negligible. The advantage of Roe-HLL scheme with MUSCL extrapolation for multidimensional detonation in terms of resolution, computational time and resource can also be found in the same work [38].

2.5.6 Algorithm of the Reactive Euler Solver

The reactive Euler solver used in this study is Roe-HLL solver for multistep mixtures.

- Initialize the solution and create tables for $c_p(T)$ and $h(T)$ within a range of temperature.
- After initialization, (ZND profile when solving for detonation) the solver calculates standard Roe averages of variables such as ρ, u_n, T, Y_k and H at the cell interfaces. The solver uses MUSCL reconstruction for the interfaces.
- Calculate standard Roe average for thermodynamic properties such as γ, R and W at the cell interface.
- Calculate ϕ_i at the cell interface using the averaged h_i . The ϕ_i is used for T_i calculation.
- A constant Jacobian matrix replaces the original Jacobian matrix. The Jacobian matrix, eigenvalues and the right eigenvectors for the multistep Euler equations can be found in the Appendix of [38].
- The interpolated flux is calculated using the Roe scheme with entropy fix or HLL scheme depending upon the criteria met by density and internal energy to avoid unphysical effects.
- The time marching is performed using Hancock-Van leer scheme which results in a second order for time integration [38]. The CFL number is estimated with the following relation

$$CFL_{ROE,HLL} = \max\left(u_{1,j+\frac{1}{2}} + c_{j+\frac{1}{2}}\right)\left(\frac{\Delta t}{\Delta x}\right) \leq 1 \qquad \text{2-93}$$

2.6 WENO-CD Solver

Compressible flow with smooth flow features demands the special treatment of the governing equations. The temporal evolution of shock interaction with vortex illustrates the importance of choosing the right numerical scheme [81]. When considering the requirement of the problem, a numerical scheme based on WENO which can resolve both smooth regions and discontinuities is a good option. For a mixed type of partial differential equations like the Navier Stokes equation, a better approach to solve for different behaviors is to have a local criterion to determine the ideal numerical method. The hybrid WENO-TCD numerical scheme was derived for this purpose for LES based governing equations by Hill et al. [82]. A LES based solver using the WENO-TCD scheme with SAMR was created by Pantanos et al. [83]. This solver was modified with the WENO-CD scheme with higher-order accuracy for the DNS study of

detonations using multistep chemistry by Zeigler et al. [34]. The version of the scheme used in this study is fourth-order accurate in time and sixth-order accurate in space. A Riemann solver based switch that flags the presence of high gradients in the flow is used to switch from flux-based centered differencing formula to WENO formula [34]. A detailed derivation of the scheme and implementation of the solver can be found in [34] and is not repeated here. The verification, validation, and performance of the WENO/CD solver used in this work for shock and detonation-based simulations can be found in [84].

2.7 Boundary Condition

Time-dependent, compressible, higher-order simulations demand control of wave reflections within the domain [73]. Non-dissipative higher-order schemes create numerical waves, 'wiggles', which interacts with the boundary conditions. The acoustic waves in the domain may lead to an additional mechanism for the production and destruction of combustion in a turbulent environment. Depending upon the type of boundary and numerical method, two methods can be used to specify boundary conditions [77]. The first method involves calculating special formulas known as a numerical boundary condition. The second method involves using additional ghost cells and calculating its values from the interior domain. Four different boundary conditions are planned to be used for this research. Supersonic inlet/outlet, symmetric/slip wall boundary conditions. These boundary conditions are to be modeled for both multistep chemistry Euler solver and single equation LES solver. For the primitive variables which are not specified by the physical boundary conditions, numerical boundary condition must be determined. By using the supersonic outlet boundary condition, the rarefaction wave is not solved for which matches the atmospheric conditions. This approximation is supported by the works published by Gamezo et al. [49] [4] in which the influence of rarefaction waves on a fully developed detonation is mentioned to be negligible within the reaction zone.

2.7.1 Computational Setup

Two different setups are used in this research. The first setup is a stationary frame of reference where the detonation is fixed in a quasi-steady position by having a reactant entering the domain at CJ velocity. The second setup is a rectangular tube with a wall at the left end and outlet BC at the right end. With the multistep chemistry model, the instabilities can form on its own due to numerical noise. Discussion

on causes and quantification for numerical noise in a CFD algorithm has been recorded in sources such as [85]. Many previous works have addressed the issue of the influence of numerical noise in detonation instabilities [86] [4] [87]. Specifically, a detailed analysis of the influence of numerical noise on varying detonation stability has been discussed by Gamezo et al. [4]. The role of numerical noise is to create microscopic perturbations equivalent to thermal perturbations in dynamic mode decomposition analysis. This gives rise to transverse wave instability due to nonlinear feedback interactions between heat release and shock strength [12]. It was demonstrated in the same study that though the initial evolution of the structures such as cell pattern is noise dependent, the self-similar pattern was eventually achieved by adding numerical noise. The effect of heat transfer along the wall is negligible on the detonation when the computational domain is wide to form more than one cell and the flow features remain the same in a periodically bounded domain [35]. Numerically when the development of micro perturbation does not happen early enough, the initial solution is artificially perturbed [4]. This method also overcomes the dependence on the frequency and amplitude of numerical noise since the induced perturbation is macroscopic. For a self-supported detonation wave, the characteristic wave $u + c$ should travel at the velocity of detonation wave D forming a sonic plane and separating the trailing expansion waves [44]. When performing a stationary detonation simulation, corruption due to information reflecting from the outflow boundary can influence the detonation front via $u + c$ wave making it to travel faster than D. The minimum length of the domain depends on the activation energy of the reactant mixture [64]. A procedure to avoid this and choose a domain to investigate a stationary detonation has been derived in [50]. A parametric study on the effects of a domain on detonation is also made in the same work. If D is the non-dimensional velocity and A is the eigen value of right travelling wave then, the non-dimensional time T at which the wave intercepts the detonation wave is given as

$$D = \frac{V}{\sqrt{\frac{P_o}{\rho_o}}} = \frac{V}{\sqrt{RT_o}} \tag{2-94}$$

$$A = u + c \tag{2-95}$$

$$T = \frac{L}{A - D} + \frac{L}{D} \tag{2-96}$$

The velocity u is the velocity of particle in the laboratory reference frame and c is the local speed of sound [88]. Cell reinitiation study is acceptable only when the detonation is self-sustaining. Detonation initiated by a slightly overdriven ZND profile tends to reach self-sustaining mode easily compared to the detonation initiated using blast waves [42]. For global one-step chemistry, the detonation is initially run in one dimension to form its stable ZND structure to avoid startup errors and then the solution is used to initialize in two dimensions. Instead of initiating the perturbations using artificial patches, the detonation wave is assumed to be at a given angle to the x-axis. This causes the detonation to slap on the wall of the domain and create triple points as performed in the work of Oran et al. [42, 89].

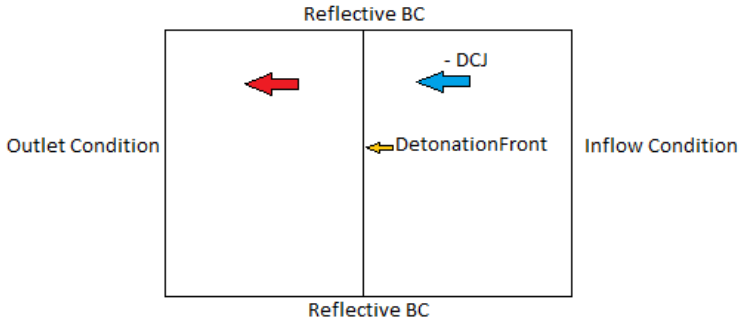

Figure 2-1 Illustration of Moving Reference Frame Setup

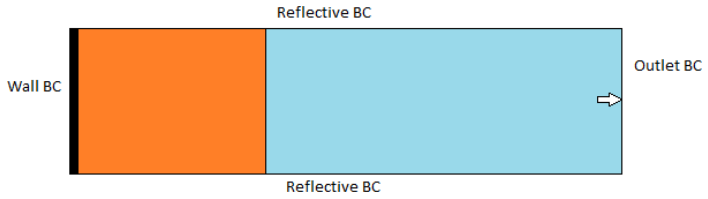

Figure 2-2 Illustration of Laboratory Reference Frame Setup

The instantaneous detonation front velocity must be tracked to be compared with experimental velocities patterns. In this thesis, local maximum pressure is determined from the maximum pressure gradient using the threshold jump and limits of pressure obtained analytically. With the location of shock at every time step, the velocity is obtained using second-order differentiation of the data points [51, 34].

2.7.2 Grid Resolution, Artificial Perturbation & Startup Error

The transverse instabilities are initiated artificially to reach a steady state faster. Two methods are used to initiate instabilities. The first method is to initiate using a pocket of unburnt gas behind the detonation

front. Typically, an unreacted pocket of gas is placed in the reaction zone (past the induction zone) with 15 % higher pressure than products. The disturbance from the combustion of this pocket propagates and hits the reactant front to initiate transverse oscillations. The second method is to initiate a triple point at the bottom wall by initiating a CJ detonation with an angle. Startup error plays a role in multistep chemistry simulation, especially for hydrocarbon chemistry. When a discontinuous solution is used for initialization, the smearing of shock waves on grid points induces truncation error, resulting in artificial perturbations [2, 77]. This perturbation destabilizes the reaction front resulting in an overdriven detonation causing local high temperatures, which is also reported by Ziegler [34] Hence the initial ZND solution run in one dimension for few times steps after which it converges to a steady pulsating solution [2] and then is extended to a two-dimensional solution to avoid startup error [44].

2.8 Adaptive Mesh Refinement Method

Adaptive Mesh Refinement has its advantages when a problem has localized gradients such as shock waves with other areas of smooth solutions. Approximately a ratio of 1 m (experimental setup) to 1 μm (spacial gradients), a range of 10^7 length scales may have to be solved for a complete resolution of a detonation simulation [27]. The AMR architecture used in this research is handled by the AMROC framework both for Roe-HLL and WENO codes [38]. AMROC is a data management engine which enables the parallel adaptive computation on structured grids. Based on the data structure an AMR strategy can be generally categorized into the block-based structure and cell-based structure [90]. The integration algorithm used in this research is the block-based adaptive mesh refinement method by Berger and Collela which is a recursive algorithm [91]. In 2D it uses patch-based grid refinement technique with interpolation functions to transfer cell values between cells of different levels. Block-based SAMR has its advantages in lighter data management and easier implementation of numerical schemes when compared to cell-based SAMR. Complications of block based SAMR arises in the clustering of the domains to multiple nodes in a distributed memory architecture. Usually, a distributed memory cluster has limited memory for every node. A detailed review of available block-structured adaptive mesh refinement (SAMR) packages has been given elsewhere [92]. To implement SAMR no additional modifications to the discretization stencils in flux form

for a single rectangular grid are necessary. The methodology followed in block based SAMR is explained briefly in the following section. This SAMR algorithm has five important sections of operations namely error estimator, grid generator, data structure, interpolation and flux correction [93].

Consider a rectangular domain E which forms the base level $l = 1$. The domain is converted into a control volume mesh depending upon the mesh spacing provided by the grid generator. The grid generator uses a smart bisection algorithm [93]. That rectangular base grid is discretized into X sub grids to be distributed to n nodes using load balancing domain decomposition technique aiming at minimum data syncing.

$$E_1 = \bigcup_{x=1}^{X} E_1^x \qquad \text{2-97}$$

By defining levels $m = 1, \ldots., l_{maximum}$, we get the relation

$$E_1^x = \bigcup_{m=1}^{M} E_{1,m}^x \qquad \text{2-98}$$

The parallelization or distribution of the grid hierarchy to multiple processors is made possible using the global indexing system provided by space-filling curves (SFC). The SFC is a mapping function that transforms a grid of n-dimension to 1-dimension and provides unique indexing. This index is used as a key for application domain partitioning and communication scheduling. The data of a partitioned base domain along with individual subdomains are stored in one node and are not shared between another node. The interlevel data transfer between processors is performed using an extendible hashing technique. A space-filling curve is a continuous curve that maps a multidimensional domain index to a single-dimensional global index by following an algorithm in this case the Hilbert load balancing algorithm [72]. The given domain is first decomposed into a collection of rectangular sub-grids for optimum load balancing using distributed memory machines. This forms the base level. Each level has a common space and time step size. Domain decomposition between advancing each timestep is performed in such that the refined grids follow the base grid. For example, a domain is mapped to a single curve and is split into three base domains in the following diagram.

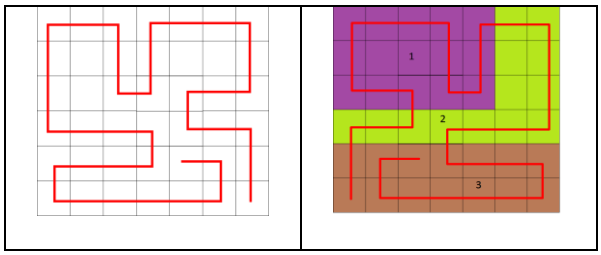

Figure 2-3 Schematic Diagram showing Domain Decomposition on Parallel Nodes

Now let us consider a single base level domain contained in node 1. The cells in domain 1 are flagged based on local error. The grid adaptation is performed along discontinuity using scaled gradients and along smooth solutions using heuristic error estimation by Richardson extrapolation [38]. Richardson extrapolation is used to measure the numerical error caused due to the discretization, artificial dissipation, lack of grid convergence, computer round-off, boundary non-continuity and lack of conservative property [94, 95]. When a single cell is highlighted or flagged based on the error indicators instead of replacing that single cell, a subgrid patch with a higher refinement level is wrapped around that cell. An additional layer of buffer cells is added around the refined patch called the buffer zone [91]. The clustering of new rectangular patches is performed according to a clustering algorithm proposed by Bell [93] which is based on signatures. An efficiency factor must be specified which controls the ratio of the flagged cells to the cells refined. Consider the cells highlighted in the previously segregated domain 1 below. Let the coarser grid with no refinement be the root level.

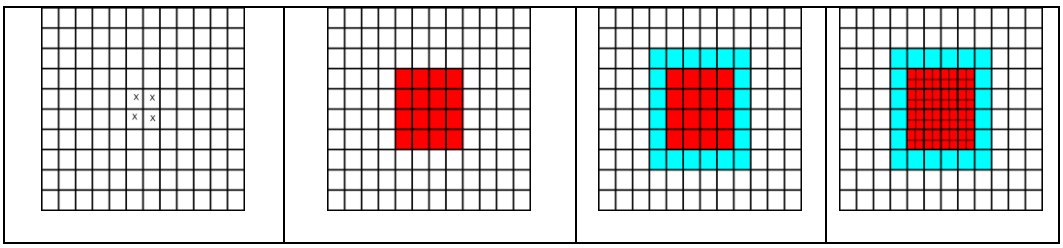

Figure 2-4 Schematic Diagram showing Grid Refinement Stages

The cells with a cross mark in domain 1 are highlighted for refinement. After the clustering algorithm notices the signature, it flags the marked cells along with the buffer layer. The layer around the buffer layer is a layer of ghost cells. The communication between the same level and between different levels is made possible using a ghost cell patch around each domain. The packets of data required by another cell for updating a level are performed by ghost cell syncing algorithms. Three different boundary conditions can

be applied to the ghost cell region. When the ghost cells extend the physical domain, physical boundary conditions are synced. When the ghost cells extend into a different domain with the same refinement level, interpolation is not required, and the values can be synced directly. But when the ghost cell of a refined grid coincides with cells of a coarser level, then time and space interpolation are necessary. Each grid patch which forms a new level contains its boundary conditions formed by ghost cells. The grid refinement factor is constant across all the levels. The ghost cells after interpolation are shown below.

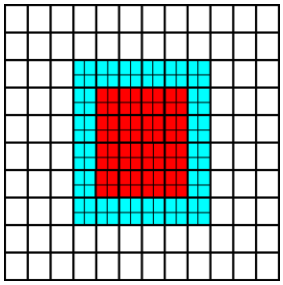

Figure 2-5 Ghost Cell Region Highlighted (Blue)

After the fine grid level reaches the same time as the coarser grid, the values of the fine grid are averaged and replaced with the cell values in the coarser grid. The value of state variables and fluxes are replaced using conservative average methods. When a fine grid is created during the initialization, the process is called a prolongation step and after the integration on the fine grid, the values are updated on a coarse grid which is known as a restriction step. The numerical stencil changes due to finer grids, giving rise to the issue of conservation loss and demands a conservation fixup. A conservative fix should also be applied to faces of coarse cells neighboring fine cells. The mathematical formulation of conservation average and conservation fixup methods used in AMROC can be found in detail in [72] The overall AMR architecture of the code can be split into two parts: application dependent routines with numerical operations and problem independent routines that handle the grid adaptation process. The problem-dependent part includes the initial and boundary conditions scheme and integration scheme. The integrator operates on individual subgrid and performs the above-mentioned tasks for a single timestep to output the cell fluxes. This represents application-level abstraction and is programmed in Fortran. The problem independent routines include error estimator, data structures, memory management, grid generation, local sub cycling,

interior boundary conditions, logic controlling the time stepping and interfacing algorithms to conserve fluxes at coarse-fine boundaries [93].

2.8.1 Problem Independent Algorithm and Data Structure - AMROC DAGH

An adaptive mesh algorithm that can operate on parallel heterogeneous machines is challenging without programming abstractions. Programming abstractions are split into program algorithms, dynamic data structure, and data abstractions. When using a multiprocessor cluster care must be provided to internodal or distributed memory communication. Programming abstractions as split into three abstractions; namely grid geometry abstraction, grid hierarchy abstraction and grid function abstraction. The dynamic data-structures supports the implementation of the abstractions in parallel environments and preserve efficient execution while providing transparent distribution of the grid hierarchy across multiple processors. The grid geometry abstraction contains the BBox, Cords and BBoxlist classes. This abstraction level is used to identify a geometric area by performing arithmetic operations on them such as unions, intersection, cluster, refine/coarsen, difference, etc. The grid hierarchy abstraction level is responsible for declaring the grid hierarchy formed due to AMR as the first-class object. It takes in the geometry of the base grid; grid refinement and grid extend information to store the hierarchy bounded by the input. During the partitioning process, this object is split between multiple processors using SFC and forms the template of splitting for grid functions. Operations performed include indexing of individual component grid in the hierarchy, refinement/coarsening/ recomposition of the hierarchy after regridding and querying of the structure of the hierarchy at any instant [96]. The re-partitioning dynamic load-balancing, and the required data-movement to initialize newly created grids, are performed automatically and transparently during regridding. The grid hierarchy class contains Gridbox and Gridboxlist classes. The Gridbox class stores a rectangular domain in the global index and the Gridboxlist class stores the list of Gridbox objects allocated for local processors as well as the global Gridboxlists. In AMR solver, the GH class is called inside the recompose algorithm. The final abstraction level is the grid function which stores the application variables of the grid hierarchy. The input for grid functions can be both dependent variables such as spatial/temporal stencil, dimension, type as well as Fortran functions for updating boundary/ghost cell values, inter grid transfers, etc. Each

Gridfunction object creates a GriddataBlock box object which stores the data in the Fortran format. The Gridfunction base class can contain a different form of the GriddataBlock object derived from it depending upon the required template such as Q_i and ∂Q_i. The AMR solver calls the Grid hierarchy or Gridfunction object depending upon the respective command in the AMR algorithm.

2.8.1.1 Algorithm – 1 – Recursive Algorithm

The AMRSolver class is responsible for three major operations, advance level, update level and regrid. The recursive algorithm for the update level is given below.

$Advance\ Level$

$$If\ time, Regrid\ (i)$$

$$Set\ Ghost\ Cells\ for\ Level(i)$$

$$Set\ same\ dt\ for\ all\ cells$$

$if\ level\ (i+1) exists$

$$Integrate\ Level\ (i+1)$$

$$update\ grid()$$

$end\ if - Recursion$

$$update\ grid(i=0)$$

end

The update level and advance level algorithm specified in [38] along with the parallel algorithm forms the middle stage. It involves flagging, clustering and fixup operations and is in C++ language. It is written independently of the specific numerical scheme at the application level. The base-level handles the grid hierarchical data and is modeled after the Distributed Adaptive Grid Hierarchy (DAGH) framework by Parashar and Browne [97].

2.9 Analytical Methods

A detailed layout of the chronology of different theoretical analysis of detonation is given in [75]. In this thesis, two of the analytical methods are used for calibrating one-step chemistry and comparing unsteady one-dimensional detonation with steady-state solutions.

2.9.1 *Chapman - Jouguet Theory*

Consider a shock wave moving from left to right with a velocity U_s in the laboratory frame. We can perform a control volume analysis more conveniently with fixing the reference frame to the shock. Hence

Upstream flow velocity = $U_s - u_1 = w_1$

Downstream flow velocity = $U_s - u_2 = w_2$

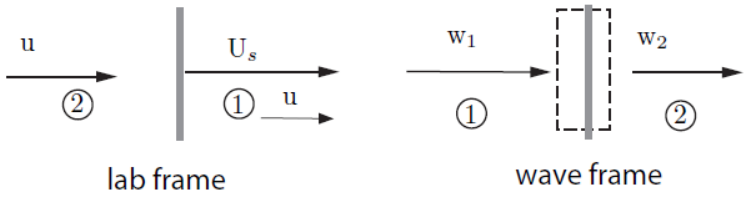

Figure 2-6 Illustration of Reference Frame Chosen in CJ Theory [75]

Now the one-dimensional steady-state jump conditions can be given using the following balance equations

$$\rho_1 w_1 = \rho_2 w_2 \quad \text{2-99}$$

$$p_1 + \rho_1 w_1^2 = p_2 + \rho_2 w_2^2 \quad \text{2-100}$$

$$h_1 + \frac{1}{2} w_1^2 = h_2 + \frac{1}{2} w_2^2 \quad \text{2-101}$$

$$p = \rho R T \quad \text{2-102}$$

Specific gas constant

$$R = \frac{\boldsymbol{R}}{W} \quad \text{2-103}$$

$$h = \sum Y_i h_i(T) \quad \text{2-104}$$

$$h_i(T) = \Delta_f h_i + \int_{T_o}^{T} c_{p_i} dT \quad \text{2-105}$$

After applying the CJ criteria, which is to solve for the minimum velocity for which the jump conditions are satisfied for the path taken by reactants to products at equilibrium and travel at supersonic velocity respective to laboratory frame, the products reach sonic point behind the detonation wave, $\left[\left(\frac{ds}{dv}\right)_{CJ} = 0\right]$.This minimum velocity is achieved when the Raleigh line is tangent to the Hugonoit curve for a fixed exothermic heat release q. From the CJ theory, for ideal detonations, there exists a sonic point

that isolates the reaction zone from the perturbations behind it. It assumes that the sonic plane is immediately behind the shock front but in the real case, the sonic plane lies at the end or within the reaction zone [2]. The CJ theory has its advantage in predicting close values of experimental detonation velocities without any dependency on the structure reaction front. The products traveling with velocity higher in multiples of the speed of sound, which sets the combustion products in motion in the direction of wave propagation is termed as detonation. The combustion product which travels subsonic relative to the wave is a strong detonation and the combustion product traveling supersonic relative to the wave is a weak detonation. Hence with strong detonation approximation, we obtain the following relations for a single γ model approximation

$$D_{CJ} \approx \sqrt{2(\gamma^2 - 1)q} \quad \text{2-106}$$

$$\rho_{CJ} \approx \frac{\gamma + 1}{\gamma}\rho_1 \quad \text{2-107}$$

$$P_{CJ} \approx \frac{1}{\gamma + 1}\rho_1 U_{CJ}^2 \quad \text{2-108}$$

$$a_{CJ} \approx \frac{\gamma U_{CJ}}{\gamma + 1} \quad \text{2-109}$$

$$u_{CJ} = \frac{D_{CJ}}{\gamma + 1} \quad \text{2-110}$$

2.9.2 ZND Theory

The ZND theory assumes an one-dimensional, compressible, inviscid flow conditions. According to this theory, detonation can be segregated as a shock wave traveling at CJ velocity producing compressed and heated gas. After the induction zone, the reaction begins increasing the temperature but reducing the density and pressure. The reaction progresses until it reaches equilibrium which is also marked by the sonic plane (also known as C-J plane) [98]. The sonic plane is followed by expansion waves. The governing equations are given as follows

$$w\frac{d\rho}{dx} = -\frac{\rho\dot{\sigma}}{1 - M^2} \quad \text{2-111}$$

$$w\frac{dw}{dx} = \frac{w\dot{\sigma}}{1-M^2} \quad \text{2-112}$$

$$w\frac{dP}{dx} = -\frac{\rho w^2\dot{\sigma}}{1-M^2} \quad \text{2-113}$$

$$\dot{\sigma} = \sum_i^N \frac{\Omega_i}{\rho c^2}\left(\frac{\partial P}{\partial Y_i}\right) \quad \text{2-114}$$

As we can see, the thermicity should approach to zero to avoid singularity when Mach number goes to 1 forming sonic plane at the end of the reaction zone in exothermic systems. The above two theories give a good picture of a steady detonation wave with no instabilities.

2.9.3 Summary

To conclude, a brief description of the governing equations of the models, calibration techniques, schemes used by the solvers, SAMR algorithm, appropriate boundary conditions used by the solvers and analytical model were presented in this chapter. The following chapter proceeds with the verification and validation of the models mentioned in this chapter to quantify the errors and check for grid convergence with simple cases.

Chapter-3 CFD Code Accuracy & 1D Instability Analysis

A CFD code chosen for a predictive study must be subjected to four processes as mentioned by Stern et al. [95] namely preparation, verification, validation, and documentation. The verification involves assessing the accuracy of the solution by determining the numerical uncertainty (U_{SN}) [95]. The numerical uncertainty can be gauged through the magnitude of numerical error and is generally measured with benchmark solutions of simplified analytical model problems [99]. The validation involves assessing the accuracy of the solution by determining the modeling uncertainty (U_{SM}) [95]. It is measured with post processing the results of the numerical model to one or more quantities to compare it to experimental data to find the modeling error [99]. The overall simulation error is the sum of numerical error and modeling error. Different definitions for terminologies such as verification and validation used in CFD can be found in [95]. In a $x-t$ diagram, if $u(x,t)$ is a solution of a k^{th} order pde function $F(x,u,Du,\dots,D^k u)$(like Cauchy problem), a strong or classical solution of a pde is when $u(x,t)$ is k times continuously differentiable [100]. A weak solution is the solution with $u(x,t)$ discontinuous about a curve with classical solutions on both the sides of a discontinuity in the solution and $u(x,t)$ satisfies the Rankine-Hugonoit jump condition. When the time scale of source terms is shorter than the time scale of homogenous equations, the source terms are stiff. When the grid is coarse to not represent the influence of the source term, the solution converges to a different weak entropy solution of the inhomogeneous equations [38]. The shock front of an unsupported detonation survives on the feedback from reaction front which when predicted wrongly, results in wrong shock front speed [38]. It is also important to note that the mass fraction of species is conserved over the admissible shock and rarefaction waves [38]. A parametric study of mesh size with fixed reactants shows coarse mesh resolution with ignition temperature close to unreacted mixture temperature leads to instances were a weak detonation wave was followed by an ordinary shock wave in place of a strong detonation wave [101]. The wrong solutions are the convergence of solutions towards non-physical weak solutions. The velocity of burnt gas behind the detonation wave is also compared with the exact solution to discard the non-physical solution [101]. In the same study, the wrong location of the reaction zone was also predicted for a few other cases. Iterative convergence and grid convergence are two necessary convergence studies for any CFD simulation [102]. Since the Riemann solver is a direct explicit solver, the iterative convergence

error quantification is not possible, but grid independence study is necessary. A grid-independent solution can be obtained through local refinement based on a criterion instead of a global refinement [102]. AMR based on scaled gradient and heuristic error approximation satisfies this criterion.

3.1.1 Sod's Shock Tube Analysis

In the presence of a shockwave, the numerical formulation which is strictly conservative only in a mathematical point of view results in wrong shock propagation speeds and wrong solutions. Rarefaction waves have a gradual change of flow properties across them and when a rarefaction wave is transonic or sonic it may give rise to nonphysical entropy violating discontinuous waves (rarefaction shocks) [78] . An inevitable test case for numerical methods solving discontinuities is the Sod's shock tube problem [80]. The analytical solution was calculated using exact Riemann solver (HE-E1RPEX) for the time-dependent one-dimensional Euler equations using ideal gas [78]. All the variables were nondimensionalized. Three levels of the grid were used: coarse with $\Delta x = 1/1000$; medium with $\Delta x = 1/2000$ and fine with $\Delta x = 1/4000$. Both the second order Roe-MUSCL code and fourth order WENO/CD code were compared with the solution of exact Riemann solver. All the results are plotted at T=0.16.

Table 3-1 Initial Data for Sod's Shock Tube Problem

$Flow\ Variable$	$Value$	$Location$
ρ_L	1.00	$x < 0.5$
p_L	1.00	
u_L	0.0	
ρ_R	0.01	$x \geq 0.5$
p_R	0.01	
u_R	0	

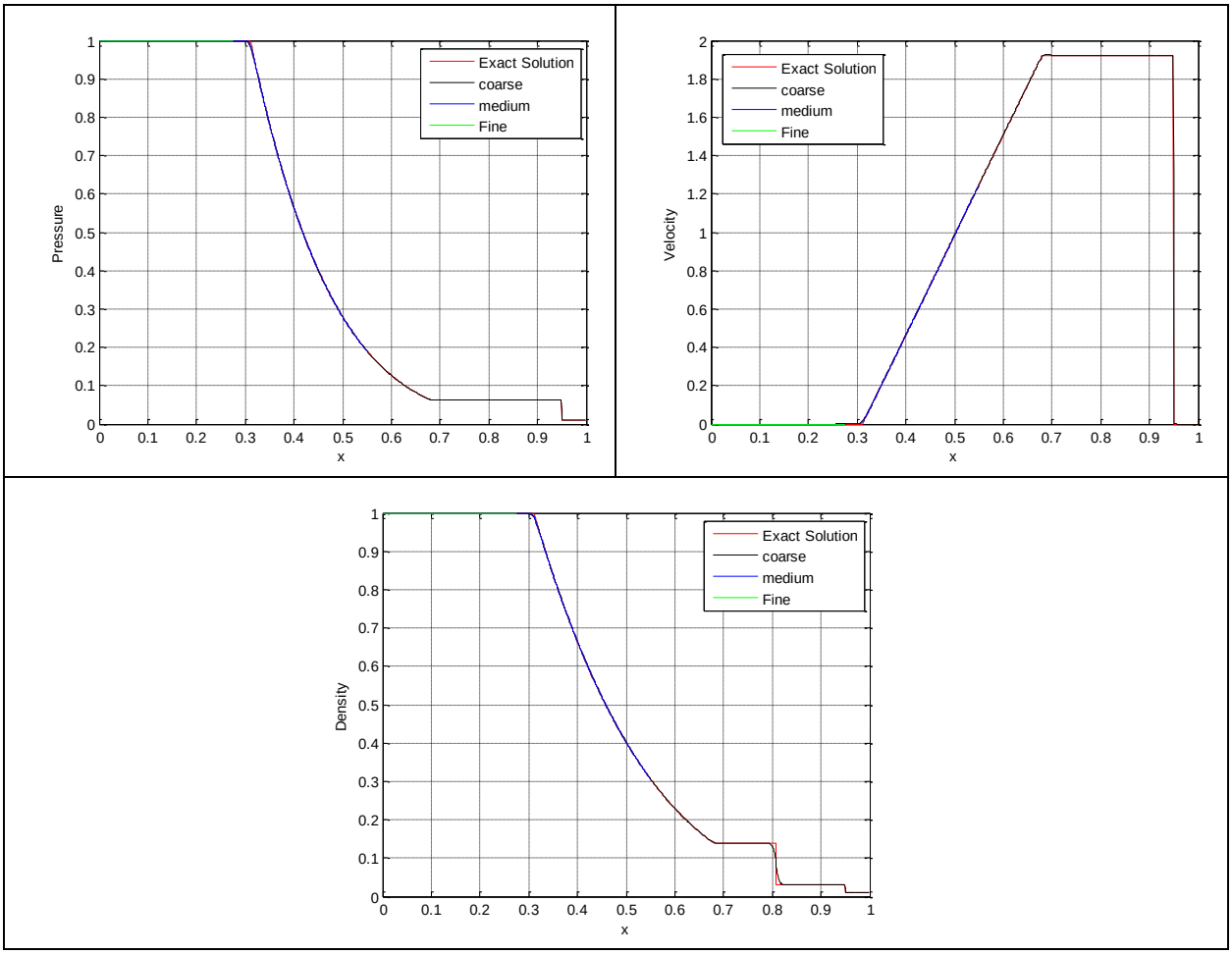

Figure 3-1 Comparison Plot Between Exact Solution and Numerical Solution for Sod's Shock Tube Problem (Rho-MUSCL)

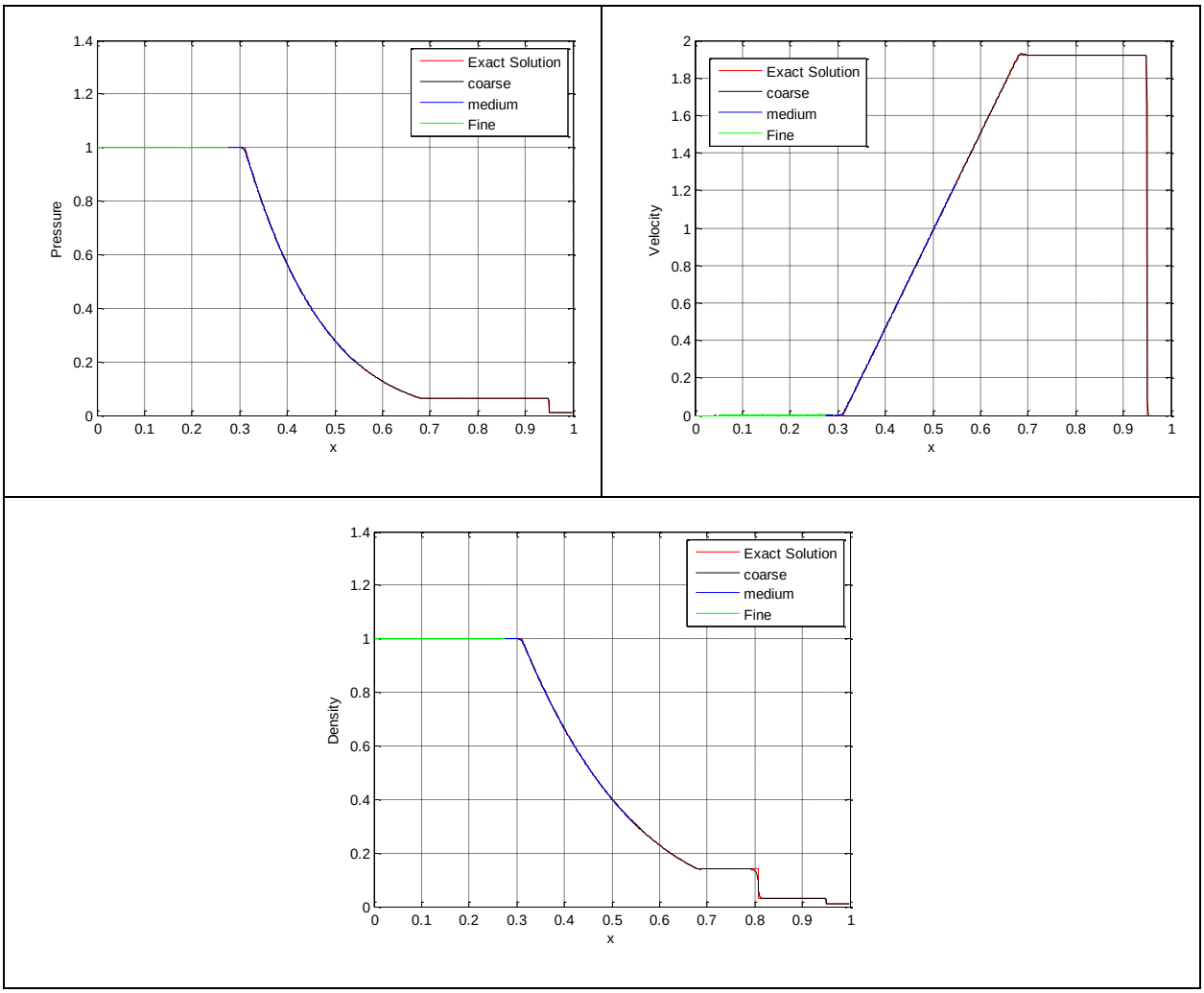

Figure 3-2 Comparison Plot Between Exact Solution and Numerical Solution for Sod's Shock Tube Problem (WENO-CD)

Visual comparison between the variables from the exact solution and discretized solution does not show differences except at sharp discontinuities. No spacial oscillation error was visible. The observed order of accuracy of a scheme can be estimated by analyzing the behavior of the norms of the spacial error of the variables solved for. Since the global order of accuracy reduces to one in the presence of discontinuities [103], the norms of the solution for three levels of the grid without adaptive mesh refinement are compared. The norm of the dependent variables is calculated as [104]

$$L_1\ norm = \sum_{1}^{N} \frac{|f - f_{exact}|}{N}$$

Table 3-2 Comparison of L_1 Norm for Roe-MUSCL and WENO/CD Schemes

$\Delta x\ (r = 2)$	Rho-MUSCL Second-Order Accurate			WENO-CD Fourth-Order Accurate		
	Density L_1 norm	Velocity L_1 norm	Pressure L_1 norm	Density L_1 norm	Velocity L_1 norm	Pressure L_1 norm
1×10^{-3}	8.48×10^{-4}	3.5×10^{-3}	4.62×10^{-4}	6.74×10^{-4}	2.3×10^{-3}	4.45×10^{-4}
5×10^{-4}	4.69×10^{-4}	1.7×10^{-3}	2.28×10^{-4}	3.54×10^{-4}	1.1×10^{-3}	2.24×10^{-4}
2.5×10^{-4}	2.65×10^{-4}	7.75×10^{-4}	1.21×10^{-4}	2.00×10^{-4}	4.54×10^{-4}	1.04×10^{-4}

It can be seen from the residual table that the second-order Roe-MUSCL scheme performs competitively with the fourth-order WENO-CD scheme in the Sod's shock tube problem. This performance trend was also observed in [103] when comparing fifth-order accurate WENO code with a second-order accurate Godunov's code for Sod's shock tube case.

3.1.2 Mach Reflection - Validation

The Sod's shock tube problem was used to verify the stability of the solver with one-dimensional discontinuities. A two-dimensional oblique shock reflection problem involving Mach reflection containing nonlinear wave interactions is chosen in this section for benchmarking the WENO/CD solver. A detailed experimental study on oblique shock reflection performed in the University of Toronto has was chosen to validate the inviscid version of the WENO-CD code for a non-reactive Mach reflection problem [105]. The shock tube used for the experiments was 10 cm × 18 cm in dimension. The objective of this test was to test the flagging and switching of the scheme in the presence of shocks. It also allows us to understand the flow physics in the absence of physical viscosity which alters the diffusion of the slipstream. This is also important to understand the dynamics of the curving slipstream in the absence of the boundary layer as the slip wall boundary condition is assumed [105]. Since the problem setup is inviscid, the solution is self-similar. Hence a geometry of 40×40 mm and a base grid resolution of 1600×1600 was chosen. The working gas was air at initial conditions of 33 kPa pressure and 298 K temperature. The bottom wall and wedge were assigned to be a slip wall and the rest of the boundary conditions were supersonic outlet

boundary conditions. A normal shock wave with a Mach number of 2.03 was rotated to $27^o\ deg$ and placed on an inclined wedge with the same angle. This shock wave interacts with the wall by traveling from right to left and forms the Mach reflection configuration which can be calculated analytically using shock polar relations. The density field was studied in the experiment using interferometer which allowed us to view the isopycnics of the flow field [105].

Table 3-3 Grid Resolution Description for The Mach Reflection Validation Case

Grid Level	Grid Size
Base Grid	0.1 mm
Level – 2 (r=2)	0.05 mm
Level – 3 (r=2)	0.01 mm
Level – 4 (r=2)	0.005 mm

The density profile obtained from experiments is compared with the density contour from the WENO/CD inviscid simulation below. It can be seen that the solver predicts the correct weak triple point structure (T) with a curved reflected shock (R) and slip line (S). Further, the density measurements along the wall are compared with the fine grid resolution shows good agreement in the plot below.

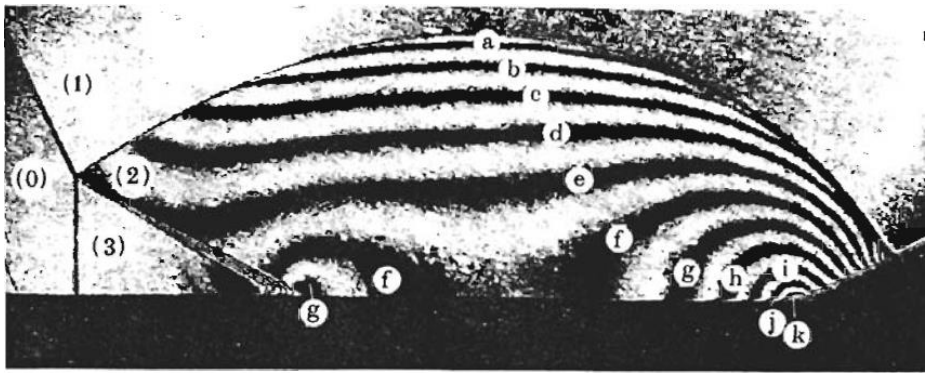

(a)

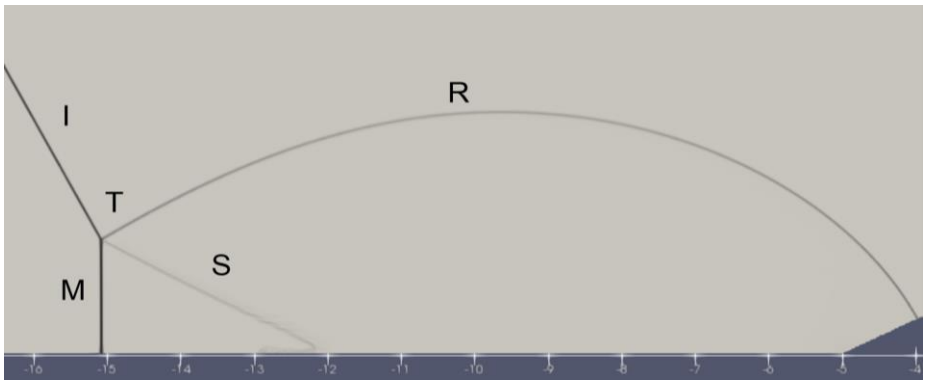

(b)

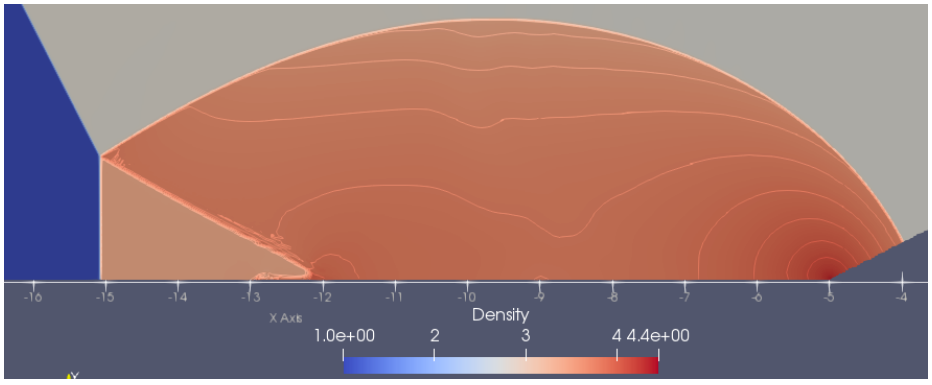

(c)

Figure 3-3(a) Density Profile Record with isopycnics from Experiment [105] (b) Density Gradient Contour from Simulation and (c) Density Contour with Isolines

The isopycnic lines were visualized from the density contour and were found to be comparable in position with the experimental description. The density measurement along the wall and the density jumps around the triple point configuration were also compared with the experimental results which are shown below.

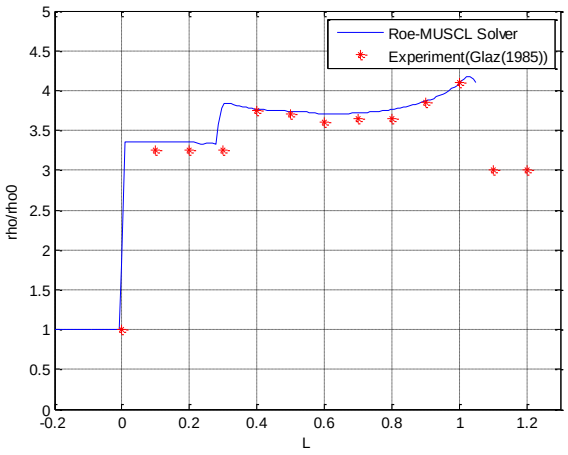

Figure 3-4 (a) Comparison of Density Measurements Along the Bottom Wall

Table 3-4 Comparison of Density Jumps Around the Triple Point Region

Zone	Experimental Density Ratio	Numerical Density Ratio (Fine Grid)
0	1	1
1	2.71	2.74
2	3.68	3.67
3	3.33	3.35

As mentioned in the numerical scheme section of Chapter-2, a Riemann based switch tracks the location of the shock to switch from the centered difference scheme to the WENO scheme to avoid overshoots at a sharp discontinuity. The flagged region for the use of WENO is shown below.

Figure 3-5(a) Region Flagged For Scheme Switching

As the Mach reflection structure grows after reflection, the slip line undergoes instability to produce the Kelvin-Helmholtz “willow” structures resulting in a spatially growing mixing layer. Though there is an

absence of shear stress terms, the inflection profile between the two tangential velocity results sets in a KH instability. The density contour plot showing the transition of the slip line is shown below along with its two-dimensional vorticity plot displaying the interaction between the coherent structures.

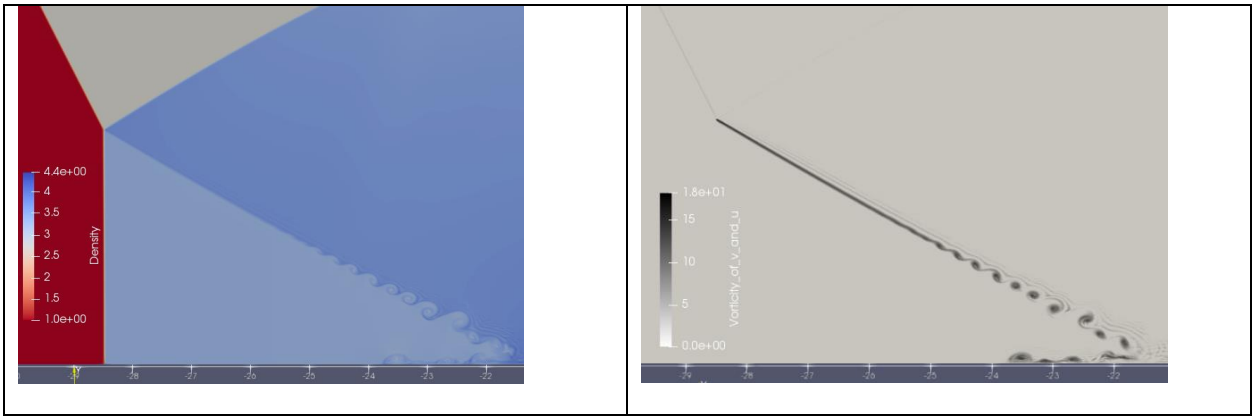

Figure 3-6(a) Density Contour (b) Vorticity Contour of Mach Reflection

The curving of the slip line towards the shock occurs due to the high-pressure region formed behind the collision point of the slip line along the wall where the flow behind the slip line impinges. A more detailed review of slip line curvatures behind triple point configuration can be found in [106]. The high-pressure region is shown in the pressure contour below.

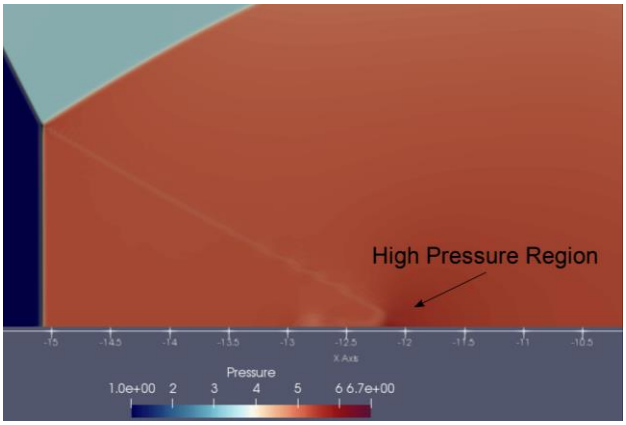

Figure 3-7(a) Pressure Contour showing the High-Pressure Region Behind the Slipline Reattachment Point

3.1.3 One Dimensional Detonation

The concept of one-dimensional instability sheds light on the nature of detonation before proceeding to study instabilities from two-dimensional simulations. Several theoretical models have been

established to analyze the feedback mechanism causing instability in characteristic space especially for CJ detonation [107, 108, 109]. Two main timescales which control the feedback mechanism are the acoustic timescale and reaction timescale. One-dimensional stability analysis on detonation has been performed either by analyzing for instability in linearized Euler equations using eigenmode analysis or numerically solving Euler equations [110, 2]. This parametric study is conducted to study the different regimes of stability and the variation in reinitiation between them. The one-dimensional domain is initialized with a steady-state ZND solution and perturbated with 10% perturbation in the pressure profile behind detonation. The instabilities formed are then analyzed by tracking the shock strength when marched in time using the one dimensional, second-order, inviscid, global one-step chemistry solver. The chosen set of parameters to be constant are $Q = 45\,; \gamma = 1.2\,; f = 1.0$. The activation energies are varied to demonstrate the neutral, weakly unstable and highly unstable detonation instabilities. From the neutral stability curve determined through linear stability analysis using normal mode approach by Lee et al. [111], the stable limit for the chosen set of parameters is $E_a = 23$. The value of activation energy chosen in this study are increased from $E_a = 22.5$ to check the stability limit and then increased till detonation limit in one dimension is lost. By fixing all other properties and increasing the activation energy, we increase the induction length of the detonation but the velocity and change in heat of formation of the mixture are constant. With the increase in activation energy, the length of the reaction zone also reduces due to the increase in sensitivity of the reaction rate towards the temperature. This controls two important parameters, first the $\frac{\tau_i}{\tau e}$ ratio which represents the detonation stability and second the τ_a/τ_e which is the ratio between acoustic time scale and exothermic time scale. The τ_a/τ_e decides on the response of the gas after heat addition. The length of the one-dimensional domain was $50\Delta_{HRL}$ for each simulation with stationary frame of reference and had a grid resolution of $128\Delta_{HRL}$ grid points. The half reaction length (HRL) scale is the sum of induction length and half the length of energy release pulse obtained from the ZND theory. All the solutions were marched until T=210 and the instantaneous velocity history of the shocks is shown below

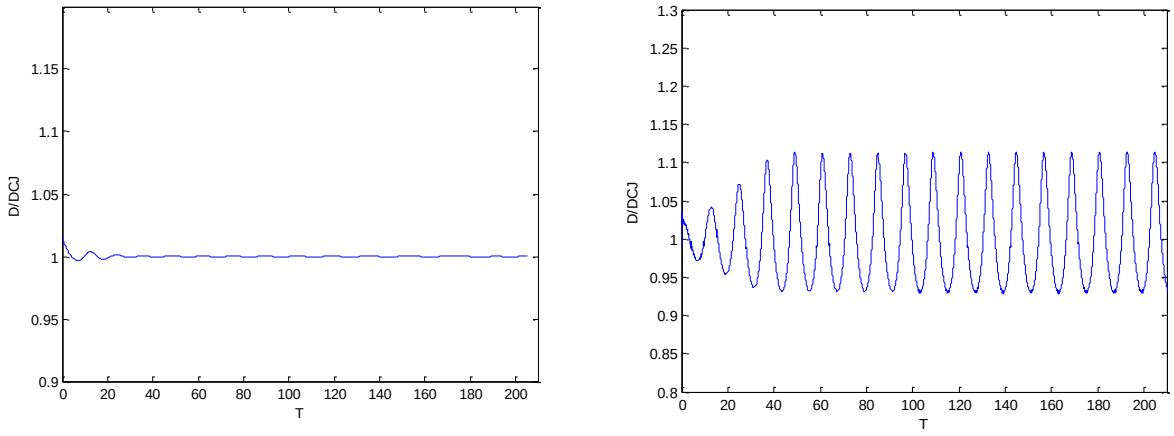

(a) (b)

Figure 3-8 Instantaneous Velocity Ratio of Detonation at (a) $(E_a = 22.5)$ (b) $(E_a = 25)$

The above plot shows the velocity ratio profile for $E_a = 22.5$. Though it is close to the stability limit, the oscillation damps and returns to constant CJ velocity showing that the detonation is still stable. For an $E_a = 25$, the oscillation grows and settles at a cycle limit after T ≈ 3 with a single unstable mode. The range of the velocity limits is narrow. Increasing the activation energy further, to $E_a = 26$ results in detonation with two unstable modes within a limit cycle. For $E_a = 27$, we can see that the detonation contains three unstable modes. The detonation also spends more time in the initial transient with the increase in unstable modes and limits of the detonation velocity increases in range. The limit cycle time also increases further. The irregularity of the detonation increases further with $E_a = 28$ and $E_a = 29$ making the limit cycle measurement not applicable. The detonation could no more survive with unstable modes operating in only one dimension at $E_a = 29.1$ and dies at T=180. When the strength of the detonation falls below the minimum temperature with which the reaction can be explosive, during the lower limit of the cycle, the detonation decouples and dies.

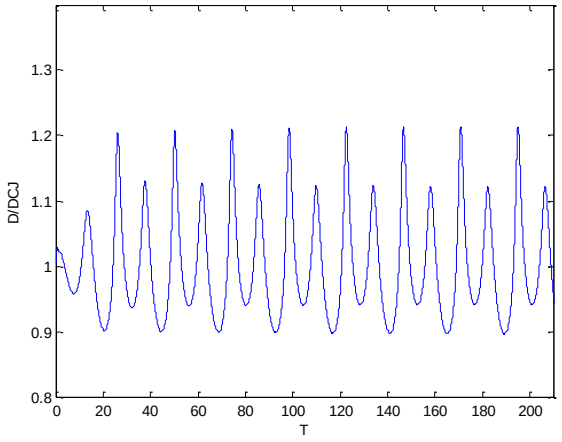

(a)

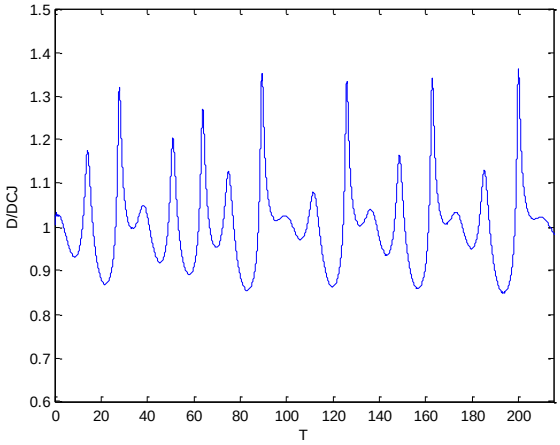

(b)

Figure 3-9 Velocity ratio of Neutrally Stable Detonation $(E_a = 26)$ and Weakly Unstable Detonation $(E_a = 27)$

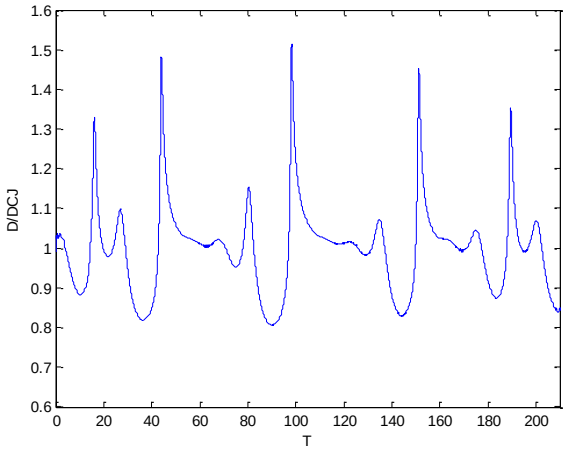

(a)

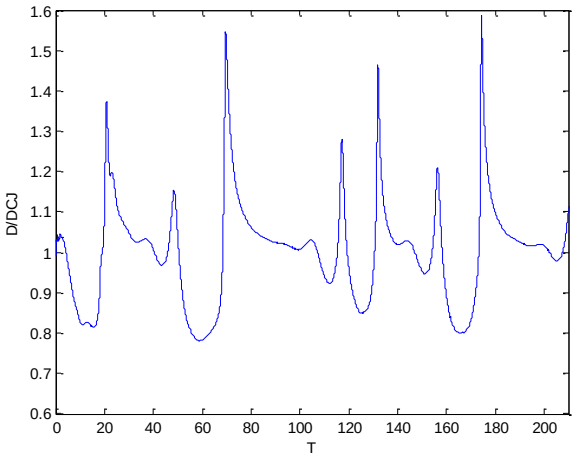

(b)

Figure 3-10 Velocity Ratio of Highly Unstable Detonation $E_a = 28$ & $E_a = 29$

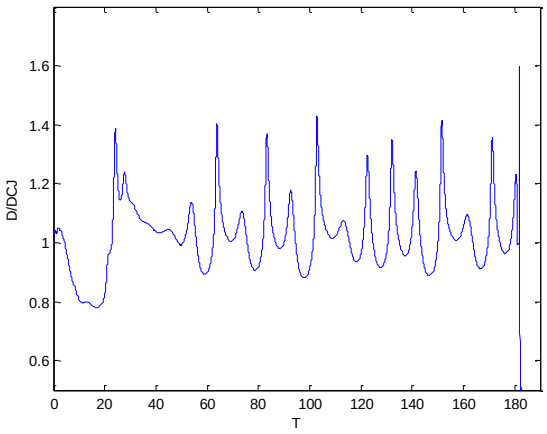

Figure 3-11 Velocity Ratio of Highly Unstable Detonation at $E_a = 29.2$

Even in one dimension, the instability mechanism and its reinitiation are necessary for the survival of the detonation. With an increase in the sensitivity of the reaction rate to temperature, new unstable modes appear. The propagation mechanism for the flame contact surface is only through convection. The difference between the reinitiation mechanism with increasing instability is briefly demonstrated by analyzing the cases with $E_a = 25$ (single mode) and $E_a = 26$ (dual mode) further. The following set of graphs shows one reinitiation cycle in a single-mode unstable detonation in a sequence. The peak pressure from T=19 drops, and the shock loses its strength from T=20 to T=22. This communication from shock is transmitted to the reaction zone through rarefaction waves. Interaction of rarefaction wave and contact surface accelerates the reaction zone at T=23, creates compression waves and accelerates the detonation till it peaks again at T=25 completing one cycle. The interaction of this compression wave and shock can be seen in the T=22 plot where there is a local peak just behind the shock front. All these interactions responsible for reinitiation occur between the shock front and the reaction zone.

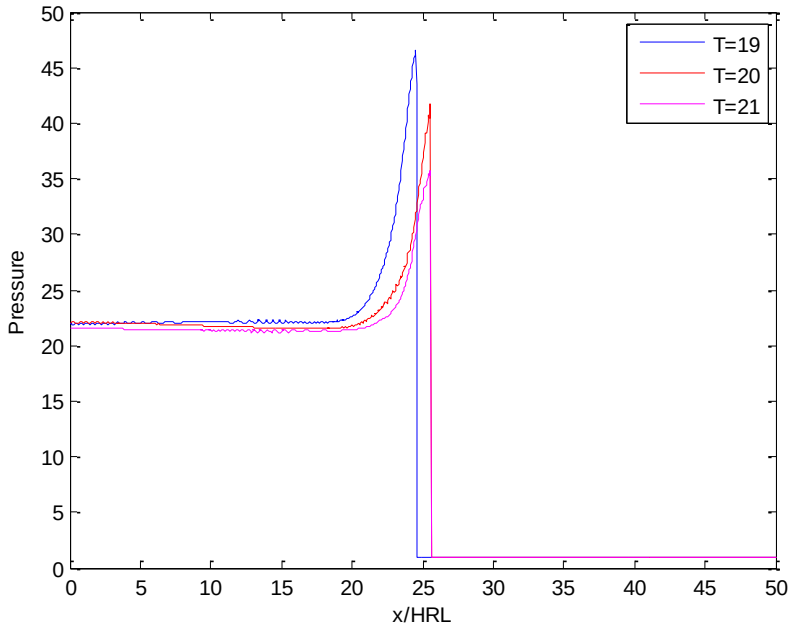

(a)

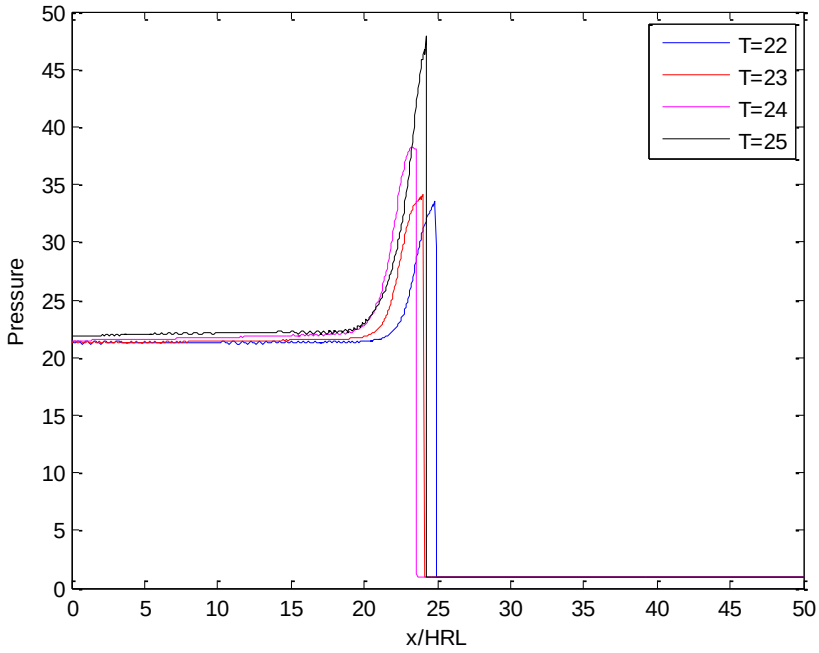

(b)

Figure 3-12 Pressure Profile of Detonation with $E_a = 25$ from (a) T=19-21 (b) T=22-25

To visualize the above reinitiation event, the width of the domain was set to 10 HRL discretizing with only one cell for the breadth of the domain in a two-dimensional solver and dynamics of the shock and the reaction zone was captured for one limit cycle. The following contours show product contour overlapped with pressure gradient contour which shows the position of the shock in a sequence. The shock decay begins at T=20 with the thickness of the induction zone increasing and the reacceleration of the reaction zone is visible at T=23. The reaction zone accelerates and supports the shock until T=25 completing one limit cycle.

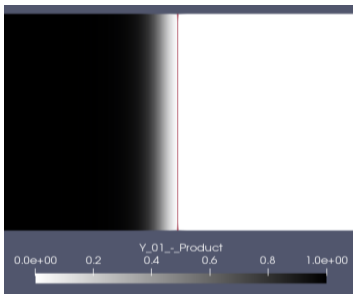

T=19

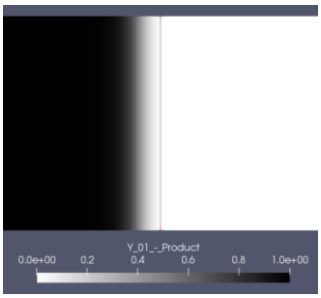

T=20

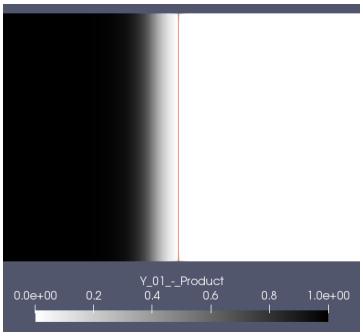

T=21

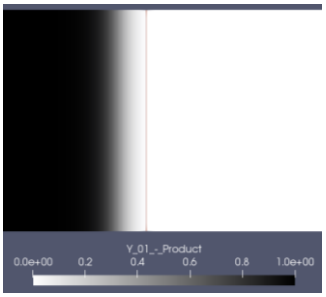

T=22

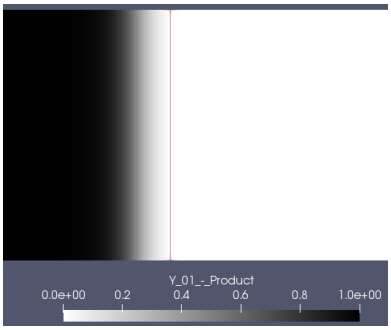

T=23

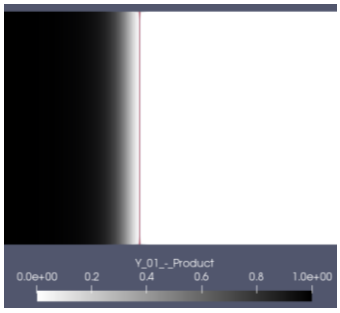

T=24

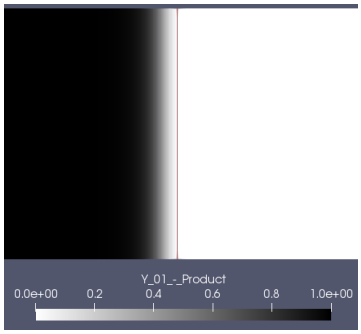

T=25

Figure 3-13 Sequence of Reinitiation of Detonation $E_a = 25$ using Pressure Gradient and Product Contour

The reinitiation mechanism of a weekly unstable detonation is through regular interaction between the shock front and the reaction zone through mechanical waves. From the instantaneous velocity profile the wavelength of the oscillations was understood to be larger than the induction zone. This reinitiation mechanism was also observed by Short et.al [20] in a detailed numerical study of the interaction of gas dynamics and chemistry for detonations in one dimension. The reinitiation mechanism of two-mode detonation is analyzed further. In this reinitiation, there is one high amplitude unstable mode and a low amplitude unstable mode. A cell cycle starting at T=20 is considered in the following plots. The detonation starts decaying until T=23. At T=24, the reaction zone accelerates creating compression waves. At T=25, we see a shock front formed which is stronger than the precursor shock. At T=26, the second shock merges with the precursor shock and forms the high amplitude unstable mode. This detonation front loses its strength immediately at T=27 and T=28. At T=30, the reaction zone accelerates again and accelerates the primary shock front forming the second low amplitude instability. The mechanism of production of shockwaves through sudden energy deposition (acoustic time scale $\approx$ exothermic time scale) by reaction zone was demonstrated and studied by Regele [112] though a one-dimensional analysis. The velocity profile peaks at T=26 creating the largest pressure peak of the limit cycle, where the shockwave has merged with the primary shock.

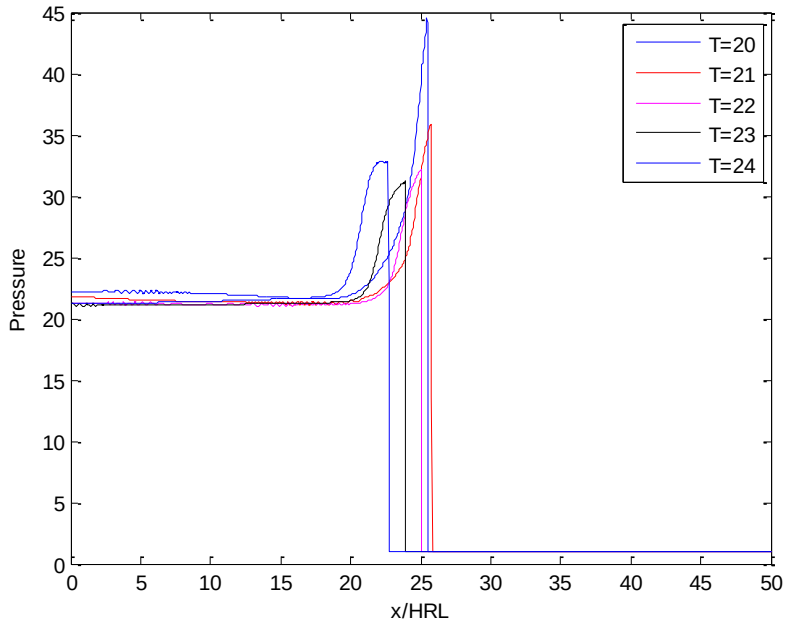
T=20
T=21
T=22
T=23
T=24
Pressure
x/HRL
0
5
10
15
20
25
30
35
40
45
50

(a)

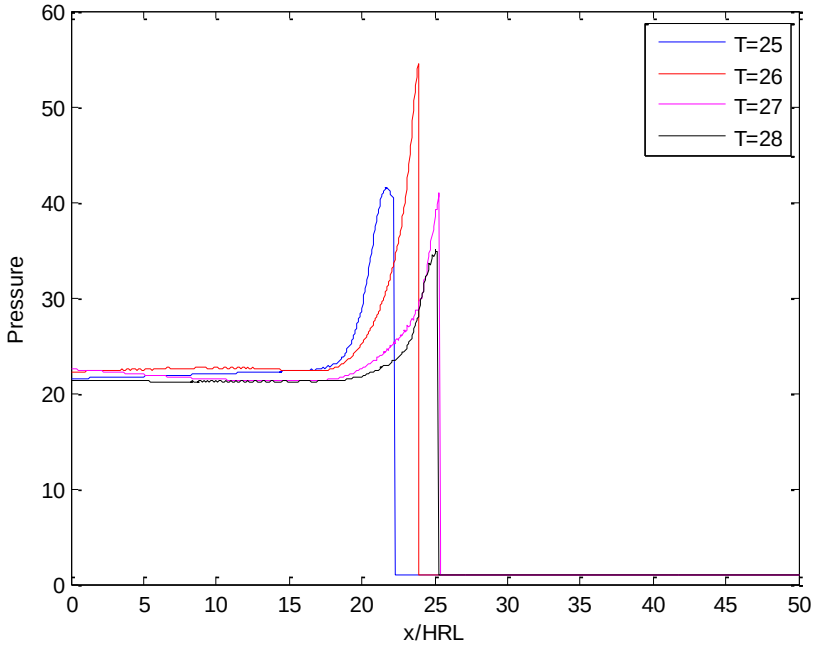
T=25
T=26
T=27
T=28
Pressure
x/HRL
0
10
20
30
40
50
60

(b)

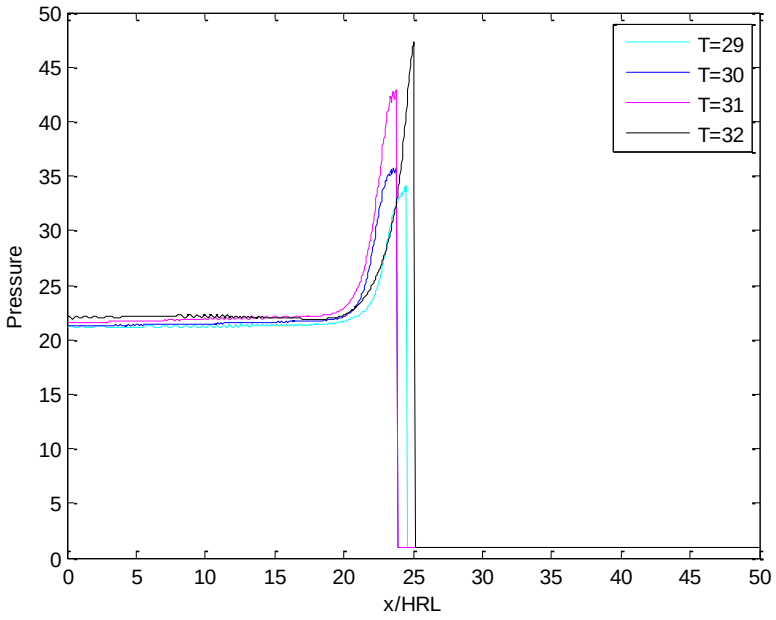

(c)

Figure 3-14 Pressure Profile of Detonation with $E_a = 26$ from (a) T=20-24 (b) T=25-28 and (c) T=29-32

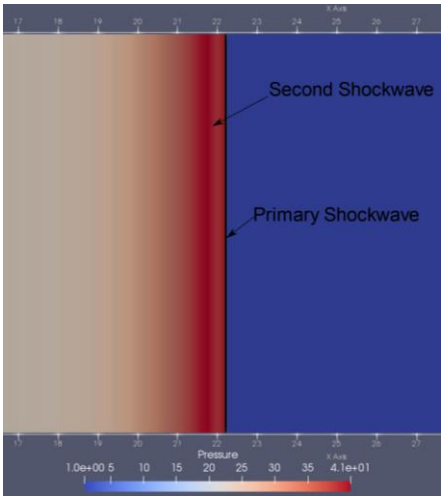

Figure 3-15(a) Pressure Contour Overlapped with Gradient of Pressure showing the Formation of Second Shockwave at T=25

The overall reinitiation event is again visualized using a one-dimensional equivalent product contour overlapped with the pressure gradient. The high amplitude instability occurs at T= 25 and the low amplitude instability at T = 30 completing one limit cycle.

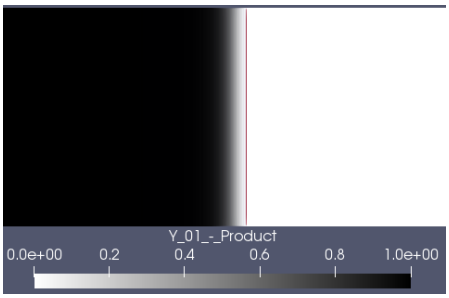

T=20

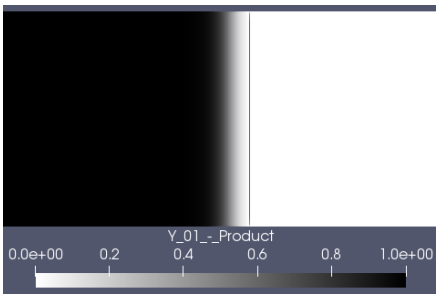

T=21

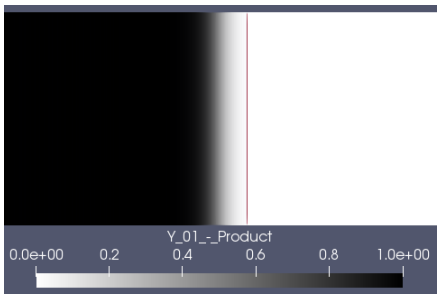

T=22

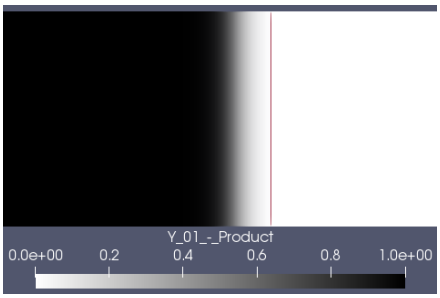

T=23

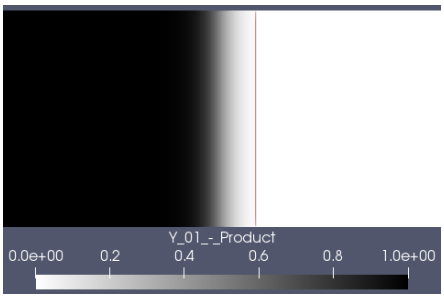

T=24

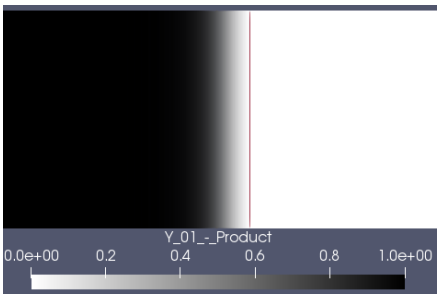

T=25

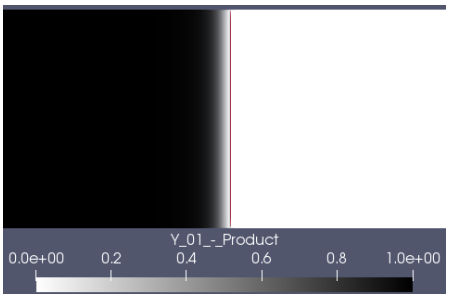

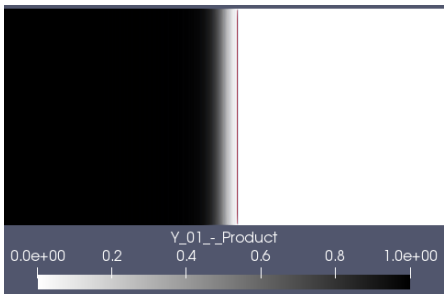

T=26

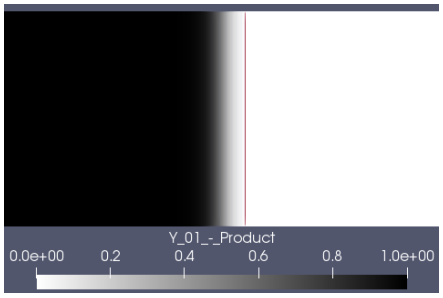

T=27

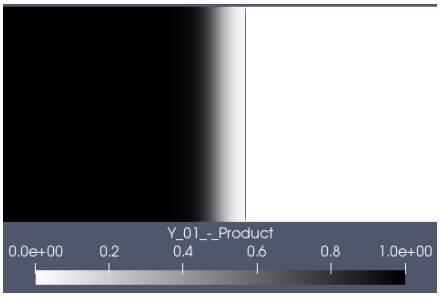

T=28

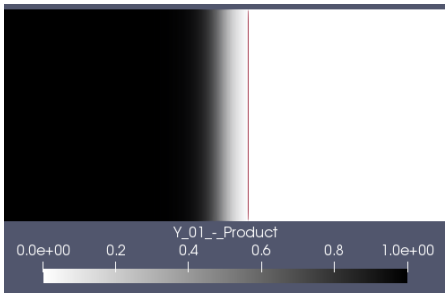

T=29

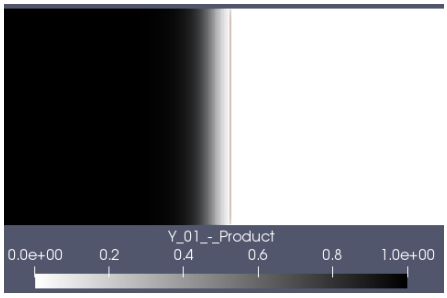

T=30

T=31

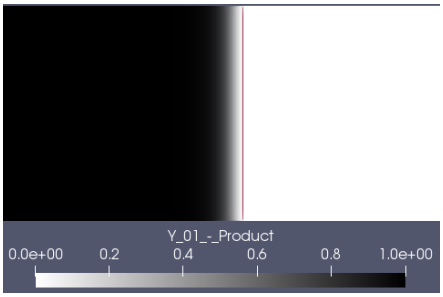

T=32

Figure 3-16 Sequence of Reinitiation of Detonation $E_a = 26$ using Pressure Gradient and Product Contour

Thus the amplitude and frequence of the feedback from reaction zone varies with the nature of the detonation has been demonstrated in this one dimensional study.

3.1.4 Summary

To summarize, the verification of the Roe-MUSCL and WENO-CD code was completed using the Sod's shock tube problem. With strong discontinuities present in the domain, the second-order code performed equivalently with fourth-order accurate code in terms of discretization error. A non-reactive, inviscid two-dimensional validation was performed using a Mach reflection study to validate the performance of the scheme switching capacity of the WENO-CD code. The analysis shows that the scheme was able to perform without any discrepancy which can occur at level interfaces for an AMR solver. The triple point structure and the density measurements obtained from relevant experiments were compared. Further, the concept of instability in detonation was briefed using one-dimensional instability for mixtures with varying stability parameters. The dynamics of high amplitude and low amplitude instability and its effect on the shock front was discussed. In the next chapter, the reinitiation mechanism of a regular detonation in two dimensions will be analyzed.

Chapter-4 Reinitiation in Regular Ordinary Detonation

This part of the study aims to validate inviscid global one-step chemistry, inviscid multistep chemistry and viscous one-step chemistry versions of the code used in this thesis for its ability in predicting detonation-based flows by studying the reinitiation of a regular detonation. The drawbacks of using one step calibrated chemistry over multistep chemistry are shown. The following parameters are chosen as variables for the validation study

- Shock velocity profile of detonation
- Structure of the triple point
- Cell aspect ratio, mode of detonation
- Averaged flow profile contours
- Numerical soot foil
- Reinitiation mechanism and formation of the secondary triple point

Validation with irregular detonation such as methane-based detonation requires more than one experimental sample since its stochastic behavior for the same initial conditions and experimental setup was studied and shown in [62]. Interest in gaseous hydrogen-oxygen detonation diluted with argon began with the experimental studies in the 1960s by Strelow [113, 114, 115]. This was followed by Fickett and Davis [3] to study the general structure of a regular detonation in both narrow (rectangular) and cylindrical tubes. Their results suggested that the triple point structure transitions from a weak form to a strong form after transverse wave collision. To add to the interest of this problem since the strong structure of the detonation is often correlated with marginal detonation [56], the categorization of 70% argon diluted hydrogen-oxygen detonation to either ordinary or marginal detonation has been inconclusive. Since the possibility of studying the transitional triple point structure was limited in experiments due to the small scales several numerical analysis simulations were performed in 2D/3D, with simplified/complex chemistry, etc. to understand this transition phenomenon further. Early numerical study on argon diluted hydrogen-oxygen detonation was performed by Taki et.al [116] with one step chemistry and focused on transverse wave structures. Stable modes of self-sustaining detonation, periodic reinitiation of detonation, and the effects of artificial diffusion on the structure of detonation were discussed. The final number of triple points for a

detonation was attributed to the acoustic resonance of the downstream flow. Overall structure study in three dimensional of an argon diluted hydrogen-oxygen detonation was performed by Williams et.al [117] using one-step chemistry. Slapping wave structure on numerical soot foil and intricate vorticity field were determined to be present when the third dimension was considered. Two different modes of detonation in a square duct were determined in an experimental study by Hanana et al. [118] for argon diluted hydrogen-oxygen detonation in two different pressures. The soot foil with slapping wave was categorized to be the rectangular mode (movement of triple points parallel to the x-z axis of the duct) and without the slapping wave is the diagonal mode (movement of triple points diagonal to the x-z axis). In a three dimensional study of hydrogen-based detonation by Dou et al. [119] two different sizes of rectangular ducts were analyzed for the rectangular and diagonal mode of the detonation. It was concluded that both the modes existed in the smaller duct, but only rectangular mode existed in the larger duct and that the triple point interactions are the major mechanism of detonation propagation. The triple point dynamics causing the reinitiation of the detonation was identical in both 2D and 3D simulations. A highly diluted hydrogen-oxygen mixture with argon has been experimentally studied due to its highly regular cellular pattern [57, 42, 3]. These detonations occur when the reaction rate is less sensitive to temperature fluctuations. Stoichiometric, homogenous, hydrogen-oxygen mixture diluted with argon $(2H_2 + O_2 + 7Ar)$ at initial pressure of 6.67 kPa with mode 2 planar detonation case is chosen for validation [27] [38]. The first part of this chapter studies the overall structure of the detonation and helps categorize the detonation to be of regular ordinary detonation. The second part of this chapter discusses the reinitiation mechanism of the detonation and compares the features obtained between three different simulations.

4.1 Problem Setup

The structure of a detonation wave is influenced by the confinement it travels inside especially when the system is not large enough to contain one cell [12]. The strength of a detonation in a confined environment is proportional to the size of the setup. Careful consideration has to be made when interpreting the experimental result since the experimental setup could have been modified for several reasons such as isolating or suppressing the instabilities in one dimension to obtain a two-dimensional flow for more detailed. Schlieren images [12], diluting the mixture with inert gases to artificially decrease the post-shock

temperature and increase the reaction zone [27] or lowering the initial pressure of the reactants for an increased regularity in cell structures of soot foil [120]. Hence all the computational domains in this chapter have been modeled after experiments [69, 16, 13]. The domain is a two-dimensional rectangular channel with a supersonic outlet on the right side and a reflective wall for all the other three sides. No heat transfer and no wall friction are modeled along the wall. The height and length of the domain was 3 cm × 127 cm [38]. The solution is time marched until 800 microseconds. This height permits only one cell detonation by mode-locking to two triple points. The reactant mixture is stoichiometric hydrogen-oxygen mixture diluted with 70% argon at an initial pressure of 6.67 kPa and 298 K. The solution is initiated by extending a one-dimensional ZND solution using single-step chemistry in the y-axis. Careful calibration of the unreacted pocket placed behind the detonation is required since a weak perturbation will not generate instability and a strong perturbation tends to overdrive the detonation causing a longer time for detonation to attain mode equilibrium [121]. The instability of the detonation front was initiated by placing a square reactant pocket, 3 mm behind the shock. The inviscid and viscous simulations using one-step chemistry are tailored to be compared with the multistep chemistry simulation. The computational setup for multistep chemistry consists of a rectangular domain of size 10 cm x 3 cm matching the size used in benchmark cases [35]. A stationary detonation wave is positioned at 8.6 cm with an unburned pocket of gas behind it. Only the location of the averaged sonic plane is of interest and the rarefaction wave behind the sonic plane is not solved. The hydrogen-oxygen sub mechanism derived from the Westbrook detailed mechanism is used in this study for a multistep chemistry case as well as for calibrating the parameters for one-step chemistry [122, 38]. This sub mechanism was also validated and used for CFD validation studies in [72]. Another CFD work for the same experiment that was performed by Oran et al. [35] is also used as a reference case to compare the results. Two other CFD works which are not used as reference but are based on the same experiment can also be found in [121] and [123]. The results of the thermochemistry parameters (each variable non-dimensionalized with its maximum value) obtained from ZND analysis using the detailed chemistry is shown below

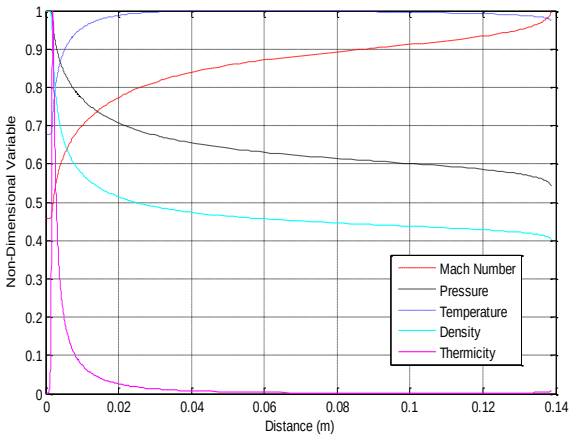

Figure 4-1 ZND Solution of $2H_2 - O_2 - 7Ar$ at 6670 Pa Using Westbrook Chemistry [122]

Thermicity provides a measure of overall chemical reaction progress [124]. For a multistep chemistry model, the thermicity is defined using the following equation

$$\sigma = \sum_{i=1}^{N} \sigma_i \left(\frac{DY_i}{Dt}\right) \tag{4-1}$$

where

$$\sigma_i = -\frac{\alpha_T}{c_p}\left(\frac{\partial h}{\partial Y_i}\right)_{P,\rho,Y_{k\neq i}} \tag{4-2}$$

From the above graph, we can see that thermicity peaks aftershock heating and falls sharply representing faster reactions and then dropping to zero gradually representing slow recombination reactions. The effect of reactions on other thermodynamic and flow variables with rapid changes in the exothermic region and gradual relaxation can be seen. The flow is marched one-dimensionally until it reaches sonic point approximately at 14 cm. Though the thermicity reaches zero approximately at 5 cm, denoting the product state is closer to attaining chemical equilibrium, the flow reaches sonic conditions close to three times this distance. This effect is due to the addition of argon in the hydrogen-oxygen mixture. To understand this the following graphs show a comparison of temperature and thermicity profile behind the detonation with varying argon dilution using a steady-state ZND solution. For 62% dilution, the temperature profile is higher as well as shorter when compared to 67% dilution followed by a further reduction for 70% dilution. No significant difference in the induction zone length or the Von-Neumann

conditions was observed. Hence for the same static enthalpy jump over the shock, the temperature increase along the reaction zone is lower for the highly diluted case due to the increase in the value of specific heat at constant pressure. This reduction in temperature influences the reaction rate. Similar conclusions were obtained in [125] where the effect of argon dilution was investigated for an acetylene-oxygen based detonation.

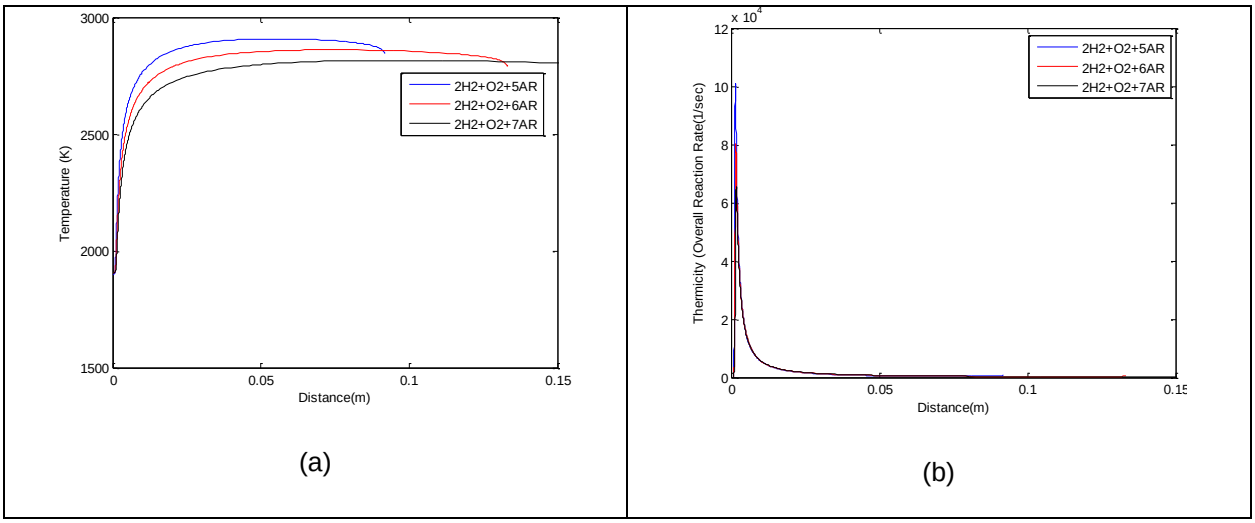

Figure 4-2 Comparison of Steady ZND (a) Temperature Profile and (b) Thermicity Profile with Increase in Argon Dilution

A scale comparison for two dimensional Navier Stoke simulation is necessary to understand to level of physics which is solved for. The order of laminar flame thickness for the diluted hydrogen-oxygen mixture for the chosen initial condition is given by using the Von Neumann conditions from the steady-state ZND solution.

$$k_{products} = \frac{thermalconductivity}{\rho C_p} = \frac{0.288}{0.152 * 812} = 0.0023\ W/mK$$

$$l_{diff} = \sqrt{\kappa \times t_{reaction}} = \sqrt{0.0023 * 2.74103 * 10^{-6}} = 0.08\ mm$$

$$\frac{\Delta_{\frac{1}{2}}}{l_{diff}} = \frac{1.404}{0.08} = 17.55 \approx 18$$

The order of viscous scales relevant to the time scale of reaction can be estimated using the following relation

$$l_{viscous} = \sqrt{\nu \times t_{reaction}} = \sqrt{1.05 * 10^{-4} * 2.74103 * 10^{-6}} = 0.0169\ mm$$

$$\frac{\Delta_{\frac{1}{2}}}{l_{viscous}} = \frac{1.404}{0.0169} = 83.07 \sim 83$$

Hence to solve for viscous scales that have a time scale of the order of exothermic reaction, 33 cells per half-reaction zone will be enough. For inviscid one-step and inviscid multi-step chemistry, a maximum of 44.2 cells per half-reaction length is fixed and for viscous one-step chemistry, a maximum of 88.9 cells per half-reaction length was utilized. Hence all the viscous scales 2.6 times smaller than the scales of reaction time scale are solved for in the viscous model. The details of the base grid and refinement ratios are provided in the table below.

Table 4-1 Computational Setup of $H_2 - O_2 - 7Ar$ @$6.67\ kPa$

	Grid Resolution		
	Inviscid Global One Step Chemistry Model	Inviscid Global One Step Chemistry Model	Viscous Global One Step Chemistry Model
Base Grid	0.1254 mm	0.1254 mm	0.0627 mm
Level - 2	0.0627 mm	0.0627 mm	0.0313 mm
Level - 3	0.0313 mm	0.0313 mm	0.0157 mm

The following table shows the details of the computational setup of multistep detonation in the stationary frame of reference.

Table 4-2 Computational Setup for Detailed Chemistry Model

Parameter	Value	Unit
Length of Channel	10	cm
Height of Channel	3	cm
Initial Pressure	6670	Pa
Initial Temperature	298	K
Pocket Temperature	2086	K
Pocket Pressure	46690	Pa

The transport properties are obtained using the power-law mentioned below

$$\nu = \nu_{ref}\left(\frac{T}{T_{ref}}\right)^{\frac{3}{2}}\left(\frac{P_{ref}}{P}\right) \quad 4\text{-}3$$

$$\kappa = \kappa_{ref}\left(\frac{T}{T_{ref}}\right)^{\frac{3}{2}}\left(\frac{P_{ref}}{P}\right) \quad 4\text{-}4$$

$$D_Y = D_{Yref}\left(\frac{T}{T_{ref}}\right)^{\frac{3}{2}}\left(\frac{P_{ref}}{P}\right) \quad 4\text{-}5$$

The following set of graph shows the comparison charts of the transport properties using a viscous one-step model after calibration of constants with a steady-state ZND solution using detailed chemistry. A good match in the trends of transport property was obtained using the power law for the hydrogen-oxygen argon detonation case.

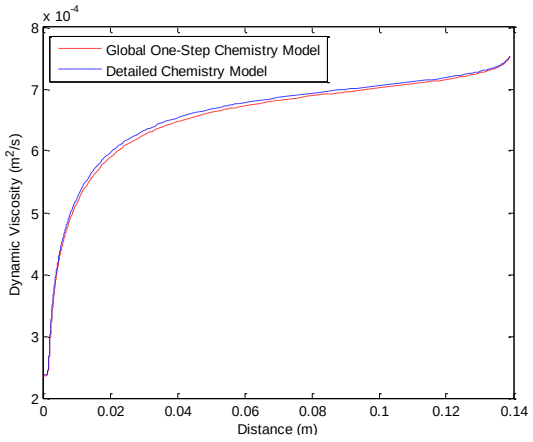

(a)

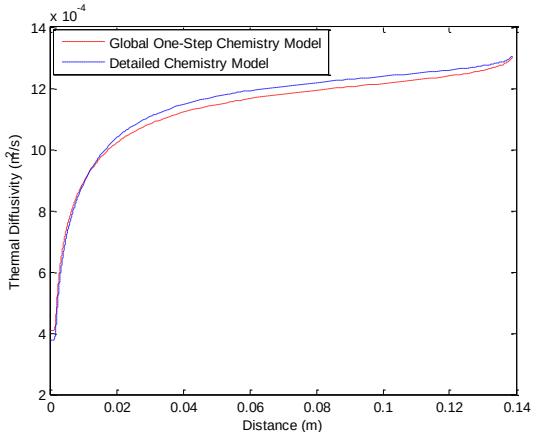

(b)

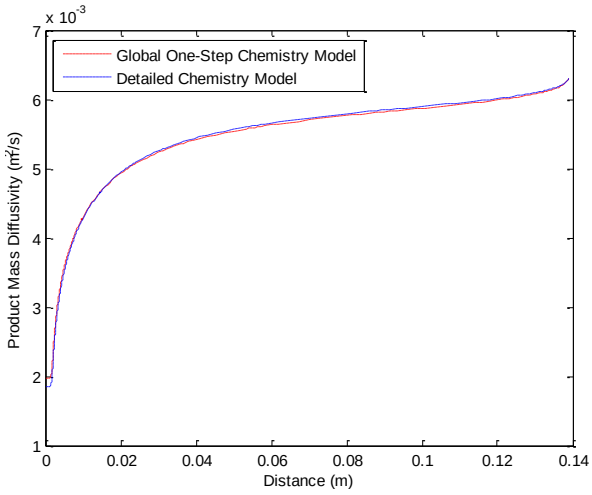

(c)

Figure 4-3 Comparison of (a) Dynamic Viscosity (b) Thermal Diffusivity (c) Product Mass Diffusivity using Global One-Step and Multistep Chemistry @ 6.67 kPa

The average of Lewis number and Prandtl number obtained using multistep chemistry (mean) which was used to derive the transport coefficients for one step chemistry was found to be 0.2 and 0.57, respectively. The variation of the Prandtl number and the Lewis number from the multistep chemistry model is shown below using its instantaneous value. It can be concluded that choosing an average of the Prandtl number and Lewis number is a valid approximation since the influence of one diffusivity on the other does not change.

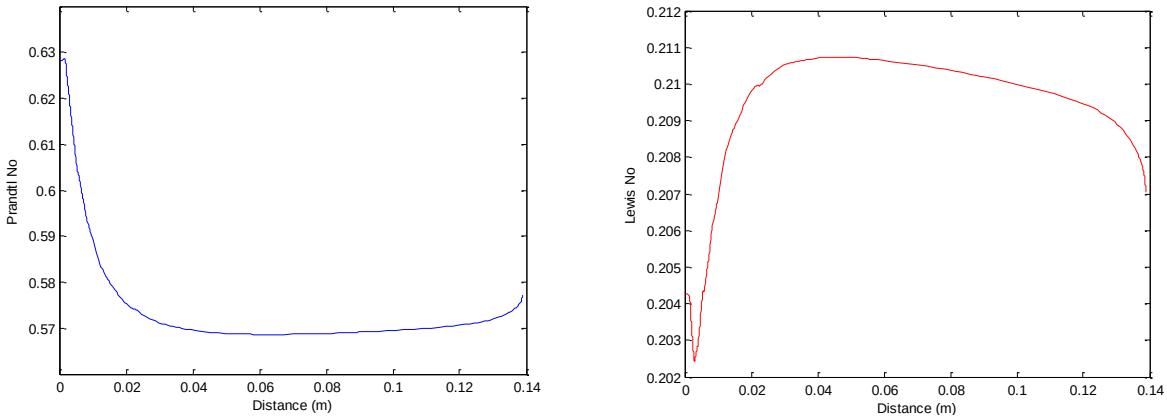

(a) (b)

Figure 4-4 (a) Instantaneous Prandtl Number (b) Instantaneous Lewis Number of $2H_2 + O2 + 7Ar$ Detonation with Multistep Chemistry @ 6.67 kPa

The heat of formation Q between reactants and products along with the value of specific heat constant is obtained at the intersection of curves governing the CJ detonation velocity and adiabatic flame temperature of the mixture at specified initiation condition, as explained in Chapter – 2. The thermodynamic values at the intersection for hydrogen-oxygen with 70% argon dilution are shown below.

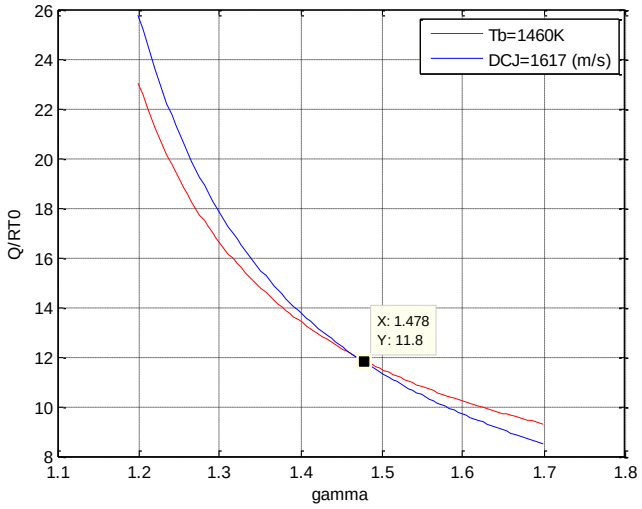

Figure 4-5 Plot to Determine Thermodynamic Properties for $2H_2 + O2 + 7Ar$ Detonation @ 6.67 kPa

The Von-Neuman station flow properties and single-step reaction variables after calibration of the global one-step model are shown below.

Table 4-3 Post Shock and Chemical Properties of $H_2 - O_2 - 7Ar$ Mixture @$6.67\ kPa$

Variable	Reference Value	Unit
D_{CJ}	1617.9	m/s
p_{VN}	177.3	kPa
u_{VN}	395.5	m/s
T_{VN}	1921.7	K
Chemistry Parameters	Values	Units
γ	1.478	
M	0.031	gm/mol
$Q/R_{univ}T_o$	11.8	
$E_a/R_{univ}T_o$	26	
A	8× 10^6	s^{-1}

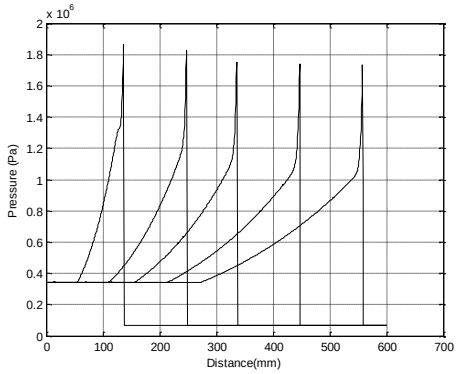

Figure 4-6 Pressure Profiles of Unsteady One Dimensional Solution of $2H_2 + O2 + 7Ar$ Detonation @ 6.67 kPa

The above graph shows the propagation of the detonation traveling from left to right in one dimension with a grid resolution of 22.4 per HRL up to 600 HRL. The profile shows the detonation followed by an expansion wave that matches the wall boundary condition to the left of the domain. The pressure peak stays consistent after 213 HRL (300 mm) approximately at 170kPa which is close to 173 kPa computed using multistep chemistry. The grid convergence comparison with 11.2 Cells/HRL and 22.4 Cells/HRL is shown below.

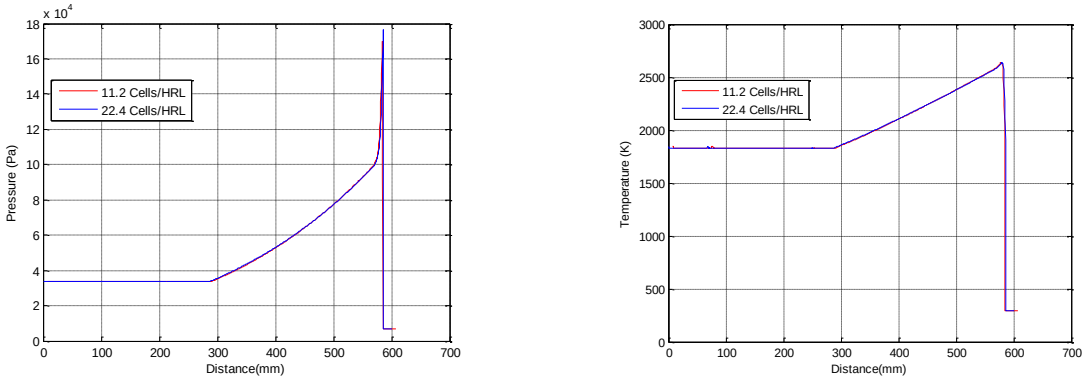

(a) (b)

Figure 4-7 Grid Convergence of Unsteady One Dimensional Solution (a) Pressure (b) Temperature of $2H_2 + O2 + 7Ar$ Detonation @ 6.67 kPa

To evaluate the one-step chemistry model, the values of the thermodynamic quantities are compared with the steady-state, stationary ZND results and are shown in the table below.

Table 4-4 Comparison of ZND Results with Unsteady 1D Inviscid Global One Step Result of $2H_2 + O2 + 7Ar$ Detonation @ 6.67 kPa

VN State	**ZND**	**Unsteady 1D Results**	**Difference (%)**
Pressure	173660	170021	2.1
Temperature	1904	1846	3.0
Density	0.346	0.312	9.8
Velocity	394	391	0.7
Induction Zone Length	1.404	1.4	
CJ State	**ZND**	**Unsteady 1D Results**	**Difference (%)**
Pressure (Pa)	93928	89210	5.0
Temperature (K)	2742	2509	8.5
Density (kg/m^3)	0.138	0.136	1.4
Velocity (m/s)	978	1010	3.2
Sonic Plane (cm)	13.88	3.2	76.9

.

From the above tabular column, we can understand that though the primary thermodynamic variables are within a difference of 10%, the sonic plane is reached in within 23% of the distance downstream predicted by the multistep chemistry model though the induction zone thickness is comparable. This behavior can be attributed to the single preexponential factor in the reaction rate equation which is calibrated to reflect the induction zone thickness. This early sonic plane position was also observed in other studies [34, 123] where the global one-step chemistry was calibrated for low pressure, argon diluted hydrogen-oxygen detonation. Though the global one-step model predicts the sonic plane very early, the flow properties at the sonic plane do not have an error of more than ten percent and the shock velocity as well is agreeable with experiments. The advantage in this scenario is the regular detonation where the majority of the combustion occurs due to the shockwaves and within the predicted sonic plane without detached unburnt reactant pockets. Quantitatively, the non-dimensional activation energy θ_{VN} is 4.06 for

multistep chemistry and 4.22 for one-step chemistry. Since both are within the weekly unstable limit of $\theta_{VN} < 5$, the performance of this global one step model is evaluated for two dimensional inviscid and higher-order viscous simulations by comparing the cell size and the mode of detonation. The ratio of induction to an exothermic timescale with varying argon dilution is shown below. The increase in the dilution increases reaction length which in turn decreases this ratio and increases the stability of the detonation.

Table 4-5 Comparison of Time Scale Ratio of Hydrogen Oxygen Detonation with Varying Argon Percentage

Mixture Composition	τ_i/τ_r
2H2+O2+5AR	1.99
2H2+O2+6AR	1.89
2H2+O2+7AR	1.80
Global One Step	2.29

The complete profile comparison of the global one-step chemistry and detailed chemistry for one-dimensional detonation is shown in the graph below. We can see that the sonic plane is achieved faster in global one-step chemistry, but the values of the flow properties are comparable at the sonic planes.

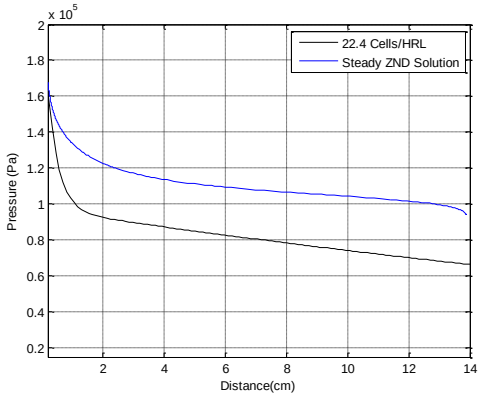

(a)

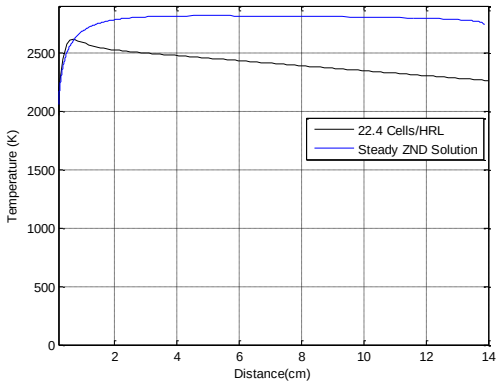

(b)

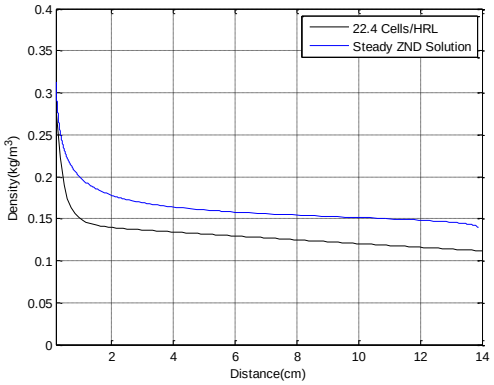

(c)

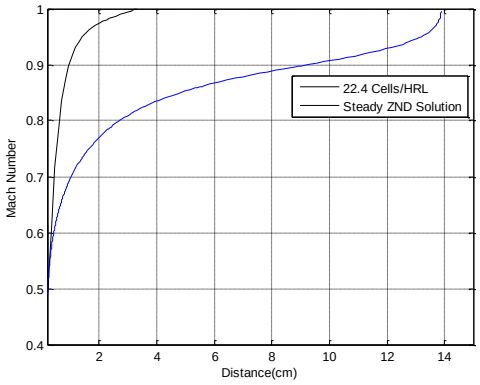

(d)

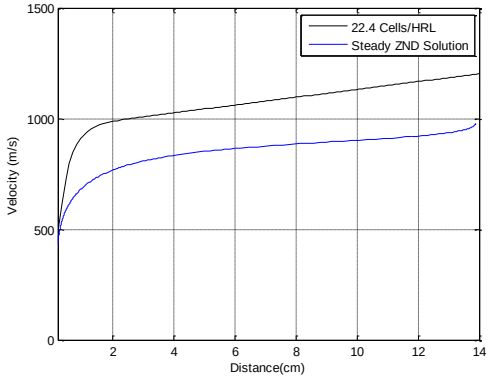

(e)

Figure 4-8 Comparison of (a) Pressure (b) Temperature (c) Density (d) Mach Number (e) Velocity between Steady ZND and Unsteady Inviscid, One Step Chemistry Solutions

4.2 Results and Discussion

4.2.1 Grid Resolution and Global Structure Analysis

In this section, we address the convergence of the two-dimensional solution with different grid resolutions by studying the behavior of the detonation globally. The non-dimensionalized detonation front velocity versus the axial length is studied to determine the limits of velocity in a cell cycle and classify the detonation into marginal/regular. We can see that after the start-up process, the oscillations of detonation become regular indicating self-sustaining detonation. One cell cycle includes a cycle starting with the

highest velocity ratio peak and ending with the lowest velocity ratio peak in the instantaneous velocity profile plot. Every shoot of detonation velocity above one is caused by cell reinitiation which is then followed by deceleration of Mach stem to incident shock phase. The small oscillations along the plot occur because of Von-Neumann clipping which is due to the difficulty in capturing the maximum pressure in the domain. These oscillations become significant in irregular detonations when the global maximum of pressure may be higher than the von-Neumann pressure peak [38]. The shock front velocity is determined by tracking the position of the shock by capturing the maximum pressure gradient on a constant y-axis horizontal line. The shock front velocity for this thesis was recorded along the bottom wall for Euler one-step chemistry, Euler multi-step chemistry and Navier Stokes one-step chemistry are shown below.

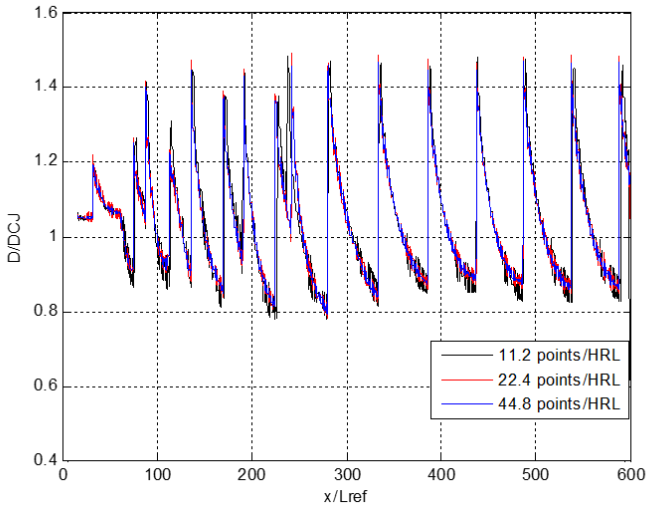

Figure 4-9 Detonation Front Velocity Profile of $2H_2 - O_2 - 7Ar$ Detonation using Inviscid One-Step Chemistry Model

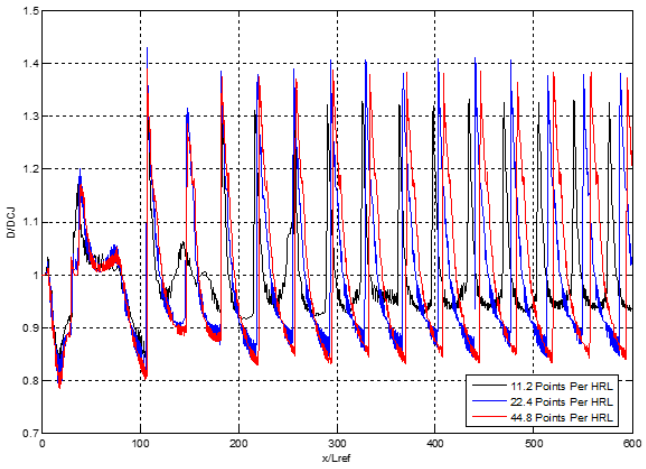

Figure 4-10 Detonation Front Velocity Profile of $2H_2 - O_2 - 7Ar$ Detonation using Multistep Chemistry Model

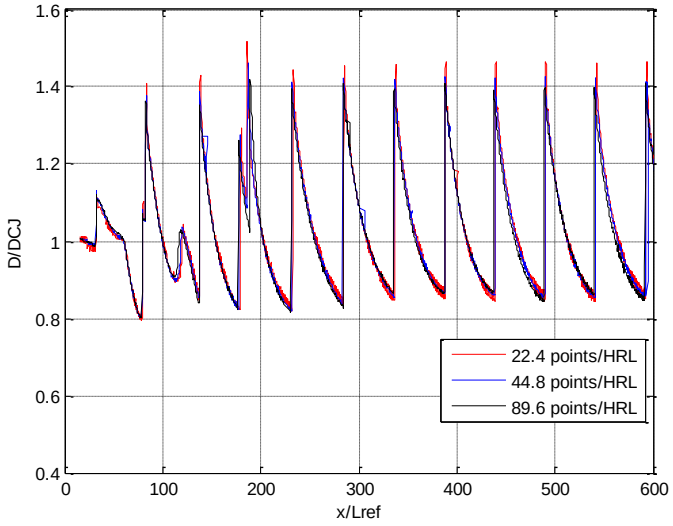

Figure 4-11 Detonation Front Velocity Profile of $2H_2 - O_2 - 7Ar$ Detonation using Viscous One-Step Chemistry Model

All the velocity profiles show the detonation becoming sustained and periodic after 250 x/Lref. All the three-grid resolutions overlap each other for inviscid and viscous global one-step chemistry. The multistep chemistry is the most sensitive to the grid refinement study where both the upper and lower limit of the shock velocity increases with grid resolution. Since the time step is fixed based on the grid size in an

explicit method though CFL number, the coarser grid ignores the chemical reaction with shorter time scales influencing the limit velocity of the shock during reinitiation. The mean velocities with each run are compared with Galcit experimental results [10] as shown in the table below

Table 4-6 Comparison of Average Propagation Velocity of Argon Diluted Hydrogen Oxygen Detonation with Experimental Measurement

	11.2	22.4	44.8	Error %	Experimental [10]
Inviscid – Global One Step	1670	1686	1686	4.2	1617
Inviscid Multi Step	11.2	22.4	44.8	Error %	
	1623	1618	1619	0.1	
Viscous Global One Step	22.4	44.8	89.2	Error %	
	1626	1637	1636	1.2	

Considering the average detonation velocity is always close to or above D_{CJ}, this criterion points out that the detonation which is being studied is a regular ordinary detonation. The second-order accurate, inviscid, global one-step chemistry setup was found to be having the highest deviation from the experimental results. This deviation has been recorded by researchers stating that the increase is due to the absence of boundary layer losses and wall heat losses. Deviation in the sixth order accurate, viscous, global one-step chemistry is less than the inviscid case, but the multistep chemistry had the least amount of deviation from the experimental counterpart. Further comparison has been made with the numerical soot foil. The numerical soot foil is usually obtained by tracking the pressure or vorticity in the domain at every time step since both the quantities max at the vicinity of the triple point. For a 2D simulation in a Eulerian framework, the soot foils $\varepsilon_{i,j}$ is obtained using the following relation

$$\varepsilon_{i,j} = \int_{t=0}^{t} |\nabla \times V| dt$$

Though the computational setup is a moving reference frame making the detonation stationary for multistep chemistry, an auxiliary grid is created which accumulates the vorticity tracks for every timestep until the final time step along the x-axis. The following diagram presents the numerical soot foil of the 3 cm domain obtained from the viscous one-step chemistry setup with 88.9 cells per HRL. The height of the domain was equal to one cell width to mode lock the detonation with two modes. A description of the features responsible for forming the soot foil record is labeled for one cell cycle.

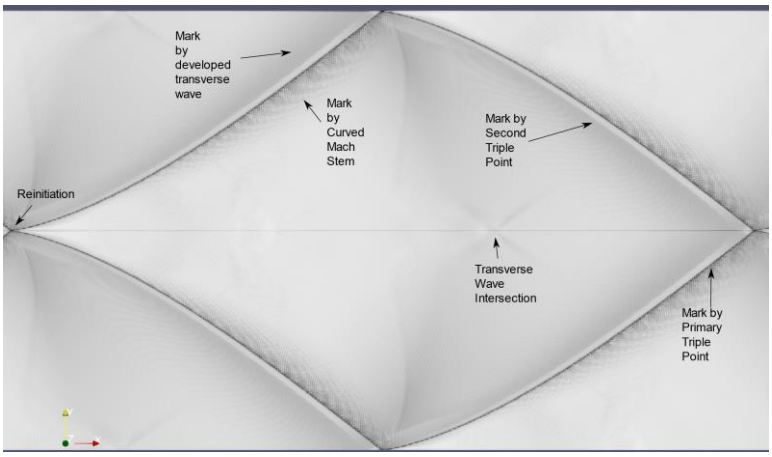

Figure 4-12 Description of Features Recorded on a Numerical Soot Foil of $2H_2 + O2 + 7Ar$ Detonation $@6.67\ kPa$ using Viscous, Global One Step Model

Because the movement of the triple point is constrained in two dimensions, it results in rectangular mode with slapping, relatively weaker, waves and appears in the middle of a cell.

Figure 4-13 Numerical Soot Foil Showing of $H_2 - O_2 - 7Ar$ $@6.67\ kPa$ using Inviscid, Global One Step Model

Figure 4-14 Numerical Soot Foil Showing of $H_2 - O_2 - 7Ar$ $@6.67\ kPa$ using Viscous, Global One Step Model

Figure 4-15 Numerical Soot for of $2H_2 - O_2 - 7Ar$ Detonation using Inviscid, Multistep Chemistry Model

A comparison of numerical soot foils obtained using inviscid global one step, multistep chemistry, and viscous one-step chemistry is shown in the figure above. The initial period of propagation where the number of triple points is not steady is referred to as a rearrangement period after which the shock becomes self-sustained [116]. It can be observed that the number of triple points in this rearrangement period varies with different models. This variation was also noted and attributed to the variation in artificial diffusion by Taki et.al. [116]. Lesser the artificial diffusion, more prominent were the influence of small perturbations on a weak shockwave. The transverse waves during the initial period are weak and gradually gain strength as detonation becomes sustained [3]. Compared to the global chemistry case, grid dependence has seemed to increase by looking at the instantaneous velocity profile, but the mean detonation front velocity lies close to each other.

Table 4-7 Comparison of Cell Aspect Ratio of $2H_2 + O2 + 7Ar$ Detonation @$6.67\ kPa$

Method	Cell Size (mm)
Experiment	57×30
Inviscid Multi-Step	59×30
Inviscid Global One Step	50×30
Viscous Global One Step	52×30

All the cell measurements were taken using the ruler feature in Paraview. The soot foil measurement provides a way of understanding the chemical energy distribution in a cell cycle. Additionally, to see the variation in cell patterns, the same case above was simulated in a domain with a height permitting two cells using 22 cells per HRL. Though in the above tabular column, the single-step chemistry seems to predict the length of the cell a few percentages less. The height of the channel was increased to 6 cm to compare directly with the experiment conducted with the same mixture and initial condition at the Caltech GALCIT laboratory [10]. This time the instability was initiated by tilting the detonation an angle of 5^o to the bottom wall. This initiation is similar to the setup where instability is initiated by the interaction of a detonation

with a wall after passing through a C-D nozzle [3]. We can see that the detonation operates in four modes with intermodal interactions. The peak velocity shoots higher than the usual value with the modes collide with each other which can be seen at 100 cm in the graph below. A more direct comparison can be made when the channel height has the same height as in the experiment which was 6 cm [10]. The plot of instantaneous detonation front velocity as a function of time for $22.4\ \Delta_{\frac{1}{2}}$ is shown along with mean velocity profiles compared with average experimental detonation velocity [10] below.

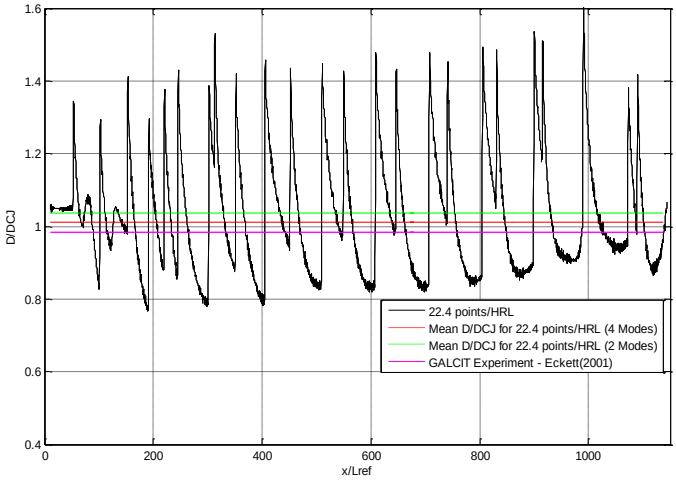

Figure 4-16 Detonation Front Velocity Profile Showing Intermodal Interactions of $H_2 - O_2 - 7Ar\ @6.67\ kPa$

The mean velocity is close to the experimental average velocity. The soot pattern of the four-mode detonation is shown below.

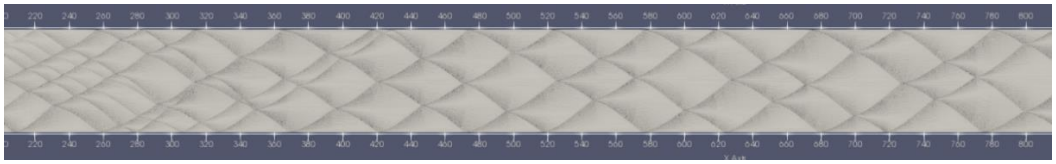

Figure 4-17 Numerical Soot Foil of $H_2 - O_2 - 7Ar\ @6.67\ kPa$

A brief region of regular fish scale patterns was observed followed by internodal interactions which are compared with the experimental soot foils obtained from Strelow [114, 126]. In the same experiment, the detonation had a cell width of 3 cm and traveled at a velocity of 1600 m/s where the experimental losses

were considered [114]. The cell width measured from the simulation measured exactly 3 cm in mode-locked setup and close to 54×33 mm in a four-mode detonation setup as shown below.

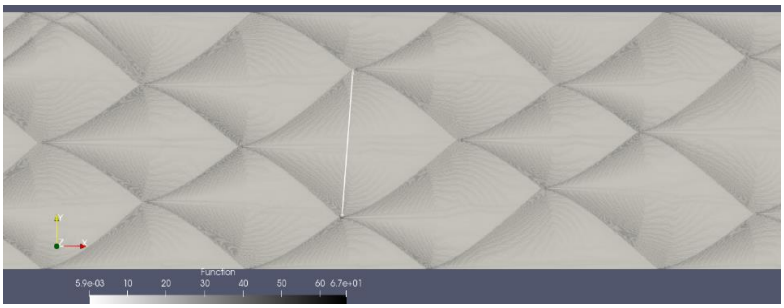

Figure 4-18 Single Cell Measurement (54×33 mm) from Numerical Soot Foil of $H_2 - O_2 - 7Ar$ @6.67 kPa

The experimental soot foil is shown for comparison with the numerical soot foil below.

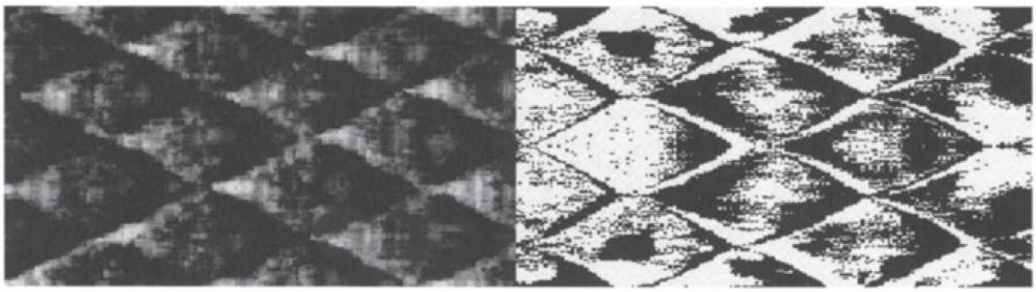

Figure 4-19 Experimental Soot Foil Data for $H_2 - O_2 - 7Ar$ @6.67 kPa [120, 114, 126]

Figure 4-20 Numerical Soot Foil Showing Intermodal Interactions of $H_2 - O_2 - 7Ar$ @6.67 kPa

4.2.2 Favre Averaged Flow Profile

The two-dimensional flow can be compared with an analytical approach using an averaging technique at a common reference station. Being a highly compressible flow, Favre averaging along Y-axis is suitable for this purpose. The reference station is taken to be the CJ plane where the flow Mach number reaches one when the reference frame moves along with the detonation front. The Favre averaging for space is performed for any variable using the following relations

$$\bar{\rho}(x) = \frac{1}{H}\int_{y=0}^{y=H} \rho(x,y)dy \qquad 4\text{-}6$$

$$\bar{u}(x) = \frac{\left[\frac{1}{H}\int_{y=0}^{y=H} \rho(x,y)u(x,y)dy\right]}{\bar{\rho}(x)} \qquad 4\text{-}7$$

The samples are then ensemble averaged about time. A total of 20 random samples are taken at various locations along the x-axis. The averaged quantities and the ZND results at the CJ plane are compared in the table below

Table 4-8 Comparison of Favre Averaged Flow Properties with Steady State ZND Solution

Parameter	Inviscid	Difference (%)	Multi-step	Difference (%)	Viscous	Difference (%)	ZND
Pressure (Pa)	102986	9.6	97276	3.5	91442	2.6	93928
Temperature (K)	2508	8.5	2793	1.8	2486	9.3	2742
Density (kg/m^3)	0.137	0.07	0.14	1.4	0.139	0.07	0.138
Average Sonic Plane (cm)	2.5	81.9	20.2	45.5	2	85.5	13.88

As shown above, the flow variables follow the same trend as it did in the unsteady one-dimensional equations. The deviation from the analytical value was within ten percent, except that of the average sonic plane. A direct comparison with the analytical result for the sonic plane is not applicable since the analytical model assumes a constant shock strength whereas, in two dimensions, the detonation front encompasses dynamical variation. The least variation in the average sonic plane is achieved using the multistep chemistry.

4.2.3 Triple Point Structure

The instability of the detonation is initiated using a hot spot placed in the induction zone of the ZND solution. The sequence of this initiation is shown below using density contours.

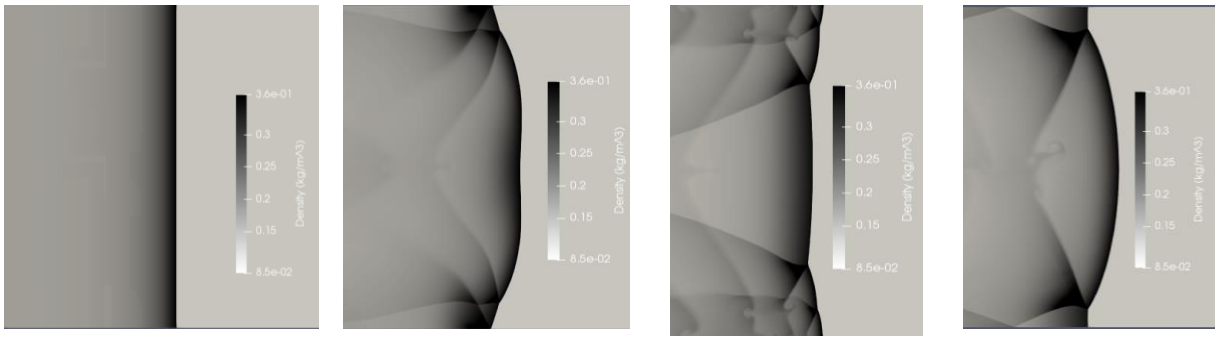

T=0 T=13.79 T=38.01 T=45.88

Figure 4-21 Triple Point Transients During Detonation Initiation

Initially, a system of non-coordinated triple points forms until the moving gas behind the detonation reaches resonance. A very transient dynamics is observed from T=13.79 to T=45.88 when four triple points interact with each other till it settles down to two triple points. When T=38.0, we can see multiple detached slip lines from these triple points and T=45.88 we can see the number of triple points settles to a resonant mode of two. This configuration was also compared with the microcells formed in an inert gas by a row of exploding wires in [3]. The survival of the triple point depends on these acoustic resonant modes [116]. Fickett et.al [3] explain from the observation that this resonant mode is achieved when the spacing between triple points contains an induction zone which that is large enough to support reinitiation and small enough to not initiate the formation of another triple point. This frequency is also mentioned by Lee [2] as to be dependent on the eigenvalue of the transverse oscillations. The coalescence of initial unsteady perturbations to resonant unstable modes can also be seen in the work by Ng et.al [127] where a parametric analysis of the wavelength and amplitude of sinusoidal perturbations using two dimensional inviscid one step chemistry simulations was performed. The triple point structure is detailed from viscous simulation due to the increased accuracy and grid resolution. A comparison of the major features involved in the reinitiation process is explained below. More in-depth features in marginal regular detonations can be found elsewhere [38, 37]. The gradient of any scalar quantity S is determined using the following formula

$$\nabla S = \left[\left(\frac{\partial S}{\partial x}\right)^2 + \left(\frac{\partial S}{\partial y}\right)^2\right]^{0.5} \qquad 4\text{-}8$$

A series of scalar contours of a triple point bouncing from a wall is shown below. The contour below shows the static pressure and its gradient.

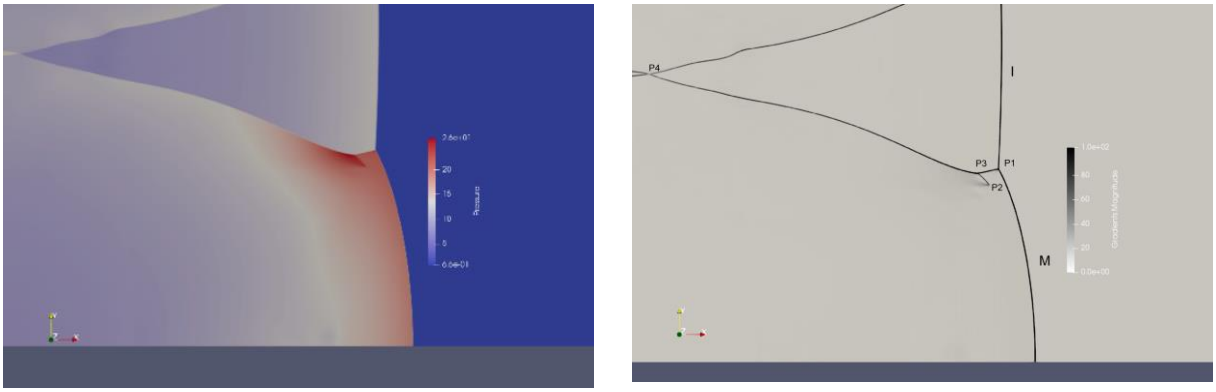

(a) (b)

Figure 4-22 (a) Pressure Contour and (b) Gradient of Pressure Contour of Triple Point for a $H_2 - O_2 - 7Ar$ *Detonation* @6.67 kPa

The expanding Mach stem (M) and incident shock (I) is identified in the pressure gradient contour. This contour was obtained when the triple point structure is mature after forming a strong structure. The transverse wave can be considered in two parts P1-P3 and P3-P4. The primary triple point consists of Mach stem, incident shock and the transverse wave (P1-P3). The secondary triple point is formed at P3 which is the intersection of the first section of the transverse wave P1-P2 and the shock wave P2-P3. The transverse wave P1-P3 is a weak wave compared to P3-P4 since P1-P3 is not strong enough to ignite the preheated reactants after passing through the incident shock. The bending or the kink of the extended transverse wave is found at P3 which coincides with the beginning of the reaction zone behind the incident shock. The bending of the transverse wave is attributed to the higher speed of sound in the product gases [3]. The heated reactants behind the secondary triple point are burnt as the strong transverse shock wave P3-P4 sweeps it. The shockwave P2-P3 lies within the attached unreacted pocket and is not strong enough to combust the heated reactants. The pressure contour also shows P4 which is the intersection between the transverse wave of the opposite family. The pressure difference along the shock P3-P4 from the pressure contour shows that the strength of the transverse wave reduces as it travels downstream. It can also be seen that the pressure behind the transverse wave in the early stages of P3-P4 is the highest after

the triple point is mature. The strength (S) of the transverse waves P1-P3 and P3-P4 was also measured at this instant.

$$S_{P_1-P_3} = (Pratio - 1) = 1.68 - 1 = 0.68$$

$$S_{P_3-P_4} = 2.08 - 1 = 1.08$$

To classify as a marginal detonation, Fickett [3] notes a pressure ratio value of 1.5 for the transverse wave strength attached to the primary triple point. Hence the strong structure observed in this case can be counted as a regular detonation. In addition to pressure discontinuities, density discontinuities are identified in the density gradient contour shown below. The slip line S1 was formed at the intersection P2. The dynamics of S1 evolves with the cell. It separates the gas passing through the Mach stem from the rest of the heated gas. S2 is the slip line from the previous cell cycle which is detached due to the triple point collision and is acted upon by transverse waves as it moves downstream.

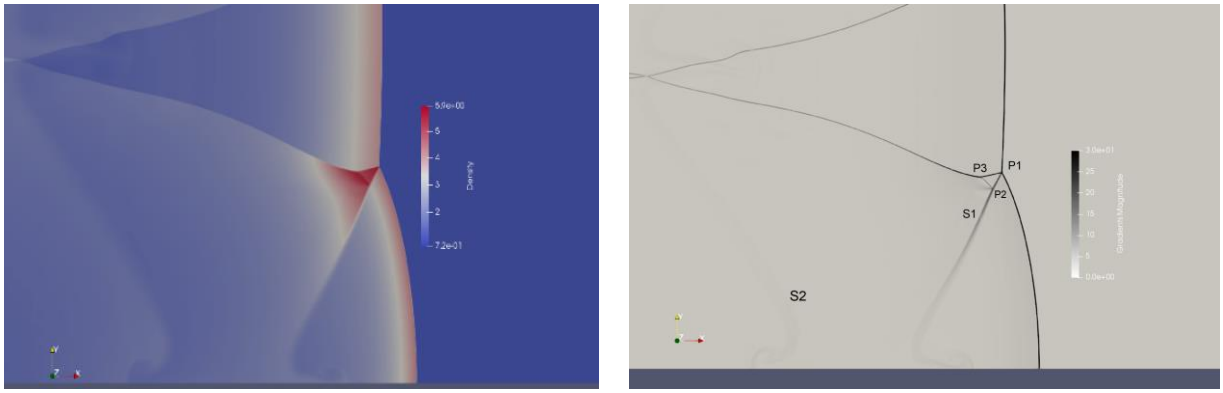

(a) (b)

Figure 4-23(a) Density Contour and (b) Gradient of Density Contour of Triple Point for a $H_2 - O_2 - 7Ar\ Detonation$ @6.67 kPa

The contour below shows the temperature and its gradient. The slip line S3, emanating from the point P3 was captured well in temperature gradient contour forming a boundary between shock entering through P2-P3 shockwave and P3-P4 transverse wave.

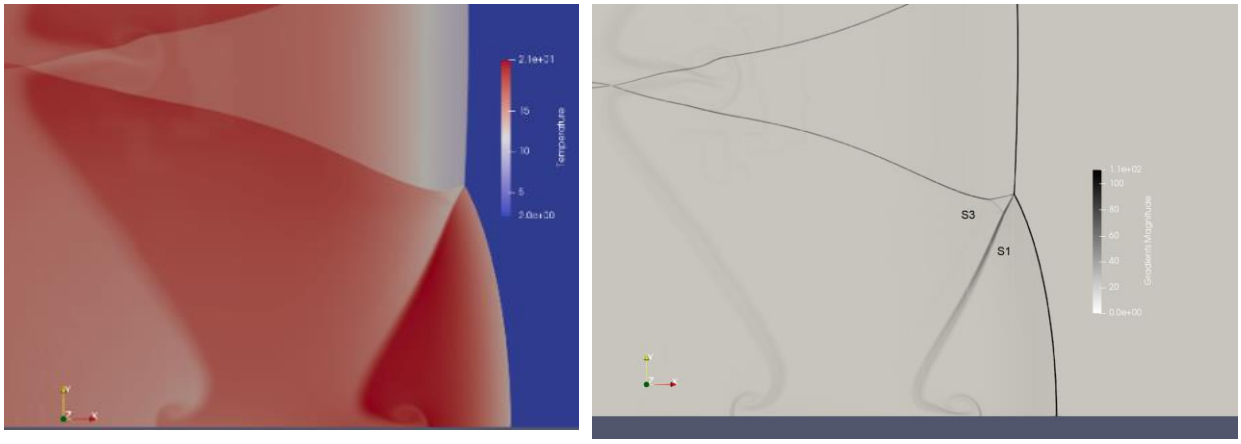

(a) (b)

Figure 4-24 (a) Temperature Contour and (b) Gradient of Temperature Contour of Triple Point for a $H_2 - O_2 - 7Ar\ Detonation\ @6.67\ kPa$

Another shock BD bounds the unreacted pocket between the weak transverse wave and the slip line S1. These slip lines become detached whenever there is a reinitiation event and move downstream. A detached slip line from the previous cell cycle is labeled as S2 in the temperature contour. The influence of grid resolution on solving the structure of the triple point is shown below. All the contours were obtained from the inviscid global one-step setup. The presence of the second triple point and the P2-P3 shock wave was not captured by the lowest grid resolution of 11.2 cells/HRL. Though the 22.4 cells/HRL captures the P3 kink, detection of the P2-P3 shock wave is still faint. The effect of coarse grid resolution also leads to thicker shocks in the gradient contours. Both secondary triple point P3 and the shock P2-P3 are detected by the grid resolution of 44.8 cells/HRL. This grid dependency on the structure of triple points were also observed for regular detonations in [18, 128]. Though the details of the triple point are not accurate in the coarse resolutions, from the velocity profile comparison we know that global behavior does not vary significantly.

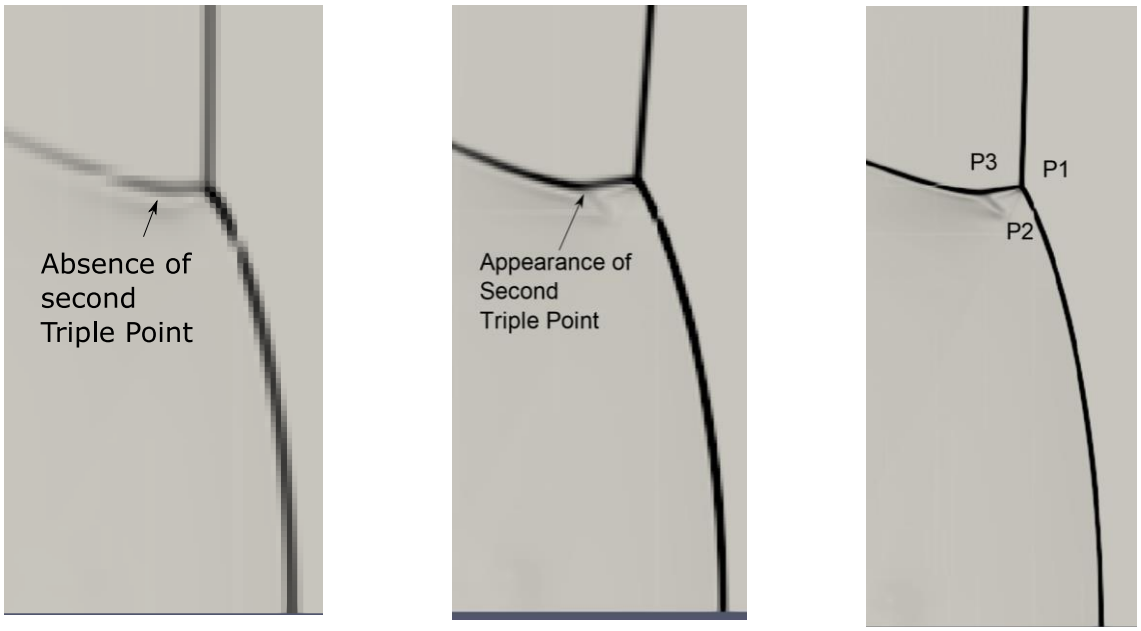

(a) 11.2 cells/HRL (b) 22.4 cells/HRL (c) 44.8 cells/HRL

Figure 4-25 Comparison of Triple Point Structure with Varying Grid Resolution

Visualization of the velocity vector can be performed in three ways, in moving detonation reference frame, stationary detonation reference frame, and the triple point reference frame. The reaction zone expands and pushes the column of gas towards the shock to sustain the motion of the precursor shock. This can be understood by studying the flow streamlines in the moving reference frame. The reactant particles entering the shock wave interacts with this column of gas and reaches the reaction zone to contribute to the recombination. This interaction can be studied with the streamlines in the stationary reference frame. The shock front and triple point have longitudinal and transverse instabilities as they interact with the reactants at zero velocity. This interaction is highlighted in the triple point reference frame. The streamlines in the moving reference frame overlapped on a density contour for a growing Mach stem is presented below.

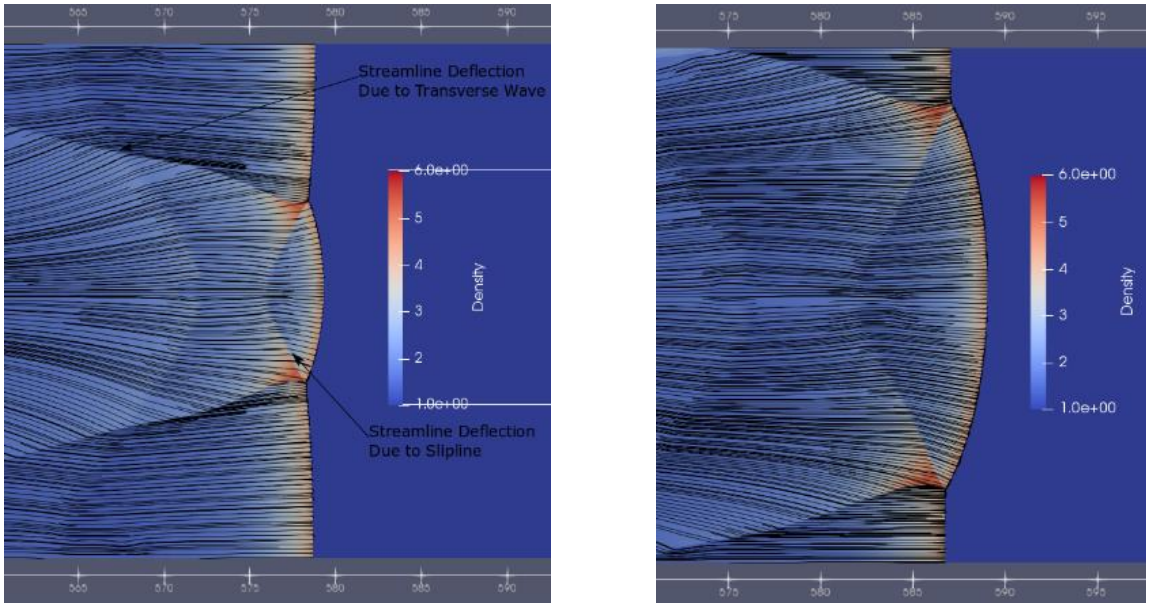

T=119.29 T=121.73

Figure 4-26 Streamline Plot of Flow Behind a $H_2 - O_2 - 7Ar\ Detonation$ @$6.67\ kPa$ in the Moving Reference Frame

A very common analytical approach to study the angle between shocks around a triple point is the shock polar analysis [12, 51]. The self-similarity of the Mach reflection gives the advantage to fix the frame of reference to the triple point to make a steady-state approximation. In this approach, a coordinate transformation is performed so that the flow meets the shock at an angle. In the following contour, a transformation of $\theta = 33°$ is performed to the incoming reactant flow. The following contour shows the velocity vector represented using 2D arrows from every 10th cell in the domain. From the triple point reference frame, we can see that maximum deflection occurs behind the Mach stem. The formation of a slip line and its curving is also evident.

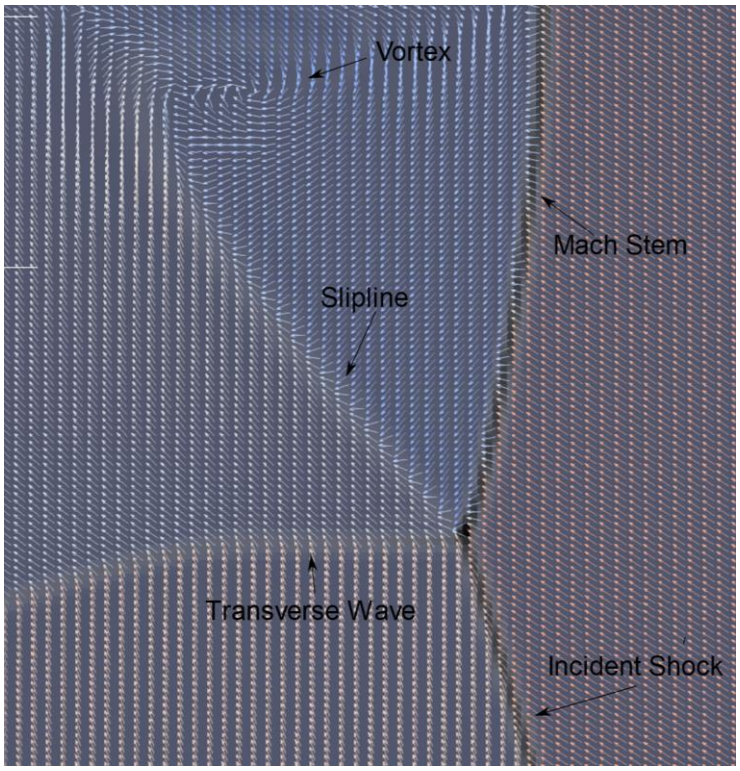

Figure 4-27 Velocity Vector with Triple Point Steady State Frame of Reference

The movement of the triple point and its influence on the products is showed by the streamlines in the moving reference frame above in sequence from left to right as a new cell is formed. These streamlines are tangent to the bulk moving velocity of the gas column. The dynamics of products behind the shocks can be explained in two steps, the influence of gas on the triple point and vice versa. The precursor shock gains its thrust from the radially expanding gas after reinitiation making it stronger than incident shock [2]. The flow as it expands and is directed towards the shock gets deflected by the transverse waves and slip lines. It also pushes the triple point along the Mach stem in a longitudinal direction. The gas particles in the moving column of gas encompassed between the shock front and the rarefaction waves go through oscillations in longitudinal and transverse directions as it is acted upon the transverse waves as shown below.

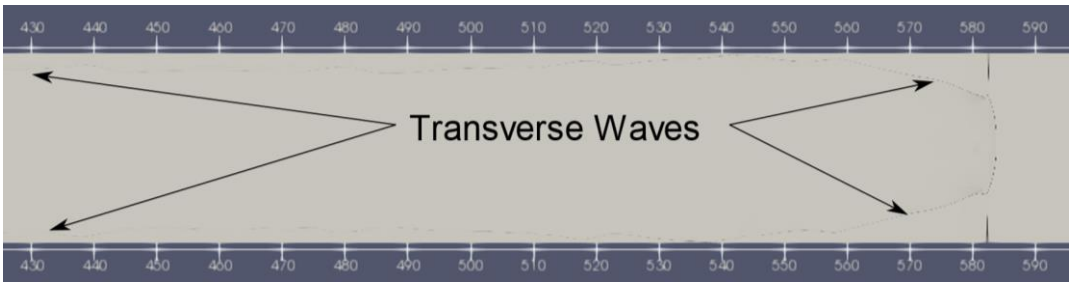

Figure 4-28 Pressure Gradient Contour at T=120.48

We can see from the pressure gradient contour at T=120.48 where the detonation is located at 583 mm roughly, but the transverse wave extends well into the domain. Though the dynamics of the triple points are causing this transverse oscillation, the transverse oscillation should meet certain criteria to maintain the dynamics for self-sustaining as detailed by Lee [2]. For a highly marginal detonation, this oscillation should correspond to the natural acoustic frequency of product gases which is a function of the characteristic dimension of the domain cross-section. For an ordinary detonation, where the cell size is smaller than the characteristic dimension, the transverse oscillation should be coupled to the characteristic chemical reaction rate. The cell height is roughly proportional to the reaction zone length by two orders of magnitude [3]. The correlation between the cell size and the movement of the gas column downstream has been a topic of study in several works in literature [2, 3, 129]. Manson [130], Taylor [43], Fay [129] and Chu [131] all studied the interaction between spinning detonation head and the oscillating product gas column using acoustic theory.

The effect of the column of gas on particles entering the flow can be seen in the streamline contour in the stationary reference frame shown below. As the gas particles undergo rotational, translational, and dilatational motion as they cross the shock front, they also experience thermodynamic state change. The flow particles are subsonic behind the incident shock and Mach stem. Their interaction with the transverse wave and slip lines decides on the location of a sonic plane in an average sense. Strong vortices created behind the slip line during the initial transients of cell creation is relaxed as the Mach stem expands.

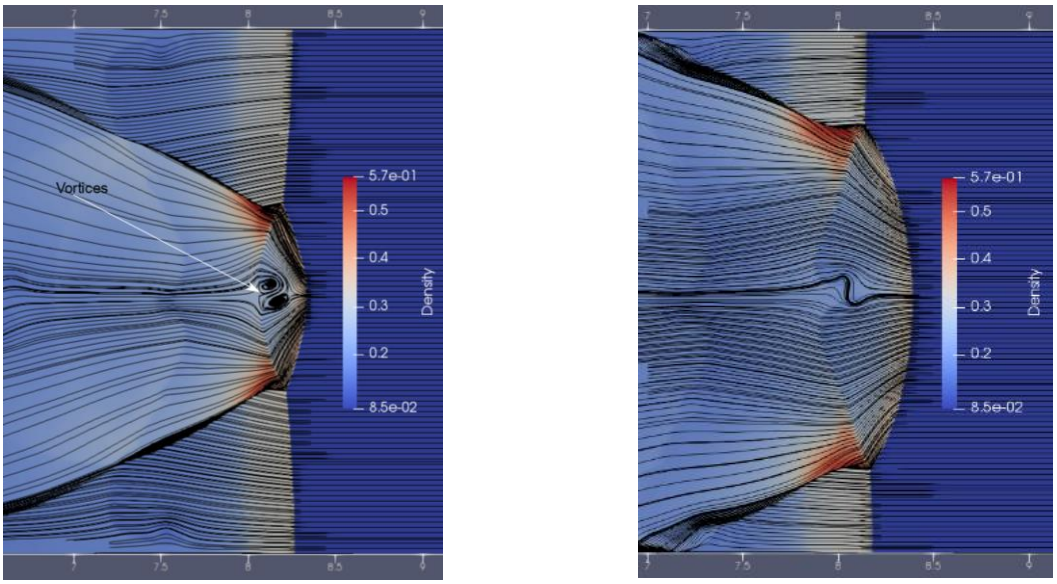

t=18.3 ms t=18.7 ms

Figure 4-29 Streamline Plot of Flow Behind a $H_2 - O_2 - 7Ar\ Detonation$ @6.67 kPa in a Stationary Reference Frame

An important concept which connects the effects of thermodynamics on fluid dynamics is Crocco's theorem [132]. It states that a compressible flow that passes through a curved shock becomes rotational due to the difference in total enthalpy and entropy between the streamlines passing through different sections of a curved shock [29]. Hence though the flow is inviscid, vorticity is not zero. The vorticity (acting in the z-axis direction) imparted by the shock front can be seen in the contour showing the absolute value of the vorticity magnitude below. The vorticity created by the detonation diffuses eventually since the velocity becomes zero at the end wall.

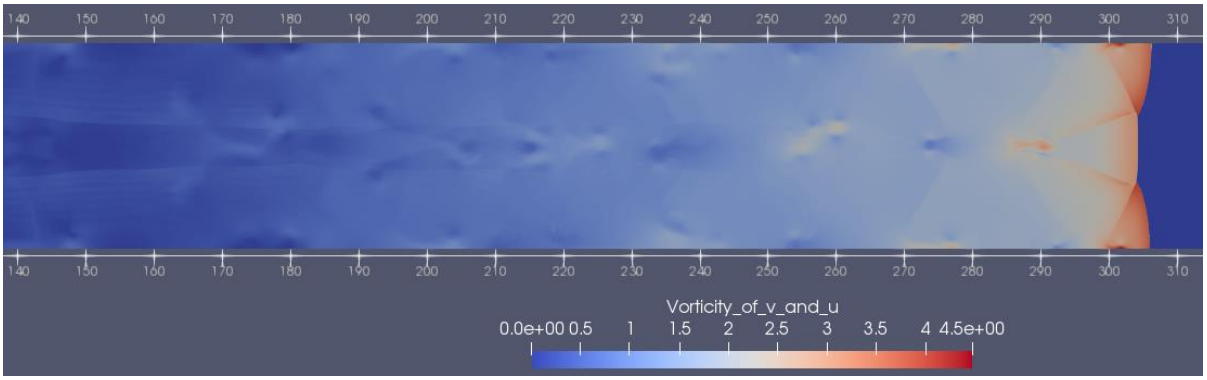

Figure 4-30 Vorticity Contour Displaying the Vorticity Field Behind Detonation Front

4.2.4 Comparison of Triple Point Structure

Since both the global one-step chemistry model and multistep chemistry model are validated against same experiments [69, 16, 13], it gives an advantage of comparing the flow features obtained at the similar time. All the contours were captured at roughly around 0.0007 seconds when detonation had relaxed to periodic oscillations with two modes. The potential of the global one-step model to predict the thickness of the induction zone when compared to the multistep chemistry model with two-dimensional instability was analyzed. Approximately, the induction zone behind the incident shock, Mach stem and the attached pocket of reactant were measured and found to match closely. The length unit system of global one-step chemistry is mentioned in mm and the multistep chemistry is mentioned in cm.

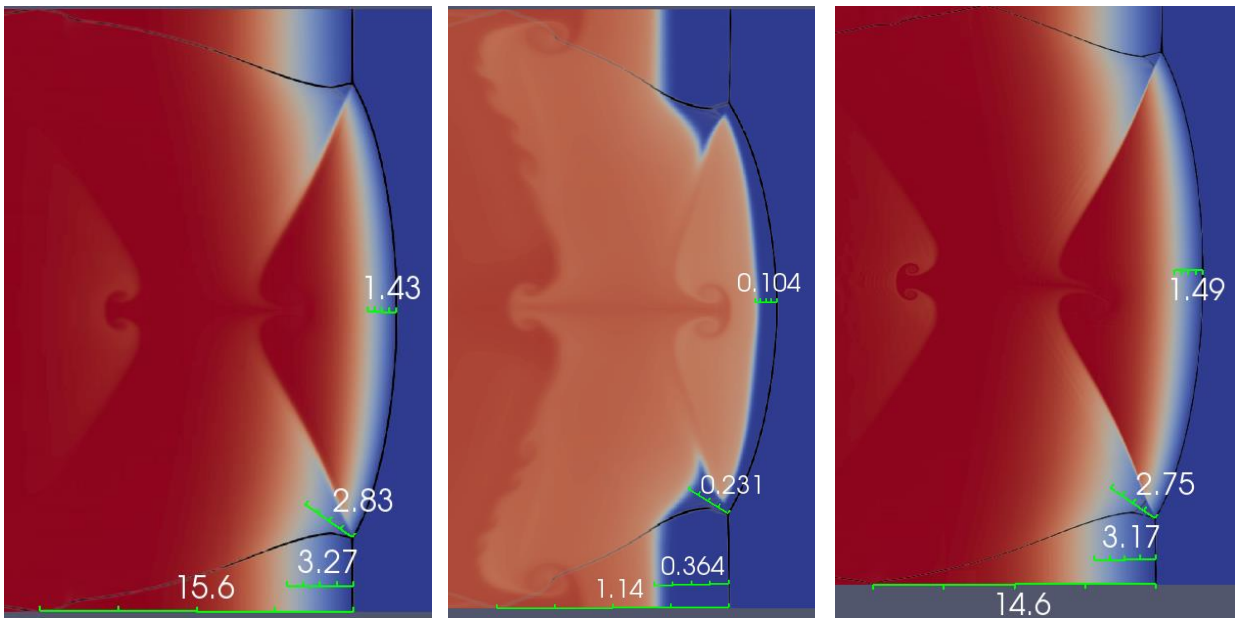

(a) (b) (c)

Figure 4-31 Length Measurements of Induction Zone of $2H_2 - O_2 - 7Ar$ Detonation using (a) Inviscid, Global Chemistry Model (b) Inviscid, Detailed Chemistry Model (c) Viscous, Global Chemistry Model

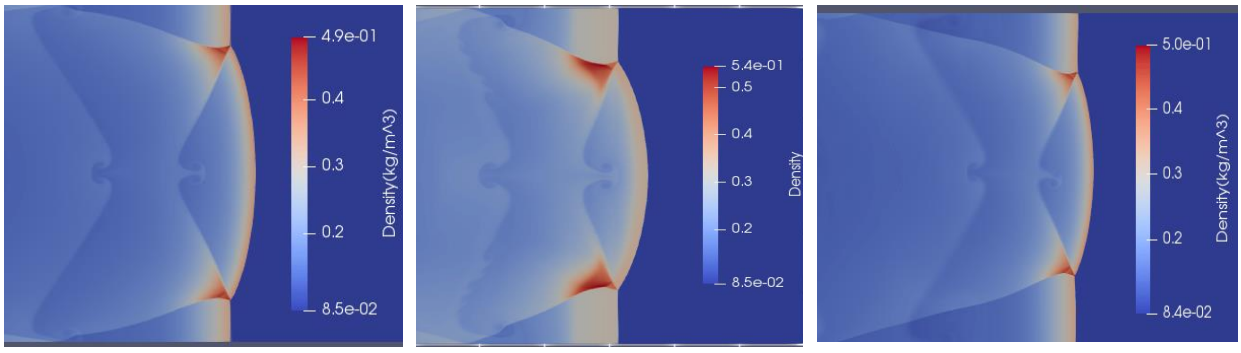

Figure 4-32 Density Contour Comparison of $2H_2 - O_2 - 7Ar$ Detonation (a) Inviscid, Global Chemistry Model (b) Inviscid, Detailed Chemistry Model (c) Viscous, Global Chemistry Model

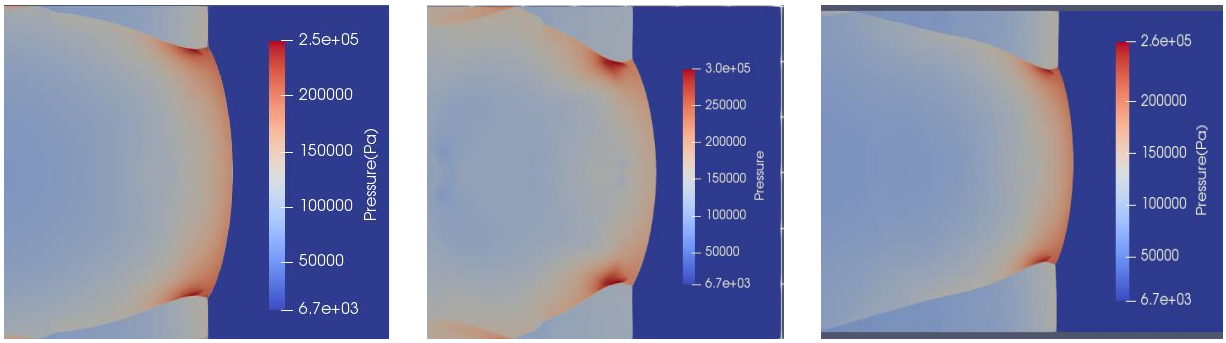

Figure 4-33 Pressure Contour Comparison of $2H_2 - O_2 - 7Ar$ Detonation (a) Inviscid, Global Chemistry Model (b) Inviscid, Detailed Chemistry Model (c) Viscous, Global Chemistry Model

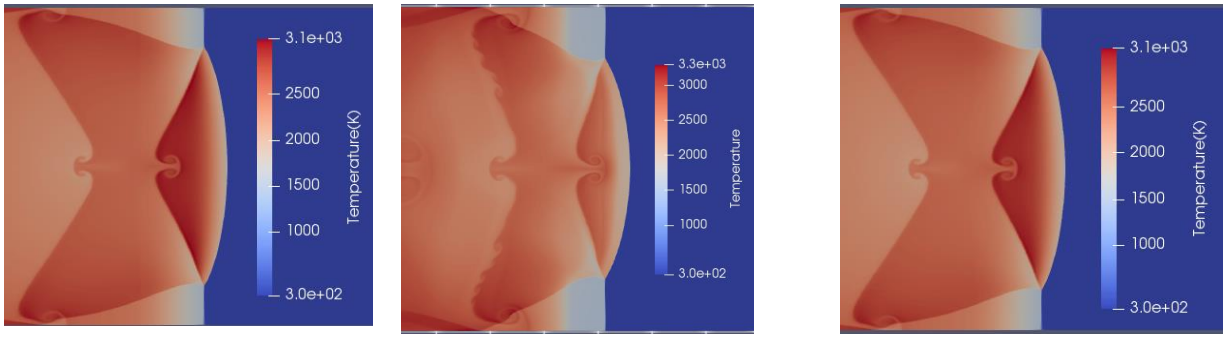

Figure 4-34 Temperature Contour Comparison of $2H_2 - O_2 - 7Ar$ Detonation (a) Inviscid, Global Chemistry Model (b) Inviscid, Detailed Chemistry Model (c) Viscous, Global Chemistry Model

When comparing the structure of the triple point between all the three models above, slight differences in the upper limits of the variables such as pressure, temperature, and density can be noticed. The curvature difference of transverse waves between multistep chemistry and global one step chemistry

are captured well by the pressure contour comparison figure. The velocity at which the transverse wave travels downstream depends on the local speed of sound as per the eigenvalue, $u - c$. The molecular mass influences the local speed of sound by a factor of $1/M$. For a regular detonation traveling with D_{CJ} the transverse waves are slightly above the sonic Mach number when the equilibrium speed of the sound of the product was used [38]. The difference in the distribution of temperature is also clearly identified by the curvatures of the transverse wave in multistep chemistry when compared to the single-step reactions. The slip lines detached from the previous reinitiation interaction becomes unstable in the multistep chemistry simulation shown in the following density contour comparison figure. The detached slip lines in global one-step chemistry do not undergo this transition. The reason for this instability is not influenced by the artificial diffusion since the viscous code is simulated using a globally fourth-order code with a resolution twice as much as the multistep chemistry. A sequence of transverse wave interactions with slip lines is presented from the inviscid - multistep chemistry simulation below. The contour below shows the gradient of temperature at T=0.6 milliseconds. Newly formed slip lines that did not interact with a transverse wave are shown using temperature gradient contour below.

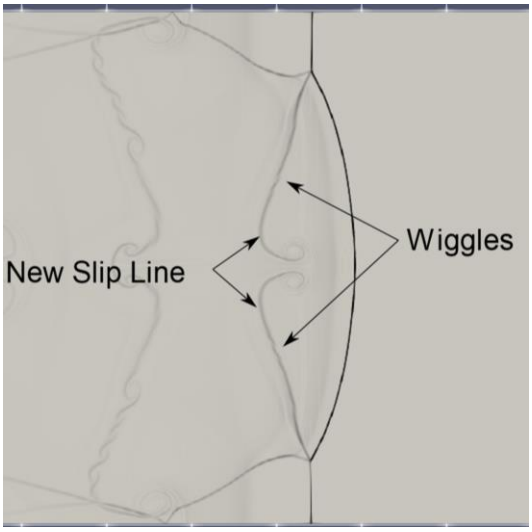

T=0.000607 s

Figure 4-35 Early Stages of Instabilities in Slipline Behind Detonation using Inviscid Multistep Chemistry Model

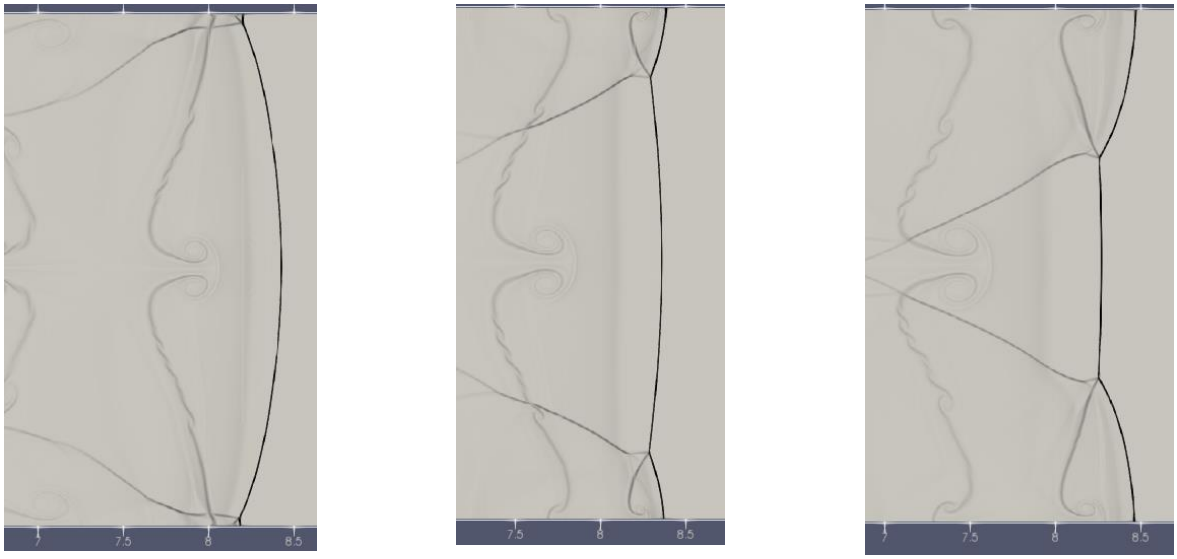

T=0.000611 s T=0.000616 s T=0.00062 s

Figure 4-36 of Evolution of Instabilities in Slipline Behind Detonation using Inviscid Multistep Chemistry Model

Though the transverse wave has not interacted with the slip lines, the formation of wiggles along the slip line is visible. Since the instability does not seem to originate with the interaction of transverse waves, the RM instability mechanism is ruled out and KH instability can be concluded to be the operating mechanism considering the tangential flow profile. From the one-dimensional analysis, it was clear that the velocity and density distribution through the reaction zone varied for multistep chemistry when compared to one-step chemistry. This distribution favors the growth of disturbances along the slip lines.

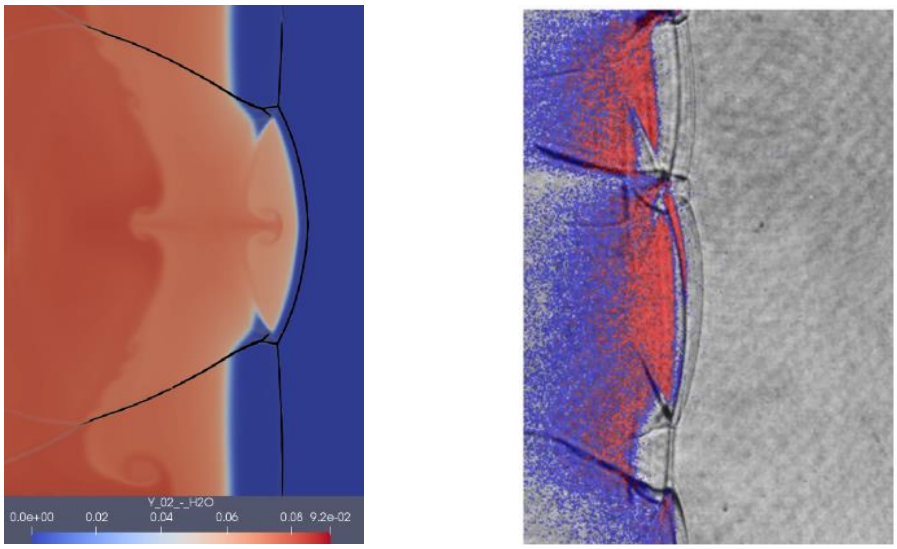

(a) (b)

Figure 4-37 (a) Product Mass Fraction of $2H_2 - O_2 - 7Ar$ @6.67 kPa compared to (b) $2H_2 - O_2 - 12Ar$ @20 kPa Chemiluminence Image from Experiment [47, 133]

Keystones appear along the detonation front due to the change in the position of the reaction front which is a function of post-shock temperature. When the velocity of the shock varies along the transverse direction the temperature behind shock varies accordingly. The formation of a diamond-like region of high pressure which is bounded by transverse wave interaction and shear layers are displayed in the density/pressure gradient contour to the left along with the keystone feature from the experiment of Austin [12] on a hydrogen-oxygen detonation with higher portions of argon shown in the right side of the figure above.

4.2.5 Reinitiation Sequence in Ordinary Regular Detonation

The reinitiation mechanism which was introduced to the Chapter 1 for a regular detonation is analyzed and detailed in the following sequence of plots. The reinitiation sequence is described using the results from the viscous simulation since it has the highest resolution. The experimental equivalent of the reinitiation process in hydrogen-oxygen detonation diluted with argon using time-resolved shadowgraph can be found in the work of Austin [12]. To get a better understanding of the role of shockwaves, the pressure gradient contour is overlapped over every product contour to track the movement of shockwaves. The time sequence is mentioned in non-dimensional time for one-step chemistry. At T=116, two opposing

triple points approach each other. The shock waves are shown by the solid black lines which represent the pressure gradient and the blue region behind the shockwaves are the heated but unreacted reactants. Using any other scalar gradient might confuse contact discontinuity with shockwave. The induction zone is encompassed between the slip lines and the transverse waves. At T=117.05, it forms a diamond-shaped region of the unreacted zone. The transverse waves and primary triple points have interacted with each other, but the secondary triple point interaction proceeds at T=117.46. The transverse wave attached to the secondary triple point has not vanished yet. The reaction proceeds in the diamond pocket and the transverse waves have flipped and started to move in the opposite direction following their reflection.

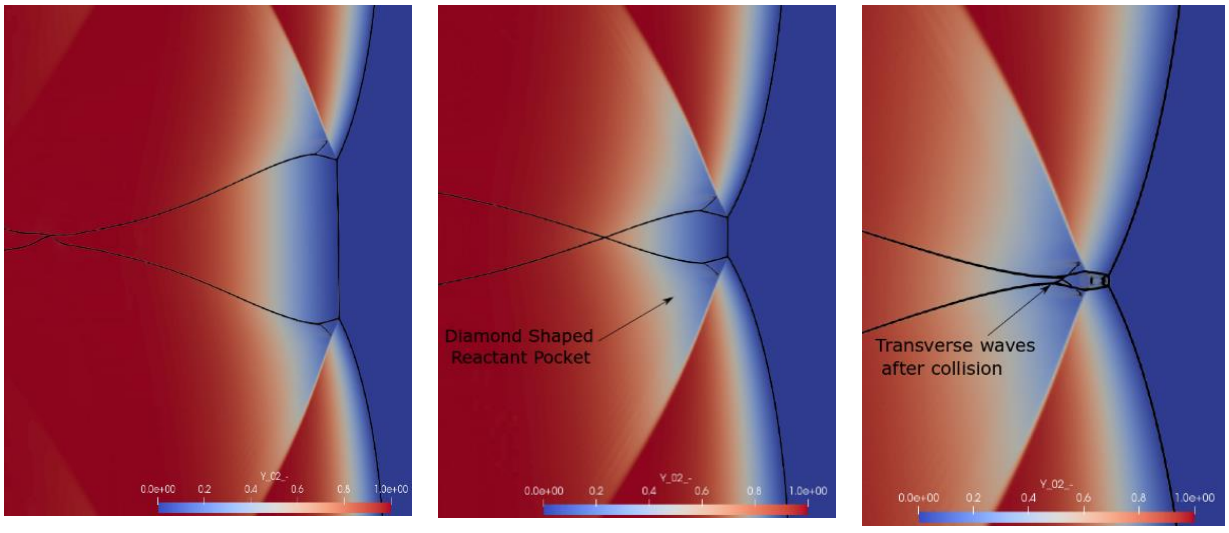

T=116.21 T=117.05 T=117.46

Figure 4-38 Initial Stages of Reinitiation of a $2H_2 - O_2 - 7Ar\ Detonation$ @6.67 kPa using Viscous One Step Chemistry

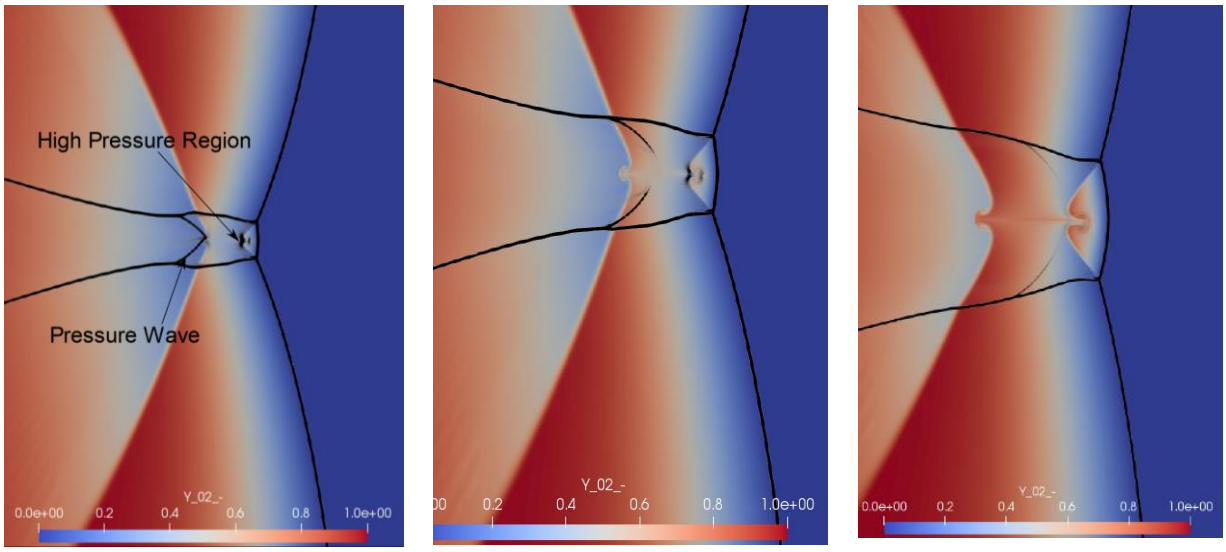

T=117.64 T=117.82 T=118.18

Figure 4-39 Dynamics of Reinitiation After Collision in a $2H_2 - O_2 - 7Ar$ *Detonation* @6.67 kPa using Viscous One Step Chemistry

At T=117.64, we can see that the primary triple point interactions have led to a high-pressure region, responsible for the curving of the new slip line which is formed as a new Mach stem is initiated. The diamond-shaped region is still intact along with a shock wave which has formed as a result of secondary triple point interaction and is moving towards the new Mach stem. The old slip lines from the two triple points have merged and become one contact discontinuity as also observed by Deiterding [38]. The burning of this diamond region can be seen to progress at T=117.82 with the transverse wave moving opposite to each other. The shock wave travels asymmetrically upstream and gradually becomes weaker with time. This shock wave does not gain momentum even after entering the induction zone at T=118.18. A slight asymmetry after the initiation of detonation was noted in the soot foil that might cause this asymmetry in shock strength. We can see the growing Mach stem, burnt diamond pocket, as well as the pressure wave interaction with the slip lines at T=118.18. The kink responsible for the secondary triple point has formed at T=118.63 even before the pressure wave reaches the shock front. The combustion is complete behind the old slip line and the Mach stem increases in size at T=118.91. The structures of the transverse wave are also prominent. The development of the triple point into a strong structure is observed to happen only at T=121.14 completing one reinitiation cycle.

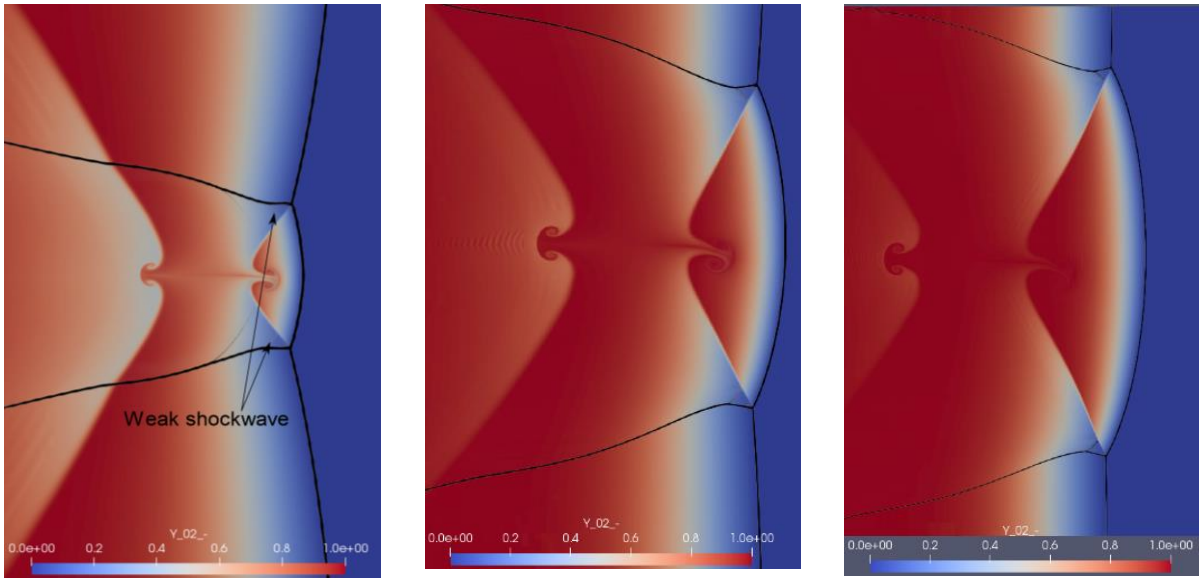

T=118.36 T=118.91 T=121.14

Figure 4-40 Final Sequence of Reinitiation of a $2H_2 - O_2 - 7Ar$ $Detonation$ @6.67 kPa using Viscous One Step Chemistry

The combustion of the diamond pocket did not result in any pressure waves during its combustion. The following sequence of contours shows one reinitiation cycle for the same argon diluted hydrogen-oxygen detonation setup with an inviscid, multistep chemistry model. The pressure gradient contour is overlapped on the H_2O contour which represents the product. The time below each contour is mentioned in seconds. The entire reinitiation occurs within 26 microseconds. Two strong triple points approach each other at t= $770\mu s$ and the extended transverse waves have started to interact with each other at $t = 780\ \mu s$. The induction zone grows and extends into the envelope of transverse waves. At $t = 785\ \mu s$, the unburnt diamond shaped pocket has started to take shape with its end almost overlapping with the transverse wave intersection point leaving the entire transverse wave interaction to occur within the unburnt reactant pocket.

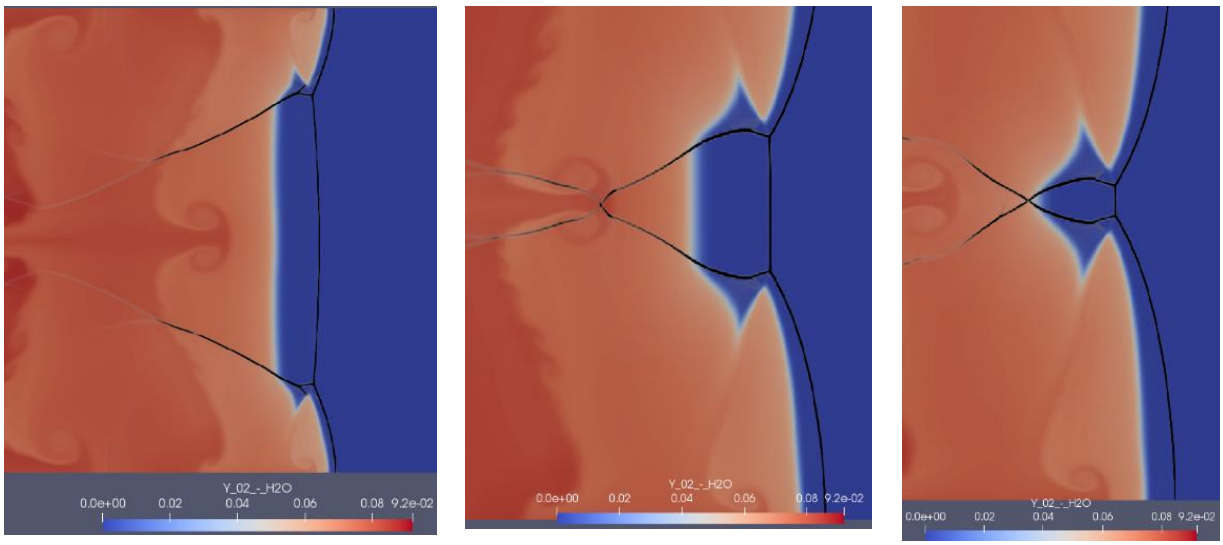

t=0.00077 s t=0.00078 s t=0.000785 s

Figure 4-41 Initial Stages of Reinitiation of a $2H_2 - O_2 - 7Ar\ Detonation$ @$6.67\ kPa$ using Inviscid Multistep Chemistry

At $t = 787\ \mu s$, the collision of a transverse wave and the primary triple point is complete with secondary triple points approaching each other. The reflection of the transverse waves happens in the timescale at around 1 μs. At $t = 788\ \mu s$, the unburnt reactant pocket burning results in a strong shock wave behind a weaker pressure pulse. This weaker pressure pulse resulted due to secondary triple point interaction as observed in the global one-step chemistry mechanism. The strong shock wave merges with the weaker shock wave and travels upstream. The transverse wave burns the reactant pockets as it translates upwards. A new Mach stem with a high-pressure region behind the slip lines is also noticeable. At t=790μs, we see that the weaker pressure waves coalescence with the primary triple point of the new Mach stem initiating a kink. At t=791.2 μs, the stronger pressure wave interacts with the new slip lines and curves towards the Mach stem. At t=792.3 μs, this pressure wave merges with the shock wave as well as merges with the kink structure and strengthens the strong structure.

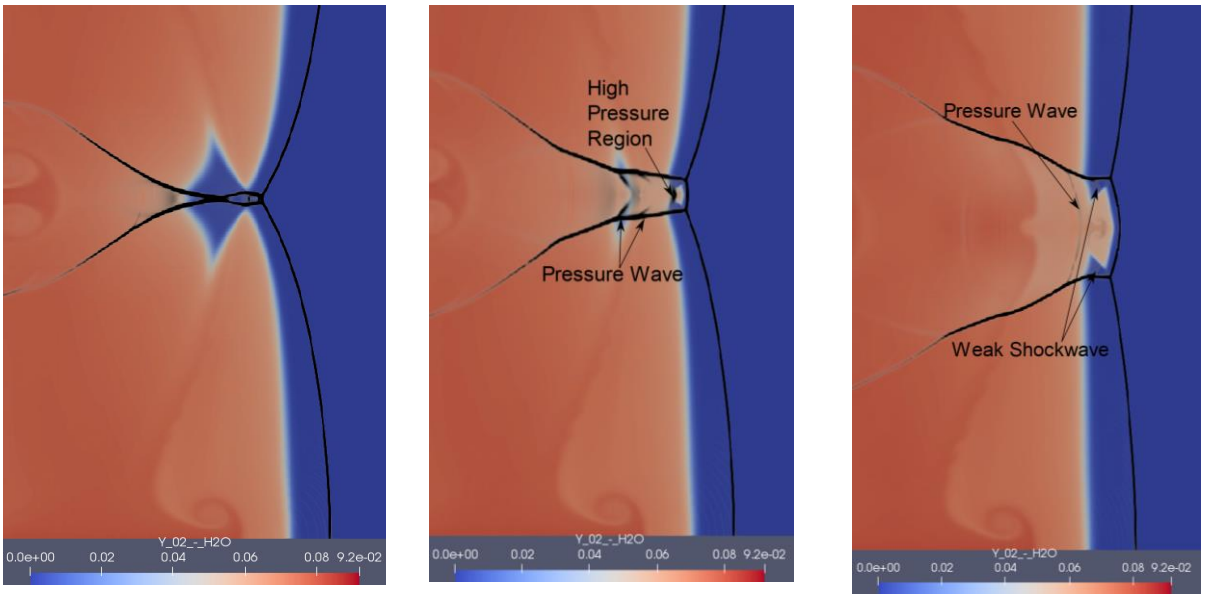

t=0.000787 s t=0.000788 s t=0.00079 s

Figure 4-42 Dynamics of Reinitiation After Collision in a $2H_2 - O_2 - 7Ar\ Detonation\ @6.67\ kPa$ using Inviscid Multistep Chemistry

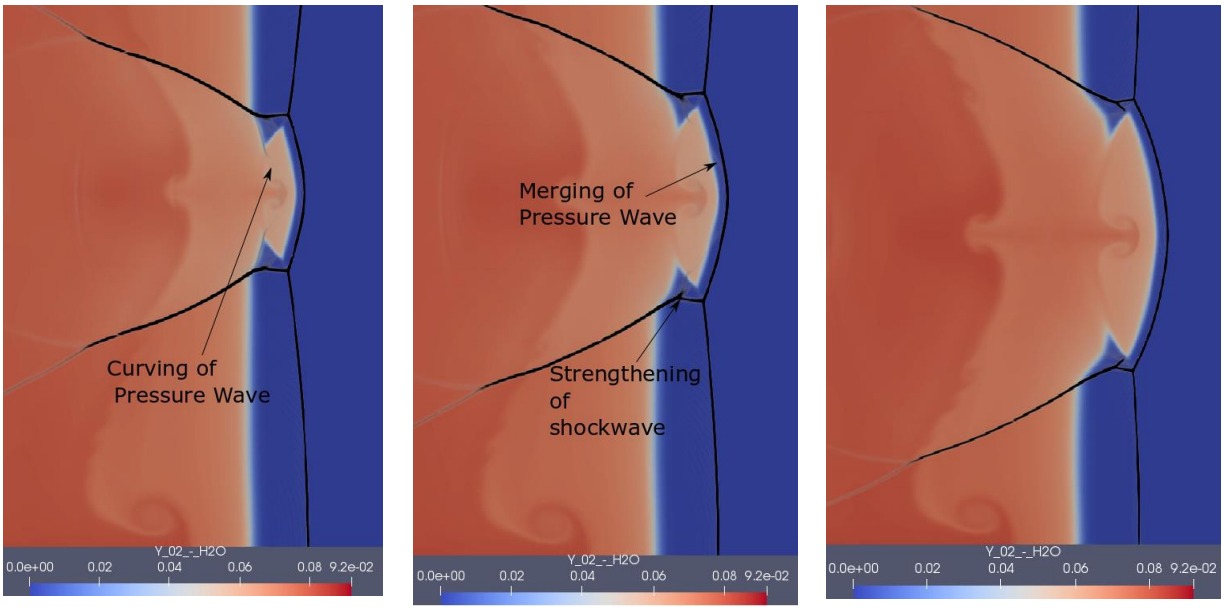

t=0.0007921 s t=0.000793 s t=0.0007956 s

Figure 4-43 Final Sequence of Reinitiation of a $2H_2 - O_2 - 7Ar\ Detonation\ @6.67\ kPa$ using Multistep Chemistry

A clear thermally neutral induction zone can be observed in the temperature plot of a detailed chemistry model in the left when compared to the global one-step chemistry model which is one of the drawbacks of the global one-step chemistry model. The cell cycle is complete with a new expanding Mach stem at t=795.6 μs.

4.2.6 Discussion

The reinitiation sequence shows two events of a collision causing enthalpy increase. The collision between transverse waves followed by a collision between primary triple points after which the collision between the secondary triple points initiates the new cell cycle. This sequence was also observed by Hu et.al [37]. The reaction due to the triple point collision occurs due to autoignition whose reaction rate is a function of pressure and temperature. The time scale of exothermic reaction (t_e) and the acoustic time scale (t_a) at that temperature decides the behavior of the hot spot. A detailed review of different models predicting the behavior of the gas in the presence of hot spots with variation in these time scales can be found elsewhere [134, 135, 131, 136]. If the exothermic timescale is significantly less than the acoustic time scale, then the triple point collision results in constant volume combustion where the gas does not have time for the response to the change of state. This leads to shock formation. When the acoustic time scale is smaller than the exothermic time scale, then as the gas reacts, it can expand leading to constant pressure type of combustion resulting in only weak acoustic waves. When both the timescales are comparable partial confinement occurs. Depending on the nature of the surrounding environment, the shock might transfer into a detonation through the SWACER mechanism. For this to occur, the reaction time scale should match with the time scale of the traveling shock. Though the one-step chemistry reinitiation cycle predicted the shock wave after the secondary triple point collision, no shock waves were emitted from the burning of the diamond-shaped pocket since the rate of the reaction was not in the same magnitude of what we can observe in multistep chemistry. The autoignition rate was gradual in one step chemistry compared to multistep chemistry permitting an expansion along with reaction. The difficulty for predicting accurate reaction rate at the pockets is due to the single preexponential constant. The drawback faced in predicting the increased reaction rate for highly diluted mixture demands for a smaller preexponential factor for reaction in a two-step reaction to reduce the rate of the reaction. This would make the timescale for the

burning of the pocket even larger. The lagged region burning pattern was almost instant following the transverse wave reflection in multi-step chemistry. Though this does not play a significant role in the reinitiation of regular detonation, this might need considerable importance in highly irregular detonation which tends to form multiple hotspots.

4.2.7 Summary

To summarize this chapter, the global one-step chemistry, and the multistep chemistry Euler model were validated against experimental observations [10]. The one-step chemistry parameters were calibrated to reproduce major features of detonation such as cell size, half-reaction length, and velocity profile. Variations in types of transverse instability initiation, global one-step, and multistep chemistry, two and four-mode detonation, moving detonation with wall boundary condition and stationary detonation with supersonic outlet boundary condition were considered when choosing the computational setup. The grid convergence, effect of grid resolution, flow streamline pattern, global parameters such as instantaneous velocity, mean velocity, cell shape, the structure of the triple point were compared between different studies followed by the reinitiation mode analysis. No clear evidence of the decoupling of the reaction zone from the shock triple point configuration was visible. No difference between primary triple point collision was observed but a difference in the reaction pattern of diamond-shaped pockets was observed. In the next chapter, the reinitiation mechanism of highly unstable detonation will be detailed.

.

Chapter-5 Inviscid Oxymethane Detonation Simulation using Global One Step Chemistry

The primary goal of this chapter is to study the ability of the two-dimensional inviscid simulation to capture global hydrodynamic features of highly irregular detonations. The stoichiometric oxymethane detonation is studied for two initial pressures of 3.5 kPa and 6 kPa. For a 3.5 kPa pressure, the detonation should contain only a single unstable mode and the 6 kPa pressure should permit two unstable modes as per the cell measurement from experiments. The presence and survival of secondary cells contribute to the interaction between multiple triple points making the reinitiation mechanism of primary triple point hard to occur within the domain length chosen. The single-mode detonation favors this aspect since the presence of intermodal interaction is minimized. In the first half of the chapter, the structure and reinitiation of detonation is studied for a single-mode detonation. When considering a practical application, the presence of multiple triple points is essential for the survival of the detonation. In the second half of the chapter, dual-mode detonation at 6 kPa is studied to understand the interaction between primary triple points. A highly unstable mixture is often categorized with multiple peak thermicity which does not support a predominant cell size. The transverse cell size is dependent on its confinement since it is also reflected from its wall boundaries in all the three dimensions independent of its shape (circular or rectangular) [12]. A rectangular channel is often used in detonation studies to avoid spinning detonations [113] and is also chosen for our study. The minimum initial pressure which sets the propagation limits of the detonation was seen to vary with its experimental configuration [137]. Considering the uncertainties, the geometry of the case must also be chosen and fixed for the case of the study to compare the features of the detonation with the experiment. The setup and boundary conditions of this simulation are chosen to match with the experimental works of Radesculu in [44], Maxwell [46] and Kiyanda et al. in [59].

5.1 Case A- Single Mode Detonation

5.1.1 Computational Setup

A two-dimensional rectangular channel with a length of 303 cm (equivalent to is 3400 $\Delta_{\frac{1}{2}}$) and a height of 10 cm was chosen to be the computational domain. Wall boundary condition at the left end and supersonic outflow boundary at the right end was implemented. The top and bottom walls were modeled

with inviscid walls. The height of the tube is fixed to obtain a dual-mode detonation when the operating pressure is at 6000 Pa based upon the cell size reported in the detonation database [138]. When the setup cross-section is bigger than half-reaction zone size but smaller than one complete cell, a single-headed detonation is formed with a single triple point configuration [4] [44]. With an even smaller cross-section equivalent to one or two half reaction zone lengths, a steady-state detonation with weak transverse perturbations in the absence of transverse waves is formed [4]. When the cross-section is larger than the cell size, these transverse oscillations are subjected to amplification. A steady-state ZND solution with a highly overdriven state of $f = 1.05$ was used to initialize the solution with a 5-degree angle to the bottom wall. The time marching was performed until a maximum of nondimensional t=400. The calculations for thermo-chemical parameters were matched for 3500 Pa. The GRI 3.0 detailed mechanism was used for the derivation of parameters for global one-step chemistry. The global one-step model is first calibrated for 3500 Pa using the same method followed in the previous chapter and the result is shown in the plot below.

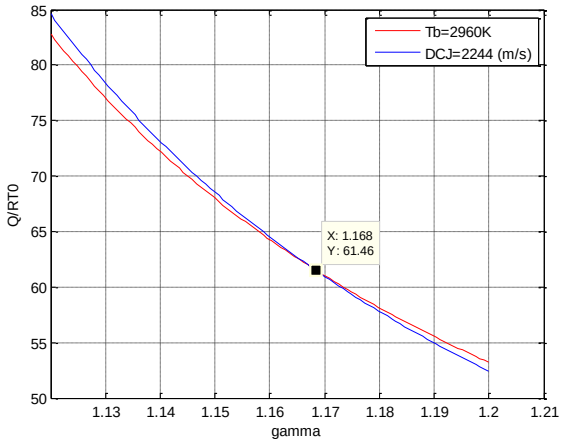

Figure 5-1 Plot to Determine Thermodynamic Properties for $CH_4 + O2$ Detonation @ 3.5 kPa

The base grid was fixed at 16 grid points per $\Delta_{\frac{1}{2}}$ with up to three levels of refinement being performed. Grid convergence for highly unstable detonation using inviscid simulation is controversial even in one dimension. Grid convergence is considered to be attained in this study when an increase in resolution does not affect the mean of the detonation front velocity along with similar primary and secondary cell patterns [40, 46]. Oran et al. [35] point out that care must be given to not over resolve a solution using the Euler method resulting in seeing non-physical structures. Ng [11], in a research to estimate the randomness

in the system [11], determined that as the instability increased for detonation and the rate of divergence due to the deviation in the initiation condition was also increasing. A compelling finding of this sensitivity to initial conditions was found in the experimental work of Bhattacharjee [62, 52] for stoichiometric oxymethane detonation in a rectangular channel with a height of $20\Delta_{\frac{1}{2}reactionlength}$. High stochasticity for oxymethane detonation for the same operating conditions was clearly demonstrated. The same sensitivity to initial conditions and discretization error was observed in this thesis as it will be demonstrated in the following sections. Due to drawbacks played by the reduction in artificial viscosity with increase in grid resolution [64, 139, 35] a maximum of only 128 $\Delta_{\frac{1}{2}}$ is performed in Euler simulations by referring to other similar works on highly irregular detonation. This is also in accordance with an inviscid study by Mahmoudi et al. [139] which recommends at least 125 cells per $\Delta_{\frac{1}{2}}$ in order to capture the hydrodynamic features of irregular detonations correctly.

Table 5-1 Grid Resolution Setup for Case A

Case – I H=10 $\lambda_{\frac{1}{2}}$	Minimum Resolution Δx & Δy	Levels $(r = 2)$
Base Grid – 16 points per $\lambda_{\frac{1}{2}}$	0.60 mm	1
32 points per $\lambda_{\frac{1}{2}}$	0.3 mm	2
64 points per $\lambda_{\frac{1}{2}}$	0.15 mm	3
128 points per $\lambda_{\frac{1}{2}}$	0.075 mm	4

The solution is initialized using a one-dimensional, steady-state, ZND profile of a CJ detonation at 3500 Pa and 298 K which shown below.

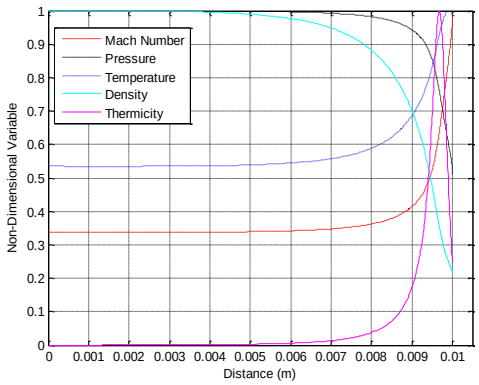

Figure 5-2 ZND Solution of Methane Oxygen Detonation at 3500 Pa

The above diagram shows the methane-oxygen detonation in a standing reference frame with reactants entering the domain from the left. The thermally neutral induction zone is approximately seven times longer than the argon diluted hydrogen-oxygen detonation analyzed in the previous chapter. This results in the decaying of Mach stem to incident shock wave in a cell cycle to be faster than in hydrogen-based detonation. The reaction zone length is generally smaller than the induction zone thickness by an order of magnitude [140] and especially in thermal explosive cases. It can also be noticed that the acceleration of the products to reach the sonic plane is rapid. The reaction length scale is two orders of magnitude smaller than the argon diluted hydrogen-oxygen detonation. This length scale ratio positions the possibility of hotspots within the induction zone due to high sensitivity towards an unevenly distributed temperature field. The steady-state ZND results of the chosen case are shown below.

Table 5-2 Initial and Post Shock Conditions of $CH_4 - 2O_2$ Detonation at 3500 Pa

Variable	Value	Units
p_o	3500	Pa
T_o	298	K
ρ_o	0.0363	kg/m^3
c_o	356.4	m/s
M	20.18	g/mol
D_{CJ}	2243	m/s
P_{VN}	1.672	atm
T_{VN}	1726.74	K
ρ_{VN}	0.315	kg/m^3
$\Delta_{\frac{1}{2}}$	9.68	mm

The density contour of detonation traveling towards the end of the 340 cm tube is shown below (Figure 5-3) followed by the numerical soot foil (Figure 5-4) captured along the domain for the same detonation. The detonation self-sustained in a two-dimensional, inviscid, global one-step chemistry

simulation. To confirm the extent to which the detonation physics is captured, it is compared with experimental and numerical data available in literature in respective subsections.

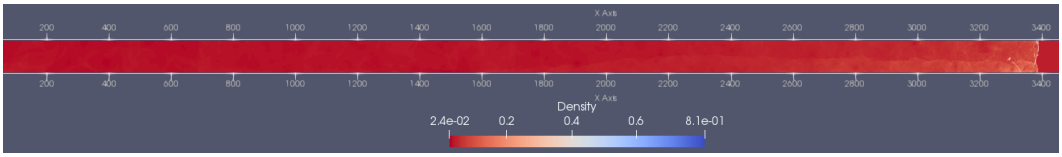

Figure 5-3 Density Contour showing the Detonation at the End of Computational Domain

Figure 5-4 Numerical Soot Foil of $CH_4 - 2O_2$ Detonation for H=10$\Delta_{\frac{1}{2}}$

5.1.2 Detonation Front Velocity Profile

The detonation velocity profile is studied to determine the stages of the detonation when it is decoupled. The detonation shock front is irregular, especially for highly unstable detonations. The detonation front velocity in a single cell cycle consists of the Mach stem stage which is above D_{CJ} and incident shock stage which decays below D_{CJ}. Hence when a detonation operated in a single mode, the average detonation velocity tends to be a few percent below CJ velocity [48]. Three average velocities for this case were reported in the experiments of Kiyanda, et al. [58] based on pressure transducers (2020 m/s), streak measurements (2170 m/s) and ignition time measurements (2170 m/s). For the same conditions, experimental results from Radesculu et al. [9, 44] gave an average velocity of 1792 m/s which is 20% less than average CJ velocity which was measured using PCB pressure transducers. The following graph shows the instantaneous velocity of the detonation front recorded at the bottom wall and is normalized by the CJ velocity.

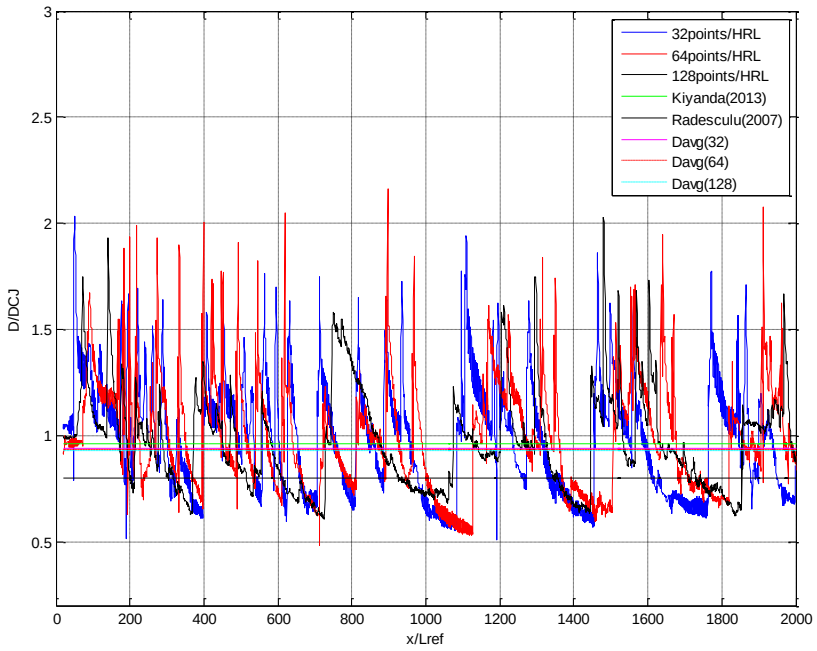

Figure 5-5 Instantaneous Detonation Front Velocity Profile Comparison of $CH_4 - 2O_2$ Detonation at 3500 Pa

The first difference observed is the variation in instantaneous velocity peaks and patterns with an increase in grid resolution. From the Chapter 4, we know that the grid convergence was attainable for weakly unsteady detonation. The difference we observe in the flow pattern is due to the appearance of the secondary cells along the Mach stem. With grid resolution, the unstable modes causing secondary cells to become resolved and are captured by the maximum pressure gradient subroutine along the wall resulting in multiple peaks. The primary triple point interacts with all the minor triple points before it moves past them longitudinally, deviating from the pattern followed in the previous grid resolution. This offsets the distance between two consecutive primary triple point collisions along the wall at different grid levels. The lower bound of the instantaneous velocity is close to $0.5D_{CJ}$. This is roughly the velocity reached by critical deflagration before the onset of detonation in a smooth channel [2]. Hence it is clear that before reinitiation, the detonation is a decoupled complex of precursor shock and flame. The difference between CJ deflagration and decoupled shock flame complex is; flame instability is responsible for the onset of detonation in a DDT whereas shock instability plays the key role for the reinitiation of detonation.

Considering the global features, the detonation operated with half cell cycle as observed in the experiment [59]. The initial transients of detonation roughly became regular after 900 x/L_{ref}. One consecutive peak high and bottom low of the velocity ratio plot represents one cell limit cycle. The secondary modes of detonation represent additional velocity peaks which are smaller than peaks created by the primary mode. A rough mean velocity was calculated to confirm the grid convergence and plotted along with this graph. The mean of the detonation front velocity ratio converges close to the experimental value report by Kiyanda [58] and within the bounds of experimental CJ velocity by Radesculu [44]. It also confirms that the case chosen for validation study is a marginal detonation by averaging at 0.9D_{CJ} which was expected and shown below.

Table 5-3 Mean Detonation Velocity Ratio at Different Grid Levels

Case	32cells/HRL	64cells/HRL	128cells/HRL	Difference %	Experimental [59]
Case-A	0.938	0.933	0.93	1.5	0.944

The random longitudinal oscillation of the detonation front due to primary and secondary triple points for 128 cells per HRL can also be observed from two cell cycle as shown in Figure 5-6 (b). The lead shock oscillation within a cell cycle, especially for hydrocarbon detonation having almost twice the oscillation magnitude of hydrogen-based detonation has been mentioned by Austin in [12]. More specifically to methane-oxygen detonation, this behavior was also observed in an inviscid simulation using one-step chemistry [44] as shown below. From the aperiodic nature of the limit cycle, it is implicit that the detonation is highly irregular.

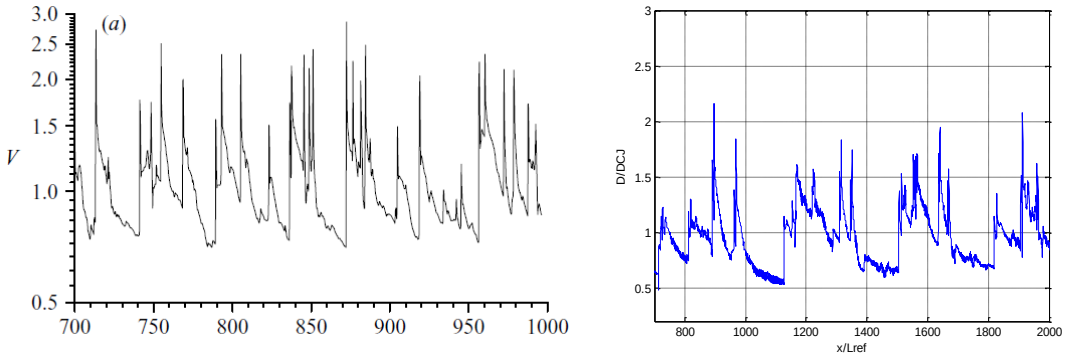

(a) (b)

Figure 5-6 Instantaneous Detonation Front Velocity Profile obtained for Methane-Oxygen Detonation with same Initial and Boundary Condition (a) By Radulescu [44] (b) Current Study

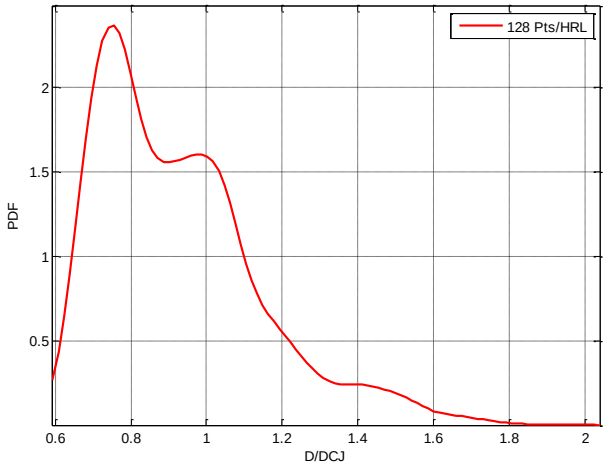

Figure 5-7 Probability Density Function Plot of Instantaneous Detonation Velocity Ratio of Case-A

The distribution of shock velocity is visualized using PDF based on nonparametric estimates [141] to understand the time spent by the detonation in various velocities during its propagation. A PDF of a regular marginal detonation with detailed chemistry is skewed towards propagation velocity lower than CJ velocity [12, 10, 12]. Similarly, detonation front velocity analysis of methane-oxygen detonation for the same initial conditions using LES study was reported by Maxwell [46] and shows skewness at $0.84D_{CJ}$. The reason for observing 20% less mean average velocity in the experimental results published by Radulescu [44] when compared to others [58] can be explained by this plot. Since the detonation spends a maximum fraction of the time in the decaying phase, the pressure transducers pick up this velocity more often than the average CJ velocity.

5.1.3 Favre Averaged Flow Profile

The quantitative validation of detonation is extended in this section by comparing the two-dimensional data with the analytical result. The two-dimensional flow profile was Favre averaged as per the procedure explained in Chapter 4 and compared with the one-dimensional steady-state ZND profile at the

theoretical CJ plane which is when the flow Mach number is equal to one in the stationary frame of reference.

Table 5-4 Comparison of Favre Averaged Profile with ZND Results for 128 cells/HRL For Case A

Flow Variable	ZND Value	Favre Averaged Value	Difference	Unit
Pressure	86632	90951	5.1%	Pa
Temperature	3213	3465	7.8%	K
Density	0.067	0.07	4.4%	kg/m^3
Velocity	1253	1184	5.5%	m/s
Average Sonic Plane	1.14	13.4	-	cm
Reactant Mass Fraction (Theoretical)	0	0.58	-	-
Reactant Mass Fraction (Favre Averaged)	0	0.03	-	-

The flow variables at the Favre averaged CJ plane falls within a ten percent difference when compared to the steady-state ZND theory. As we discussed in the previous chapter, a direct comparison cannot be made with the sonic plane obtained analytically for the purpose error quantification purpose. At the theoretical sonic plane obtained from the ZND theory, the averaged reactant mass fraction is 0.58. On the Favre averaged sonic plane, the reactants seem to be almost combusted completely (Y_{react}~3%). The same behavior was also observed in an inviscid simulation of methane oxygen detonation [60], where the flow was determined to have reached chemical equilibrium before reaching the averaged CJ plane where thermodynamic variables reached CJ state values. For a 3.4 kPa, the unburnt pockets were consumed

within 10 cm in experiments [44]. Maxwell reported a length of 9.7-9.8 times (~ 9.5 cm) the ZND length in [46] using LES simulation and 16-17 times the ZND length (16.4 cm) using Euler simulation with one step chemistry.

5.1.4 Detonation Cell Pattern

The numerical soot foil for this case obtained by tracking the vorticity is shown below. A minor difference between the tracks for both grid resolutions can be observed. Globally, the primary triple points form the half-cell pattern followed by the patterns formed by the secondary cells. More secondary triple points are resolved with an increase in grid resolution. In the analysis of regular detonation in the previous chapter, a similar effect of the grid resolution to resolve the secondary triple point was demonstrated. The absence of secondary triple points when the grid resolution is low has been reported earlier [46]. The cell width of the detonation was 10HRL. Though the detonation is mode-locked to half-cell size if the height of the domain is reduced further, the characteristic length scale (coupling between a chemical reaction and transverse perturbation) of a marginal detonation is lost and the detonation will fail. Direct measurement of the length of the cell in a rectangular tube for this case was not available in the literature where this soot foil was published [46] but by using the scale of reference in the soot foil, an approximate length of 36-38 cm was measured. Consecutive cells were measured in the numerical soot foil and were averaged to estimate a length of 38.4 cm. A diagram below shows the measurements made in mm using the standard ruler filter in the Paraview visualization tool [142].

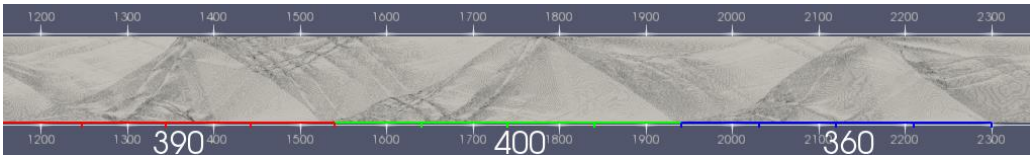

Figure 5-8 Measurements (mm) of Cells of $CH_4 - 2O_2$ Detonation at 3.5 kPa

The numerical soot foil is compared with its experimental equivalent [46] with increasing grid resolution as shown below.

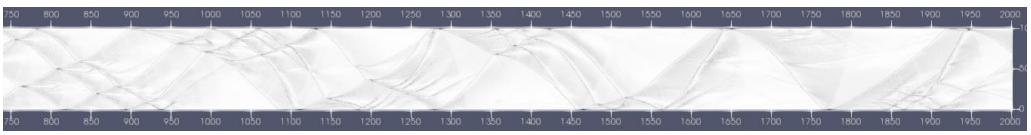

(a)

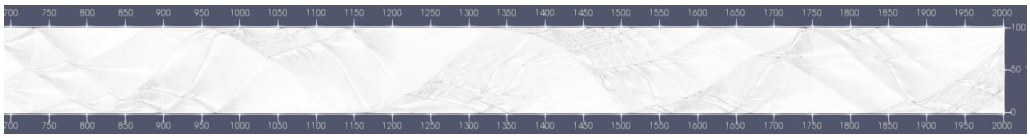

(b)

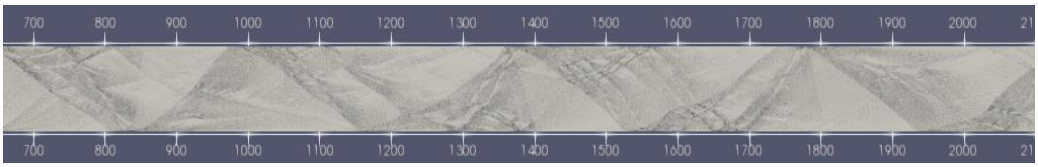

(c)

(d)

Figure 5-9 Numerical Soot Foil Comparison of $CH_4 - 2O_2$ Detonation at 3.5 kPa (a) 32 points per HRL (b) 64 points per HRL (c) 128 points per HRL (d) Experimental Soot Foil [60]

With grid resolution, more modes of instability are activated. Only the trace mark of the primary triple point is visible in the experimental soot foil. Secondary cells have been reported in marginal detonations with high activation energy when the height of the channel allows only one or a few primary triple points to operate, reducing its degree of freedom of irregularity [40, 48, 39, 143]. These secondary cells have been identified as transverse instabilities in the overdriven part of the detonation and are different from the transverse detonation [40]. The formation of secondary cells can be understood by comparing the soot foil images with corresponding pressure contours below.

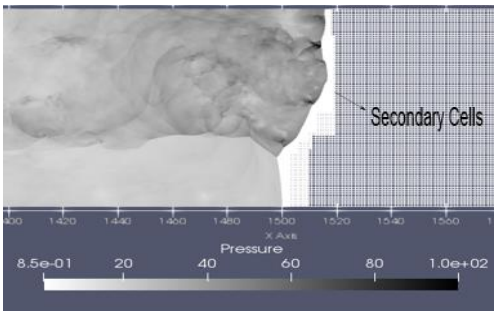

(a)

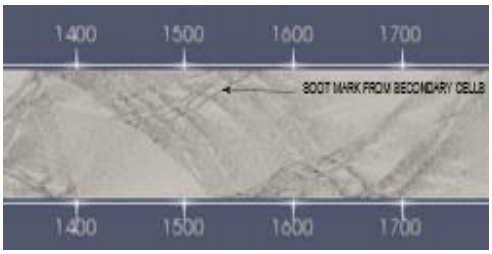

(b)

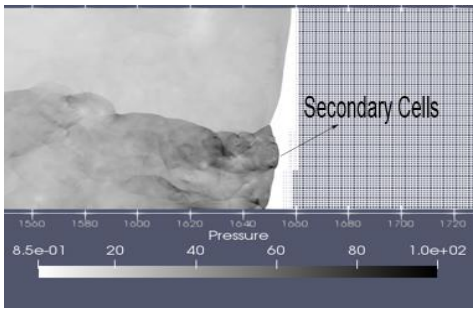

(c)

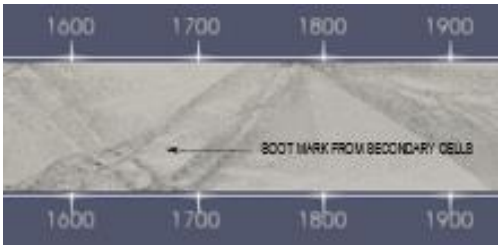

(d)

Figure 5-10 Frame (a) & (c) Pressure Contour and Frame (b) & (d) Soot Foil Comparison for $CH_4 - 2O_2$ Detonation at 3.5 kPa

A sequence of reinitiation is shown in the figure above to demonstrate the secondary cells soot recordings. In Figure 5-10 (a), an overdriven detonation forms due to reinitiation along the top wall and the primary triple point moves downwards towards the bottom wall. In Figure 5-10 (c), the primary triple point collides and reinitiation occurs along the bottom wall. These secondary cells start to disappear when the detonation decays into incident shock and loses strength. From the instantaneous velocity plot, we know that when detonation reinitiates, it results in an overdriven detonation. Stronger detonation results in the thinner induction zone. These perturbations, as shown in Chapter - 3, from the reaction zone can reach the shock front faster and more efficient than if it was an unsupported pressure wave traveling in a thicker induction zone. For further validation, the obtained numerical soot foils are compared with a single-mode oxyacetylene detonation experiment conducted by Gamezo et al. [40] at 0.03 atm. This pressure regime also resulted in transverse detonation which was not observed in our study. Both the results display a strong presence of secondary cells.

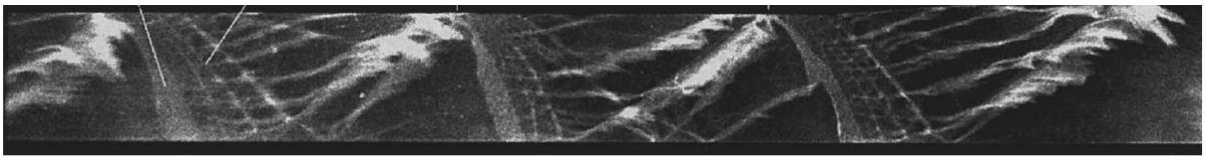

(a)

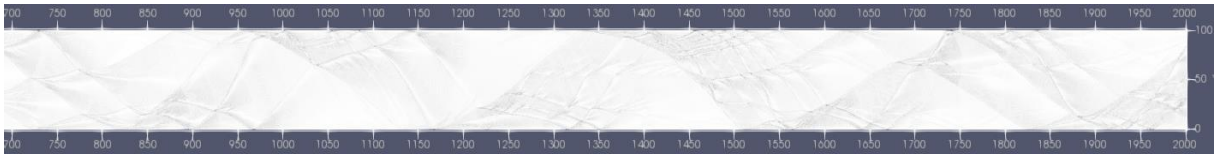

(b)

Figure 5-11 Comparison of (a) Experimental Soot Foil [40] of oxyacetylene detonation to (b) Numerical Soot Foil of $CH_4 - 2O_2$ Detonation at 3.5 kPa

5.1.5 Structure of the Triple Point

Features that are resolved and clear from flow contours will be discussed in this section with a gradient of density and pressure contours. In Figure 5-12, a primary triple point moving towards the bottom wall is chosen and analyzed at a nondimensional time of T=117. The primary triple point is labeled as P1 in density gradient contour (Figure 5-12 b) and as T1 in pressure contour (Figure 5-12 c). Figure 5-12 (b) shows that the flame following the triple point T1 has a short induction zone. The thickness of the induction zone behind the incident shock (I) is the thickest. The structure of transverse shock is different compared to a regular detonation. From the pressure gradient contour (Figure 5-12 c), the transverse wave system is defined using the points P1, P2, P3, P4, and R1. The P2 point forms the secondary triple point. In density gradient contour (Figure 5-12 b), the point P2 is formed due to the intersection of the transverse waves (P1-P4 & P3-P5) which are also curved. The formation of the transverse wave shock system can be better understood when analyzing the reinitiation process in the following sections. This transverse wave shock system interacts with the curved jet of reactants as it moves through it. The point P5 is labeled at the interaction of the transverse wave with the flame. The curvature of the transverse shock also makes it interact with the wall twice at R1 and R2 in the pressure gradient contour. A reactant jet labeled as J in the density contour (Figure 5-12 a) forms since the interacting shock waves are non-reacting. The density distribution along the wall jet shows a high-density region right behind the interacting shockwaves at P2,

compressing the reactants and a reduction in density as we move away towards the top of the jet marking potentially increased reaction rate. The inner layer of the wall jet is slightly curved towards the Mach stem. A hot spot (H) can be spotted in the induction zone in the density contour (Figure 5-12 a). An unburnt pocket of heated reactant (U) which is detached from the previous cell cycle is also found to drift downstream in the density contour (Figure 5-12 a). The dark borders around the unburnt pockets (U) and jet (J) represent the sharp gradient in density due to the flame surface.

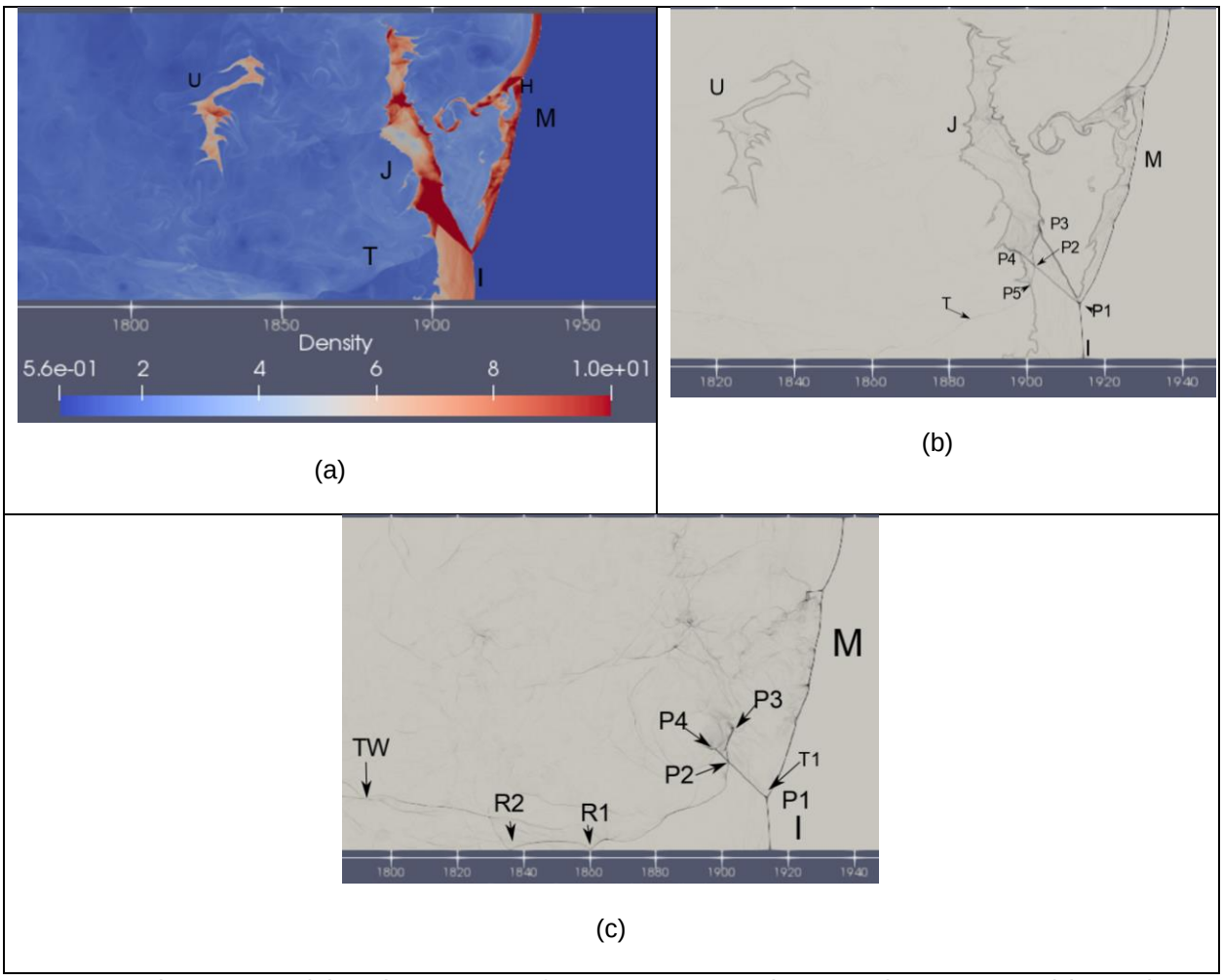

Figure 5-12 Triple point structure of $CH_4 - 2O_2$ Detonation at 3.5 kPa at T=117 (a) Density Contour (b) Density Gradient Contour (c) Pressure Gradient Contour

The next comparison of the triple point is performed at T=160; in this case, the triple point is about to collide with the upper wall. The primary triple point is marked with T1 and the secondary triple point is

marked with T2 in the pressure gradient contour (Figure 5-13 c). Along the Mach stem, two secondary cells S1 and S2 are evident. Secondary triple points form in overdriven detonation and these structures have their minor transverse waves and Mach stems. Minor pocket formation behind S1 and S2 confirms their triple point structures and interaction. The transverse wave interacts with the wall at R1 and moves downstream. In the density gradient contour (Figure 5-13 b), these transverse wave interactions with the reactant pockets are visible.

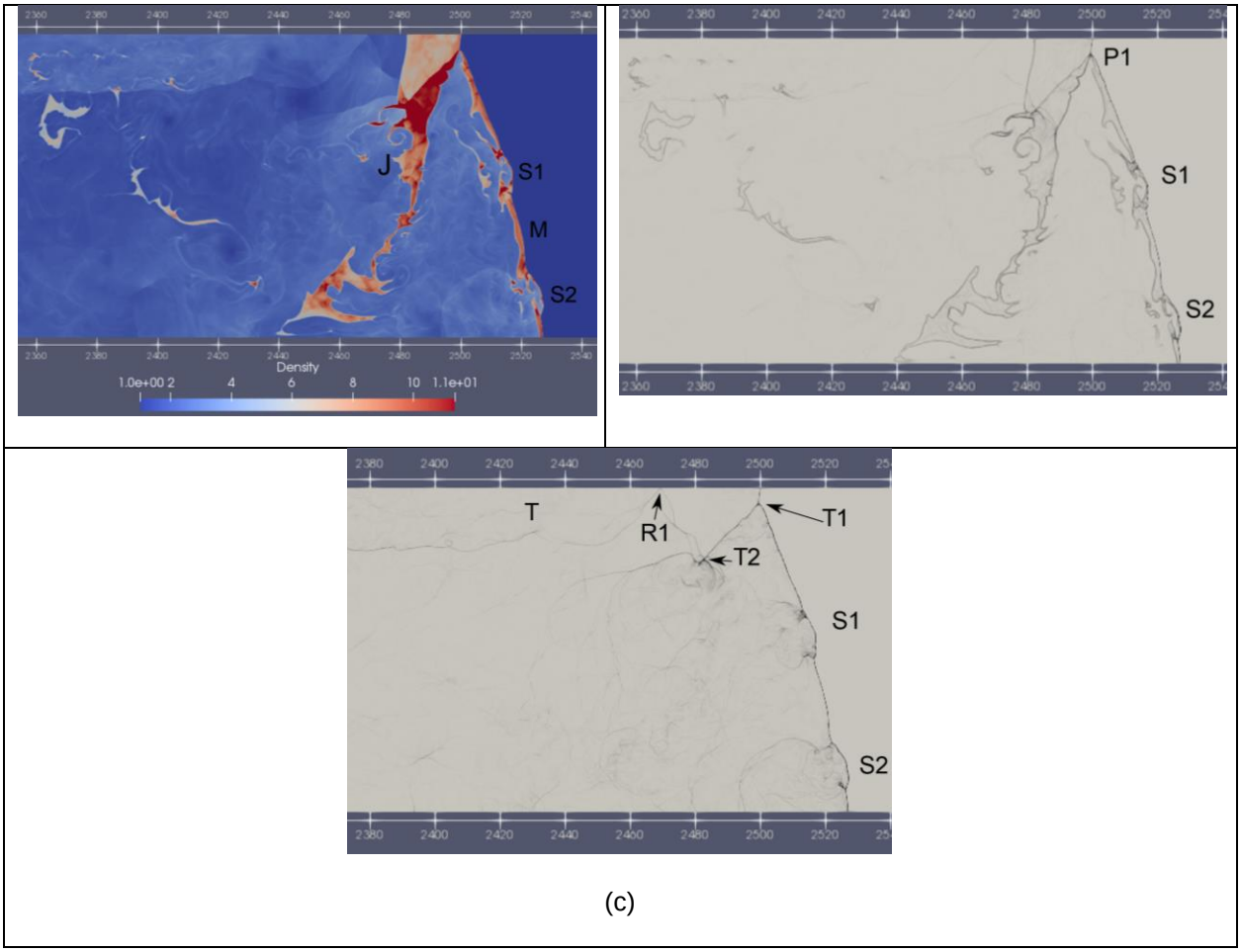

Figure 5-13 Triple point structure of $CH_4 - 2O_2$ Detonation at 3.5 kPa at T=160 (a) Density Contour (b) Density Gradient Contour (c) Pressure Gradient Contour

The structure of the detonation is highly dynamic and shows slight variations in its features for almost every single triple point collision. Two reinitiation events along the upper and lower wall are compared side by side. It is understood from the first observation that, the instantaneous structure-property

varies with position and time. All the contours in Figure 5-14 represent the instantaneous density field. The wall jet in T=44 looks slim and corrugated when compared to the wall jet in T=121. From T=44 and T=121, we can see that the thickness of the wall jet might be proportional to the strength of the previous incident stem but is not conclusive since the wall jet of a T=135 is supposed to be thicker due to the weaker incident shock when compared to T=57. This creates suspicion on the burning mechanism of the wall jet. The thickness of the wall jet potentially influences the extent of penetration of the unburn reactant pockets downstream. The curvature of the shock and the triple point dynamics also varies in comparison.

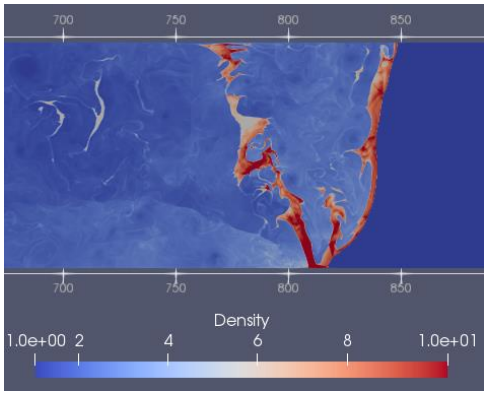

T=44

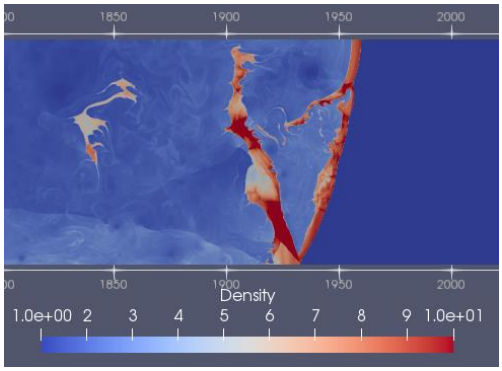

T=121

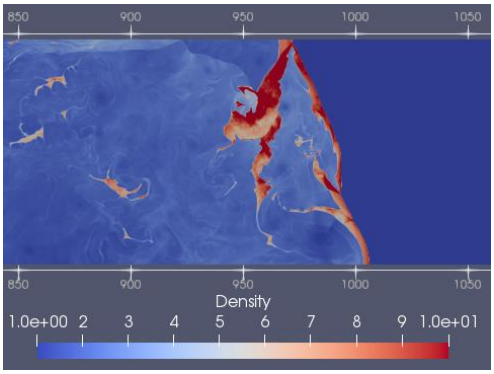

T=57

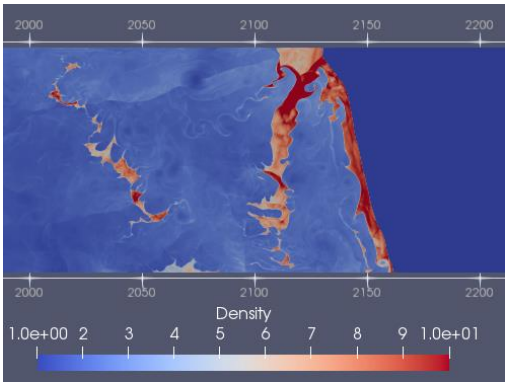

T=135

Figure 5-14 Density Contour of Detonation at Different Events

5.1.6 Local Flow Features Comparison

A brief discussion on visual comparisons with the flow field observed in the experiment of Kiyanda et al. [59] is made in this section to understand the reinitiation mechanism of methane-oxygen marginal

detonation. The following figure (Figure 5-15) shows the experimental results [59] on the left and results from the simulation on the right for comparison.

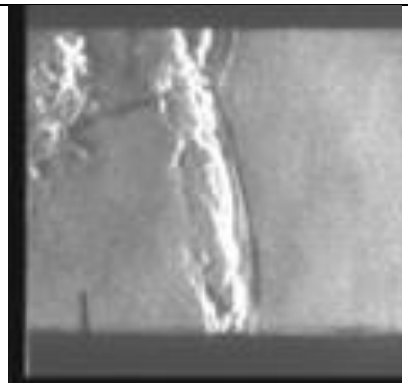

(a)

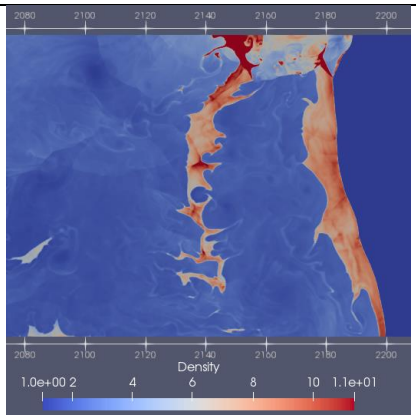

T=138

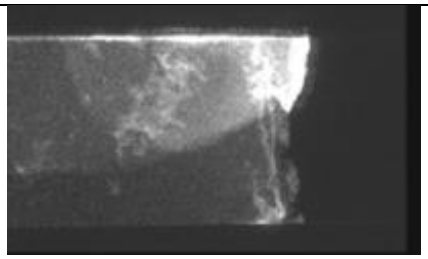

(b)

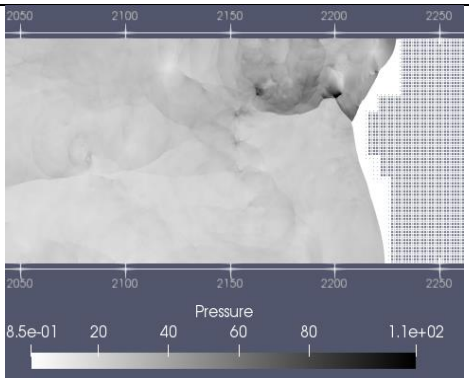

T=140

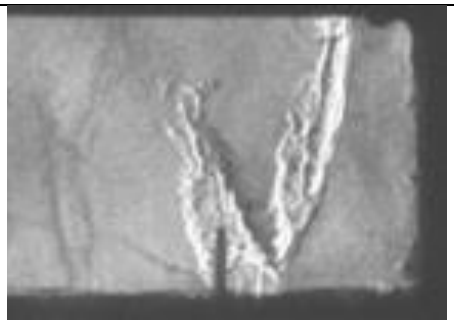

(c)

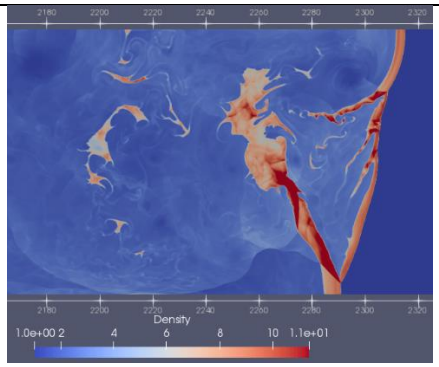

T=145

Figure 5-15 Comparison of Primary Mode of $CH_4 - 2O_2$ Detonation with Experimental Results [58] (a) & (c) Schlieren Image (left) with Density Contour (right) (b) Chemiluminence Image (left) with Pressure Contour (right)

The frame (a) and (c) of Figure 5-15 shows the Schlieren image on the left of experimental results in [59] and density contours from the current study. The Schlieren image illuminates the shear layer and unburnt reactant pockets. The frame (b) shows the self-luminous image reported in the experiment [58] on the left and pressure contour on the right to capture the shockwave dynamics. The frame (a) shows an overdriven shock created on the top wall and moving downwards. The structure of the triple point, the presence of unburnt reactant pocket and its interaction with the transverse wave are the features that can be compared qualitatively. The strong Mach structure as it evolved from the reinitiation and the structure of the transverse wave is shown in the frame (b). The final event of a cell cycle is shown in the frame (c), where the triple point is about to collide with the bottom wall. The jet is thicker in the experiment and a bifurcation in the Mach stem is noticeable in the density contour of the simulation. Thicker jets were also observed in simulation as shown in T=121 of the figure. The collision between minor triple points creating local explosions has been reported in various literature [47, 60, 39]. This explosion was identifiable in a sequence using pressure contours as shown below. In frame (a), the two minor triple points traveling towards each other collide in the frame (b) and results again in two separate minor triple points moving in the opposite direction in the frame (c). The structure of the transverse wave attached to the minor triple point is also a strong structure with the presence of a secondary triple point. Gamezo et al. [49] validated and recorded the increase in the magnitude of pressure behind triple points with an increase in high activation energy using numerical simulation.

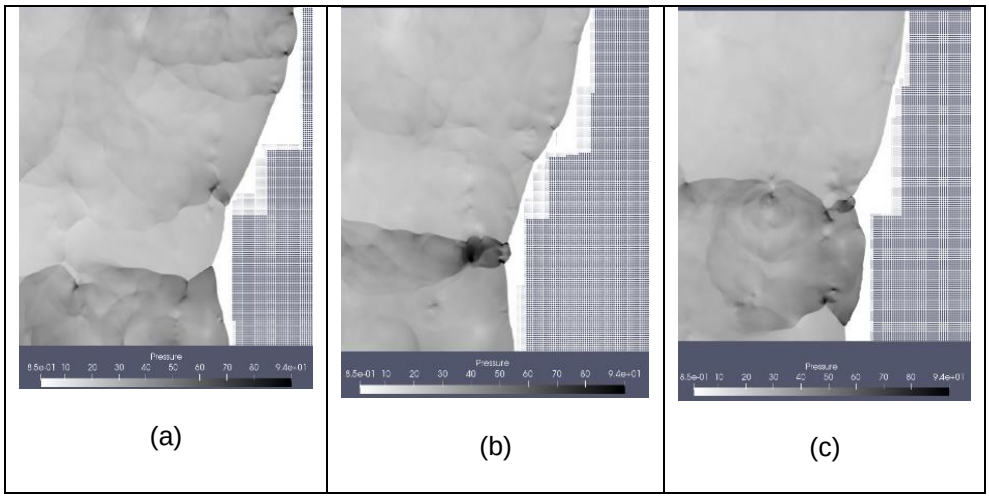

Figure 5-16 Pressure Contour Sequence of Reinitiation with Secondary Modes (a) Approaching (b) Colliding (c) Reinitiation

A similar localized explosion has been observed due to modal interactions in methane-oxygen detonation at low pressure in the experimental work of Radesculu et al. [60]. Further experimental investigation [47] of highly irregular detonation based on propane air showed evidence of this micro explosion which has been reproduced below for comparison.

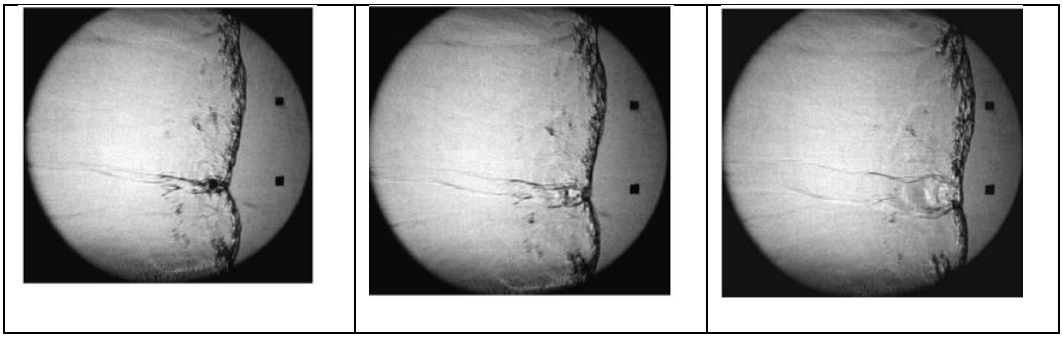

Figure 5-17 Event of Micro-Explosion Recorded for Propane based Detonation by Austin [47]

A good similarity between the collision events of minor triple points is seen between the figure above and the pressure contours (Figure 5-16) obtained from this study. The survival of minor triple points is essential for the self-sustaining propagation of the detonation as will be demonstrated in the 6kPa initial pressure case in this chapter.

5.1.7 Reinitiation Mechanisms

Understanding the reinitiation mechanism in a self-sustained highly unstable detonation is the priority of this chapter. Only the repeating reinitiation mechanisms are considered in this section. Depending

upon the strength of the triple point during reinitiation, either a triple point reinitiation mode or Mach reflection reinitiation mode is observed. The following set of events is represented using the product scalar contour where the value of 1 represents the completion of reactant along with pressure gradient contour overlapped on it to determine the position of the shock structure and the instabilities present on it. An event demonstrating the triple point reinitiation cycle is shown below.

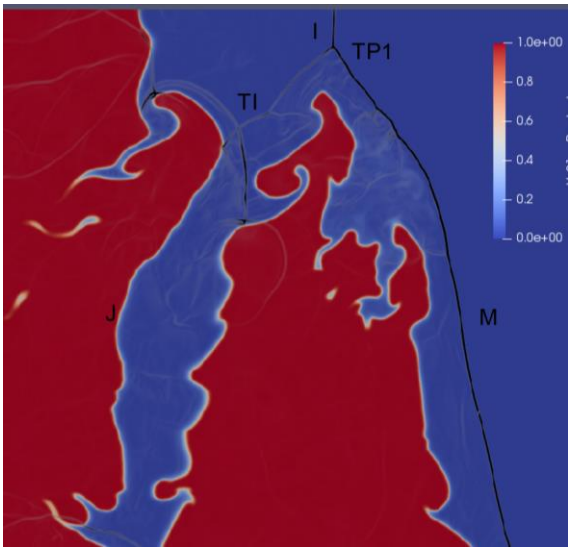

T=136

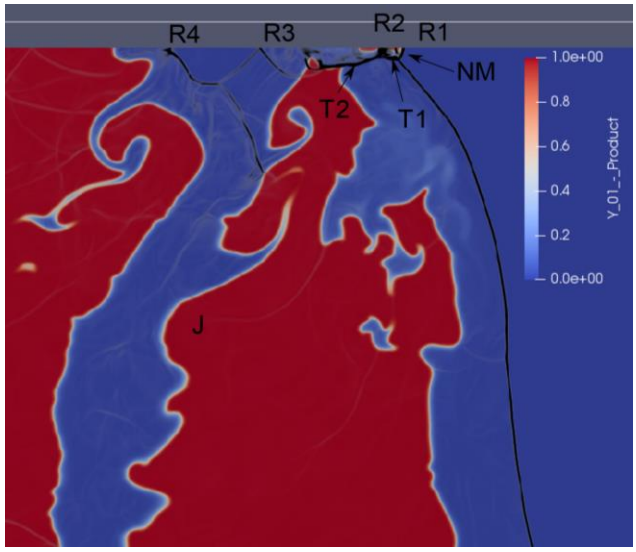

T=137

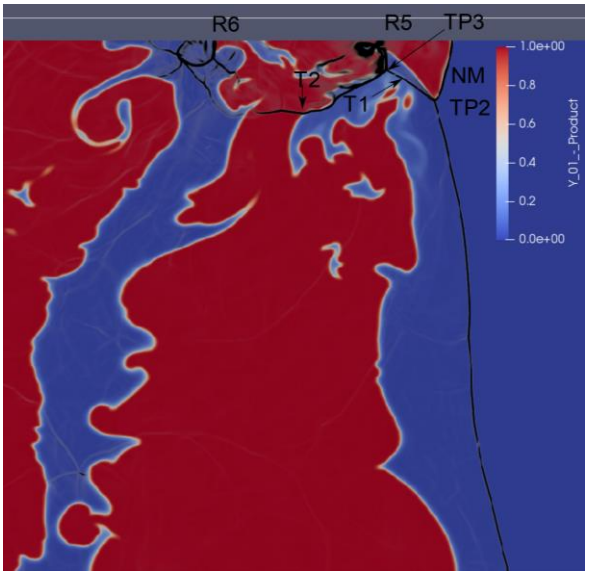

T=138

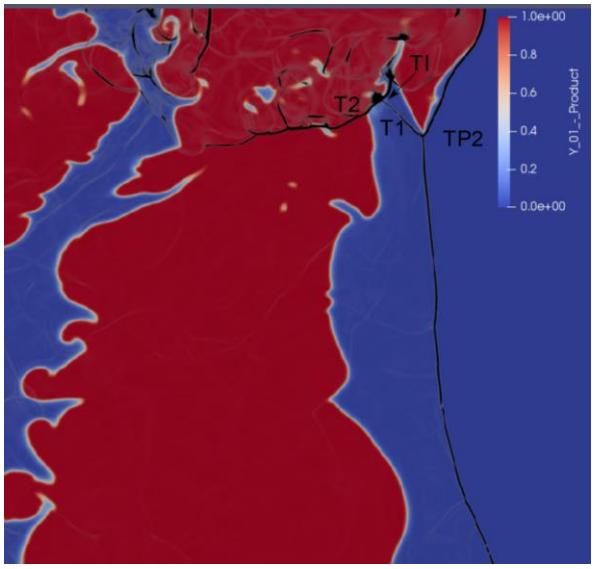

T=139

Figure 5-18 Triple Point Reintiation Event of $CH_4 - 2O_2$ Detonation at 3.5 kPa at from T=136 to T=139

At T=136 (Figure 5-18), the triple point TP1 approaches the top wall. The transverse wave interaction in the jet behind the Mach stem is labeled as TI. As the triple point collides with the top wall, a new Mach stem is initiated which contacts the wall at R1. The second triple point of this strong structure is formed along the wall at R2. The flame flowing the triple point TP1 is not responsible for the energy release supporting the new Mach stem. Localized shock-induced combustion is initiated behind R1 and at R2 at T =137. The structure of the triple point formed at this time step is a strong structure, clearly displaying the second triple point at the intersection of the transverse waves T1 and T2. The complex transverse wave structure is formed behind T2 because of the interaction of the transverse wave interaction TI from the previous cycle along the top wall at R3 and R4. Evidence of diffused coherent structures is visible along with the inner layer of the forward jet J. This new Mach stem gives rise fully formed to new triple point TP2 and the second triple point TP3 at T=138. Two regions of the hot spot, which do not actively take part in this reinitiation are seen behind the transverse wave T1. The transverse wave structure T1-T2 has become the interacting transverse wave system (TI) inside the forward jet J in T=139. The Mach stem has grown to be self-sufficient with its triple point TP2. The wavelets from the interaction of transverse wave system (TI) with the wall are scattered along with weak transverse waves still visible but weak inside the pocket of unburnt reactant which drifts further downstream. An additional influence for favoring this triple point reinitiation mode is due to the presence of minor triple point instability along with the shock wave. This scenario is shown in the triple point reinitiation sequence below.

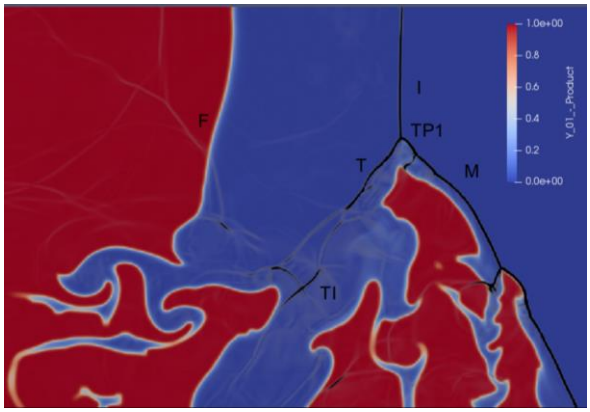

T=81

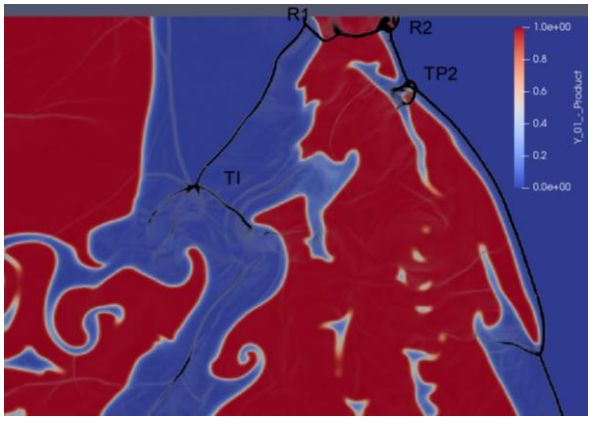

T=82

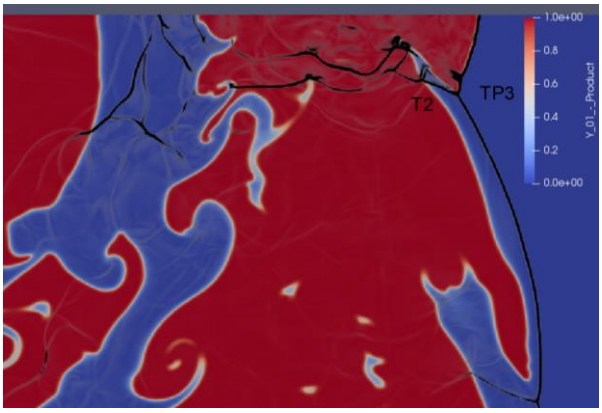

T=83

Figure 5-19 Triple Point Reintiation Event of $CH_4 - 2O_2$ Detonation at 3.5 kPa at from T=81 to T=83

In the diagram above, the triple point TP1 approaches the top wall for reinitiation as in the previous case at T=81. The forward jet is thicker compared to the previous scenario at T=136 with similar transverse

wave interaction system TI. After the triple point reflection of TP1 along the wall at T=82, triple point reinitiation is observed at R2. Additionally, a minor triple point TP2 which was following the triple point TP1 collides at T=82, increasing the strength of the Mach stem. The newly formed Mach stem now propagates with triple point TP3 at T=83. These additional secondary cells interact with newly created triple points during reinitiation and either amplify the detonation or destabilize the detonation. In this case, the collision amplifies which can be noted by very thin induction thickness. The destabilization effect will be shown in the Mach reflection reinitiation scenario. Three different modes for Mach reflection reinitiation was observed, the first reinitiation with the influence of the forward jet on the decoupled flame following the incident shock, the second reinitiation is with the influence of the forward jet on the hot spot alone and the third reinitiation shows the effect of the forward jet both on flame and a hot spot for reinitiation. In the following diagram, we see that the triple point as reflected off the wall but has not ignited the reactants behind it at T=58. This is the first evidence of a weak reflection. The flame has reached the wall and is moving in the direction of the new Mach stem M by the influence of the flow profile created by the reflected transverse wave. One the secondary triple point moves further from the wall, the influence of the jet is now to transport the flame on the heated reactants, behind the Mach stem M, in a rotational fashion. This rolled-up flame favors the Mach stem reinitiation when it couples and syncs with the moving motion of the triple flame as shown in T=59. In the same instance, the transverse wave system TI has developed and sweeps along the forward jet. The formation of overdriven Mach stem is shown at T=60 in the following figure after a successful reinitiation.

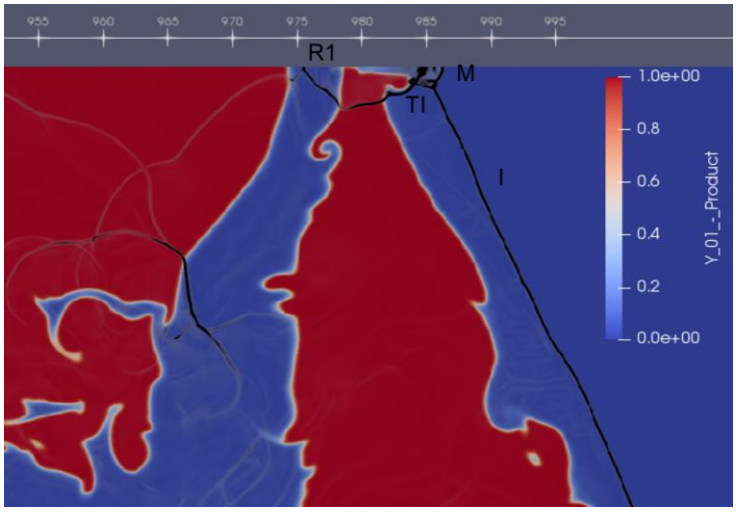
955
960
965
970
975
980
985
990
995
R1
M
TI
I
1.0e+00
0.8
0.6
0.4
0.2
0.0e+00
Y_01_-_Product

T=58

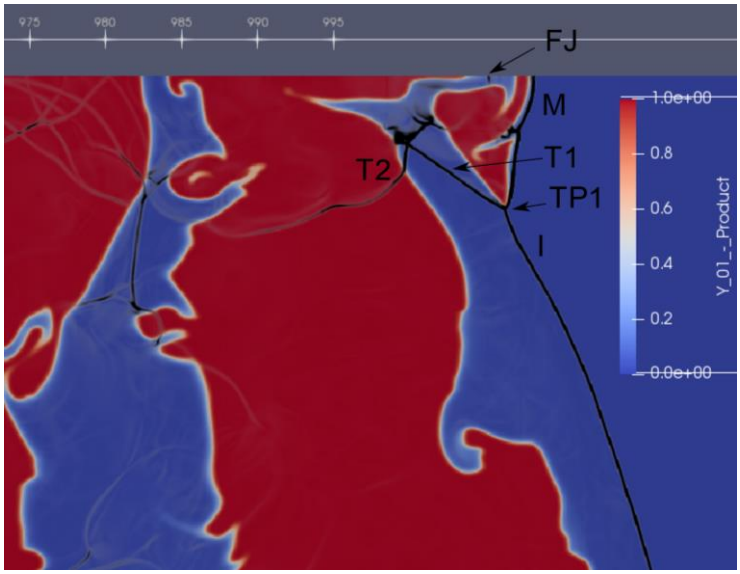
975
980
985
990
995
FJ
M
T1
T2
TP1
I
1.0e+00
0.8
0.6
0.4
0.2
0.0e+00
Y_01_-_Product

T=59

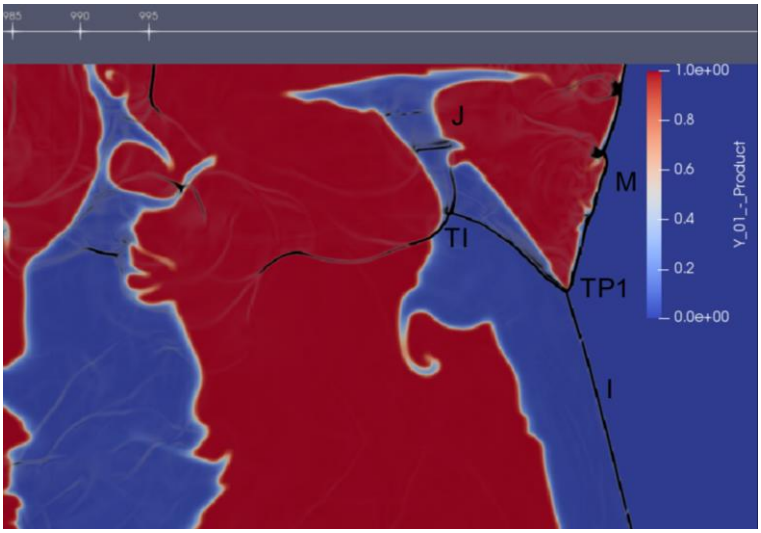

T=60

Figure 5-20 Mach Reflection Reintiation (Slipline-Flame) Event of $CH_4 - 2O_2$ Detonation at 3.5 kPa

The influence of the forward jet is shown below using streamline plots overlapped over the product contour. The following diagram (Figure 5-21) shows the streamlines of the velocity vector in the stationary frame of reference which is the path taken by the reactant particles entering the flow field behind detonation. The streamlines at T=58 show that the flow field behind the detonation front is highly inclined. The particles diverge towards the left at the reflection point R1 on the upper wall. The influence of the forward jet is felt only before the point R1. The forward jet is only at its incipient state. The movement of the flame behind R1 is also influenced by the growing transverse wave towards the right which can be seen by the curved streamlines behind the point R1. At T=59, the separation point is clear since the transverse wave as moved further from the wall.

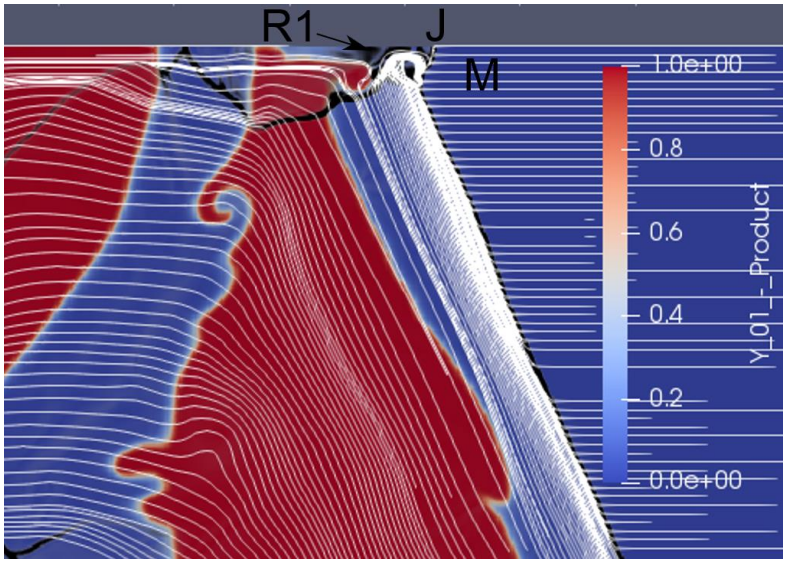

T=58

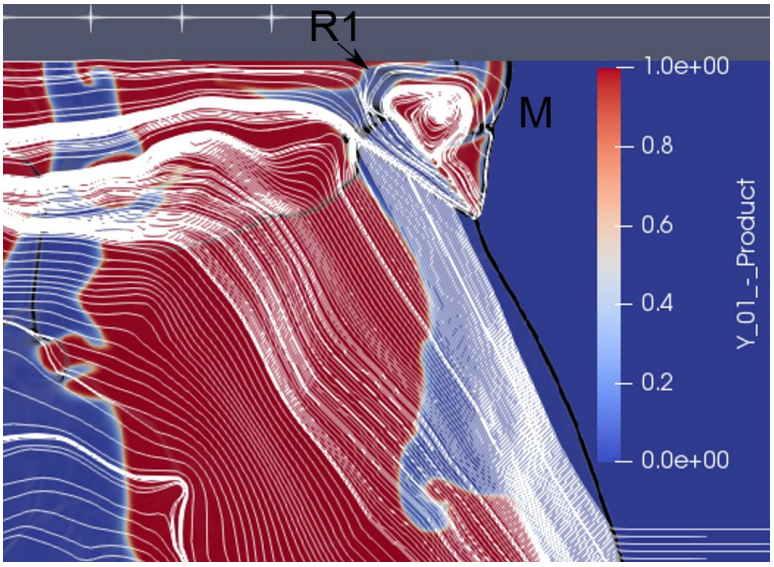

T=59

Figure 5-21 Evolution of Flow Field in Stationary Reference Frame Visualized Using Streamline Plot of Case A

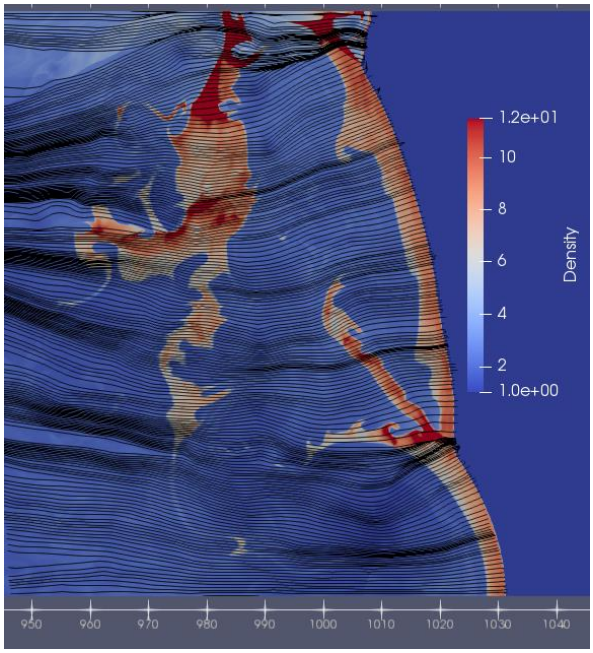

Figure 5-22 Flow Field Visualized in Moving Reference Frame Using Streamline Plot of Case A At T=59

The streamlines of the moving column of gas in the laboratory frame of reference shown at T=59 above (Figure 5-22). The curvature of the shock front and the oscillatory motion of the bulk motion of the gas behind determines on the trajectory of the reactant particles entering the detonation. The next sequence of contours shows the reinitiation through a hot spot alone. The triple point TP1 collides with the bottom wall at T=121 and results in a Mach reflection reinitiation at T=122. Three separate hot spots are formed (the region labeled as HS1) behind the incident stem at the same time. The triple points TP2 evolves with a nonreactive Mach stem at T=123. We can also see the hotspots in the regions coalescence into a single hotspot. The secondary triple point (STP1) and a bifurcation (B) in the Mach stem are also clear in this Mach reflection since no reacting regions are present. Hot spots begin to form close to the wall at T=124 as the slip line curves forward. The action of this curving slip line transports the hotspot forming a region of products behind the Mach stem. When this product region couples with the primary triple point (TP2) it immediately results in a self-supported Mach stem with the transverse shock system (TI) interacting with the forward jet. This reinitiation mode does not involve the convection of the decoupled flame from behind.

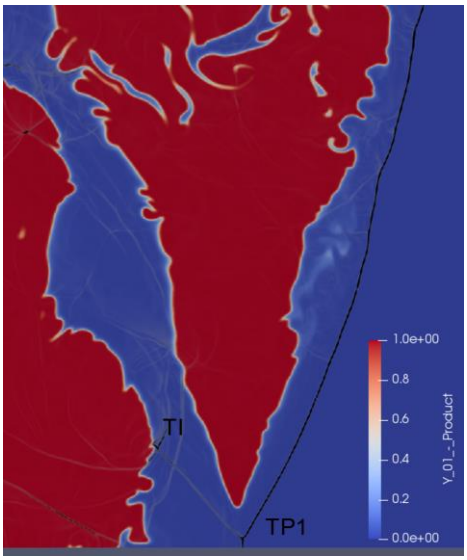

T=121

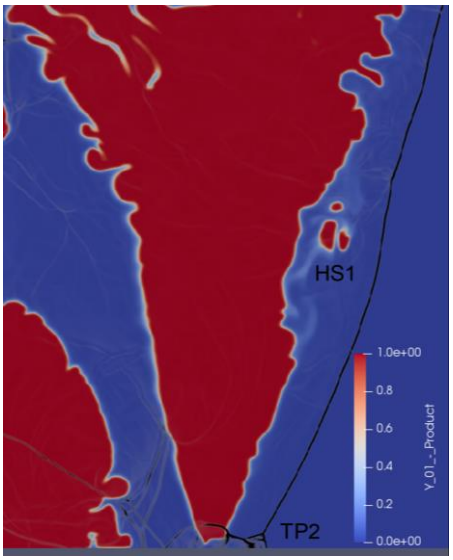

T=122

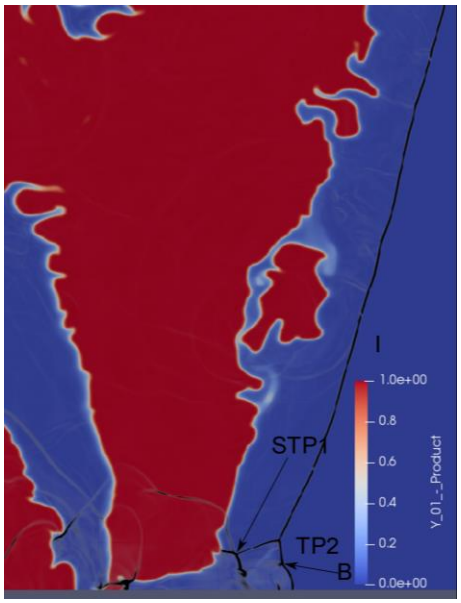

T=123

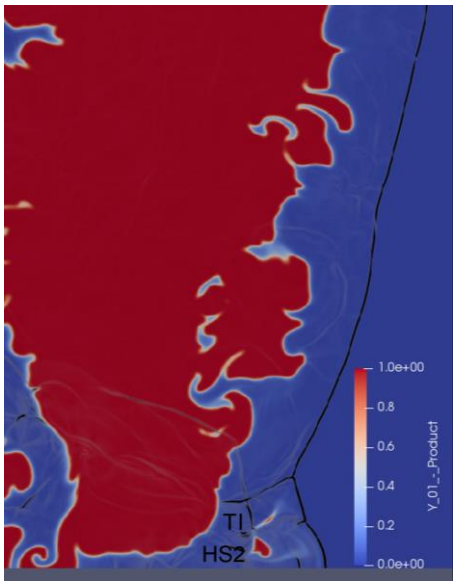

T=124

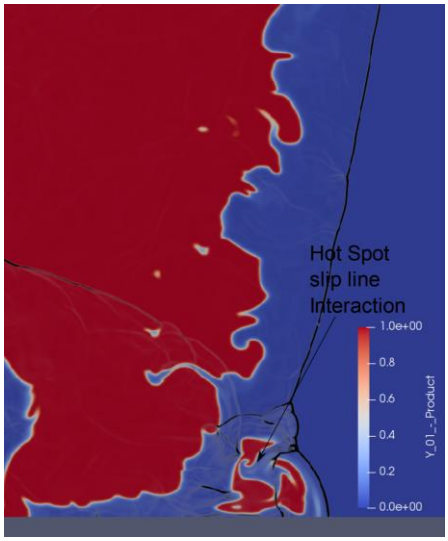

T=125

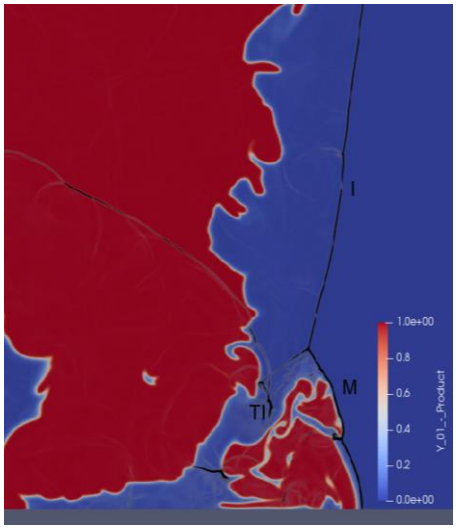

T=126

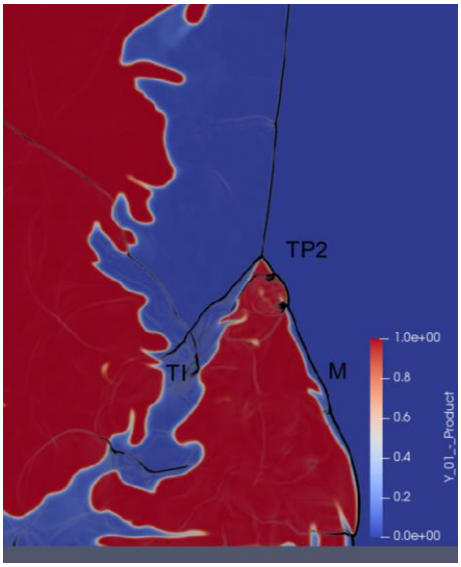

T=127

Figure 5-23 Mach Reflection Reintiation (Slip line-Hotspot) Event of $CH_4 - 2O_2$ Detonation at 3.5 kPa

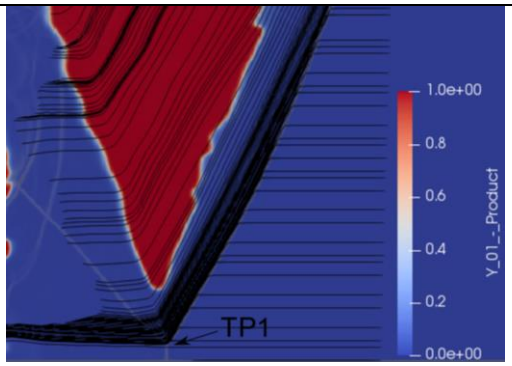

T=121

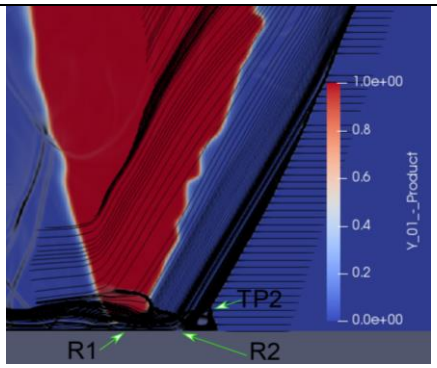

T=122

Figure 5-24 Evolution of Flow Field in Stationary Reference Frame Visualized Using Streamline Plot of Case A at T=121 & T=122

The above diagram (Figure 5-24) shows the streamline plot of the triple point collision for the above sequence of reinitiation. At T=121, the triple point TP1 is yet to collide with the wall. At T=122, the triple point has collided with the wall and has resulted in a Mach reflection reinitiation mode. The flow profile behind this Mach reflection is to be noted carefully. The flame which was following the triple point TP1 collides with the wall at R1 and the streamlines behind the detonation front collide the wall at R2. The flow profile is clearly towards the left after the point R2. Hence the flame is not influenced by the curved slip line as it happened in the previous reinitiation case. Finally, the reinitiation mode where both the decoupled flame and hotspots are initiated are shown in the following sequence. At T= 69, the triple point travels towards the bottom wall. The influence of KH instability structures can be seen along the inner side of the jet attached to this triple point. The triple point reflection results in a Mach reflection type reinitiation at T=70. The transverse wave system has moved further from the wall and the flame which was following the triple point is influenced by the curved slip line towards the Mach stem M. As the flame F is swept in, a hot spot H1 is formed in the vicinity of the triple point TP1. Before this flame is engulfed, another separate hot spot H2 is formed at the core of the vortex formed by the curved slip line at T= 72. A bifurcation of the Mach stem M is also visible. As the slip line acts to form the region of products to couple with the triple point TP1, a triple point collision occurs between an approaching triple point, which has completely decoupled from its flame, labeled as TPC at T=73. This collision (TPC) creates its hot spot H3 at T=74 and the slip lines attached to the triple point influences the flame which was following TP1. At T=75, the influence of the

curved slip line has resulted in the reaction zone capable of supporting the new Mach stem (NM) which proceeds to grow with its own set of triple point TP2, transverse wave system TI and forward jet at T= 76.

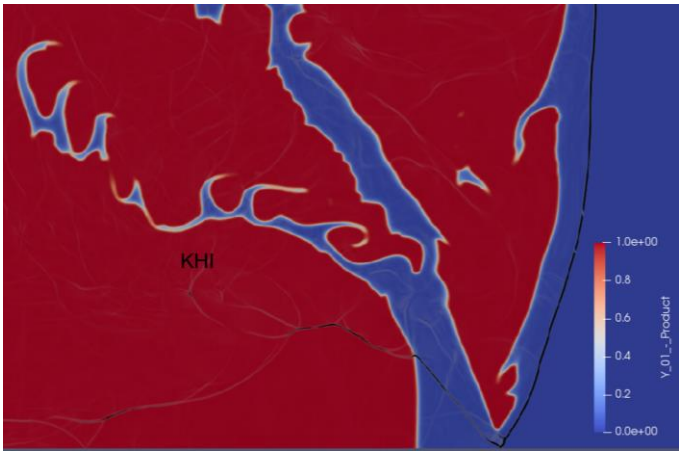

T=69

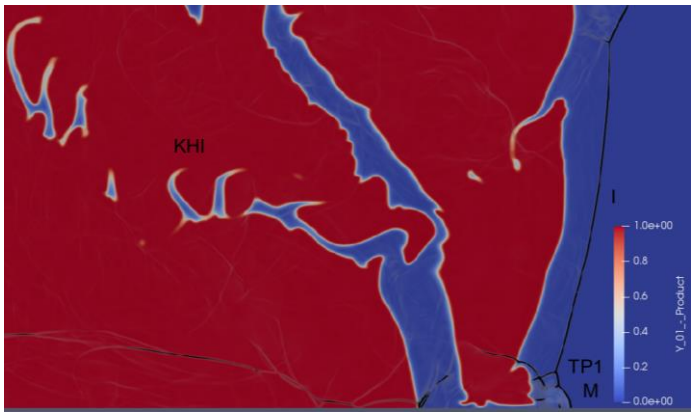

T=70

T=71

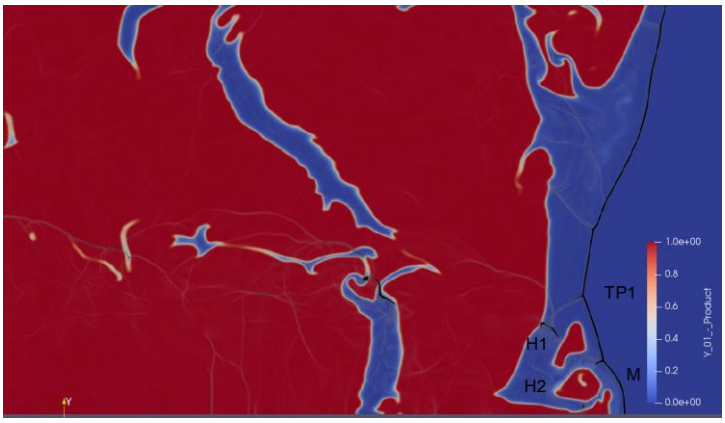
TP1
H1
H2
M
1.0e+00
0.8
0.6
0.4
0.2
0.0e+00
Y_01_-_Product

T=72

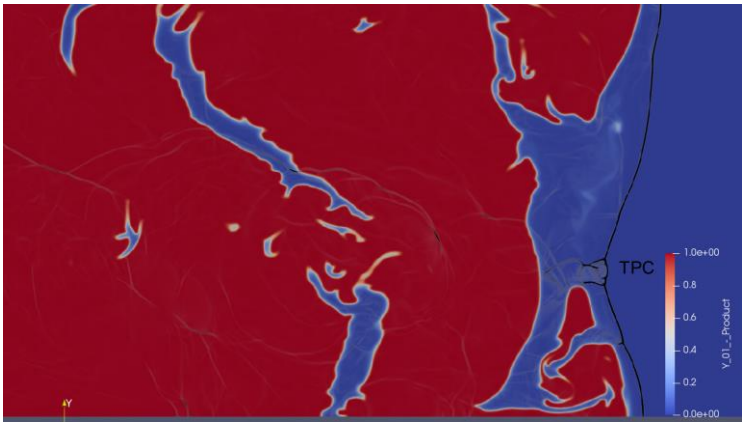
TPC
1.0e+00
0.8
0.6
0.4
0.2
0.0e+00
Y_01_-_Product

T=73

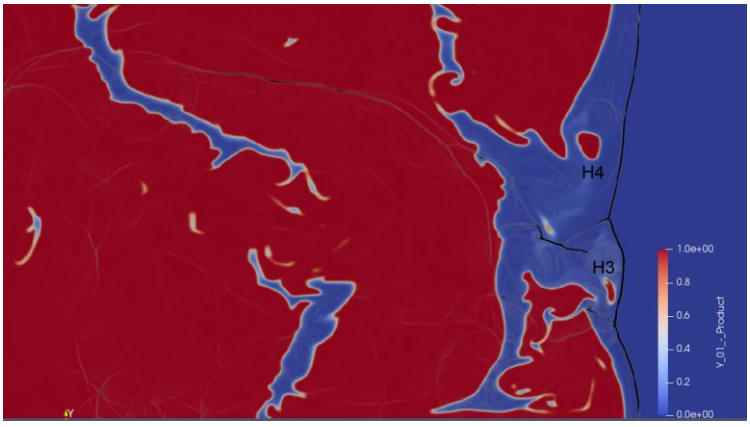
H4
H3
1.0e+00
0.8
0.6
0.4
0.2
0.0e+00
Y_01_-_Product

T=74

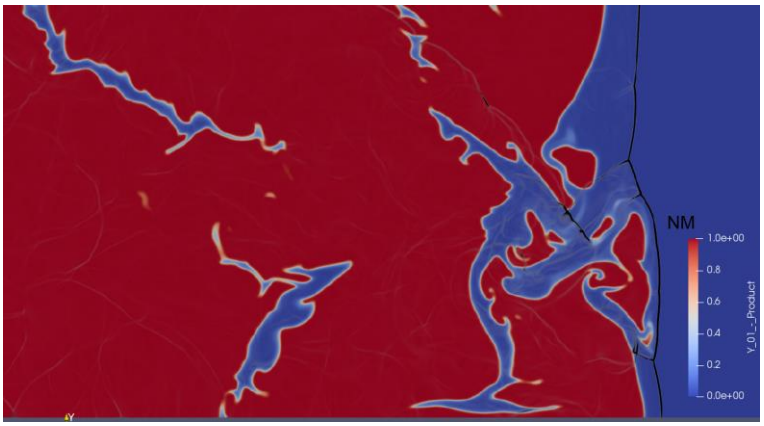

T=75

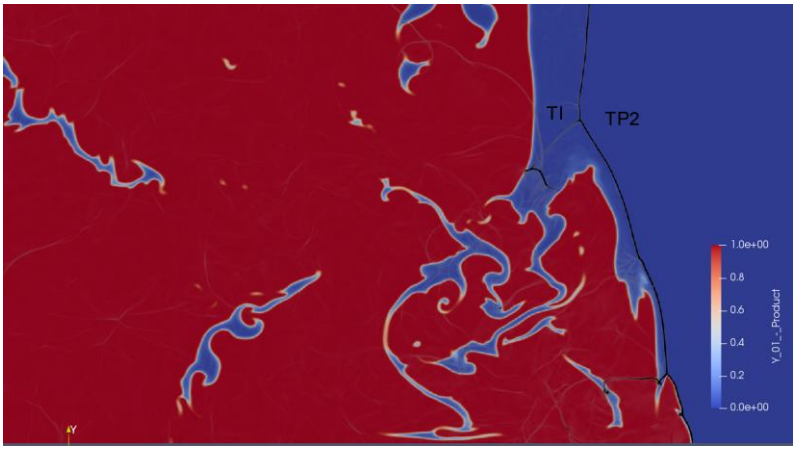

T=76

Figure 5-25 Mach Reflection Reintiation (Slip line-Flame-Hotspot) Event of $CH_4 - 2O_2$ Detonation at 3.5 kPa at from

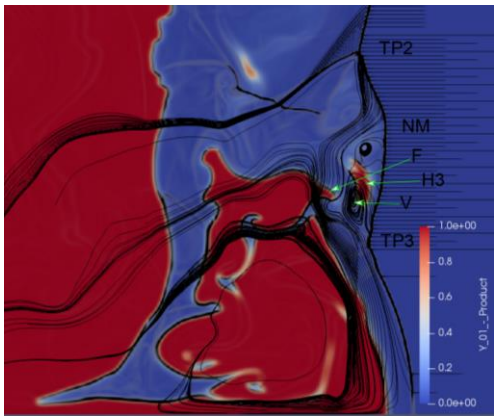

Figure 5-26 Flow Field Visualized in Stationary Reference Frame Using Streamline Plot of Case A at T=74

Figure 5-26 shows the influence of the slip line on the reaction zone. The vortex V influence both the flame F as well as the hot spot H3 to form the product region behind the Mach stem (NM) at T=75 in Figure 5-25. The reinitiation modes of case A by both triple point collision and Mach reflection have been explained in this section. In the following section, the intermodal reinitiation is studied. The similarities between marginal detonation as in case A and ordinary detonation in case B are also studied.

5.2 Case B-Dual Mode Detonation

The thermodynamic parameter for 6 kPa initial pressure was determined for stoichiometric oxymethane detonation with the same procedure used for 3.5 kPa and is shown below. Only a slight deviation of the parameters from its 3.5 kPa counterpart is noticed.

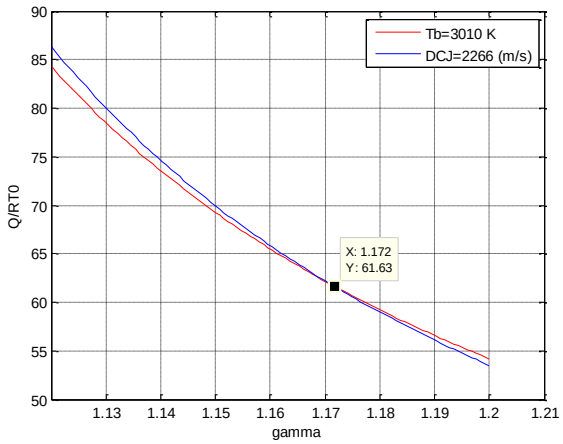

Figure 5-27 Plot to Determine Thermodynamic Properties for $CH_4 + O2$ Detonation @ 6 kPa

5.2.1 Detonation Front Velocity Profile

The instantaneous detonation velocity along the bottom wall is shown for 6 kPa case along with its mean value compared with the average experimental value [44].

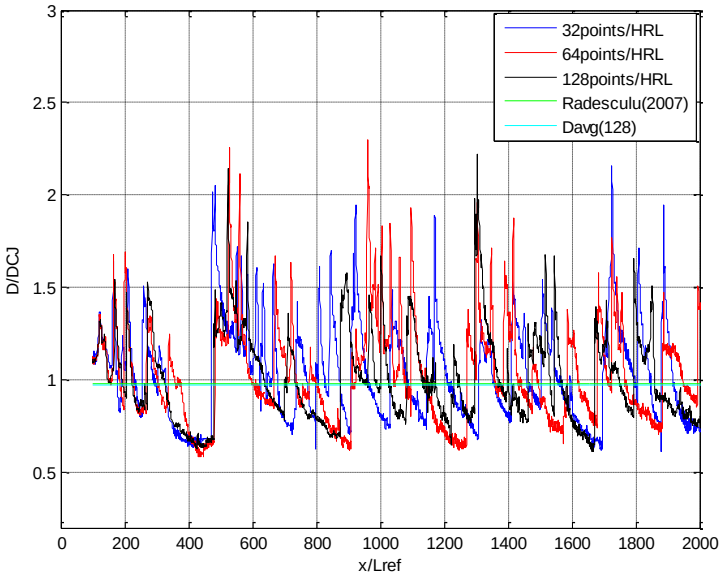

Figure 5-28 Instantaneous Detonation Front Velocity Profile Comparison of $CH_4 - 2O_2$ Detonation at 6 kPa

The mean detonation velocity ratio (D/D_{CJ}) converges and agrees well with the experimental value. Highly irregular pattern is observed again as in case A. The peak velocity is close to $2.2D_{CJ}$ and the lowest velocity is close to $0.6D_{CJ}$, which is very close to the velocity observed in critical deflagration [144]. By the criteria of Fickett et al., this average velocity can be categorized as an ordinary detonation (D/D_{CJ}~1).

Table 5-5 Mean Velocity Ratio of of $CH_4 - 2O_2$ Detonation at 6 kPa

Case-B	32	64	128	Error %	Experimental Value [44]
Inviscid – Global One Step	0.981	0.973	0.962	1.7%	0.979

The shift in the instantaneous velocity measurement profile of detonation with grid resolution is also observed in case B. The following figure is a comparison of the numerical soot foil with 64 points/HRL and 128 points/HRL. The soot foil with 128 points per HRL shows the shift in the track of detonation due to additional secondary cells getting resolved and the dynamics between them. The detonation propagates with one primary triple point for the first six reinitiation before shifting to a dual-mode detonation. Each

interaction with the corresponding set of secondary cell tracks is highlighted with green line brackets. We see that these brackets expand and move further when additional modes of instability are solved.

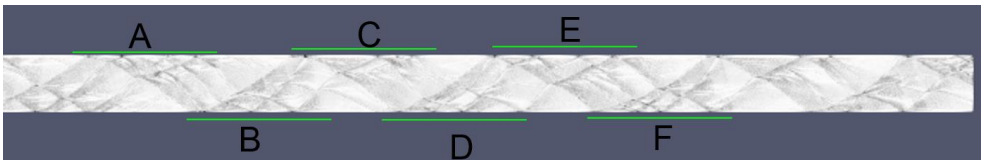

(a) 64 Cells/HRL

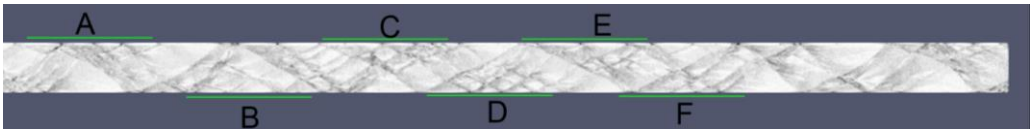

(b) 128 Cells/HRL

Figure 5-29 Numerical Soot Foil Comparison of $CH_4 - 2O_2$ Detonation at 6 kPa (a) 64 Cells per HRL (b) 128 Cells per HRL

The following chart shows the probability density function of the instantaneous velocity with 128 points per HRL. The PDF peaks approximately at a velocity ratio of 0.82 showing that though the unstable modes increase along the shock front, the detonation still spends a maximum fraction of its time decaying within a cell cycle.

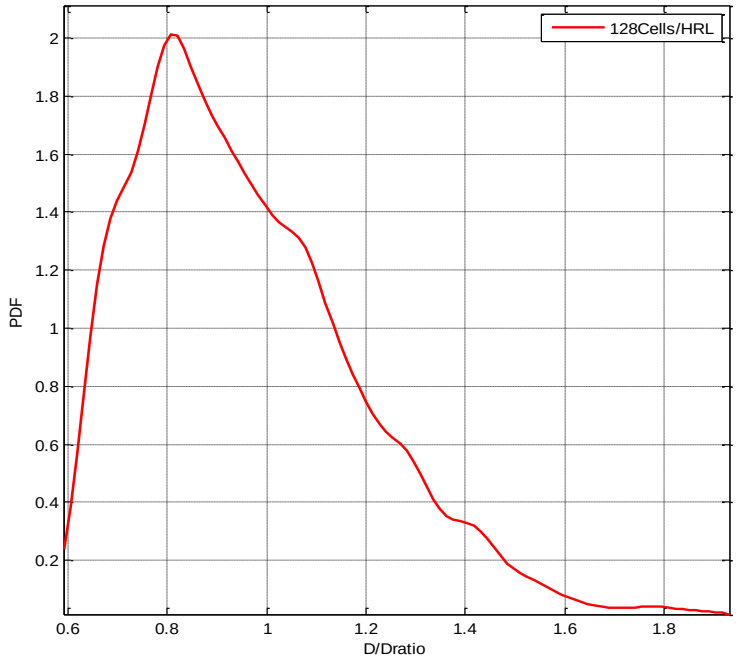

Figure 5-30 PDF of Instantaneous Velocity Ratio of $CH_4 - 2O_2$ Detonation at 6 kPa

5.2.2 Favre Averaged Profile Comparison

The Favre averaged flow profile from the two-dimensional inviscid one-step chemistry is compared with the values obtained using the steady state ZND value and was found within an overall error of 12%.

Table 5-6 Comparison of Favre Averaged Flow Profile With ZND Results for $CH_4 - 2O_2$ Detonation at 6 kPa

Flow Variable	ZND Value	Favre Averaged Value	Difference	Unit
Pressure	151283	155934	3%	Pa
Temperature	3224	3585	11.2%	K
Density	0.114	0.115	0.8%	kg/m^3
Velocity	1267	1177	7.1%	m/s
Average Sonic Plane	0.637729	14.5	-	cm
Reactant Mass Fraction (Theoretical)	0	0.70	-	-
Reactant Mass Fraction (Favre Averaged)	0	0.03	-	-

For both the 3.5 kPa and 6 kPa case, the maximum error in the flow variable manifests in the temperature. The approximation of the constant specific heat constant at constant pressure (c_p) starts to deviate the temperature value from the actual temperature. The Favre averaged reactant mass fraction (0.7) is higher for case B when compared to case A (0.58). The momentum gain due to reaction has not been achieved by these pockets until they combust, increasing the averaged sonic plane distance and deviating further from the theoretical sonic plane.

5.2.3 Structure of Triple Point

A dual-mode structure of the detonation is shown below in the Figure 5-31. The density contour along with pressure and temperature gradient at the same instant is shown to understand the structure of the triple point formed for oxymethane detonation at 6 kPa. The primary triple point approaching from the top is labeled as TP1 and from the bottom is labeled as TP2. The forward jets attached to TP 1 and TP 2 are named J1 and J2 respectively. The pressure gradient contour shows the secondary triple points (STP 1 & STP2), incident stem and Mach stems (M1 & M2). The transverse wave system (TI1 & TI2) traveling inside the jets J1 and J2 are visible in the temperature gradient contour. The overall triple point structure is similar to the single-mode detonation. Behind the detonation, several pockets of reactants can be found. This explains the reason for the higher Favre averaged reactant mass fraction in the theoretical sonic point for a 6 kPa case than the 3.5 kPa case. The density contour shows the action of transverse waves from triple point TP2 on the detached pocket of the reactant. The reactants are repeatedly acted upon by shockwaves during the beginning and end of a cell cycle, reducing their induction time.

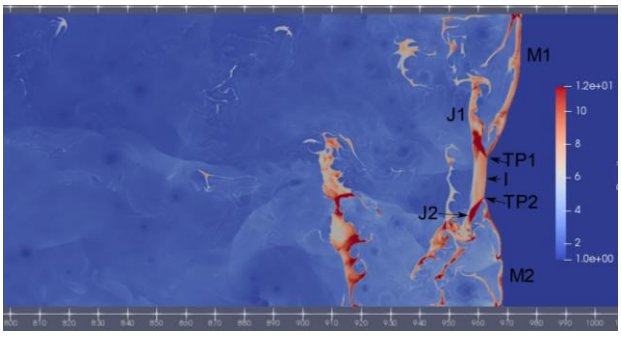

(a)

(b)

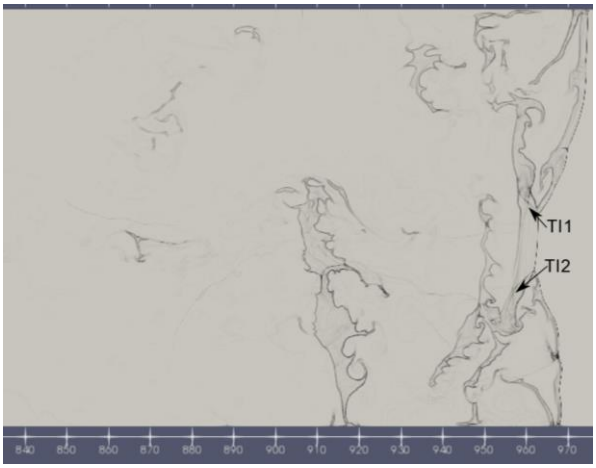

(c)

Figure 5-31 (a) Density Contour (b) Pressure Gradient Contour (c) Temperature Gradient Contour of $CH_4 - 2O_2$ Detonation at 6 kPa

The structure of the jet formed behind the triple points varies significantly and can also be seen between J1 and J2. This structural difference occurs indifference of interaction of triple points along the shock front. One such scenario is shown below in a sequence. The two triple points approaching each other at T=32 collide at T=33 (TPC) (Figure 5-32). Since there is a significant distance between TP1 and the flame following TP1, the flame does not get involved in the collision at T=33. The newly formed triple point TP3 moves past this flame in an overtaking fashion resulting in a merger of two jets (JJ) J1 and J2 at T=34 and T=35.

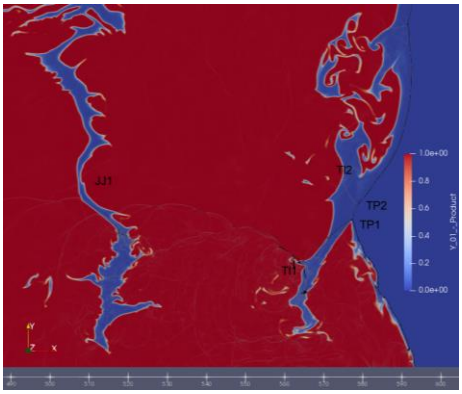

T=32

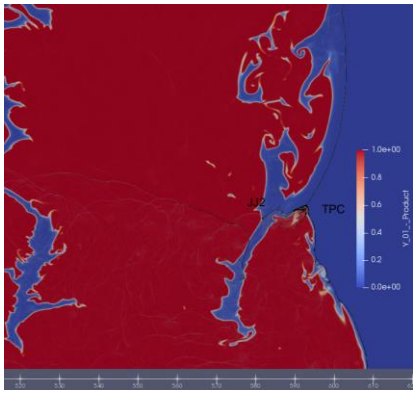

T=33

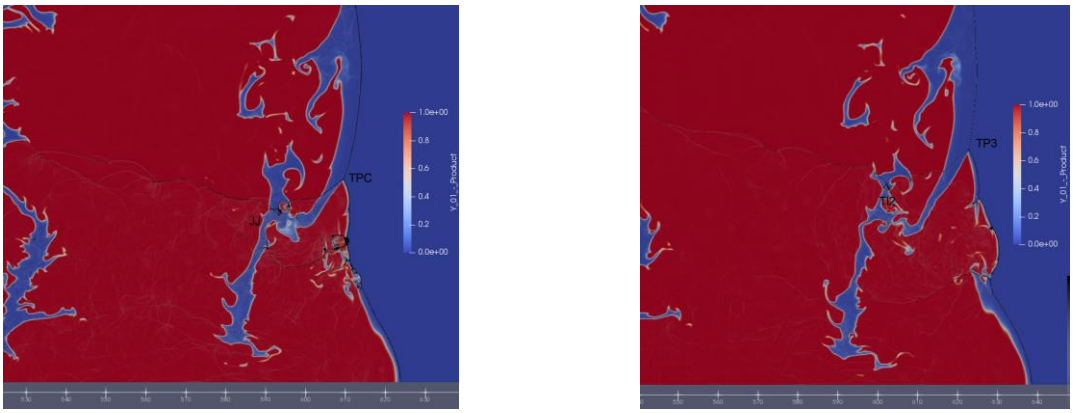

T=34 T=35

Figure 5-32 Product Contour Plots Showing the Formation of a Complex Jet for Case B

5.2.4 Local Flow Feature Comparison

In the experimental configuration [44] which is chosen for the simulation in this study, the detonation was found to operate at single, two and three-mode detonation. Similarly, three primary instability orientations were found to occur in the current simulation. The structure relevant to the schlieren image was captured and the density contour is used for comparison. Figure 5-33 (a) and (b) compares the single primary mode propagation. The bulge in the Mach stem in the lower portion of the Mach stem is due to secondary instabilities. Figure 5-33 (c) and (d) compares dual-mode propagation. The Mach stems and the incident shock are comparable. The size of unburnt pockets, as well as the jets, appear larger in the simulation when compared to experiments. Figure 5-33 (e) and (f) compares the three mode detonation structure. The experiment shows an instant where the two upper triple points have collided whereas in simulation, the triple point TP1 and TP2 are about to collide. The transverse wave structures are prominent in both experiments and simulation.

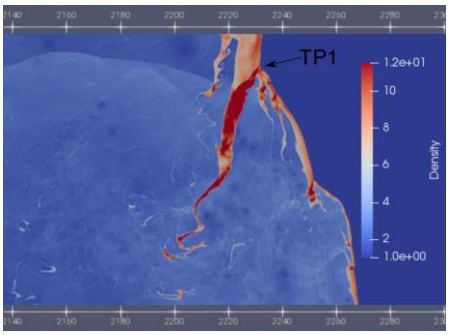

(a)

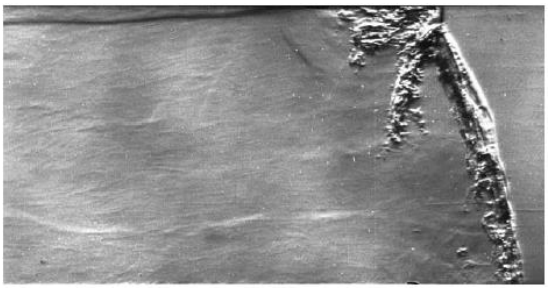

(b)

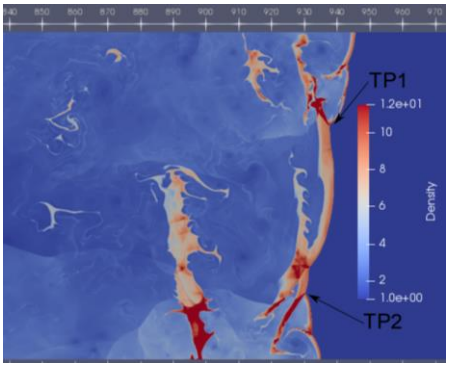

(c)

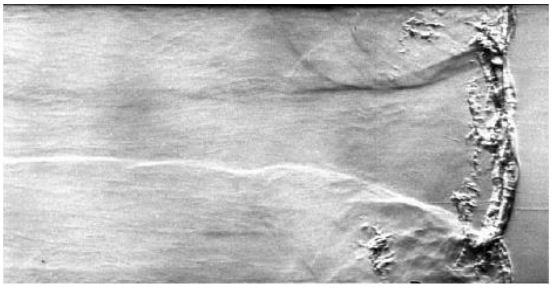

(d)

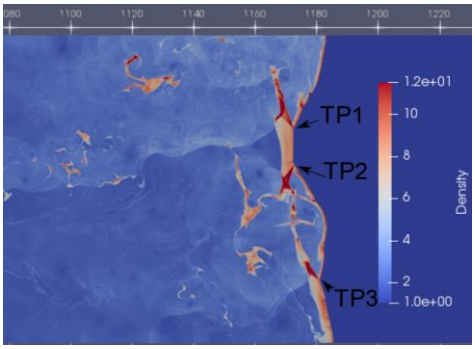

(e)

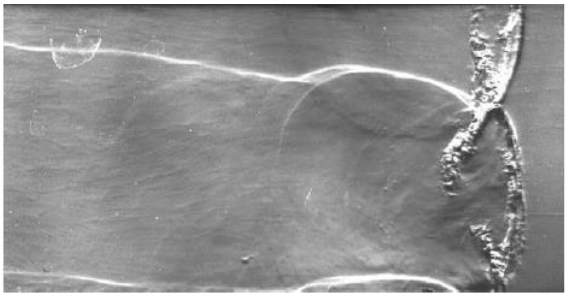

(f)

Figure 5-33 Comparison of Density Contours from Case A with Experimental Schiliren Images [44]

5.2.5 Reinitiation Mechanism

The reinitiation mechanism for 6 kPa occurs with wall triple point interaction as well as internodal interaction. Since the reinitiation mechanism of the triple point collision with the wall has been explained for a stoichiometric methane oxygen mixture for the 3.5 kPa case, only the difference observed in the reinitiation with the wall interface is explained below for brevity.

5.2.5.1 Wall Surface Reinitiation

Along the wall, the same three modes of reinitiation which were observed in the 3.5 kPa were observed to repeat. The difference between case A and case B was the additional influence of secondary triple points on the Mach reflection-based reinitiation. This interaction instantly converts the weak reinitiation into strong reinitiation. All three scenario are explained below. The following set of contours shows a Mach reflection reinitiation based on slip line interaction with the flame is shown below. The contours represent the product mass fraction and each contour is overlapped with its pressure gradient to capture the shockwave position. In Figure 5-34, the triple point TP1 collides with the top wall at T=52 and T=53. The curved slip line influences the flame which was following TP1 and reinitiates the Mach stem at T=54. As the Mach stem begins to grow, an incoming weak, decoupled triple point (ICT) collides with TP2 and amplifies the growing Mach stem at T=56.

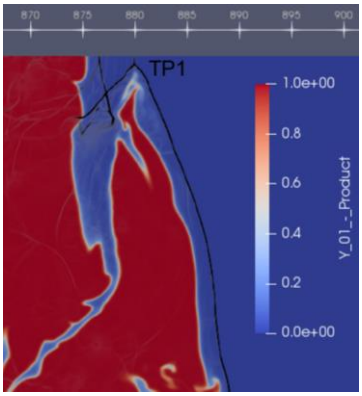

T=52

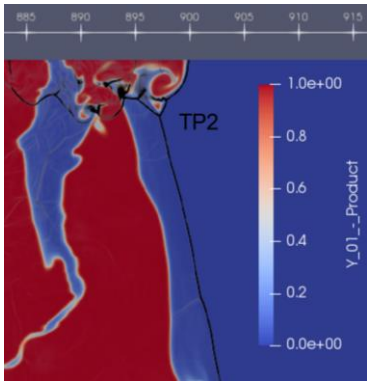

T=53

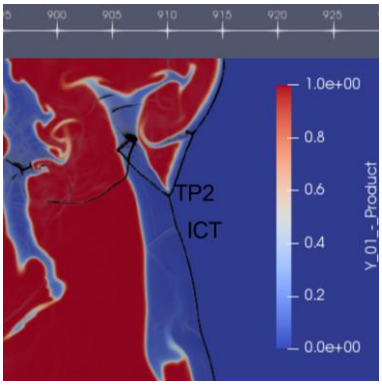

T=54

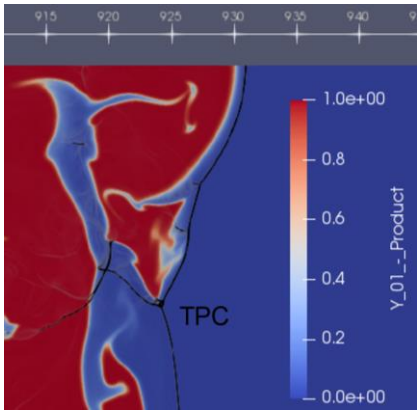

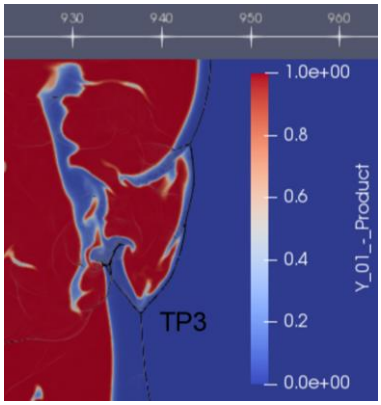

T=55 T=56

Figure 5-34 Mach Reflection Reintiation (Slip line-Flame) Event of $CH_4 - 2O_2$ Detonation at 6 kPa

The following set of contours in Figure 5-35 shows a hotspot based reinitiation. The hot spot (HS1) formed below the triple point TP1 is distributed by the curved slip line (S&HSI) at T=191. As the recoupling process is progressing, an incoming triple point (ICT) collides with TP1 (TPC) and gives rise to its Mach stem at T=192. This Mach stem (M) now travels as an overdriven detonation with secondary cells at T=193.

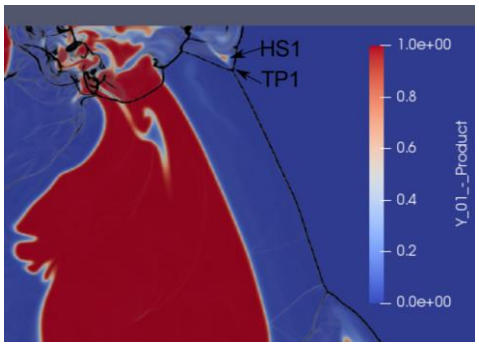

T=190

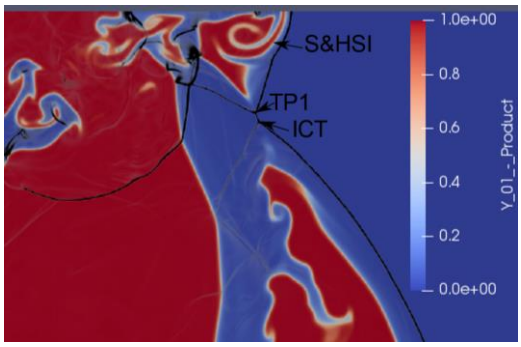

T=191

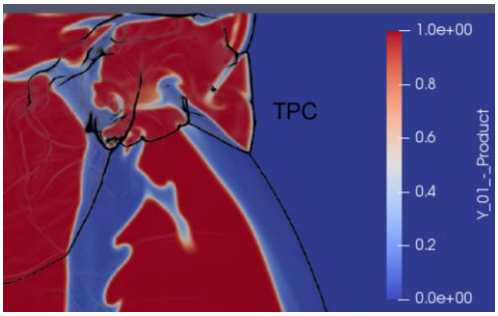

T=192

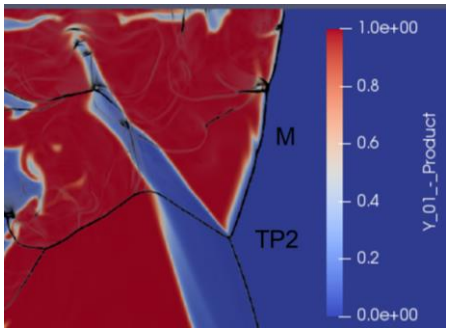

T=193

Figure 5-35 Mach Reflection Reintiation (Slip line-Hotspot) Event of $CH_4 - 2O_2$ Detonation at 6 kPa

5.2.5.2 Internodal Reinitiation

In this section, the reinitiation based on two primary triple point interaction is studied. Both the triple point collision reinitiation and Mach reflection reinitiation modes are observed through internodal reinitiation also. In the following set of contours in Figure 5-36, we see two primary triple points TP1 and TP2 approaching each other at T=157. The collision leads to triple point reinitiation of a reacting Mach stem (M)

with no additional support from any slip line at T=158. Triple points TP3 and TP4 of the Mach stem M travel in the opposite direction after the collision, forming a new cell cycle.

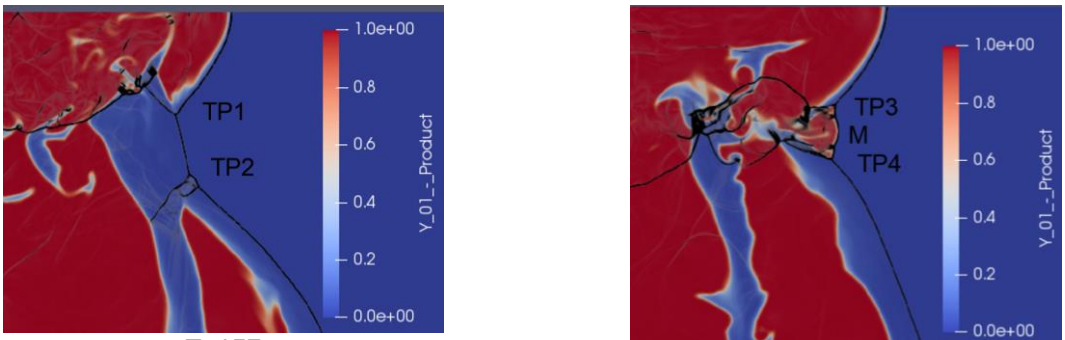

T=157 T=158

Figure 5-36 Internodal Triple Point Reintiation (Slip line-Flame-Hotspot) Event of $CH_4 - 2O_2$ Detonation at 6 kPa

The following contours show a sequence of Mach reflection-based reinitiation. As the two triple point approach each other at T=45 and collides with each other (T=46) due to the asymmetry in the structure of the detonation front, the slip line resulting from the nonreactive Mach reflection attracts the flame F1 as it is formed. This flame is distributed by the slip line attached to TP3-TP4 and a Mach stem is initiated at T=47. The incoming triple point collides with TP3 and creates its Mach stem labeled as TPC2 at T=48. This structure evolves further into a Mach stem at T=49.

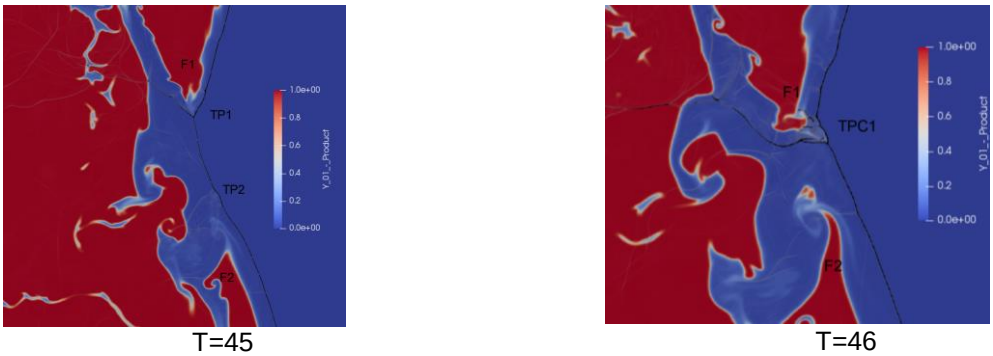

T=45 T=46

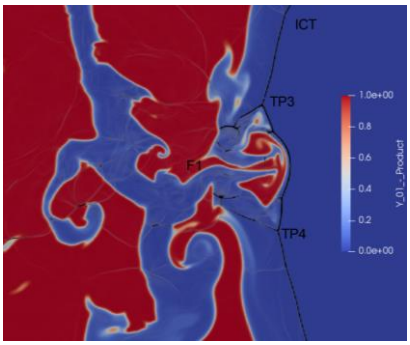

T=47

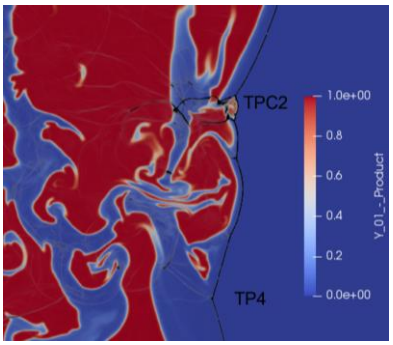

T=48

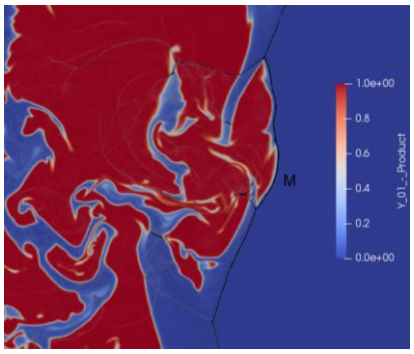

T=49

Figure 5-37 Internodal Mach Reflection Reintiation (Slip line-Flame) Event of $CH_4 - 2O_2$ Detonation at 6 kPa From T=45 to T=49

All the reinitiation modes observed in a stoichiometric methane oxygen detonation at 3.5 kPa and 6 kPa were explained in this section. In the following section, the comparison of the reinitiation mode with other observations in literature are discussed.

5.2.6 Discussion

To reiterate, the primary goal of this chapter is to study the ability of the two-dimensional inviscid simulation to capture global hydrodynamic features of highly irregular detonations. Validations to check for the qualitative and quantitative behavior were performed using published results from three experimental studies. The first key experimental database for methane-oxygen detonation is provided by Radulescu et al. [44] from performed at the Shock Wave Physics Group Laboratory at McGill University. The setup consists of a rectangular channel with a 10 cm height, 2.5 cm width and 1.1-meter-long [60]. The detonation was studied for three different initial pressure 10 kPa, 6 kPa, and 3.4 kPa. The second key literature for the

methane-oxygen detonation for the same initial and boundary condition was studied experimentally by Kiyanda et al. using non-intrusive photographic techniques [58]. The third key experiment used to confirm the observations of this study is an experimental work of Bhattacharjee where the stochiometric oxymethane detonation reinitiation was studied for different initiation pressure using artificial separation [62]. By comparing the average propagation velocity, soot foil and local flow feature with experimental results available in the literature, it is reasonable to claim that a two dimensional inviscid global one-step mechanism was able to capture the overall behavior of the highly unstable detonation correctly. The second objective of this chapter was to understand the reinitiation mechanism of a self-sustaining highly unstable detonation and the role played by hydrodynamic instabilities. More specifically, will these instabilities along the curved jet participate in reinitiation of the detonation. The reinitiation mechanism was categorized into triple point collision reinitiation and Mach reflection reinitiation. Interaction of the slip line with a hot spot, decoupled flame, or both supplies energy to the initially weak nonreactive Mach stem to become an overdriven detonation.

The time scale at which this energy is added decides if successful reinitiation occurs. The frequency of interaction of minor triple points with the specified reinitiation mechanisms increases with initial pressure as observed for 6 kPa. Understanding the timescale of reinitiation requires further resolution in time. One non-dimensional time T for both 3.5 kPa and 6 kPa is equal to 5.57 μsec. All the triple point reinitiations in this simulation occurred in less that 5.57 μsec. A time scale analysis shows that the decoupled flame based Mach reflection reinitiation consumed 5.57 μsec to 11.14 μsec to convert from an non reacting Mach stem to a fully formed detonation Mach stem. The time taken from hot spot formation to the region of burnt gas behind the Mach stem takes around 11.14 μsec and the time taken for the conversion from this region to detonation Mach stem takes 5.57 μsec. Further, the reaction and acoustic time scale is determined using steady state ZND analysis. The reaction time scale of a CJ detonation for both 3.5 kPa and 6 kPa is in the order of 0.7 μsec and 0.4 μsec respectively. The acoustic time scale between the induction to reaction zone for case A and case B are of the order of 1.25 μsec to 0.8 μsec. The time scale resolved in the current study is not sufficient to capture the interaction between the reaction zone and the shock front through compression waves as observed in for regular detonation. The different mode of reinitiation was briefed in

the reinitiation mechanism sections. The occurrence of different modes of the reinitiation was noticed to be decided by the strength of the triple point. The dynamics of the reinitiation in irregular detonation can be credited to the “explosion within explosion” mechanism observed by Oppenheim [145].

The strength of the triple point for different modes of reinitiation was obtained by measuring the density jump through point on the Mach stem which is closest to the triple point. An average value was found to be equal to approximately direct mode $\rho_{ratio} = 11.5$, decoupled flame mode = 10, hotspot mode was 9, for 3.5 kPa. For 6 kPa, approximately, $\rho_{ratio} = 12.5$ (intermodal), decoupled flame mode = 10.5, hotspot mode was 9.5. The noted trend shows that the strength of the triple point is the highest for the direct triple point reinitiation followed by the flame jet interacting Mach reflection mode and the hot spot interacting Mach reflection mode. The increase in density ratio indicates the increase in the strength of the shock, specifically the velocity of the detonation before the collision. The observations reported in this chapter coincides with the experimental observation of Bhattacharjee [62]. The time scale at which the reinitiation occurs interprets schlieren image challenging since an interframe delay of 11.53 μsec was reported. An intermodal triple point collision reinitiation was demonstrated for an initial pressure of 3.5 kPa. The structure of the triple point observed in the experiment is identical with the forward curved jet, strong triple point, and a transverse wave system moving within the jet. The wall-based triple point collision reinitiation was observed for an initial pressure of 9.8 kPa, hot spot-slip line reinitiation (Mach reflection reinitiation) was reported to occur at an initial pressure of 10.3 kPa and a slip line-decoupled flame reinitiation (Mach reflection reinitiation) was observed to occur at 10.4 and a combination of hot spot /decoupled flame slip line interaction at 12.3 kPa. Both of these reinitiation were wall interface based.

The presence of KH volute structure and thinning of the forward jet due to it were also reported to occur along with the inner layer of the curved jet. It is also interesting to note the backward propagating shockwaves in this experiment as observed in the simulation as a part of transverse waves (Figure 5-18, T=138 at R6). The reason for the occurrence of these reinitiation modes at a higher pressure than the current simulation is because they are performed in an isolated format. Hence the reinitiation modes of detonation with higher strengths reveal at higher initial pressures. Whereas in self-sustaining detonation, the strength of the detonation varies to approximately $1.5D_{CJ}$ covering the range of detonations observed

in the experiments. The reinitiation modes observed in this experiment were also confirmed in a two dimensional, inviscid, Euler based simulation using one-step and two-step chemistry by Lau-Chapdelaine [63] for five different initial pressure cases from 5.5 kPa to 17.6 kPa. The hotspot-slip line interaction reinitiation along the wall occurred at 10.3 kPa as observed in its equivalent experiment using one-step chemistry. The slip line decoupled flame interaction reinitiation was observed at 12.5 kPa using a two-step chemistry model. Hence the reinitiation mechanisms in a highly irregular detonation can be captured using a two-dimensional, inviscid, global one-step chemistry simulations. A similarity between the DDT and a Mach reflection reinitiation mode observed in this study should be noted. The hotspot is a stage that also precedes and results in DDT when the precursor shock is followed by a critical wave traveling close to half of the CJ detonation velocity. Chao concluded that the feedback from hotspots created transverse waves and the successful coupling between transverse waves with reaction resulted in DDT in a smooth wall using experiments [144]. In the current hot spot reinitiation mode, the transverse wave is present from the Mach reflection reinitiation. The slip line sweeps in the hot spot to create successful reinitiation.

Two-line sources are created over hotspot A and hotspot B which were observed at T=124 in case A, 3.5 kPa. The product mass fraction of the hotspots is shown in the graph along with it. Hotspot A is in the developing stage with a maximum product mass fraction peaking at 0.85 and hotspot B contains fully reacted products. The sudden increase in the rate of reaction, when surrounded by unreacted material as seen, is clear evidence of a hotspot. Depending upon the ratio of acoustic timescale to excitation time scale either partial confinement or confined reaction occurs and shock waves are emitted from the reaction center [136].

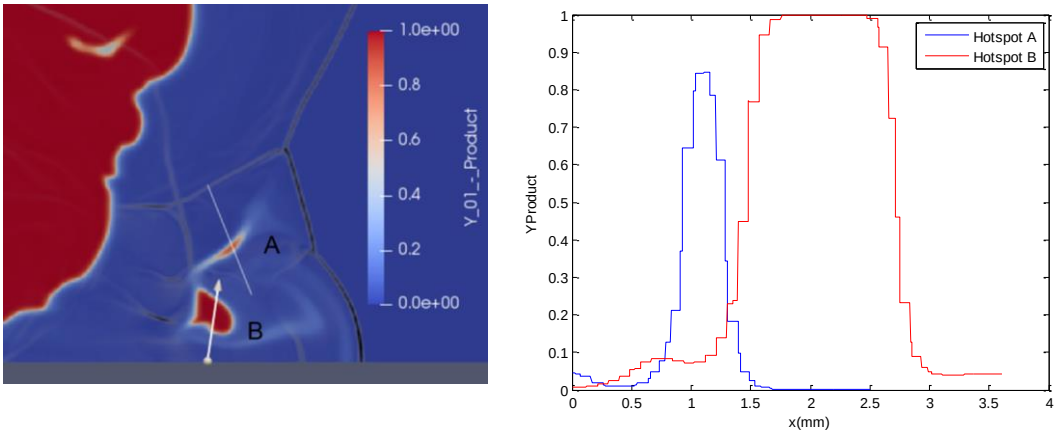

Figure 5-38 (a) Hotspots at T=124 for Case A (b) Product Mass Fraction Plot for the Hotspots

But still, a few uncertainties remain to be addressed. Transverse detonation was reported for an initial pressure of 10.3 kPa [62]. The transverse detonation was also observed in a numerical simulation of stoichiometric methane air-based detonation at 1 atm pressure [39]. No transverse detonation was found to occur for both Case A and Case B. For an initial pressure of 6 kPa, the unreacted pockets were consumed in distance of less than 3.6 cm. This length has been predicted to be 14 cm in the 6 kPa case in the current study. The mechanism responsible for the burning of the unburnt pockets is lacking. The highly unstable detonation shows a strong presence of the jet structure attached to the triple point. This jet can participate in energy addition to the Mach stem in two ways. First through curving towards the Mach stem and increasing the availability of reactants in the vicinity. It was demonstrated that this curving action of the jet was due to the vortex created by the curved slip line. The second through rapid combustion by an external mechanism operating on it such as KH instability and RM instability. Once this jet has been separated from the triple point at the end of the cell cycle, it starts drifting and as an unburnt pocket. Both mechanisms reduce or break the fraction of unburnt mixture moving downstream. It is also clear that the averaged sonic plane is shifted downstream due to the unburnt pockets. But does this burning result in a stronger Mach stem favoring direct reinitiation? Evidence of KH instability in action was seen in Figure 5-25 from T=69 to T=72. The consumption of unburnt pocket was occurring in an accelerated fashion due to the penetration of flame transported by the volutes. Though the KH instability-based increase in reaction rate was found at a different instance, evidence of reoccurrence of KH instability was not supported in this simulation. One

factor might be that even a finer grid is required to capture the KH instabilities. Before concluding the difference observed is due to instabilities or turbulence that are lacking in two-dimensional simulation, the effects of transport due to diffusion and realistic effect of chemistry are to be addressed.

5.2.7 Summary

The reinitiation mechanism of stoichiometric methane oxygen detonation in a rectangular chamber at 3.5 kPa and 6 kPa were studied using a two-dimensional, inviscid, global one-step chemistry model. A maximum of 128 cells per half-reaction length was used for grid resolution. Four modes of reinitiation were found to be operating for reinitiating the decaying detonation in a smooth tube. The formation of secondary cells and their interaction with primary triple points was also discussed. The inviscid simulation was concluded to be sufficient to capture the overall behavior of highly unstable detonation. Further investigation is carried on the reinitiation modes of the highly unstable detonation at 6 kPa using higher-order, viscous, WENO-CD code with global one-step chemistry and using reduced multistep chemistry mechanism derived for methane oxygen detonation with an inviscid model in the following chapter.

Chapter-6 Effects of Diffusion and Chemistry on Oxymethane Detonation Reinitiation

In the current chapter, the influence of diffusion and finite rate chemistry are individually investigated on the reinitiation of highly unstable detonation. In the first part of this chapter, the reinitiation of highly unstable detonation is studied using a globally fourth-order accurate WENO/CD code with finer resolution than investigated in the previous chapter. Additionally, the second-order differential transport terms are included to take the mass, heat, and momentum diffusion into account. In the second part of this chapter, the effect of realistic chemistry on the reinitiation modes observed in highly unstable detonation is investigated using the reduced chemical mechanism to model the reaction profile accurately.

6.1 Case A – Effects of Diffusion

The detonation reinitiation mechanism was investigated only up to a grid resolution of 128 cells per half-reaction length in the previous chapter. The analysis was conducted using the second-order accurate, inviscid, Roe/HLLC solver detailed in Chapter 2. The solver becomes first-order accurate when it encounters discontinuities in the flow field as demonstrated in the Sod's shock tube verification case in chapter 3. A first-order accuracy results in false or numerical diffusion of the discontinuity interface especially when the flow is not aligned with the grid [146]. The analysis performed in chapter 5 confirms, along with several numerical [30, 46] and experimental [59, 44, 62] investigations, that apart from the shock heating, several other discontinuities play a vital role in highly unstable detonation. Most of these discontinuities, for example, the boundaries of the curved jet, boundaries of unreacted reactant pockets, etc. are formed by premixed flames where species and thermal diffusion still plays are role. Since the premixed flame solved using the inviscid model does not take molecular diffusion terms into account, the exothermic structure of a premixed flame is discontinuous with a steep slope. The following contour (Figure 6-1) shows the profile of the flame sheet observed in the unburnt pockets at T=60, captured in the inviscid global one-step chemistry for a stoichiometric oxymethane detonation at 6 kPa.

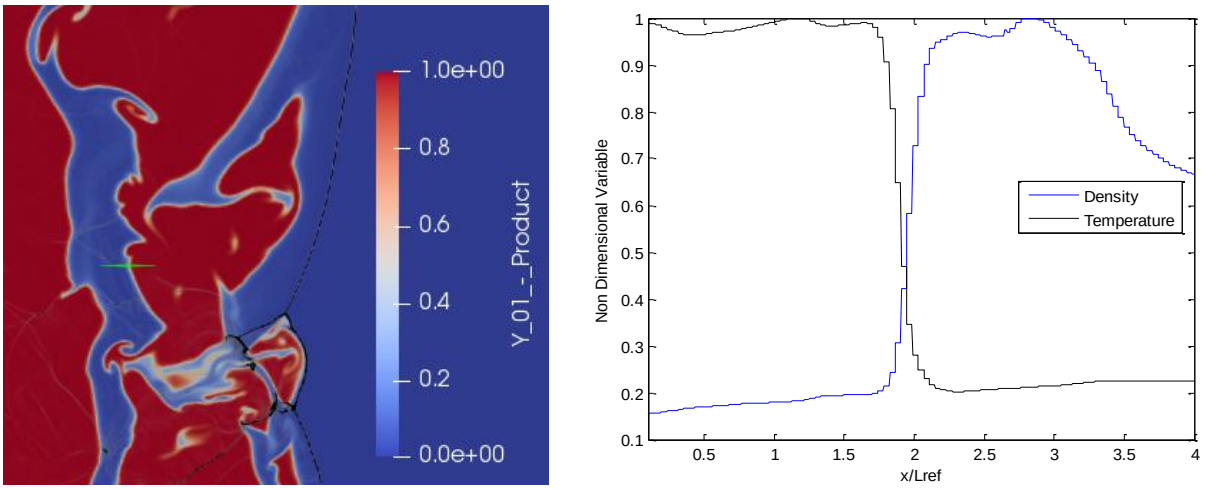

(a) (b)

Figure 6-1 (a) Line Slice (green) on Reactant Pocket Interface (b) Flow Variable Profile on Line Slice for an Oxymethane Detonation at 6 kPa

As we can see, the jump in the variables between the reactant and product has a steep slope and is resolved as a contact discontinuity. The reactants inside the jet, as well as the pockets, are heated and compressed by the incident shock.

A premixed flame can be numerically modeled at three levels; up to a hydrodynamic level where the whole flame is a single flame sheet, transport dominated level where the exothermic region is represented as a single reaction sheet with diffusion playing a role in preheating (infinitely fast chemistry) and detailed chemistry level where the exothermic region has a reaction rate profile(finite rate chemistry) [71]. The global one-step chemistry has a reaction rate profile modeled with an exponential function of temperature and the flame thickness tends to get closer to the infinitely fast reaction sheet as the activation energy increases. In the inviscid model, the heat and species transport occur through convection. Generally, the shock-capturing schemes either add artificial viscosity or slope limiters to handle discontinuities in the domain [147]. The role of artificial viscosity in a shock-capturing scheme is to smear a mathematical discontinuity such as reaction sheet into a thin layer so that the variables still follow the Rankine-Hugonoit conditions but in a slightly relaxed slope to increase stability [148]. This artificial viscosity is a function of the grid spacing and reduces with an increase in grid refinement [149]. Both artificial viscosity and limiters reduce the accuracy of the method to first-order [147]. For a premixed flame, from one-

dimensional conservation equations [98], it is known that the flame velocity is directly proportional to the thermal diffusivity and inversely proportional to the reaction zone thickness. The effect of numerical diffusion is significant when the grid is too coarse or fine. In the former case, the numerical diffusion increases the preheat zone thickness, creating an artificial mechanism of heat and species diffusion [46, 41]. When the increase in preheat thickness is larger than the increase in flame thickness, the flame velocity increases, in turn, causing an increase in the rate of the reaction. Gamezo [4] recognized the role of numerical diffusion for species and heat transport, in addition to convection, for the combustion of unburnt pockets in a two-dimensional inviscid simulation. Maxwell et al. [150] reported a variation of consumption rate of the unburnt pockets of reactants with grid resolution by measuring the average hydrodynamic thickness of stoichiometric oxymethane detonation at 3.5 kPa using two dimensional, inviscid, global one-step chemistry. Oran et.al [42] stresses the importance of accounting for the numerical diffusion in consumption of unburnt reactant pockets when studying a marginal detonation using Euler based simulation. A comparison study of oxymethane detonation at 3500 Pa and $10\Delta_{\frac{1}{2}}$H showed that physical diffusion played a role in predicting the correct average hydrodynamic thickness [46]. In a different work on hydrogen-based detonation, Oran [35] questions the possibility of over resolving the flow field of the detonation when using the inviscid model and high grid resolution. In a mildly unstable detonation analysis, using inviscid, one step chemistry, Sharpe [128] observed that the rate of consumption of reactant pockets increased with a decrease in grid resolution. Arienti et al. [151] performed both zero-dimensional and one-dimensional calculations on the shear layer produced by a triple point in a triple point frame of reference for an irregular detonation and found that the diffusion effects in a shear layer are proportional to the induction time of the detonation. Singh et al. [152] reported a significant difference between inviscid and viscous solutions of a highly unstable detonation when the numerical diffusion reduces with grid refinement. It was also recommended for the use of the viscous model for detonation simulations to avoid resolving unphysical structures at the end of the study [152]. Further, when the grid resolution is too fine, the solution slowly tends towards infinite Reynolds number in an inviscid model. The role of viscosity in a highly unstable detonation gains significance when considering the Reynolds number of the contact surface. The transition of the contact surface to unstable behavior is dependent on the Reynolds number. Hence a fine grid

resolution results in more small scale KH instabilities which are diffused when adding physical viscosity. In the research presented in [149], for a coarser resolution, the structure of the reactant jet behind the detonation was similar between Euler and Navier stokes' solution but when using a finer resolution, a considerable difference between the jet structure was observed. Mazaheri et al. [153] performed a comparison study between two dimensional, inviscid, and viscous solutions for a mildly unstable detonation using global one-step chemistry up to a resolution of 300 grid cells/HRL. A significant difference between inviscid and viscous solutions was found. Compression waves interacting within the jet of the reactants was damped in the viscous solution. A reduction of the size of the vortex formed due to the curving of the slip line due to diffusion was reported. The curvature in incident shock in inviscid flow was not present in viscous solution resulting in a normal incident shock wave. Reduction in the size of the reactant jet/shear layer and dampening of the KH instabilities were also found. It was concluded that the role of a transverse wave in detonation propagation reduces with an increase in the influence of diffusion. A non-reactive, two-dimensional, viscous simulation of a stochiometric oxymethane was carried on by Lau- Chapdelaine [30]for an initial pressure of 3.5 kPa. Even with the non-reactive case, the KH instabilities which occurred along the contact surface for an inviscid solution were absent for the viscous solution. An important observation was that the forward jet and the accompanying vortex were weak in the viscous solution and did not cause a curvature of Mach stem as it did in the viscous solution.

When considering the reinitiation mechanism determined in the previous chapter the role of the forward jet was found to play the most prominent role in distributing the reaction centers in the order of magnitude comparable to the acoustic time scale. In the following section, the role of the viscous mechanism in the reinitiation of highly unstable detonation is studied. Apart from adding the transport terms, the grid depended, artificial viscosity (entropy fix) added in the Roe scheme is avoided using a higher-order WENO scheme which does not interpolate across a discontinuity [154, 34]. To avoid the inherent numerical dissipation arising due to upwind based stencils in WENO, the centered differencing scheme is used in smooth solutions [84]. A comparison with the results obtained from the inviscid solution of 6 kPa oxymethane detonation at relevant sections is also presented. The reference transport properties used in the power-law was taken from the CJ station of an oxymethane detonation with an initial pressure of 6000

Pa. The order of the premixed laminar flamelet length scale can be approximated with thermal diffusivity k and exothermic time scale $t_{reaction}$ using the following relation

$$Thermal\ diffusivity = \kappa_{products} = \frac{thermalconductivity}{\rho C_p} = \frac{0.375}{0.1147 * 2206.82} = 0.001481 \frac{m^2}{s}$$

$$l_{diff} = \sqrt{\kappa \times t_{reaction}} = \sqrt{0.001481 * 3.95145 * 10^{-7}} = 0.024\ mm$$

$$\frac{\Delta_{\frac{1}{2}}}{l_{diff}} = \frac{5.22}{0.024} = 217.09 \approx 218$$

The order of viscous scales relevant to the time scale of reaction can be estimated using the following relation

$$l_{viscous} = \sqrt{\nu t_{reaction}} = \sqrt{8.63 * 10^{-4} * 3.95145 * 10^{-7}} = 0.0185\ mm$$

$$\frac{\Delta_{\frac{1}{2}}}{l_{viscous}} = \frac{5.22}{0.0185} = 282$$

To solve up to the reaction zone length scale, a grid resolution of approximately $218\ \Delta_{\frac{1}{2}}$ and to solve for the viscous scales present in the same time frame a grid resolution of approximately $282\ \Delta_{\frac{1}{2}}$ is required. Hence the finest grid resolution used in this study was 288 cells per HRL. The order of magnitude of 10^{-6} meter matches with the propane oxygen DNS simulation performed by Ziegler [34]. A two-dimensional rectangular domain of 600 $\Delta_{\frac{1}{2}}$ length was chosen with grid resolutions of up to 128 cells per half-reaction length and a length of 400 $\Delta_{\frac{1}{2}}$ for 288 cells per HRL was used for the viscous simulations. A width of 19.15 $\Delta_{\frac{1}{2}}$ was chosen for all the grid resolutions. The remaining setup and boundary conditions which were implemented for case-B in the previous chapter are maintained to be the same to be compared with the inviscid solution. The transport properties were validated using steady-state ZND model with GRI - 3.0 mechanism and is presented along with the transport properties predicted by the power-law below

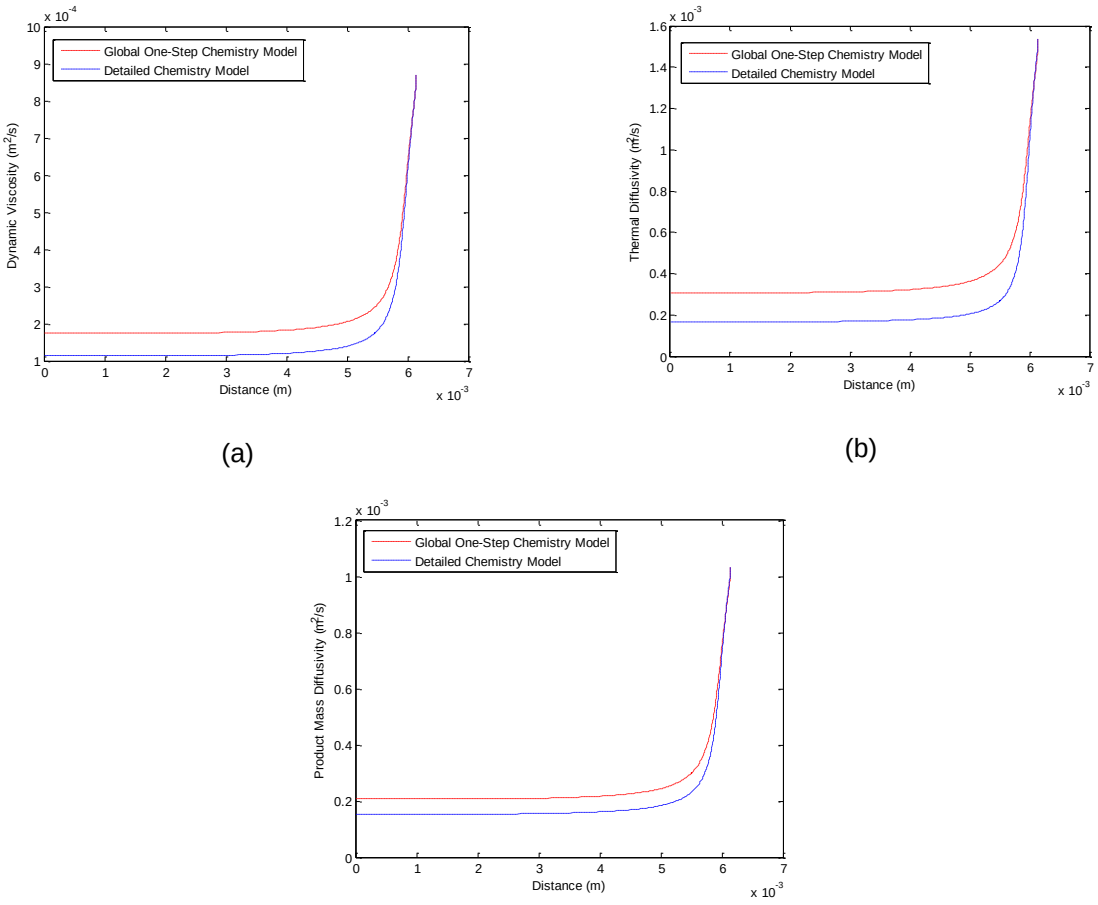

Figure 6-2 Comparison of (a) Dynamic Viscosity (b) Thermal Diffusivity and (c) Product Mass Diffusivity between Global One Step Chemistry and Detailed Chemistry Mechanism

A good match between the transport properties predicted by the multistep chemistry and power-law model was observed. The variation of Prandtl number and Lewis number in the steady-state ZND structure is shown below

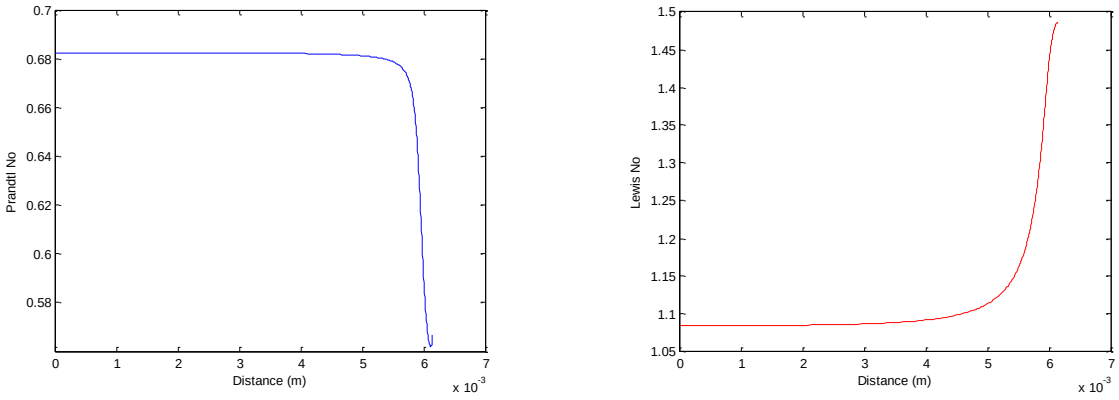

(a) (b)

Figure 6-3 (a) Instantaneous Prandtl Number and (b) Lewis Number of Oxymethane Detonation at 6 kPa using ZND Analysis

The Prandtl number varies from 0.55-0.68 and the Lewis number varies from 1.08 – 1.48. The average values of Prandtl and Lewis number obtained from multistep chemistry was 0.56 and 1.48, respectively.

6.1.1 Global Behavior

The following plot shows the instantaneous velocity profile of the detonation for all the three-grid resolutions used in this study. Exact grid convergence as observed for regular detonation is still found to be lacking due to the interaction of evolving secondary cells. The average detonation velocity was found to be 2227 m/s with a grid resolution of 288 cells per half-reaction length confirming it is an ordinary detonation. When compared to the inviscid model, the average detonation velocity has increased in magnitude and is closer to the experimental average velocity [44].

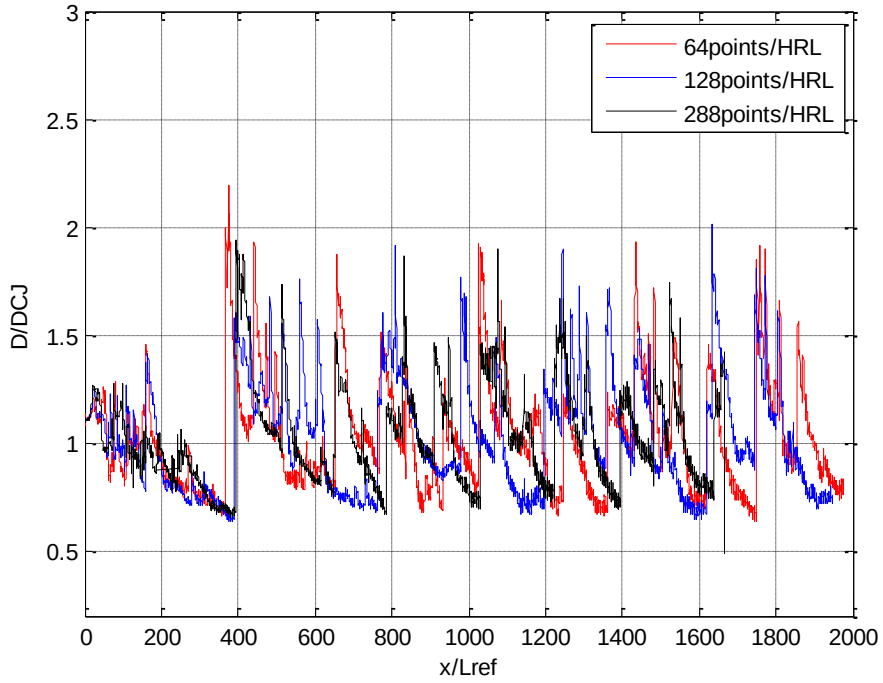

Figure 6-4 Instantaneous Velocity Profile of Oxymethane Detonation using Viscous Model

Grid convergence, with average detonation propagation velocity as a measuring parameter, was achieved for different grid resolution and is shown below.

Table 6-1 Mean Detonation Velocity Ratio Using Viscous Model at Different Grid Levels

Case-B	64	128	288	Error %	Experimental Value [44]
Viscous – Global One Step	0.989	0.988	0.983	1.7%	0.979

The probability density function of instantaneous detonation front velocity with a grid resolution of 288 cells per half-reaction length is shown below. As observed in its inviscid counterpart, the PDF peaks at D/D_{CJ} = 0.82 spending maximum fraction of the time decaying within one limit cycle. Compared to the inviscid model, the detonation also has the same detonation velocity bounds. Only a slight deviation around at D/D_{CJ} = 0.9 is seen in the viscous model with a second peak.

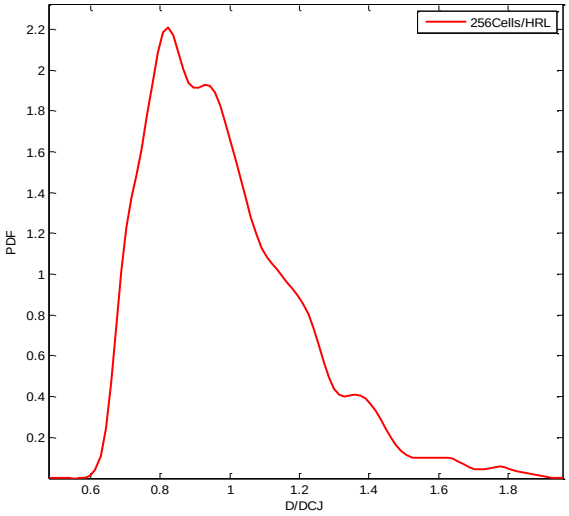

Figure 6-5 PDF of Instantaneous Velocity Ratio of $CH_4 - 2O_2$ Detonation at 6 kPa using Viscous Model

The numerical soot foil of the oxymethane detonation at 6 kPa using the viscous model showing the survival of the detonation throughout the flow domain is shown below.

Figure 6-6 Numerical Soot Foil Comparison of $CH_4 - 2O_2$ Detonation at 6 kPa using Viscous Model

The following tabular column compares flow variables at the CJ plane from the ZND model with the Favre averaged flow variables at the averaged CJ plane from the viscous global one-step model.

Table 6-2 Comparison of Favre Averaged Flow Profile With ZND Results for $CH_4 - 2O_2$ Detonation at 6 kPa using Viscous Model

Flow Variable	ZND Value	Favre Averaged Value	Difference	Unit
Pressure	151283	153931	1.7%	Pa
Temperature	3224	3608	11.9%	K
Density	0.114	0.123	0.8%	kg/m^3
Velocity	1267	1193	5.8%	m/s
Average Sonic Plane	0.637729	13.9	-	cm

Reactant Mass Fraction (Theoretical)	0	0.44	-	-
Reactant Mass Fraction (Favre Averaged)	0	0.01	-	-

Only a slight improvement in the averaged flow properties at the CJ plane was seen with the viscous model. The averaged sonic plane was achieved at 13.9 cm which is around 4.3 % shorter than the averaged sonic plane predicted by the inviscid model. The residual reactant mass fraction at the averaged sonic plane was 1% which is also less than the 3% predicted by the inviscid model. Though this can be understood as taking the diffusion into effect, the conclusion is achieved after analyzing all the other factors in the following subsections.

6.1.2 Structure of Triple Point

The triple point structure is analyzed at T= 156 where the detonation has traveled up to 175 HRL (approximately at the same location where the triple point in the inviscid case) was analyzed. A dual-mode detonation with primary triple points TP1 and TP 2 is observed in the density contour (Figure 6-8 a). Two minor triple points MTP1 and MPT2 are also labeled in the density contour. The curved reactant jets J1 and J2 are shorter compared to the jets J1 and J2 in the inviscid model. The pressure gradient contour shows that the structure of the Mach stem varies with more curvature in the viscous model. Though the transverse wave systems TI1 and TI2 are similar in both the models the extending transverse waves are well resolved with the WENO scheme. The points P1-P5 and P6-P9 forms the transverse wave system of triple points TP1 and TP2, respectively. The transverse waves extending beyond P5 and P9 are labeled as ET1 and ET2. Comparing with the result obtained with the inviscid model, there is reduced corrugation of the Mach stem of the overdriven parts of the detonation in the viscous model. The formation of complex jet due to the decoupling of a minor triple point and flame was explained in Chapter - 5. The curved jet J2 of triple point TP2 was captured to be a complex jet in the inviscid simulation. But it does not have any additional reactant

pocket attachment in the viscous simulation due to the reduced minor triple points along the front compared to its inviscid counterpart. The minor triple points caries their own reactant jets which amalgamates and develops the size of the reactant jet attached to the primary triple point during an interaction. Due to the reduction in minor cells, the size of the unburnt reactant pockets after it separated from the primary triple point is also reduced. This can be seen by comparing the unburnt pockets in the temperature gradient contour in Figure 5-31 (c) and Figure 6-8 (c).

(a)

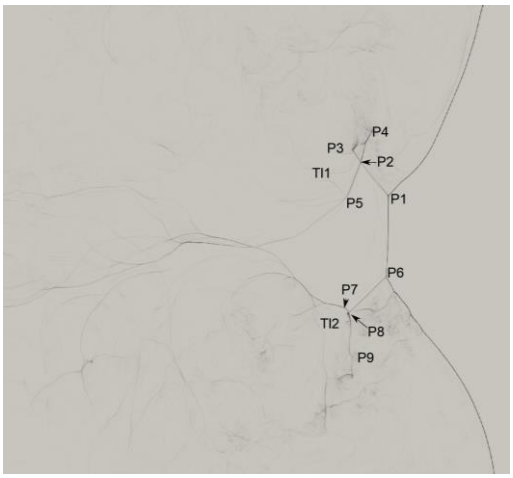

(b)

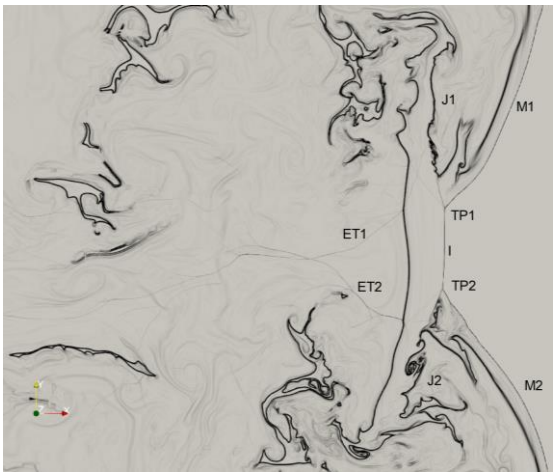

(c)

Figure 6-7 Structure of the Triple Point at T= Analyzed using (a) Density Contour (b) Pressure Gradient Contour and (c) Temperature Gradient Contour

Therefore, reduction in the mass fraction of unburnt pockets in the averaged sonic plane, as well as the shorter hydrodynamic thickness, is influenced by the formation of conjoined reactant pockets.

Additionally, the jets attached to the minor triple points MTP1 and MTP2 are also larger because of the absence of additional triple point collisions. The three orientations of oxymethane detonation at 6 kPa which was observed and compared with the experimental schlieren image was also observed in the viscous simulation. The single, dual, and triple mode detonation are presented using density contours in the figure below

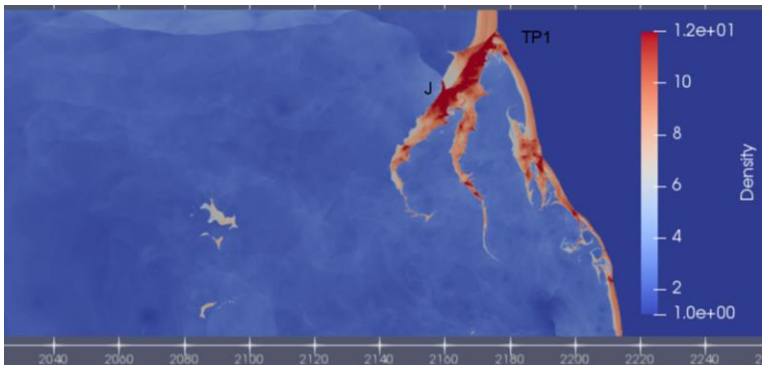

(a)

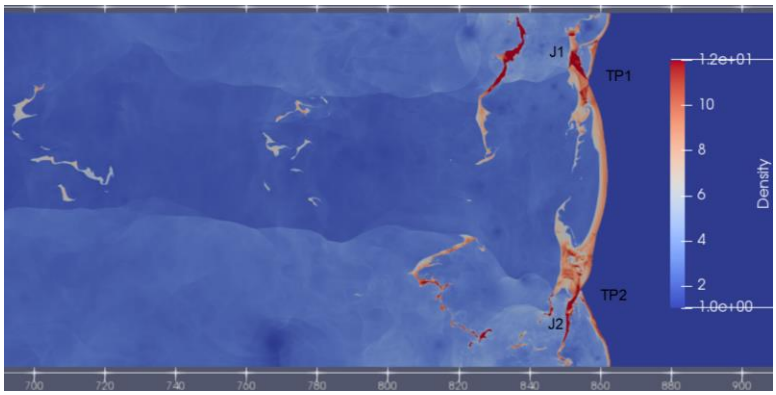

(b)

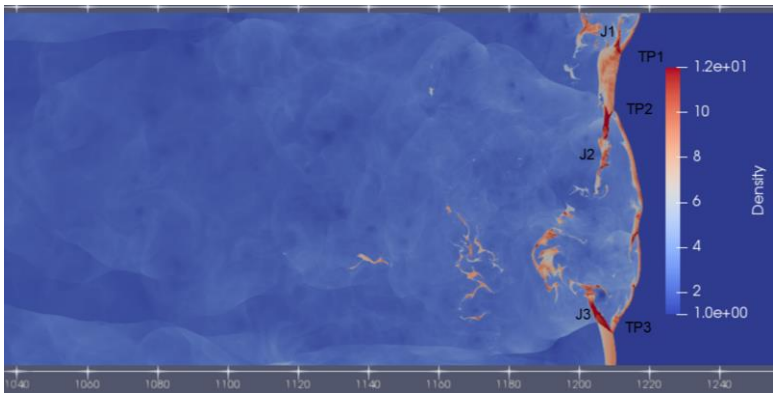

(c)

Figure 6-8 Instantaneous Density Contour of Oxymethane Detonation at 6 kPa during (a) Single Mode (b) Dual Mode and (c) Triple Mode Propagation

All the comparisons are made at a similar location on the x-axis. Thus, the global features of the detonation do not vary between inviscid and viscous simulations. Though the overall structure of the detonation is the same, few differences were still observed. The single-mode detonation shows a significant difference in the structure of the reactant jet J. The reactant jets J1 and J2 in the dual-mode detonation are thinner in the viscous simulations. The large pocket of reactant behind dual-mode detonation observed in the inviscid simulation is absent in the viscous simulation as well as the experimental image. A slight variation in inclination was noted when comparing the viscous and inviscid results. Qualitatively, the results from the viscous simulations matched more with the experimental schlieren images when compared with the inviscid results.

6.1.3 Reinitiation Mechanism

Analysis of the reinitiation mechanism from the viscous study showed that no new mode of reinitiation was observed. As observed in the inviscid model, only the direct mode reinitiation and Mach reflection reinitiation (both a jet influenced, and hot spot influenced) were observed. To avoid repetition only Mach reflection reinitiation along the wall and direct reinitiation within the primary modes are shown in this section. Since a single nondimensional time step is 2.6 μs (half of the timestep used in inviscid simulations) further clarity regarding the reinitiation process can be obtained. The following set of contours represent the reaction progress variable overlapped with pressure gradient contour. We can see that the shock structure is sharper with the WENO-CD scheme than the ROE-HLL solver used for inviscid simulations. A sequence of curved jet based reinitiation is shown below. This sequence (Figure 6-10), can be compared directly with the jet-based Mach reflection reinitiation (Figure 5-84) presented in chapter-5. At T=143 (Figure 6-10), a triple point TP1 collides with the upper wall and results in a new Mach stem with a triple point TP2 at T=144. A strong presence of KH instability can be seen along the surface of the pockets at T=143. This feature was not resolved in the inviscid simulation. The transverse wave meets the wall at R1 and R2. The

detached reactant jet from the previous cycle is labeled P1 and P2. The transverse wave travels through P1 and P2. The transverse wave meets P1 with an angle close to normal angle and P2 at an inclined angle. This results in the difference in the consumption rate of pockets P1 and P2 as it travels downstream. As soon as the contact between the transverse wave moves further from the wall (R1) at T=146, the action of the curved slip line is strong to form a reactant jet. The Mach stem (M), curved jet (CJ), backward jet (BJ), and the transverse wave system (TI) have formed and appeared prominently at T=146. The bifurcation of the Mach stem due to the forward jet is observed and labeled as B at T=147. The curved jet ends close to the backward jet (BJ). The curvature of the Mach stem relaxes as the triple point moves further and the gas behind the Mach stem expands at T=148. KH instabilities start to develop along the curved jet (CJ) and backward jet (BJ) at T=149. An incoming decoupled triple point (ICT) is also seen at the same event. The triple point collision leads to the formation of a new triple point TP3 which now propagates further at T=150.

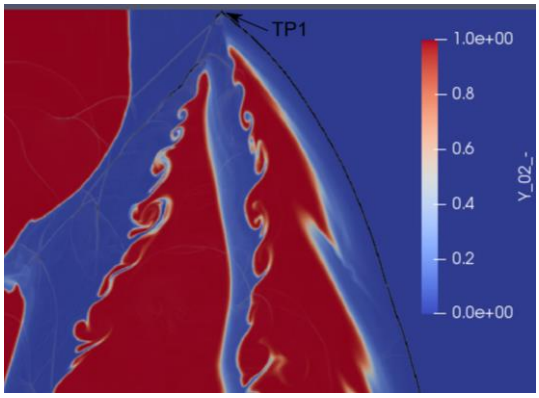

T=143

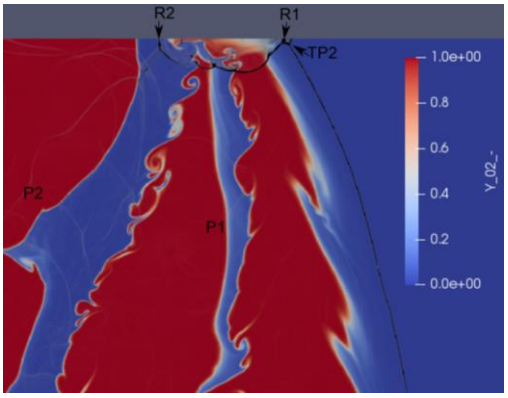

T=144

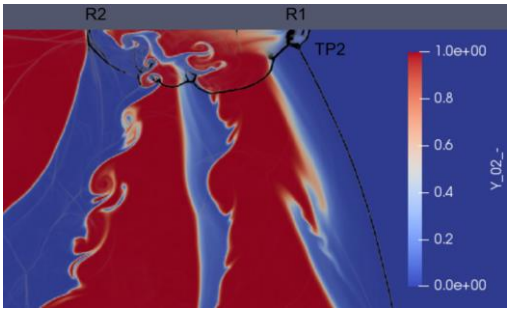

T=145

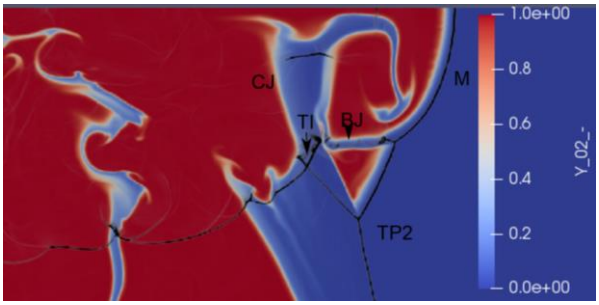

T=146

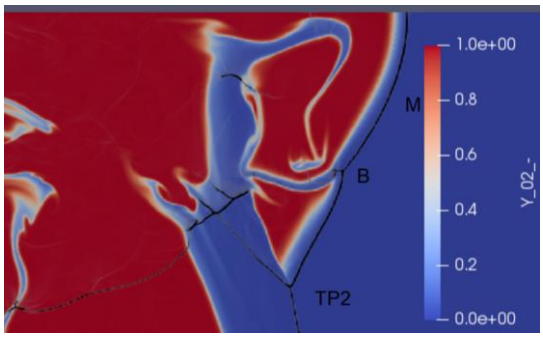

T=147

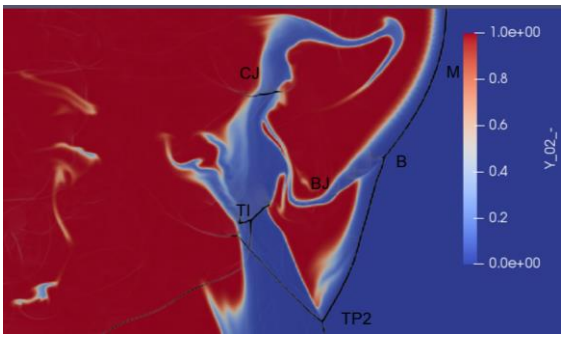

T=148

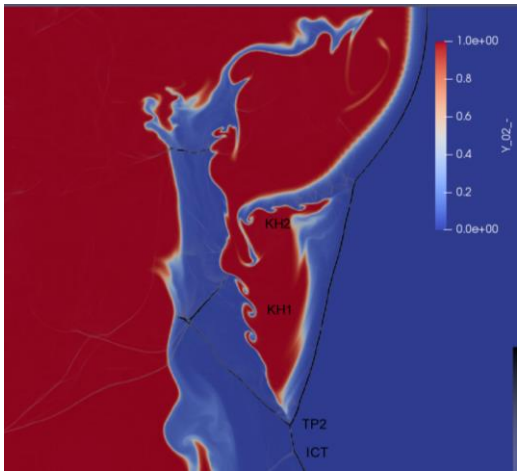

T=149

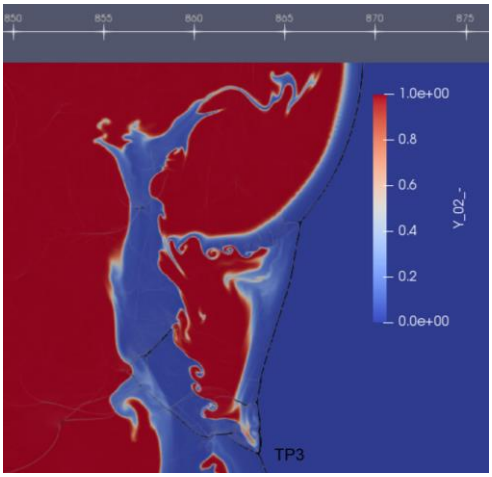

T=150

Figure 6-9 Mach Reflection Reintiation (Slip line-Flame) Event of $CH_4 - 2O_2$ Detonation at 6 kPa using Viscous Model

The frequency of KH instability occurrences is higher along the flame interface of the jets than what was observed in the inviscid simulations. These 'willows' play a role in increasing the frame surface area and engulfing the products. This action creates an active ground for reaction progress. Once such occurrence along the surface of the detached pocket at T=56 where vortex pairing occurs is labeled as KH1. This accelerates the consumption of unburnt reactant pockets reducing its travel distance as seen through the Favre averaging analysis.

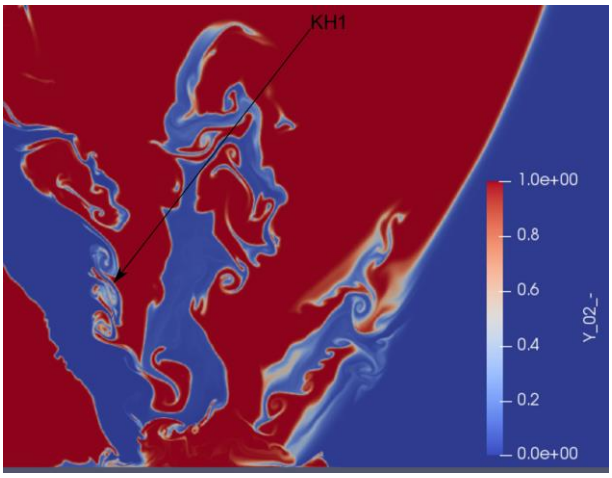

T= 56

Figure 6-10 Influence of KH Volutes on Unburnt Reactant Pockets

In the next set of events (Figure 6-12), a Mach reflection reinitiation due to hot spot influence is depicted. A weak reflection along the upper wall resulting in a triple point TP1 is seen at T= 204. At T=205, initiation of hot spots along the contact surface develops which becomes two mature hot spots HS1 and HS2 at T=206. The bifurcation B of the Mach stem is visible. Development of hot spots HS1 and HS2 forms the reactant jet regions CJ and BJ. Instabilities along the inner side of the curved jet CJ are also visible. The Mach stem grows further and the reactant pocket P1 starts drifting into the products at T= 208. The thickness of the induction zone develops quickly from T= 207 to T= 210 because of the decaying incident shock. An incoming triple point from the bottom is labeled as ICT (t=210) collides with TP1 at T= 211 forming a new Mach stem with triple points TP2 and TP3.

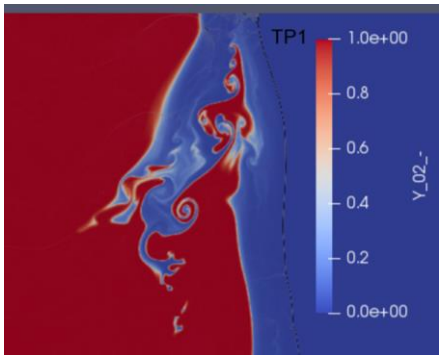

T=204

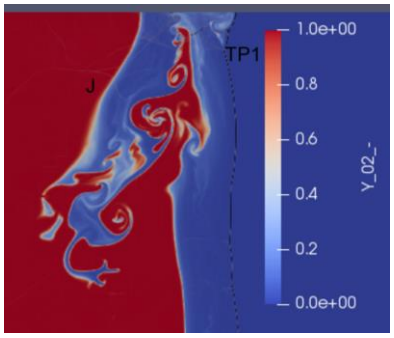

T=205

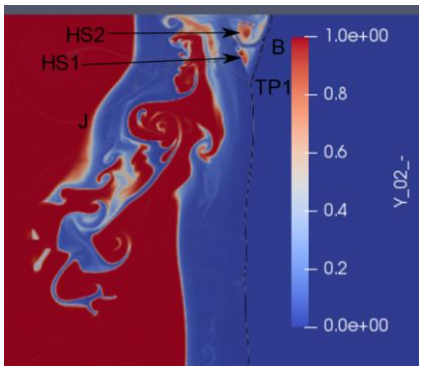

T=206

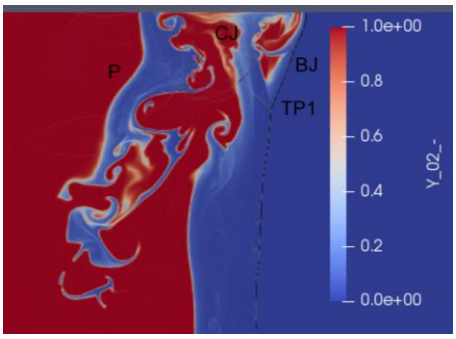

T=207

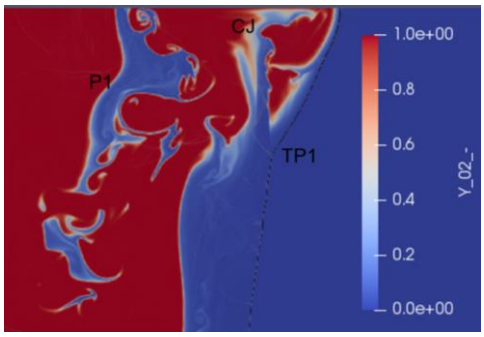

T=208

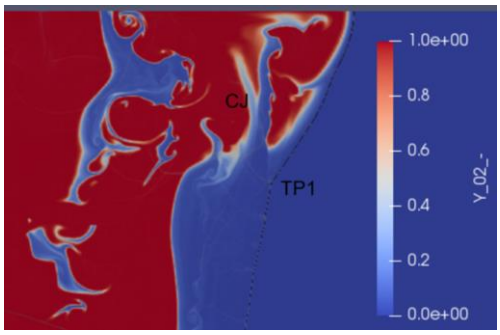

T=209

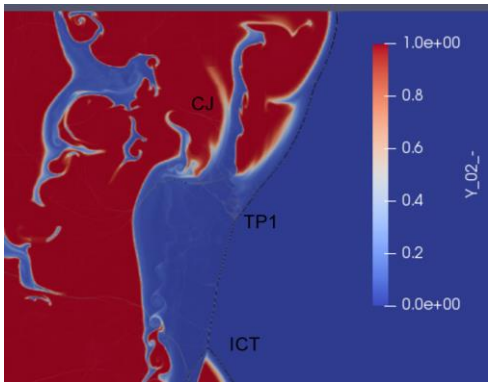

T=210

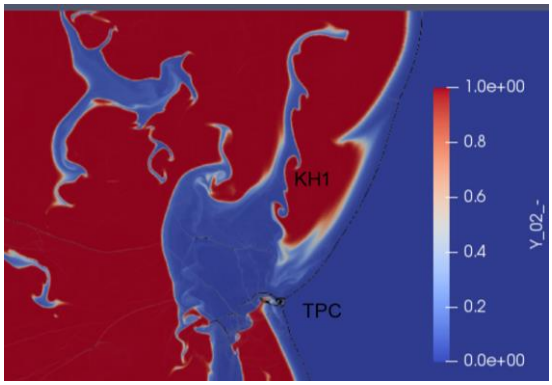

T=211

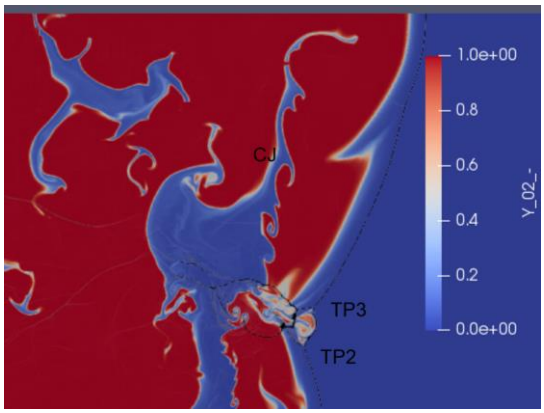

T=212

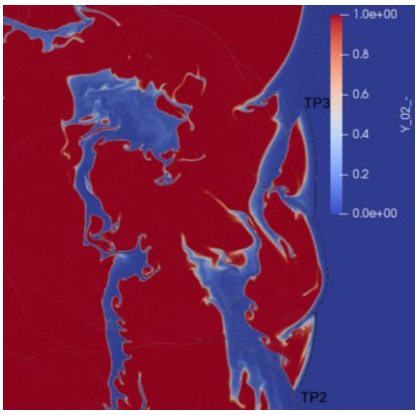

T=213

Figure 6-11 Mach Reflection Reintiation (Slip line-Hotspot) Event of $CH_4 - 2O_2$ Detonation at 6 kPa

The following sequence of reinitiation shows direct reinitiation between two primary triple points TP1 and TP2. The approaching triple points TP1 and TP2 (T=148) collide at T=149 (TPC) leading to an immediate new Mach stem formation with triple points TP3 and TP4 at T=150 without any influence of curved jet or hotspot. This Mach stem develops further at T=151.

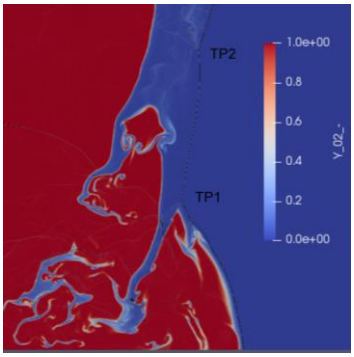

T=148

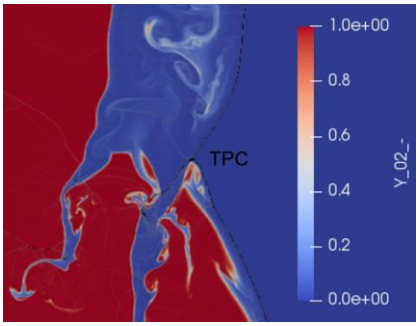

T=149

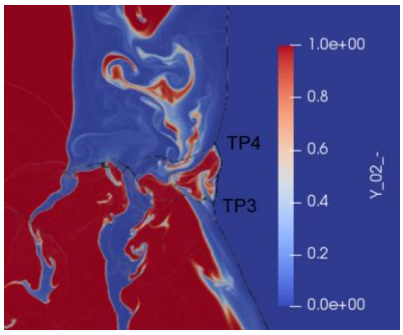

T=150

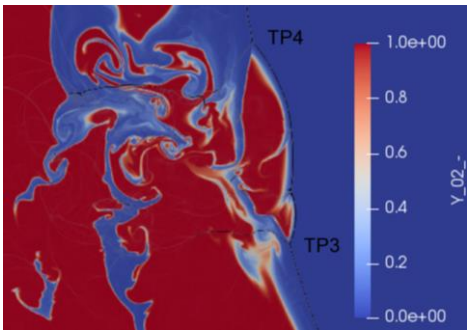

T=151

Figure 6-12 Triple Point Reintiation Event of $CH_4 - 2O_2$ Detonation at 6 kPa

6.1.4 Discussion

Several conclusions are made before moving to the next part of this study. Since the hydrodynamic features such as reactant jets and contact surfaces played a role in efficiently distributing the flame and hotspots to cause reinitiation in Chapter-5, the influence of diffusion on the reinitiation modes was studied by solving two dimensional Navier stokes equation. The first noted difference is the reduced number of minor triple points as discussed in the structure of the triple point subsection. Though a direct correlation between the minor cells and diffusion cannot be stated the relationship between both can be derived. From the triple point strength analysis for reinitiation modes in Chapter 5, we know that the flame following a triple point is responsible for the strength of the triple point. When the velocity of the flame is corrected with the presence of physical viscosity at high resolutions, an artificial increase in the strength of the triple point and reinitiation is avoided. It is also interesting to notice the increase in the averaged detonation propagation velocity by 2.1 percent when compared to inviscid simulation. In the inviscid solution along with the increase in grid resolution, the average velocity of the shock decreased, and the presence of minor cells increased. The role of these minor cells was reported to support the detonation as the detonation velocity reduced due to the loss of energy by Gamezo [40]. The energy deposited through reinitiation decides on the overdriven factor of the new Mach stem which is proportional to the minor triple points. The reduced presence and interaction between minor triple points increase the time spent by reactant jets behind an incident shock or Mach stem reducing its thickness. This is in turn aided by the formation of KH instabilities along with the jets which are damped in the inviscid simulation due to numerical diffusion. An increase in reactivity along the KH instabilities of reactant jets and pockets for highly unstable detonation have been noted earlier through open shutter photographs [2] and schlieren images [12]. The onset of KH instability can be seen in Figure 6-10 from T= 146. After the reinitiation, the curved jet (CJ) of unburnt reactant and backward jet (BJ) are formed at T=146 and develop at T=147. From a planar contact surface at T=148, the perturbations have grown to form KH willows in both CJ and BJ at T=148. With the development in the KH vortices, the reduction in the thickness of CJ can be seen from T= 148 to T=149. This influence of KH vortices in local ignition was also observed in a work by Massa et.al [155] in a two dimensional, viscous simulation of a

propane-based detonation, where the larger induction time for higher activation energy reactants was understood to be responsible. Though the increase in average hydrodynamic thickness can be credited to the missing turbulence scales in two-dimensional simulation by an inviscid model as reported by Radulescu et.al [60] the increase in the number of reactant pockets is due to the increased interaction of triple point. Even by applying slip wall boundary conditions and ignoring boundary layer effects, the bifurcation of the Mach stem was absent for a non-reactive Mach reflection in an oxymethane mixture [30]. But in case of reactive flow, this was not applicable, for example as observed in Figure 6-12, bifurcation of the Mach stem M1 with triple point TP1 was captured after reinitiation along the top wall.

6.2 Case B - Effects of Chemistry

Before concluding on the reinitiation mechanisms of the highly unstable detonation, the influence of the realistic chemistry was investigated in this section. Apart from the hydrodynamic mechanism, attention to the chemical behavior of the mixture is critical. It was demonstrated in Chapter-4 that even the smallest deviation in the instability parameter manifests a broader range of instabilities in the one-dimensional detonation. Experimental investigation of the reinitiation mechanism of stoichiometric oxymethane detonation by Bhattacharjee [62] showed evidence of transverse detonation at a parametric study with different initial pressure conditions. In those experiments, the transverse detonation was beginning to manifest during reinitiation from an initial pressure of 10.5 kPa. The transverse detonation reinitiation mode also appeared for a short period in a numerical simulation of an oxymethane detonation at 11 kPa using an inviscid, two-step chemistry model by Lau-Chapdelaine [63]. Though the initial pressure of those setups was higher than 6 kPa, the velocity of the detonation during reinitiation in the current study is overdriven up to 1.5 - 2 D_{CJ} reaching comparable velocity and strength. Capturing the transverse detonations are important since they are reported to produce a separate set of transverse detonation secondary cells [40]. As seen in Chapter-5, interactions between these secondary cells and primary cells can change and favor a mode of reinitiation making it is necessary to understand it. Though the two-step induction parameter model assumes heat release occurring through thermal explosion following a shock compression and ignition delay [156], limitations in two-step induction parameter models have been noted by Oran et al. [35] when initiating the perturbations by placing unreacted pockets of gas behind detonation

front. Bates et al. [156] also mention limitations by comparing the temporal profile of the reaction zone solving chemical kinetics and energy equation with two-step induction models. The detailed chemistry also reported twice the number of detonation cells as well as different sizes and local energy release rate than the parametric model with 99.5% accuracy of experimental CJ velocity. The two-step induction model also has its weakness in the energy release rate prediction for shocked and re-shocked gases [35]. The stability parameter is a function of induction length scale to reaction length scale. For numerical modeling of detonation, four basic reaction rate closures are global one-step chemistry reaction mechanism, ad-hoc induction parameter models, reduced elementary reaction mechanism (systematic or empirical), and detailed reaction mechanism [10]. One uncertainty of achieving proper kinetics can be removed with a detailed chemical reaction mechanism but for a hydrocarbon reaction that can demand from approximately 50 – 500 species it is challenging when coupled with a three-dimensional multiscale simulation [27]. The computational efficiency of the global one-step chemistry model (by using explicit ODE solver) allows the numerical simulation using this model for higher resolution but its limitations lie in the fact that it cannot reproduce an induction zone or quenching behavior [10]. Though previous studies have shown that an accurate model of hydrodynamics with crude modeling of chemistry has reproduced the multidimensional features of detonation seen in experiments [35], knowing their limitations helps to interpret the results clearer. The limitation of the reaction rate in the global one-step model which is modeled after an exponential function is that no profile of the reaction zone is specifically modeled. Understanding of initiation mechanisms of detonation using global one-step chemistry models has been cautioned by Liberman et al. [157] in a recent research work that was focused on the analysis of hotspot based initiation for hydrogen and methane-based mixtures. For a successive transition from the pressure pulse due to hot spot to detonation, the coupling between the pressure pulse and reaction wave (SWACER) is necessary [2]. The temperature derivative of induction time which decides the velocity of this reaction wave was found to vary by orders of magnitude between global one-step and multistep chemistry [157]. Another conclusion was that a hot spot that is smaller in size and with less temperature gradient can be responsible for the initiation of detonation when using a multistep chemistry model since the surrounding region is found to be with a temperature lower than predicted by the one-step model [157]. This is because the endothermic nature of

the reaction is not considered by the one-step chemistry model. This implies that a detonation failure credited to the absence of turbulence might be due to the absence of finite rate chemistry. The comparison of the Favre averaged profile of unsteady detonation with steady-state ZND profile also showed that the temperature predicted by the one-step chemistry was higher by a few percent since the heat absorbed by vibration and dissociation is not taken into account. This artificially increases the speed of sound in the reaction zone delaying the onset of the sonic plane. This also alters the properties of the transverse waves modifying its interaction with unburnt reactant pockets. The role of dissociative reactions tends to play a key role in fuel – oxygen reactions when compared to fuel-air reactions [158]. To determine the dependency of the reinitiation modes to realistic chemistry, a reduced mechanism is derived for oxymethane reaction and a self-sustained detonation is simulated using the inviscid Roe/HLLC solver which was detailed in Chapter 2.

6.2.1 Reduced Mechanism Verification

The activation energy is a measure of the minimum energy the colliding molecules should possess to react. A fundamental difference in the reaction progress between hydrogen and hydrocarbon fuel can be noted from the figure below.

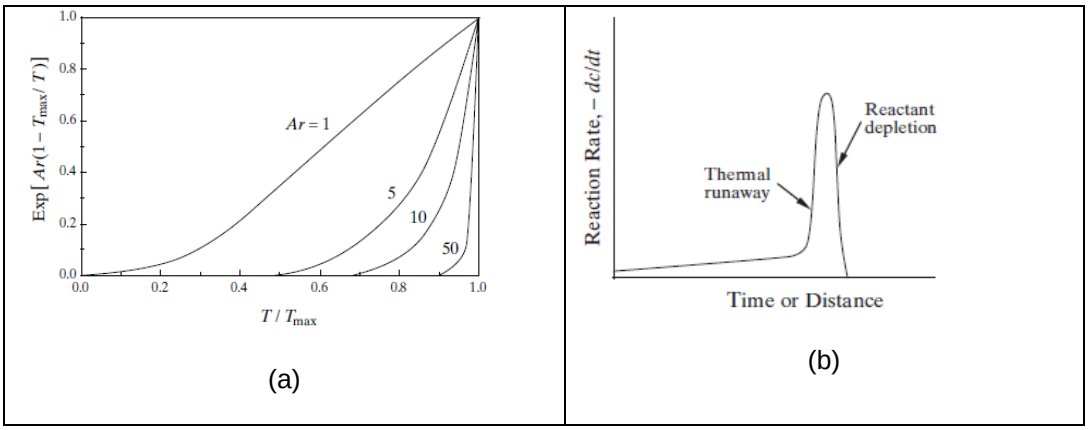

Figure 6-13 Schematic Showing (a) Difference in Product Formation For One Step Chemistry (b) Schematic of Thermal Runaway (taken from [71])

From Figure 6-14 (a) we see that the activation energy is low, the reaction progresses with an increase in temperature. But when the activation energy is increased, especially for methane-oxygen detonation ($\theta \sim 45$) the reaction is confined to a very small region representing thermal explosion

(autoignition) or a diffusion flame [71] [2]. The thermal explosion occurs when the temperature reaches magnitudes in orders of E_a/R [27] which is also a reason for irregularity in detonation structure since temperature perturbations result in thermal explosions in different regions. The reaction mechanism of fuel oxidation, especially the initiation step, by flames differs with the autoignition since the radical concentration in flames is much larger than the concentration in the induction zone [71]. Detailed fundamental studies of methane oxidation involving molecular dynamics have been performed for varying initial pressure and temperature to determine the reaction pathways and contributing factors for explosive conditions [159, 160]. The reactivity of methane-oxygen conditions was concluded to be dependent upon the concentration of the free radicals specifically ($HO_2, OH\ and\ CH_3$) [159]. The characteristic time scale of free radicals is quite fast when compared to the characteristic time scale of $CH4$ molecule [161]. The autoignition of methane can be divided into three stages. The first stage is an isothermal chain branching stage, the second stage is branched-chain explosion accompanied by strong heat release and the third stage is CO_2 formation [87]. The autoignition temperature for methane is approximately 810 K [162]. The methane – oxygen mixture requires the highest temperature than any other higher hydrocarbon to exhibit explosive behavior for given pressure [71]. Several high-temperature methane oxidations through the autoignition pathway have been provided in standard combustion textbooks [71] [98] [163]. In the derivation of a reduced mechanism from detailed methane oxidation mechanism, Li et al. [164] notes the most important intermediates and radicals can be further reduced to $H_2, OH, CH_3O, CH_2O, HO_2, H. H_2O_2, O$.For a stoichiometric reactant concentration, the most important intermediates for autoignition from those pathways are CH_3,$CH_2(S)$, CH_2,CH, CH_3O,CH_2O,HCO, HO_2,CO,CO_2 with free radicals $O, H\ and\ OH$ [71]. Several detailed mechanisms of methane oxidation reactions can be found in a review article by [165]. A skeletal mechanism based on these intermediates was derived from the GRI-1.2 detailed mechanism [166]. Then a reduced mechanism was derived empirically based on the autoignition pathway of methane oxidation as shown below. The final reduced mechanism consists of 13 (CH_3, CH_3O, CH_2O, HCO, HO_2, CO, CO_2, O, H, OH) species and 35 reactions reduced from 32 species and 177 reactions. The reaction coefficients and thermodynamic are consistent with the GRI-1.2 mechanism.

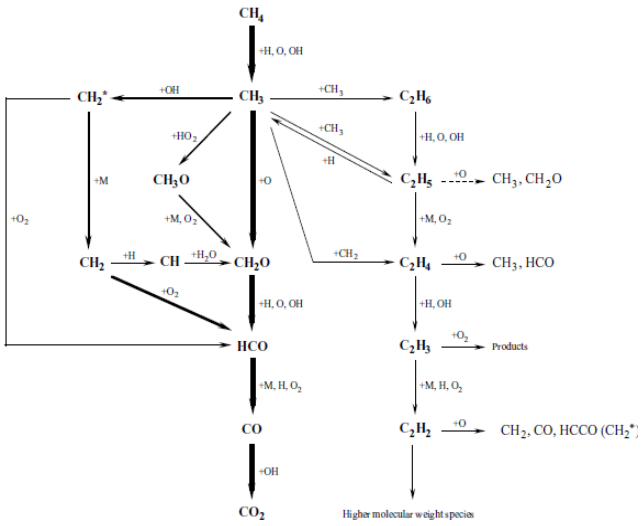

Figure 6-14: Reaction Pathway Used for Reduced Mechanism Derivation (taken from [71])

The obtained reduced mechanism is verified using a steady-state one-dimensional ZND theory. The C++ code of SD Toolbox by Shepherd et al. [124] from Explosion Dynamics Laboratory of Caltech was used to obtain the results of the ZND theory. The reaction rate of species is calculated using the chemistry code Cantera by Goodwin [167]. The SD Toolbox assumes a shock front traveling at CJ velocity and calculates the flow properties behind the shock front (Von-Neuman point) using one dimensional Rankine Hugonoit shock jump conditions in a wave fixed frame. The one-dimensional reactive Euler equations are then space marched using 'CVODE' ODE solver till the sonic plane is reached in the reaction zone. The GRI -1.2 Mechanism is chosen for the reference state over GRI-3.0 [168] since both mechanisms give similar results in terms of induction and reaction length scales as shown below. The reduced mechanism for detonation simulation can be validated by comparing the results of the ZND profile with a detailed chemistry mechanism of the oxymethane detonation at 6 kPa as shown below [10].

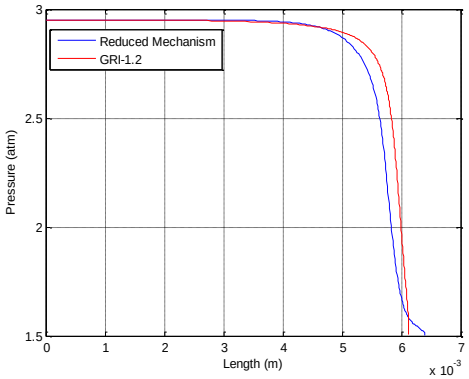

(a)

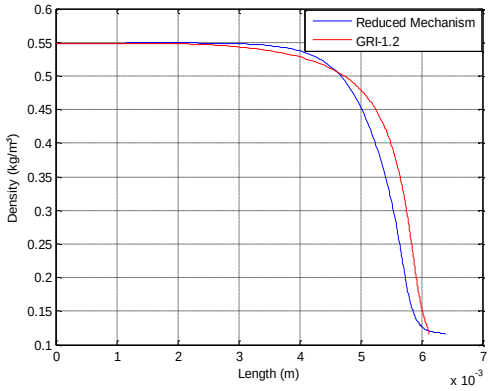

(b)

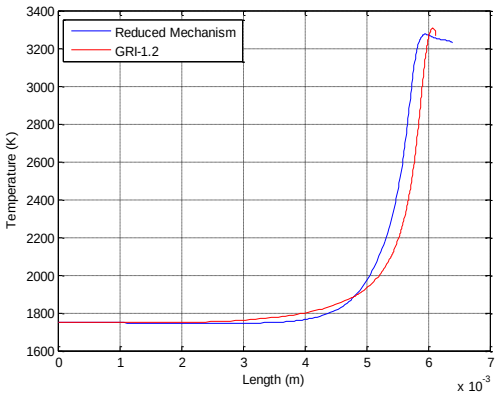

(c)

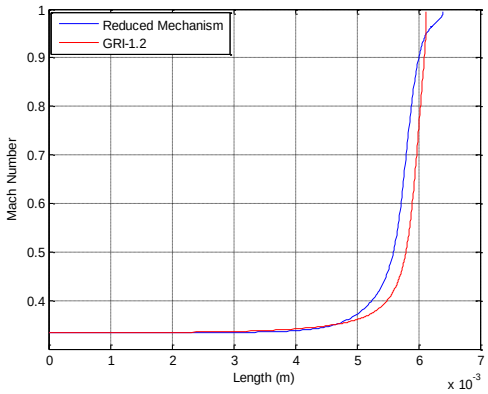

(d)

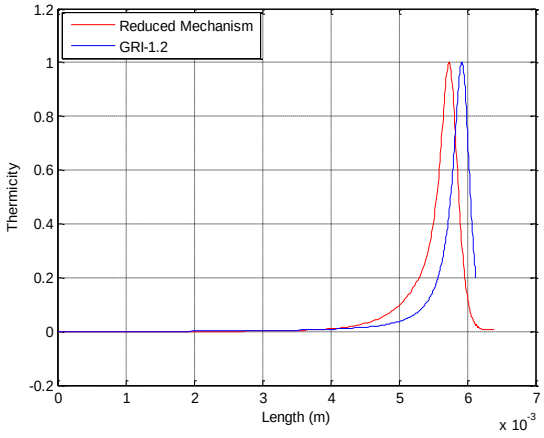

(e)

Figure 6-15 Flow Profile comparison Using ZND Theorem (a) Pressure (b) Density (c) Temperature (d) Mach Number (e) Thermicity

An important aspect of the reduced mechanism is to reproduce the thermal explosion characteristic of the methane autoignition with reasonable accuracy. In a chain branching reaction, the radical species concentration buildup causes the rapid formation of products (explosive) [163]. If the heat produced during an exothermic reaction is not sufficiently removed a thermal explosion is likely to occur [98]. A coupled chain branching and a thermal explosion occur in the reaction zone of a hydrocarbon-based detonation [27]. To calculate and compare the induction time/length scale and reaction time/length scale between detailed and reduced chemical mechanisms, thermicity was chosen as the reference parameter since it translates to the coupling between flow and chemistry. The comparison chart (d) in the figure above shows the thermicity of both the mechanisms. Since few secondary pathways were curtailed to save computational time, there is a small-time difference for the detailed mechanism to reach the sonic plane. The following tables show the comparison of important time and length scales of detonation between both the mechanism for 3.4 kPa and 6 kPa.

Table 6-3 ZND Solution Comparison of an Oxymethane Detonation at 3.4 kPa

Parameter	Gri-1.2	Reduced Mechanism	Unit
Shock Velocity	2243	2243	m/s
Induction Time	3.93	3.92	$\times 10^{-5} s$
Induction Length	0.011	0.011	m
Reaction Time	8.253	7.523	$\times 10^{-7} s$
Reaction Length	0.00057	0.00053	m

Table 6-4 ZND Solution Comparison of an Oxymethane Detonation at 6 kPa

Parameter	Gri-1.2	Reduced Mechanism	Unit
Shock Velocity	2266	2266	m/s
Induction Time	2.07879	2.01912	$\times 10^{-5} s$
Induction Length	0.00592	0.00573	m
Reaction Time	4.16925	4.67905	$\times 10^{-7} s$
Reaction Length	0.00028	0.00032	m

An increase in initiation pressure from 3.4 kPa to 6 kPa results in a decrease in both induction and reaction zone length. Further increase in initial pressure decreases the reaction zone length even more which increases the difficulty of capturing the flame with coarser grid points, requiring finer grid resolution.

6.2.2 Case Setup

The stationary frame of reference was chosen for the multistep chemistry case. The domain was chosen based on the hydrodynamic thickness of oxymethane detonation at 6 kPa. The inviscid and viscous analysis provided a distance range of 27 – 28 HRL. The solution is progressed up to 0.0006 seconds which is approximately the time taken for the detonation to travel up to a length of $250\lambda_{\frac{1}{2}}$ with CJ velocity. The global time step was taken to be in the order of 10^{-8} second which is two orders of magnitude smaller than the time step used with the global one-step chemistry. The difference in pressure profile of the detonation was determined when the domain length is not sufficient and small disturbances propagate back after reflection from the subsonic boundary condition in the absence of a sonic plane to corrupt the detonation front [50]. The domain requirement calculation was performed based on the detonation domain formulation presented by Hwang [50] and an average value was found to be 39 HRL. Hence the detonation was placed at 25 cm from the rear boundary and the length of the domain was taken to be 30 cm. A base grid resolution of 16 cells per HRL is used with a maximum grid resolution of 128 cells per half-reaction length with a 5 cm domain height. For this domain height, only a single mode detonation is expected since the size of the cell is 10 cm. The scheme and boundary conditions used in this setup are the same as used in the multistep chemistry problem in chapter - 4. From the GRI 3.0 solution, the upper and lower limits of the domain length requirement are calculated as shown in [50].

$$D = \frac{2243}{356} = 6.36$$

$$T = t_o * \left(\frac{c_o}{L_{ref}}\right) = 62.52$$

$$C = \frac{D(A - D)}{A}$$

Table 6-5 Domain Length Limits Using Stationary Reference Frame For Oxymethane Detonation at 6 kPa

Parameter	VN State	CJ State	Unit
γ	1.17	1.23	-

T	1729	3220	K
u	1976	988	m/s
c	1267	793	m/s
$A = (u + c)/c_o$	7.78	6.33	-
C	1.21	0.03	-
L_{domain}	75	2	$\lambda_{\frac{1}{2}}$

6.2.3 Global Behavior

The instantaneous velocity of the detonation is shown below for all the four grid resolutions. The grid convergence is expected to be delayed due sensitivity of the explicit solver to the difference in the global time step as shown in chapter 4 for hydrogen-oxygen detonation. The simulations up to 64 HRL was run longer (up to 0.0007 sec) compared to the fine grid resolution of 128 HRL (up to 0.0004 sec). Though the detonation propagates in a 5 cm tube, the velocity profile is comparable with the 10 cm cases used in the global one-step chemistry model. The lower limit of the cell cycle is close to 0.70 D/D_{CJ} and the upper limit is around 2.0 D/D_{CJ}using a multistep chemistry model matching the viscous global one-step results. Even though this result also matches the inviscid one-step chemistry results, few overshoots above 2.0 D/D_{CJ} and undershoots below 0.70 D/D_{CJ} are displayed in the inviscid results. The average detonation velocity using 128 cells per HRL matches very closely with the experimental average with a 0.4 percent difference. This average velocity has the least deviation compared to the global one-step chemistry simulations and the same behavior was also observed in regular detonations. Since the detonation can be categorized to be an ordinary detonation, the reinitiation mode can be compared with its 10 cm with counterparts from previous simulations.

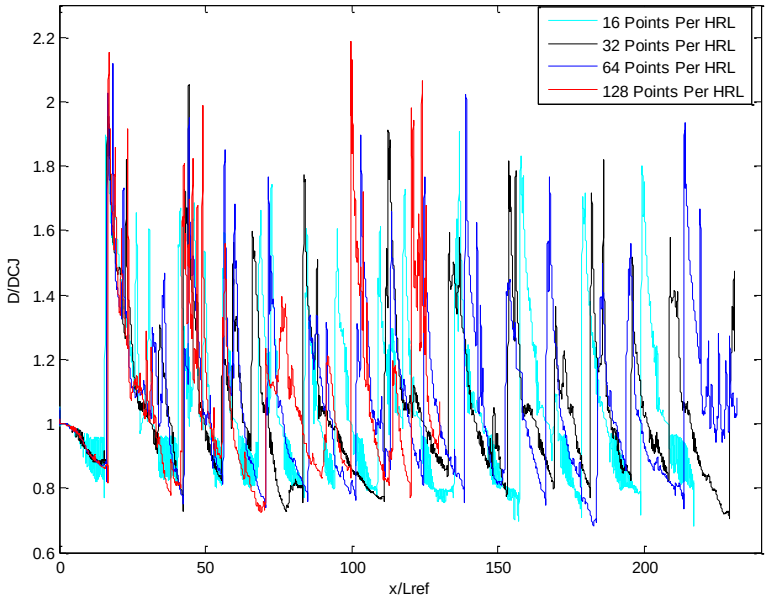

Figure 6-16 Instantaneous Velocity Profile of Oxymethane Detonation using Reduced Chemistry Mechanism

Table 6-6 Mean Detonation Velocity Ratio Using Reduced Chemistry at Different Grid Levels

Case-B	32	64	128	Difference %	Experimental Value [44]
Inviscid-Multistep Chemistry	1.06	1.02	0.983	0.4%	0.979

The probability density function of the average velocity at 128 cells per HRL is shown below. The function peaks at 0.82 D/D_{CJ} which is slightly higher than the viscous one-step chemistry model and a prominent second peak close to 1 D/D_{CJ}. This second peak was also observed in the viscous simulation but below 1 D/D_{CJ}. No second peak in the PDF was observed in the inviscid global one-step chemistry. This prominent second peak indicates that there is an energy release method that makes the detonation spend time at CJ velocity which is not captured by the global one-step chemistry.

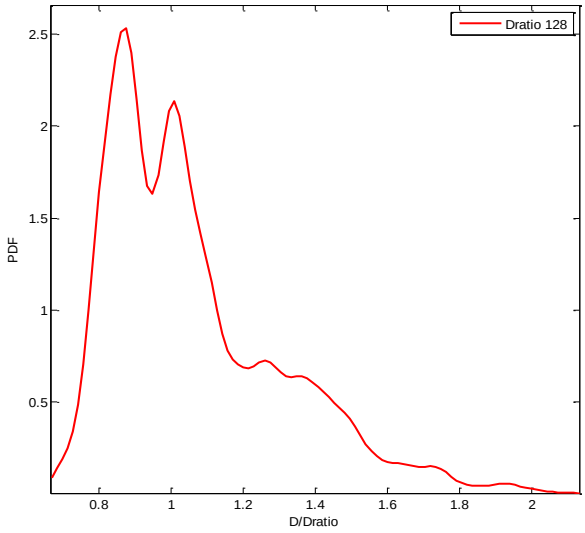

Figure 6-17 PDF of Instantaneous Velocity Ratio of $CH_4 - 2O_2$ Detonation at 6 kPa using Multistep Chemistry Model

The numerical soot foil for 128 cells per HRL is shown below. The soot foil clearly shows that the detonation operates in both a single-mode and a dual-mode detonation. The interaction of the primary triple point with walls are labeled from A-L. The detonation transitions to dual-mode in a short time at D-E. During the initial transient period, with single-mode detonation, the secondary cells are stronger which is labeled as S1 and S2. Once the detonation starts propagating with dual-mode detonation, the secondary cells were noticed to become weaker until it shifts back to a single-mode detonation (S3 and S4).

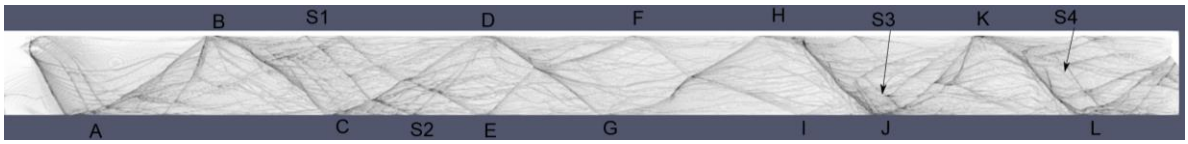

Figure 6-18 Numerical Soot Foil Comparison of $CH_4 - 2O_2$ Detonation at 6 kPa using Multistep Chemistry Model

The following tabular column shows the results of the Favre averaged variable and its comparison using the values obtained using the ZND theorem.

Table 6-7 Comparison of Favre Averaged Flow Profile With ZND Results for $CH_4 - 2O_2$ Detonation at 6 kPa using Multistep Chemistry Model

Flow Variable	ZND Value	Favre Averaged Value	Difference	Unit
Pressure	151283	167306	10.6%	Pa
Temperature	3224	3385	5%	K
Density	0.114	0.116	1.7%	kg/m^3
Velocity	1267	1259	0.6%	m/s
Average Sonic Plane	0.637729	3.98	-	cm
Reactant Mass Fraction (Theoretical)	0	Y_{CH_4} = 0.04 Y_{O_2} = 0.24	-	-
Reactant Mass Fraction (Favre Averaged)	0	0	-	-

As seen from the Favre averaged profile above, there is a major difference in the pressure and temperature quantities when compared with the theoretical values. The reason for this is the effect of high-pressure product gases produced by the transverse detonation along the detonation front on the moving column of products. This event is demonstrated in detail in the discussion subsection.

6.2.4 Structure of Triple Point

The triple point structure observed was the strong type triple points as observed in the inviscid and viscous models. But two types of structures of transverse waves were found to be reoccurring in this inviscid simulation using a multistep chemistry model. More precisely, the strength of the transverse wave complex

within the reactant jet exhibited two behaviors. First, the usually observed triple point structure with the transverse wave complex which has been observed in the previous two studies is shown and explained below. The density contour shows (Figure 6-20 a) two triple points TP1 and TP2 diverging in the opposite direction. Highly compressed regions of the density are reached behind the transverse wave systems TI1 and TI2 inside the curved jet due to repeated shock interactions. The transverse wave system TI1 and TI2 are labeled in the density gradient contour (Figure 6-20 b) with the points P1 - P3 and P4 – P7, respectively. The slip lines S1 and S2 are captured in the density contour and are found to undergo instability after interaction with the flames. It is also interesting to note interacting shockwaves inside the reactant jets beyond P3 and P6 which is not captured by the global one-step chemistry model. The pressure contour (Figure 6-20 c) also shows the highly compressed regions marked by maximum pressure inside the reactant jets. This compression by repeated shocks moves throughout the jet and increases the reaction rate of the jet as well as the unburnt pockets. The temperature contour (Figure 6-20 e) shows that the compressed region is not reacting. The darker lines in the temperature gradient contour (Figure 6-20 f) shows the instantaneous position of the flame behind the detonation. The upper and lower bounds of the variables are comparable with the bounds of flow variables obtained using global one-step chemistry.

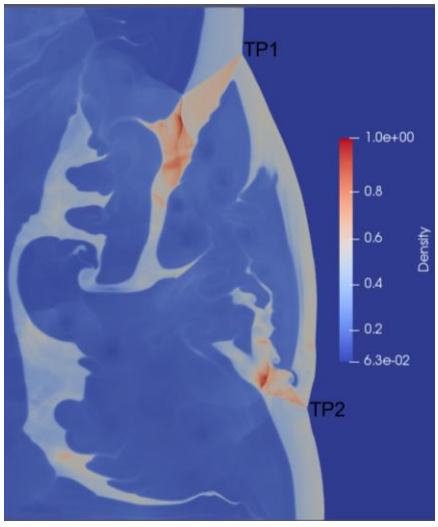

(a)

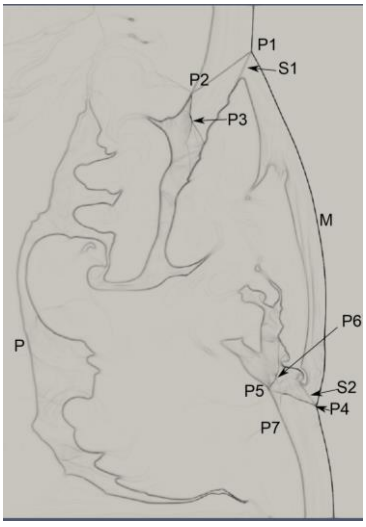

(b)

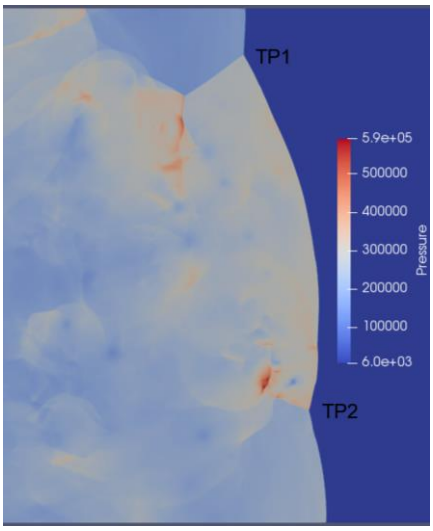

(c)

(d)

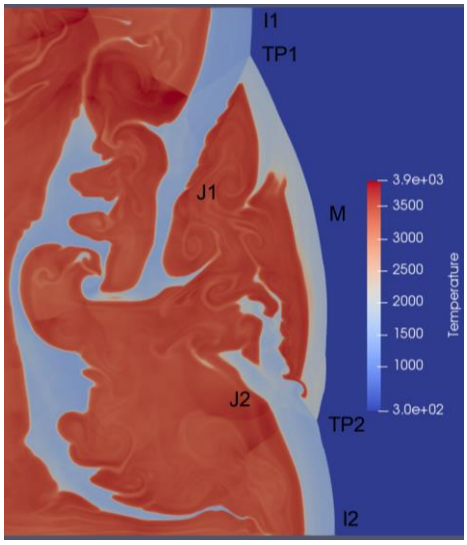

(e)

(f)

Figure 6-19 (a) Density (b) Density Gradient (c) Pressure (d) Pressure Gradient (e) Temperature and (f) Temperature Gradient Contour of $CH_4 - 2O_2$ Detonation at 6 kPa at T= 230

The newly observed transverse wave structure is formed due to the interaction between the shockwaves created during reinitiation or intermodal interaction and the transverse waves of a primary triple point. The properties and structure of the transverse wave structure are discussed using a single-mode detonation in the following set of contours. The density contour (Figure 6-21 a) shows the overall features such as the primary triple point TP1, four minor triple points MTP1-MTP4, Mach stem M, Incident shock I,

flame following the detonation F and the reactant jet J. The density contour gradient (Figure 6-21 b) shows two strong shocks present P3-P4 and P4-P5 in addition to the transverse wave system. Though these two shocks were found in the previous transverse wave system, it should be noticed that the density (Figure 6-21 a) and the pressure profile (Figure 6-21 c) created by the shock P3-P4 at the interface of the flame is more than twice in magnitude. This system also sweeps through the reactant jet as the triple point moves towards the wall. The location of the flame following the detonation behind the Mach stem, Incident shock, and along the Jet can be located using the temperature contour (Figure 6-21 e) and its gradient (Figure 6-21 f). Though the density and temperature has peaked at P4, no increase in temperature was observed. The formation of this second system of strong reflecting shocks inside the reactant jet is explained in the following section on the reinitiation mechanism.

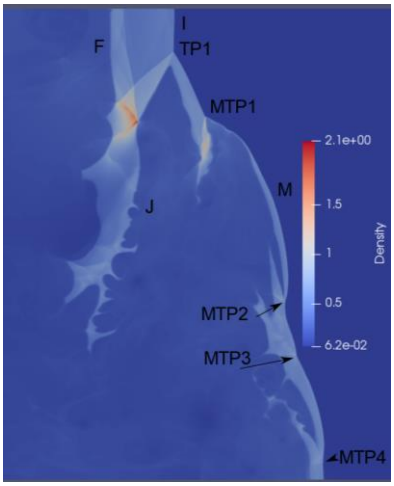

(a)

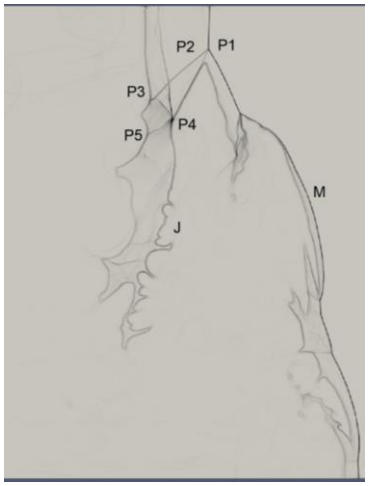

(b)

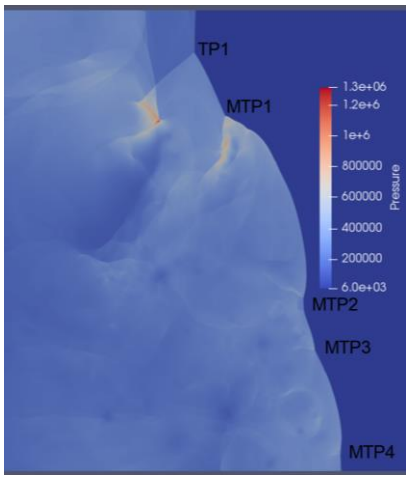

(c)

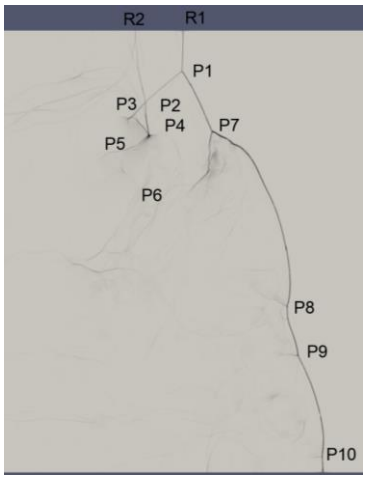

(d)

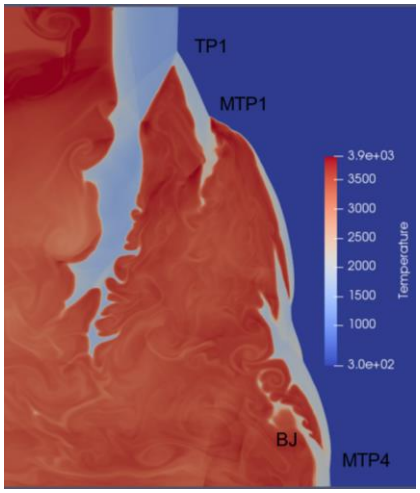

(e)

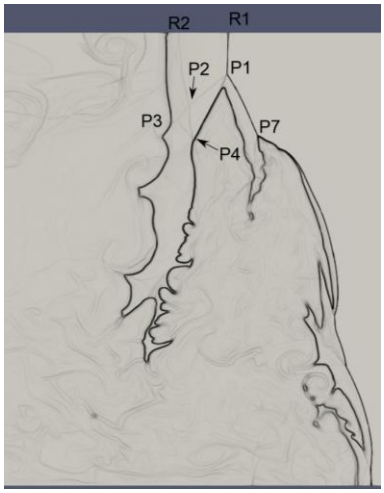

(f)

Figure 6-20 (a) Density (b) Density Gradient (c) Pressure (d) Pressure Gradient (e) Temperature and (f) Temperature Gradient Contour of $CH_4 - 2O_2$ Detonation at 6 kPa at T= 86

6.2.5 Reinitiation Mechanism

The Mach stem based reinitiation mechanism is explained first followed by the triple point reinitiation mechanism. The hotspot mode reinitiation is explained below where the position of the flame is tracked using the H20 mass fraction contour overlapped by the pressure gradient plot to identify the location of shockwaves. At t=196 μsec the triple point TP1 approaches the wall. The secondary triple point is labeled as P2 and the transverse wave system consisting of the points TP1-P2-P3-P4-R1 is moving within the

reactant jet as well as the flames. The extended transverse wave reflects off the wall at R1. At t=200 μsec, the triple point TP1 has reflected off the wall and has resulted in a non-reacting Mach reflection structure. This Mach reflection pattern consists of new triple point TP2, Mach stem M, secondary triple point STP2, extended transverse wave ET2 which reflects off the wall at R2. At t=204 μsec, the Mach stem M grows and the flame F following the Mach stem reaches the wall. The shockwave SW1 which was a part of the transverse wave system of TP1 is curved and moving forward as the flame F meets the wall. The reactant jet of TP1 is detached and becomes the reactant pocket P. The flame also produces a precursor shock SW2 which is curved along with it. At t=207 μsec the shockwaves SW1 and SW2 are decayed to weak pressure waves WP1 and WP2. The shockwave SW3 resulting from the flame wall interaction proceeds towards the Mach reflection. At t=208 μsec, the weak pressure waves WP1 and WP2 have merged to become the pressure wave WP3. The shockwave SW3 along the wall moves into the induction zone and transforms into a shocklet. Another shockwave SW4 is formed as the flame moves upstream along the wall. The product starts forming along the contact surface with a slow increase in H2O mass fraction labeled as A. At t=211 μsec, a hotspot HS1 has been formed and transported by the contact surface. The shocklets continue to move upstream. At t=212 μsec, the hot spot HS1 develops further and the curved contact surface pushes the Mach stem M to form a slight curvature.

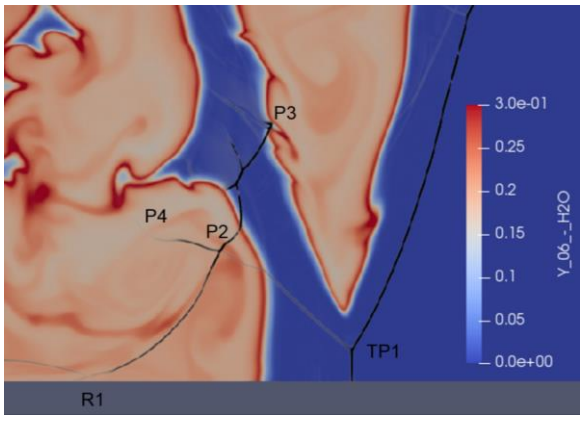

t= 0.000196 sec

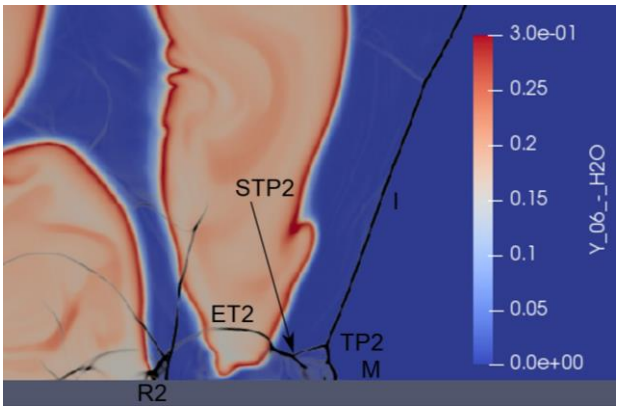

t= 0.00020 sec

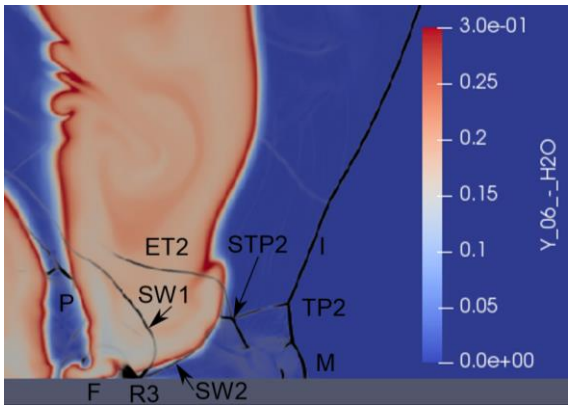

t= 0.000204 sec

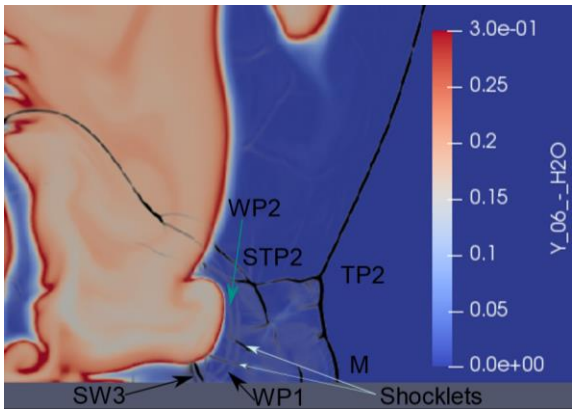

t=0.000207 sec

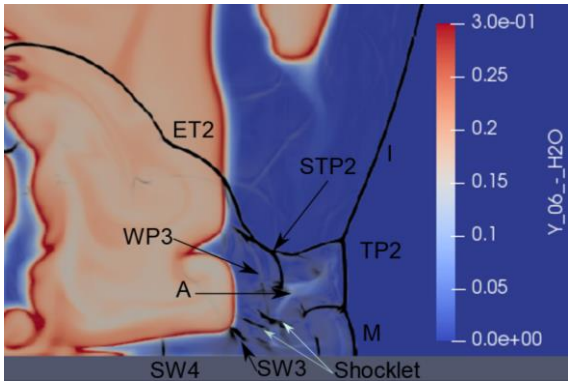

t=0.000208 sec

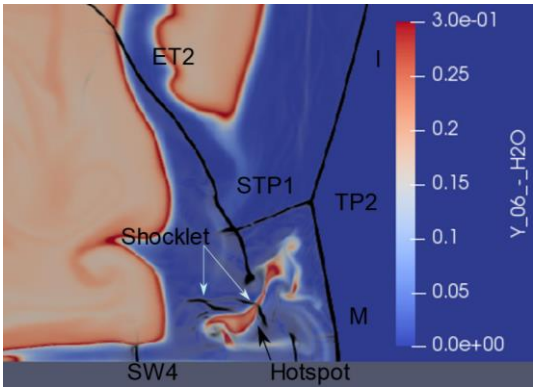

t=0.000211 sec

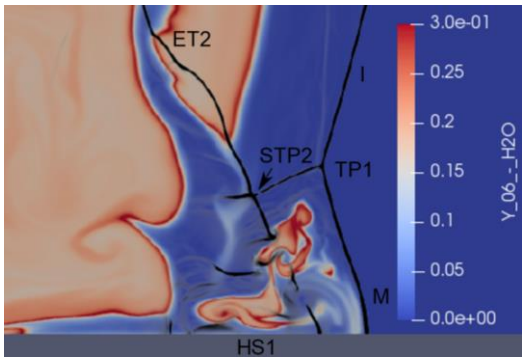

t=0.000212 sec

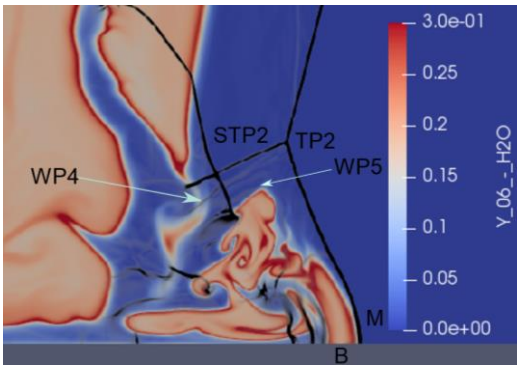

t= t=0.000214 sec

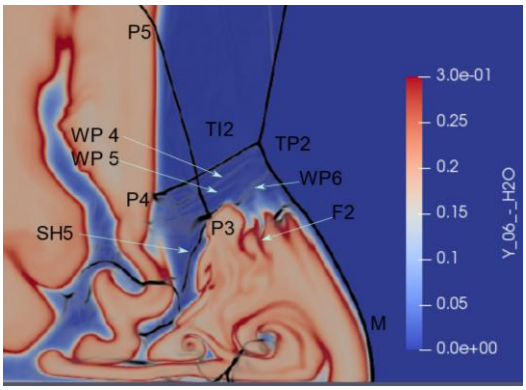

t=0.000217 sec

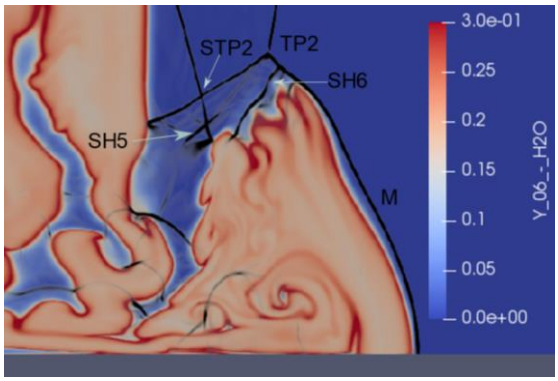

t=0.000218 sec

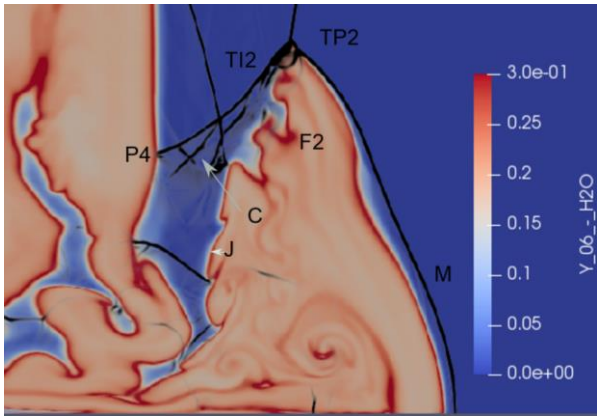

t=0.000220 sec

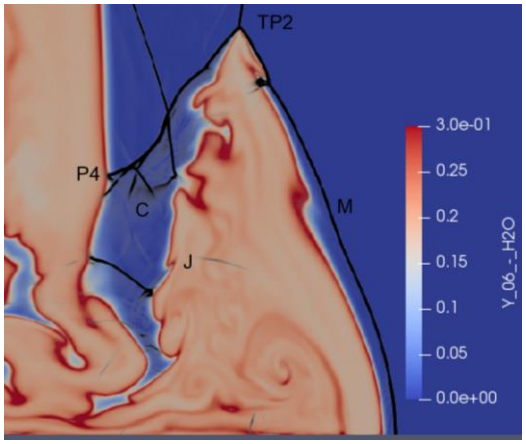

t=0.000221 sec

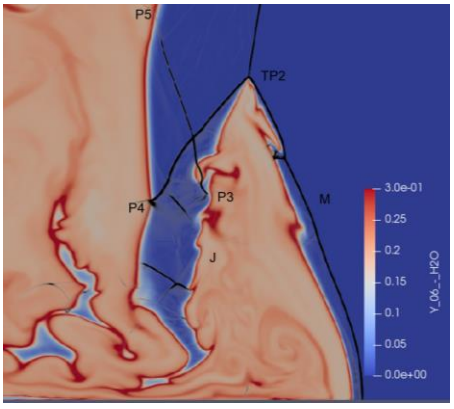

t=0.000222 sec

Figure 6-21 Mach Reflection Reintiation (Slip line-Hotspot) Event of $CH_4 - 2O_2$ Detonation at 6 kPa using Multistep Chemistry Model

At t=214 μsec, the hotspot which was incipient at the bottom of the Mach stem has progressed and coupled to the Mach stem resulting in acceleration with an increase in the curvature of the Mach stem. The development and movement of the hot spot also create weak pressure waves WP4 and WP5 moving in the upward direction. At t=217 μsec, apart from the weak waves WP4-WP6, shock waves (SH5) are created along with the flame F2 as the hot spot region grows. The transverse wave system (TI2) is also prominent and is labeled using the points TP2-P3-P4 and P5. At T=218 μsec the shock wave SH 5 slowly decays but a new shock wave SH6 is created by the flame as it moves towards the triple point TP2. The interaction of these feedback shockwaves with the transverse wave produces a transient shock wave system labeled as C. The process of these feedback shockwaves merging on the transverse shockwave TP2-P4 is captured at t= 221 μsec. The strong transverse wave structure is created after the collision of the feedback shock waves (t=222 μsec) forming the highly compressed region as shown by the pressure and density contour below.

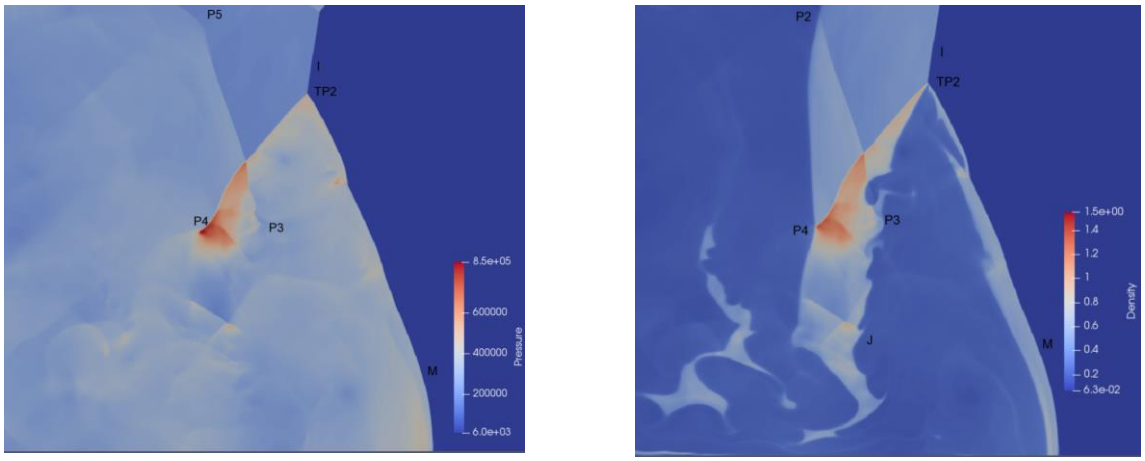

(a) (b)

Figure 6-22 (a) Pressure and (b) Density Contour of $CH_4 - 2O_2$ Detonation at 6 kPa at t=0.000222 sec

The high-pressure point is formed at P4 where the transverse wave meets the flame. Thus, depending on the intensity of the shockwaves the highly compressible region is formed. The difference between the triple point reinitiation mode observed using the multistep chemistry is briefed below. At t= 309 μs the triple point TP1 approaches the wall with a thick induction zone behind it. At t= 310 μs the reinitiation

results in the newly formed triple point TP2 and the extended transverse wave ET which reflects along the wall at R1. The reactant jet of triple point TP1 is split into two pockets of reactants P1 and P2 at t= 311 μs. The initial transient interaction of the extended transverse wave with the reactant pockets varies slightly. The transverse wave ET2 transforms into a detonation as it travels through the pocket P2 were as it is still a decoupled shock/flame complex F2 when it interacts with the pocket P1. The reaction in the pocket P1 has progressed considering the higher H20 mass fraction when compared to the pocket P2. This varies the speed of sound between the pockets causing this slight difference in the time taken for coupling of the shock wave and the flame. Both the pockets are processed by detonations formed by transverse shock at t = 312 μs and 313 μs. An 'M' shaped reactant jet is formed by the triple point TP2 due to the presence of an additional minor triple point. The flames bounding this jet is labeled as F3. The shock SH2 is a portion of the extended transverse wave ET2 which is competing with the flames F3. The shock SH2 is still inert at t= 314 μs and is starting to interact with the flame F3. It can also be seen that the detonations D2 and D3 are now decoupled shockwaves passing through the pockets P2 and P3 (t=314 μs). This decoupling may occur due to several reasons such as the loss of transverse wave strength, reduction in the reactant mass since it is being partially consumed by the flame supported by the surrounding products as can be seen by the slimming of pocket regions before the shock interacts, reaction progress of the pockets by itself, etc. At t = 317 μs, the pocket P3 is consumed completely and the pocket P2 is still reacting. Also, the secondary triple point STP2 has started to react which can be seen by the sudden combustion of the left half of the 'M' shaped Jet. The detonation D3 has grown from a small zone to half the size of the reactant jet. The shockwave before the right half of the M jet has not yet coupled with the flame F3 until t = 317 μs. At t= $318\,\mu s$, the D3 has grown successfully due to the coupling of the shock and flame. This sudden consumption of the jet also emits shockwaves labeled as SH3.

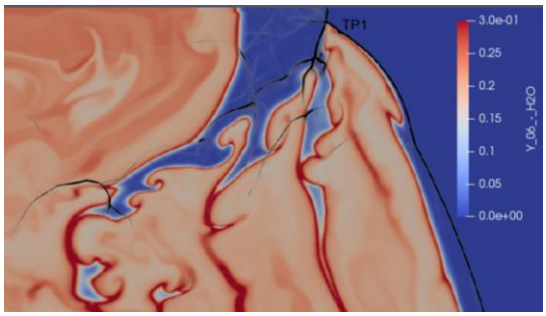

t=0.000309 sec

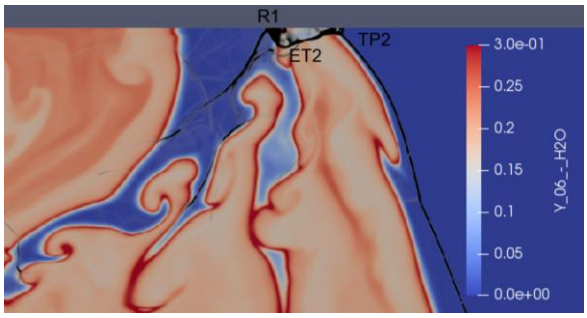

t=0.000310 sec

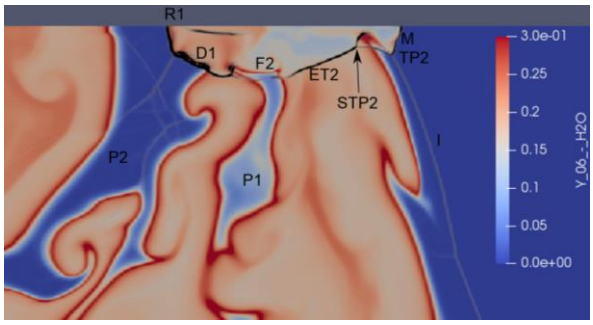

t=0.000311 sec

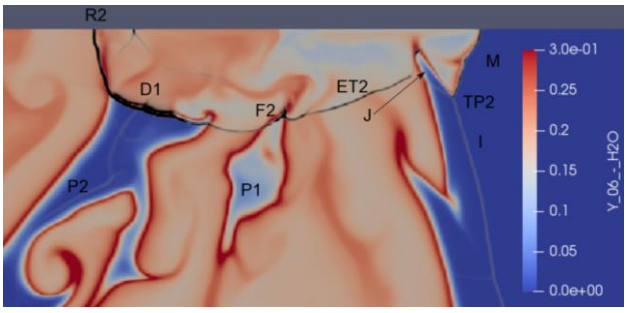

t=0.000312 sec

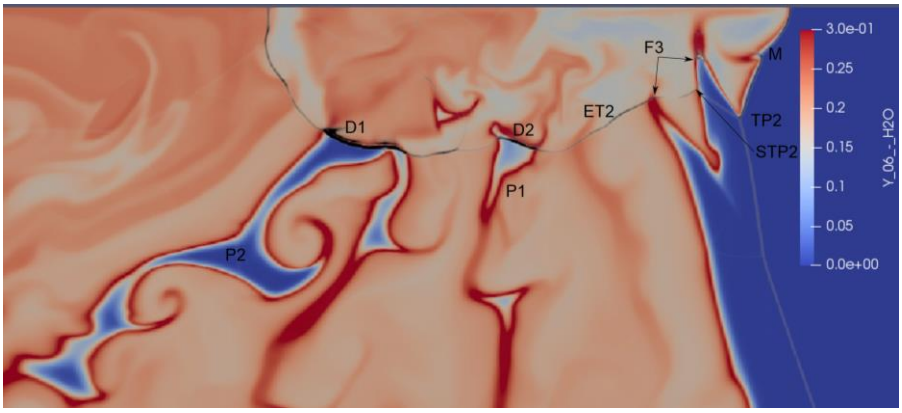

t=0.000313 sec

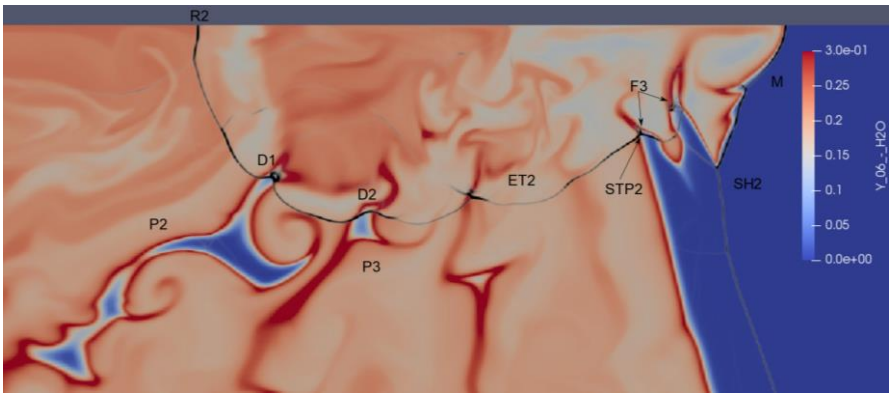

t=0.000314 sec

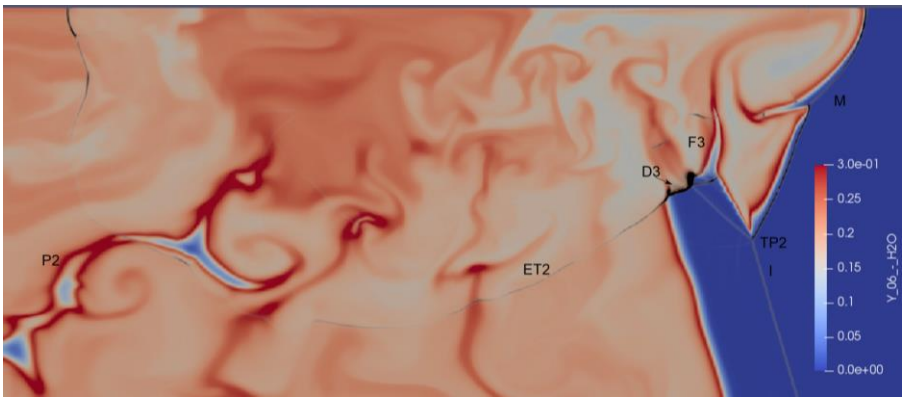

t=0.000317 sec

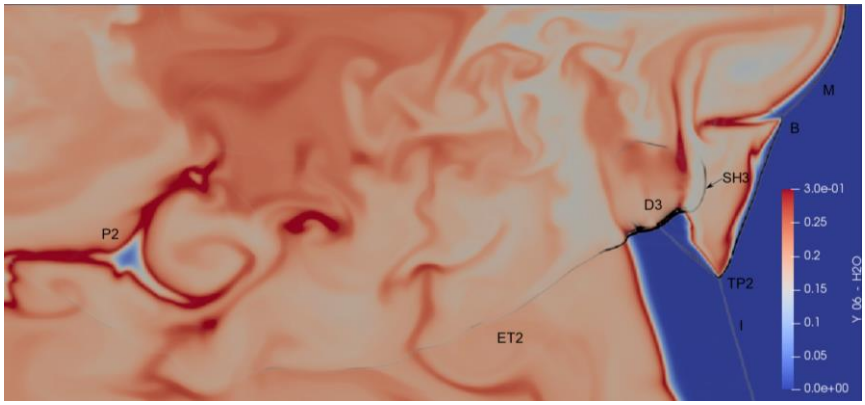

t=0.000318 sec

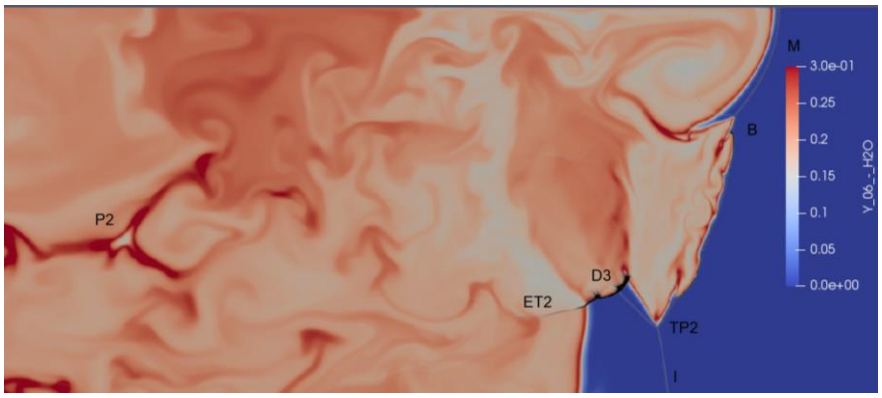

t=0.000322 sec

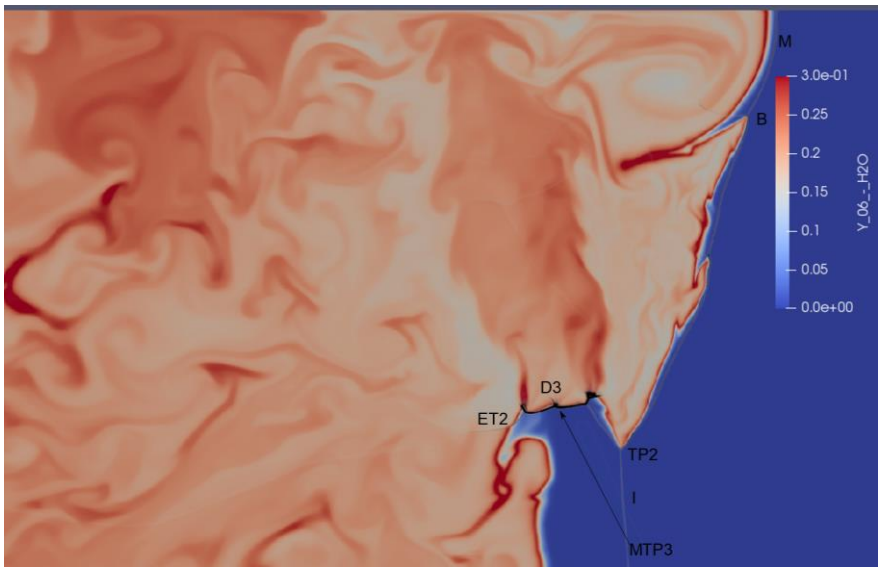

t=0.000324 sec

Figure 6-23 Triple Point Reintiation Event of $CH_4 - 2O_2$ Detonation at 6 kPa with Transverse Detonation Using Multistep Chemistry Model

At t= $322\ \mu s$, the detonation D3 consumes the heated reactants in the induction zone of the shock I. the extended transverse wave ET2 also slowly decays in strength as shown by the fading pressure gradient profile in the contour. The reactant pocket P2 which has survived after the passage of transverse shock is close to complete burn out. The transverse detonation exhibits its minor triple point marked as MTP3 at t= 322 μs and t = 324 μs. Thus, the evolution of the transverse wave was captured using the multistep chemistry model which did not occur in the global one-step chemistry model. Experimental observation [62] of transverse detonation for an oxymethane detonation is shown below

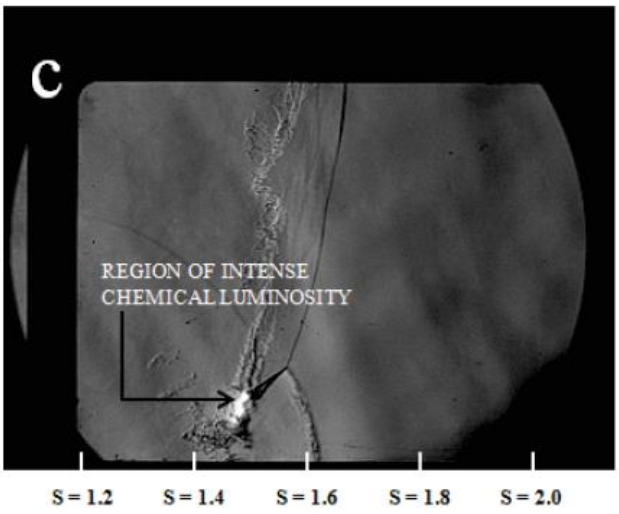

(a)

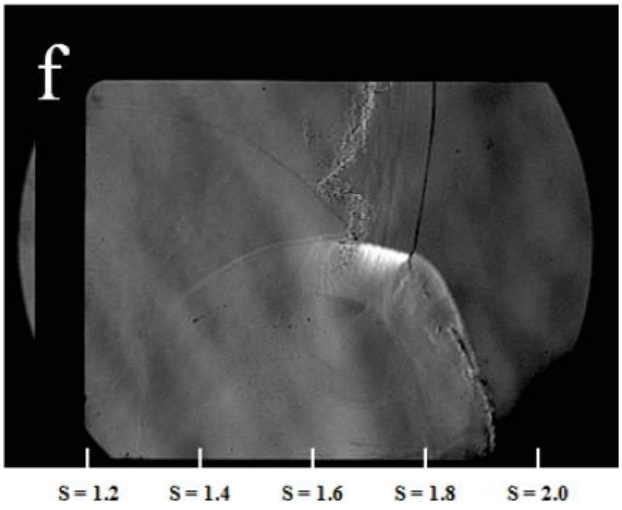

(b)

Figure 6-24 Schiliren Image Showing the Onset (a) and Propagation (b) of Transverse Detonation of an Oxymethane Detonation at 10.4 kPa (taken from [62])

The same pattern of transverse detonation originating from a localized region labeled as the region of intense chemical luminosity [62] (Figure 6-25 a) followed by spreading and propagation of transverse detonation into the induction zone (Figure 6-25 b) was also observed in this study. Transverse detonations are also reported in other research works both experimental and numerical which analyzed the structure of detonation such as in [115, 40, 39, 169]. The final Mach reflection-based reinitiation mechanism was observed due to the curved slip line mechanism is explained below. A triple point TP1 results from a Mach

reflection based reinitiation along the bottom wall at t= 156 μs . The flame F1 is about to reach the wall. At t= 158 μs, the flame contacts the wall at R1 while the non-reacting Mach reflection has grown. The high-pressure region behind the flame F2 and the curving action of the contact surface (as detailed in chapter 5) influences the flame to travel towards the Mach stem M. The shock wave SH1 which is set off by the movement of flame F2 is also captured. The flame reaches and couples with the Mach stem within the timescale of an order of 10^{-8} sec at t= 159 μs. The movement of the flame towards the triple point TP1 also triggers another shock wave PW1. The secondary triple point STP1 and extended transverse wave ET1 is also formed. The bifurcation of the Mach stem M is labeled as B. The flame couples with the triple point at TP1 at t = 160 μs and the formation of the reactant J with the curvature towards Mach stem has developed due to the movement of triple point TP1 in the upward direction at t= 162 μs.

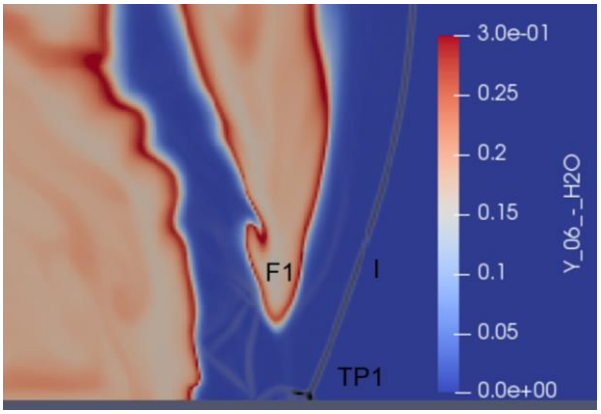

t=0.000156 sec

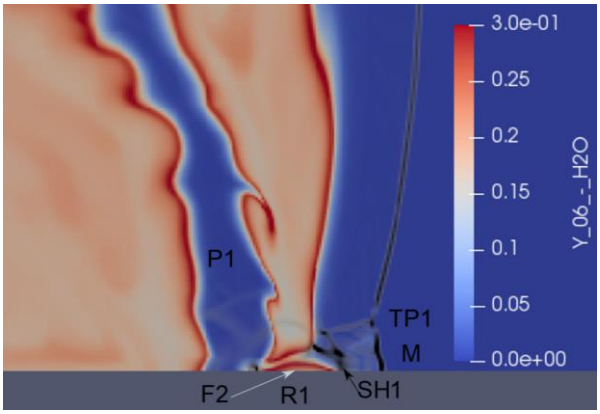

t=0.000158 sec

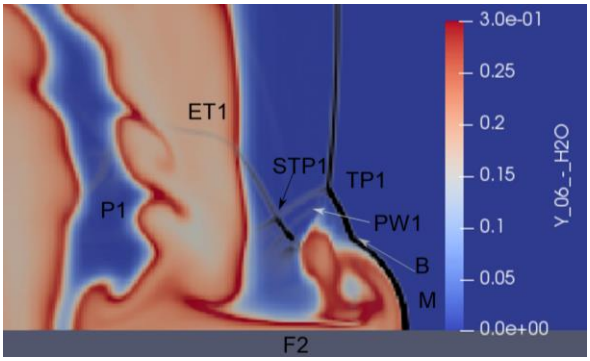

t=0.000159 sec

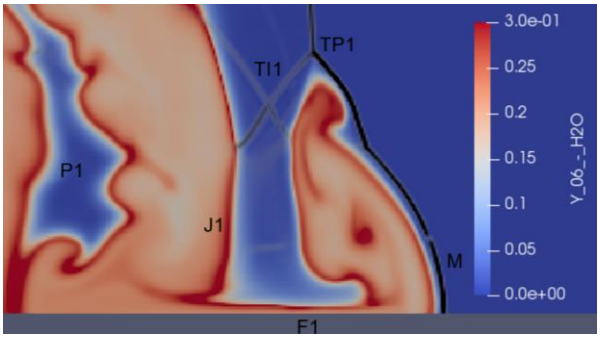

t=0.000161 sec

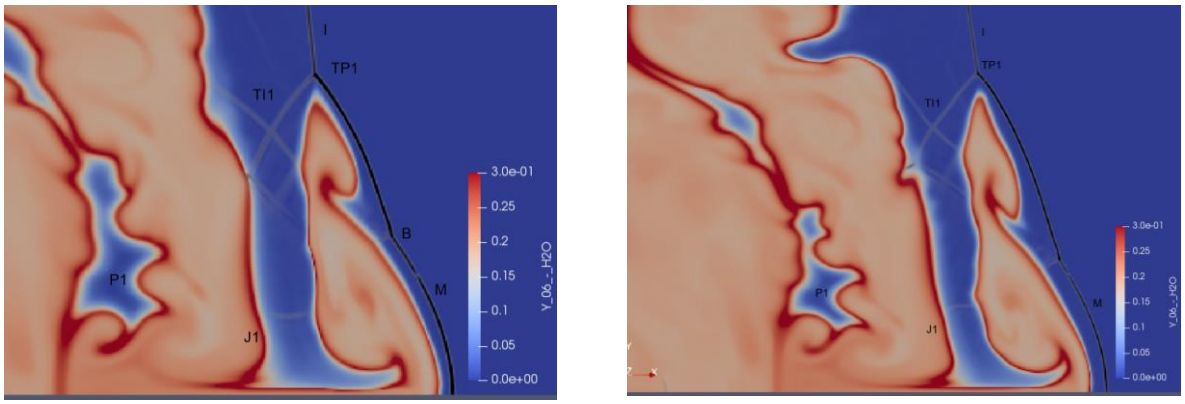

Figure 6-25 Mach Reflection Reintiation (Slip line-Flame) Event of $CH_4 - 2O_2$ Detonation at 6 kPa using Multistep Chemistry Model

6.2.6 Discussion

With all the reoccurring reinitiation modes explained using the multistep chemistry, the reason for the variation in parameters and features are explained in this section. The first major difference in reinitiation modes studied using the multistep chemistry model is the interaction between the reaction zone and the incident or transverse shock system. As briefed in the discussed reinitiation sequences, the reaction zones in both the Mach reflection reinitiation modes transmits shockwaves to the non-reacting Mach stem. Feedback shockwaves from reinitiation are also observed using Schlieren images of oxymethane detonation experiments [62]. The overall timescale of the inception of hotspot after triple point reflection was 11 μs. The reinitiation from the hotspot inception (t=208 μs) to coupling of reaction zone to Mach stem (t=217 μs) is 9 μs. As mentioned in the previous chapter, the acoustic time scale, which is the time scale of gas dynamics to react to the exothermic reaction, was in the order of 1 μs. Since the minimum time step for the solution using global one-step chemistry was 5.57 μsec in the inviscid model and 2.6 μsec in the viscous model, the gas dynamic feedback was not resolved which is evident due to the absence of the strong compression region in the triple point transverse wave structure. Even if the grid resolution is made finer to solve for the solution with a global time step of 10^{-7} sec, it may result in false flow variable values since the predicted pressure and temperature levels were observed to be at least twice the magnitude of

maximum flow variable limits predicted by the one-step chemistry models where the constant molecular weight assumption could give rise to deviation. Secondly, deviation in the Favre averaged variable profile obtained from multistep chemistry when compared with the global one-step chemistry was observed especially for the averaged pressure. As explained in Chapter 4, the Favre averaging of the variables is performed for random sets of time steps for up to 50 data sets, and a single profile is obtained using ensemble averaging. To explain the factor causing the difference two events (at t= 99.3 μs and t= 112.6 μs) are chosen and its Favre averaged flow profile is presented below. The instantaneous location of the shock front was at 17.4 cm (t= 99.3 μs) and 16.8 cm (t= 112.6 μs). The slice section was placed at 9.3 cm (ensemble-averaged sonic plane) for both the events.

Table 6-8 Favre Averaged Flow Variables at Two Events Before and After Transverse Detonation

t (μs)	ρ (kg/m^3)	Deviation	P (Pa)	Deviation	T (K)	Deviation	V (m/s)	Deviation
99.3	0.116	1.8	157165	3.9	3322	3.0	1246	1.6
112.6	0.128	12.2	188023	24.1	3472	7.6	1338	5.6

The pressure gradient contours and the slice section (S) are shown for both events in the following figure.

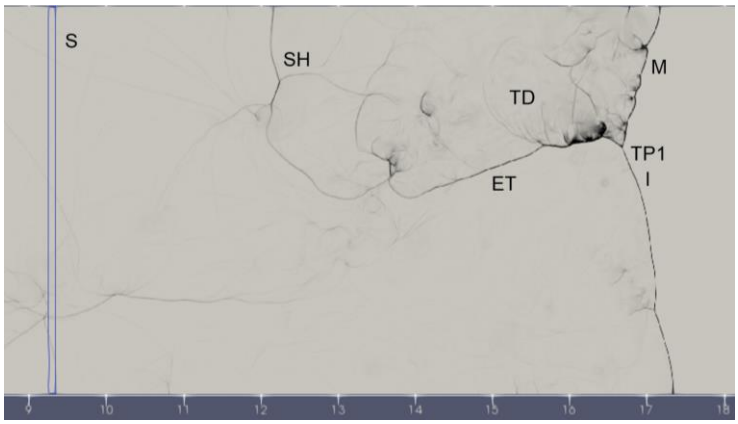

t=99.3 μs

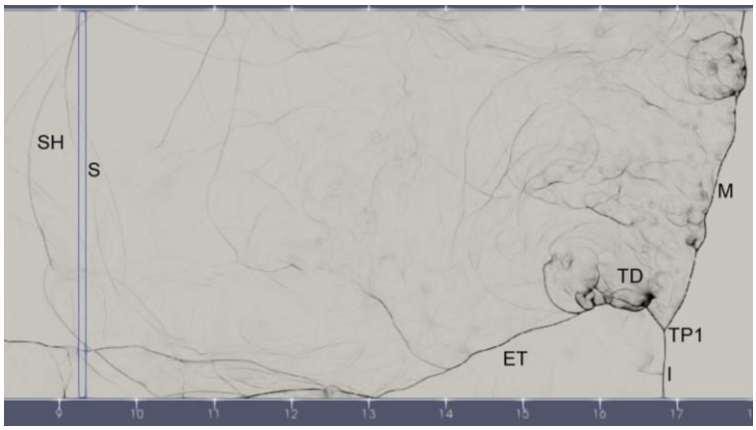

t=112.6 μs

Figure 6-26 Pressure Gradient Contour of Oxymethane Detonation at 6 kPa at Two Events Before (t=99.3 μs) and After (t=112.6 μs) Transverse Detonation

As shown in the Figure 6-27 and table 6-8 above, direct reinitiation has occurred at t=99.3 μs and resulted in the Mach stem M with a triple point TP1 and transverse detonation ET. Additionally, the strong set of shockwaves SH is produced which is often referred to as backward propagating shock in the literature [52]. Before the intervention of this backward propagating shock system, the Favre averaged value in the table was well within the bounds predicted by the ZND analysis using detailed chemistry mechanism at t=99.3 μs. At t=112.6 μs, the values of the Favre averaged variables increase as this shock wave system passes the location of averaging increasing the thermodynamic variables. We can also notice that the pressure variable had the maximum increase (~ 24%) followed by density (~ 13%), temperature (~ 7.6%), and velocity (~ 5.6%). It is to be noted that this shockwave system SH propagates through the products increasing the sonic velocity of the gas and the distance for achieving the averaged sonic plane. It also increases or decreases the velocity of moving gas depending upon its orientation and strength. With ensemble averaging at the sonic planes, the variables matched closely with the analytical values with the deviation in pressure being the highest. The third important factor to be noted from the results of multistep chemistry simulation is the average penetration distance of the unburnt reactant pockets. From seven repeated experiments of the same conditions for an oxymethane detonation used in the study, the total burnout distance of the gases was determined to be within 3 cm [44]. From the inviscid and viscous global

one-step chemistry, we observed that the Favre averaged reactant mass fraction was 3 % and 1% at the averaged sonic plane distance of 14.5 cm and 13.9 cm. But the averaged sonic plane shows 0% presence of reactant mass fraction with the multistep chemistry case. Hence, the reactant pockets are tracked using the mass fraction of the CH_4 molecule which does not take part in the hydrogen oxygen sub mechanism. A graph of the reactant mass fraction penetration distance versus nondimensional time is shown in the graph below.

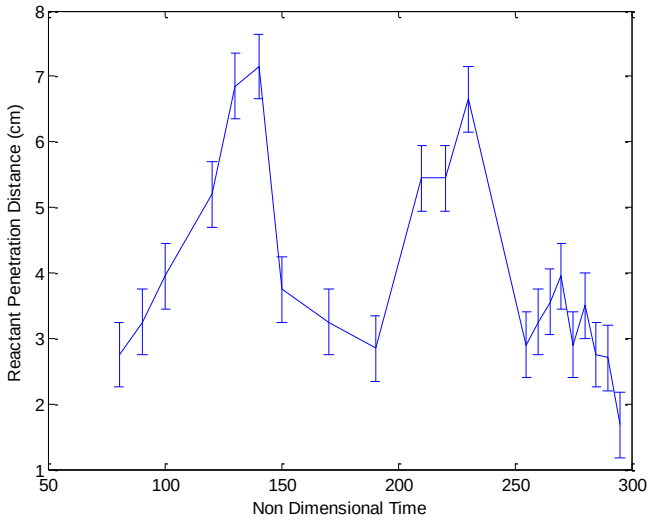

Figure 6-27 Reactant Peneratration Distance at Various Time Levels of Oxymethane Detonation at 6 kPa using Multistep Chemistry Model

Though the height of the domain was only 5 cm, the average reactant penetration distance of 3.98 cm was obtained with a multistep chemistry model which is shorter by 10.52 cm compared to the inviscid model and 9.92 cm compared to the viscous model. The penetration distance was less than 3 cm when the triple point reinitiation mode was observed. Thus, with more reoccurrence of direct reinitiation, the average penetration distance of the reactant pocket should reduce further. Finally, direct reinitiation mode along the wall resulted in transverse detonation waves in this study. It is a peculiar feature since the reactants for this transverse detonation is by the induction zone of the precursor shock itself. It also played a huge role in reducing the penetration distance of the reactants because it was strong enough to combust the gases behind it immediately as well as through the strong shock and transverse waves it resulted in. The profile

of a transverse detonation was investigated further to understand the jump conditions along with the transverse detonation. A line plot profile (L) across the transverse detonation (TD) observed at t=327 μs is shown in the Figure 6-29 a. The numerical soot foil produced by the transverse detonation is marked as SF is shown in Figure 6-29 b. From the density contour and the soot foil, we can notice that the transverse detonation has its own precursor shockwave containing instabilities.

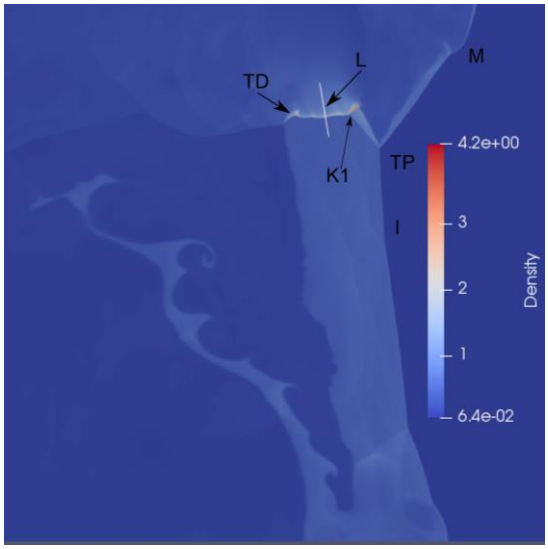

(a)

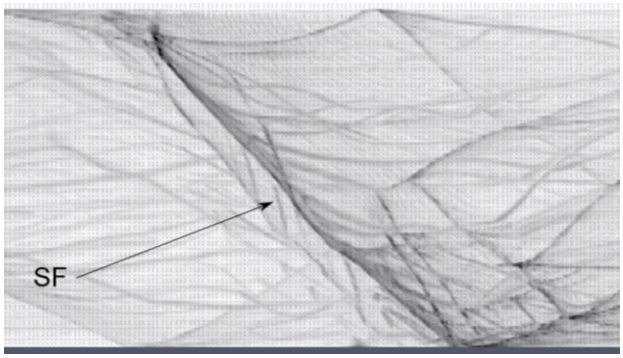

(b)

Figure 6-28 (a) Density Contour (b) Numerical Soot Foil showing the Propagation of Transverse Detonation at t=327 μs

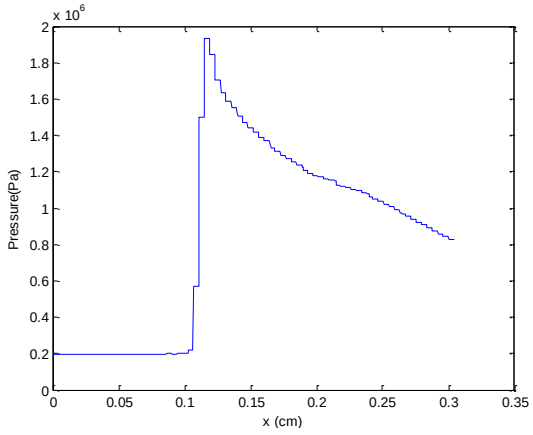

(a)

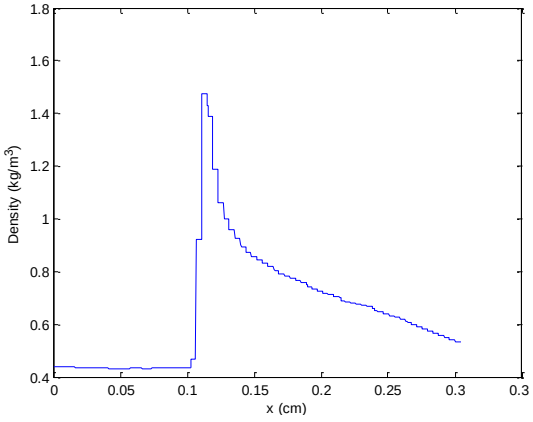

(b)

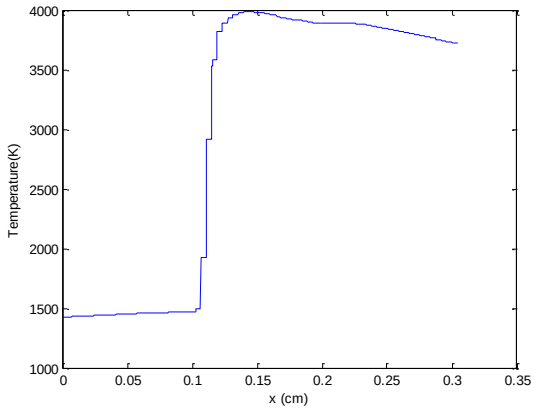

(c)

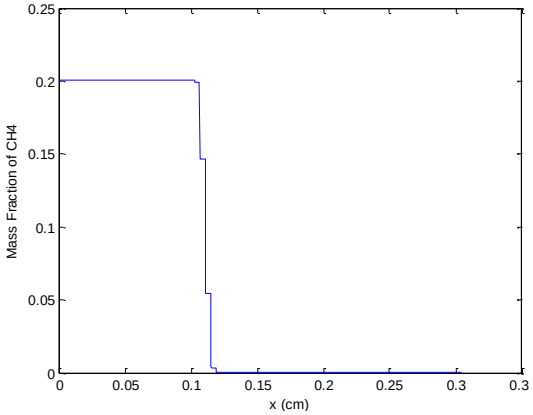

(d)

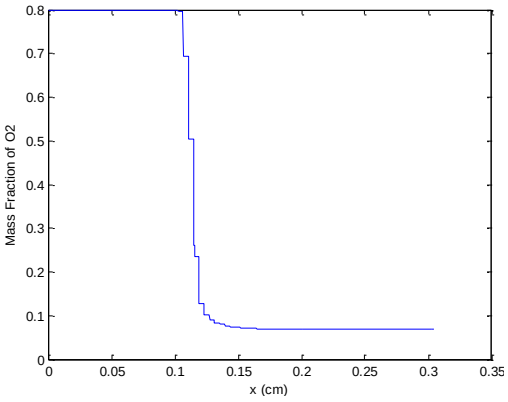

(e)

Figure 6-29 Plot of (a) Pressure (b) Density (c) Temperature (d) Y_{CH_4} and (e) Y_{O_2} across the Transverse Detonation at t=327 μs

The initial and final conditions of the flow variables through the transverse detonations can be seen in the plots above in Figure 6 - 30. We can see that the initial pressure, temperature, and density parameters are slights lower than the Von Neumann conditions predicted by the ZND theory. It is because the induction zone consumed by the transverse detonation is processed by a decaying incident shock (I). The structure of the reaction zone of the transverse detonation (TD) appeared to be reacting immediately behind the shockwave without delay. A kink K1 is formed by the transverse detonation wave which is due to the different condition of incoming gases processed by the triple point TP and incident shock I. The pressure, density and temperature jump conditions through TD at t=327 μs are $\frac{P_{TD}}{P_{VN}} = 9.7$; $\frac{\rho_{TD}}{\rho_{VN}} = 3.4$ and $\frac{T_{TD}}{T_{VN}} = 2.72$.

The temperature gradient of the transverse detonation TD is shown in Figure 6-31 (a). The transverse

detonation is labelled as TD with the kink at K1. There is a region of lagged reactants L providing evidence that the detonation burning the reactants processed by the triple point is decaying. The transverse detonation wave induces a strong normal component to the velocity field in the stationary reference frame. This results in the shock wave SH1. The shock joining the TP and K1 is the inert transverse wave ET1. The transverse wave becomes inert again after the point P1 since it travels in product gases and is labeled as ET2. A slip line SL arises at K1 which separates the gases passed through TD and Mach stem M. This slip line undergoes KH instability and proceeds to roll up as a vortex (V) on the upper wall. Figure 6-31 b shows the velocity magnitude contour along with the streamlines overlapped on it. The streamline captures the vortex V, the shock wave SH and the extended transverse wave ET2. The flow field created by the transverse detonation TD creates a strong deflection (D) to the velocity field observed through the streamline plot in the stationary reference frame. There is also another slip line formed at P1 which is the junction of the extended transverse wave ET2 and the transverse detonation TD. This slip line is also seen to undergo KH instability as it travels towards the wall.

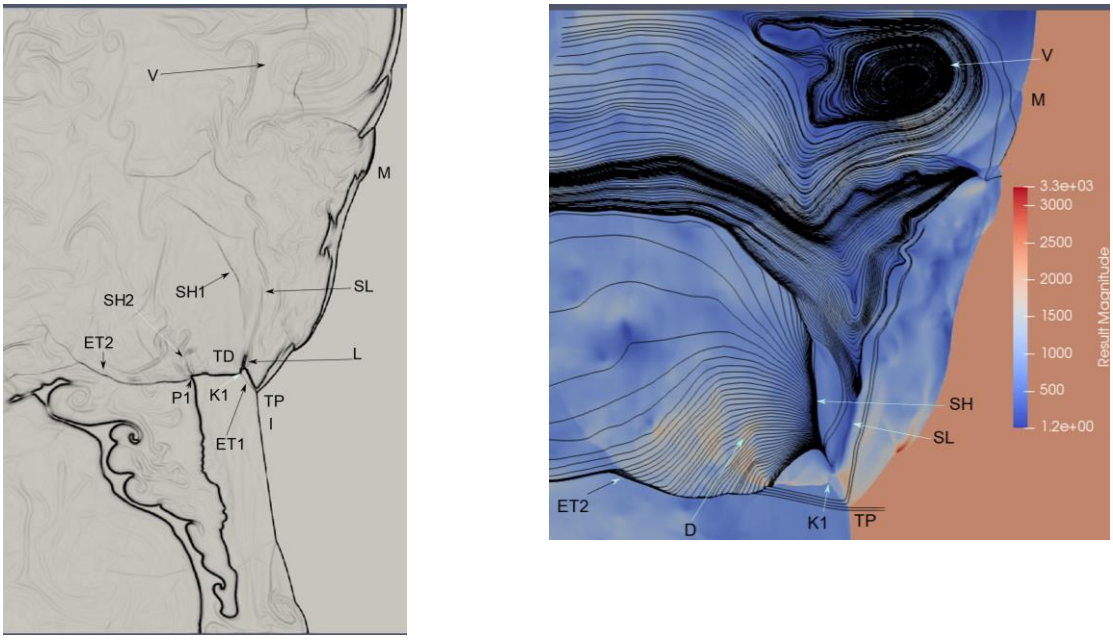

(a) (b)

Figure 6-30 (a) Temperature Gradient Contour (b) Velocity Contour With Streamlines of the Transverse Detonation at t=327 μs

The above results demonstrate the presence and importance of transverse detonation in a highly unstable detonation propagation. It is also clear that this important reinitiation and propagation mode was not captured using the global one-step chemistry models. Since all the reported features observed in experimental observation [62, 44], with the same conditions used in this study, has been found and the reasons for their evolution were discussed, the reinitiation study of the highly irregular detonation is concluded in this section.

6.2.7 Summary

The influence of molecular transport and finite rate chemistry on the reinitiation mechanism of highly unstable detonation was studied in this chapter and compared with the reinitiation modes obtained using inviscid global one-step chemistry explained in the previous chapter. The viscous global one-step chemistry model was used with a globally fourth-order accurate WENO/CD solver with the finest grid resolution of up to 288 cells per HRL. No new reinitiation mode was observed using the viscous global one-step chemistry compared with the inviscid global one-step chemistry model. Following that, a reduced chemistry mechanism was derived from the detailed GRI 1.2 mechanism and validated using ZND analysis. A two dimensional, inviscid, Roe-HLL MUSCL solver was used along with the derived reduced mechanism to analyze the reinitiation mechanism of an oxymethane detonation at 6 kPa. Three different and simultaneous modes of energy release were determined, the primary modes, secondary modes, and transverse detonation mode. Two types of transverse wave structures were observed and the reason behind this formation was discussed. The presence of transverse detonation was confirmed and its role in influencing the propagation of highly unstable detonation was also discussed. In the following chapter, the overall observations of this analysis will be summarized followed by the recommendations for future research on tangential topics.

7.1.1 Concluding Remarks

Systematic analysis to determine the reinitiation mechanism of a self-sustaining, planar, highly irregular detonation in the absence of turbulence was performed in this study. The numerical methods used in this research were presented in Chapter - 2. Verification of the one-dimensional, non-reacting, inviscid solvers was performed using Sod's shock tube case. Validation of two-dimensional WENO/CD solver was performed using an experimental Mach reflection case to check the scheme switching performance near the shocks in Chapter -3. References to find detailed material regarding the numerical methods and validation studies were cited in relevant subsections. A comparison study between inviscid/viscous solvers and global one-step/multistep chemistry was performed by analyzing the reinitiation mechanism of a planar, regular detonation operating in ordinary operation limits in Chapter - 4. A stoichiometric hydrogen-oxygen mixture diluted with argon was chosen at 6.67 kPa initial pressure for the study. The global behavior of detonation was compared with other numerical and experimental results available in the literature and was found to be acceptable. Reinitiation occurred through a sequence of a collisions between primary triple points followed by a sequence of a collisions between the secondary triple points. The 'diamond-shaped' unburnt reactant pockets formed at the end of each cell cycle were consumed by the collision between transverse waves. The one-step chemistry reinitiation cycle failed to predict the shock wave emitted in response to the secondary triple point collision and from the burning of the diamond-shaped pocket due to coarser time resolution.

The reinitiation mechanism study of planar, highly irregular detonation was analyzed in Chapter-5 using an inviscid, global one-step chemistry model. The numerical setup boundary conditions and initial conditions were chosen to match the experimental work performed by Radulescu [60]. Two cases were chosen to understand the difference in the reinitiation mechanism between marginal detonation (3.5 kPa) and ordinary detonation (6 kPa). The predicted reinitiation mechanism was categorized into triple point reinitiation, which was the reinitiation as a result of a collision of triple points within itself or a solid surface and Mach reflection reinitiation, where the influence of hydrodynamic effects was important to aid the

reinitiation. The Mach reflection reinitiation was subcategorized into slip line-flame type reinitiation and slip line-hotspot type reinitiation. The strength of the shockwave and the distance between the flame and the shockwave before the collision was found to be influencing the type of reinitiation. Time scales between different reinitiation mechanisms were analyzed. The major difference between the 6 kPa case and the 3.5 kPa case was due to the presence of additional minor triple points and its interaction with primary triple points favoring the triple point collision reinitiation mechanism. The departure of the actual average sonic plane from the theoretical sonic plane for steady ZND calculation was confirmed as reported in other research studies [60, 1, 46].

In the first part of the Chapter-6, the influence of molecular viscosity and diffusion is studied in two dimensions for the 6 kPa case to understand the significance of reduced artificial diffusion and its influence on flame speeds at very fine grid resolution using fourth-order accurate WENO/CD solver. The major difference between the inviscid and viscous one-step chemistry model was found to be the reduced presence of minor triple points. This increases the time taken by the unburnt reactant jets to detach from the triple point and increases their presence in the vicinity of the Mach stem. Reduced size of the curved jets and drifting pockets were also found due to the same reason. A two percent decrease in the unburnt pocket mass fraction was found at the averaged sonic plane which was achieved 6 mm ahead of the inviscid model predicted length. The additional time for which the slip line is attached to the triple point also permits the instabilities to grow into KH willows in a reoccurring manner which is observed to increase the consumption rate at the reactant/product interface.

The influence of the finite chemistry with the multispecies finite rate model was investigated in the second half of Chapter - 6. No studies have been performed to study the reinitiation mechanism of an oxymethane detonation using multistep finite rate chemistry according to the author's knowledge at the time of this manuscript preparation. A reduced chemistry mechanism with 13 (CH_3, CH_3O, CH_2O, HCO, HO_2, CO, CO_2, O, H, OH) species and 35 reactions was derived from the detailed GRI 1.2 mechanism and validated using ZND analysis. Feedback between the flow features created by the curvature of the slip line with the non-reacting Mach reflection or transverse waves was determined to be occurring through shockwaves or pressure waves. Depending upon the intensity of the feedback shockwave, two types of transverse wave

systems were found to occur. The first transverse wave system contained weak shockwaves and was captured in both inviscid and viscous global one-step chemistry model. But the second form of transverse wave system consisted of a strong transverse wave system with an upper limit of pressure reaching more than twice the magnitude of the weaker transverse wave system. Clear evidence of the presence of transverse detonation observed in experiments [62] was found to be present in the numerical simulation using multistep chemistry. One dimensional profile cross-section of the transverse detonation was studied to confirm the detonation instead of isobaric autoignition due to shock heating. Also, the numerical soot foil clearly shows the presence of triple points in the transverse detonation. The evolution of transverse detonation in the induction zone and unburnt reactant pockets was discussed. Consumption of burnt pockets by transverse detonations reduced the average pocket penetration distance to 3.9 cm which is within 30 percent deviation compared to the value reported in the experiments [60]. Strong shock waves were emitted by the direct reinitiation mode accompanied by transverse detonation which was found to increase the Favre averaged flow parameters at the averaged sonic plane. All the reinitiation modes observed in the experiments were successfully captured and analyzed using the inviscid, multistep chemistry model.

7.1.2 Recommendation

The next step of this study is to understand the three-dimensional effects and its significance in the propagation mechanism of highly unstable detonation. The transport equation (equation 1-3) of vorticity contains the baroclinic torque term which induces vorticity when $\frac{(\nabla\rho\times\nabla p)}{\rho^2} \neq 0$. This vorticity initiates the Richtmyer–Meshkov (RM) instability which can further influence the burning of reactant jets or pockets [170]. Evidence of the presence of vortices due to baroclinic term can be found out by calculating the $\frac{(\nabla\rho\times\nabla p)}{\rho^2}$ term. The following contour shows an event of reinitiation along the top wall at T=105 of the oxymethane detonation at 6 kPa using the viscous global one-step chemistry model. The magnitude of baroclinic torque is overlapped on the gradient of the density vector to visualize the vorticity induced by the baroclinic term. Since it is a two-dimensional solution, only the vorticity component of the z-axis (ω_z) is solved.

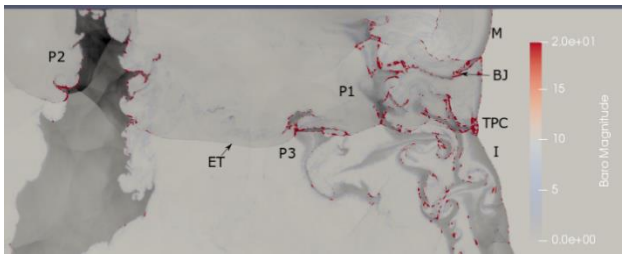

Figure 7-1 Vorticity Magnitude overlapped on the Density Gradient of an Oxymethane Detonation using Viscous Global One Step Chemistry Model at T=105.

The above figure shows a Mach stem M with a backward jet BJ, extended transverse wave ET involved in a triple point collision at TPC. Vorticity deposition along the interface of reactant and product is seen to be present as the transverse wave ET sweeps across the reactant pockets P1, P2, and P3 as well as along the interfaces of the reactant jet. The role of transverse wave interaction in producing turbulent environment was also pointed by Radulescu et al. [9] and Oran et.al. [171]. In a compressible turbulence mechanism, all the inter-scale energy transfers are due to non-linear interactions and hence the usual LES subgrid-scale models based on energy cascade are not relevant [68]. Hence to solve for the turbulent environment resulting from the RM instability, a three-dimensional, Direct Numerical Simulation (DNS) might be necessary.

It is clear from this study that highly irregular detonation is highly asymmetric. Hence the advantage of using a symmetric boundary condition to simulate a section of the detonation domain for the computational economy is not possible when simulating highly irregular detonation. Even though the above recommendations weigh to be costly, priority to use an appropriate chemistry model is necessary. A detailed review of different reduced chemistry models appropriate for detonation is reviewed by Ziegler [34]. The results from this research recommend the use of a finite rate chemistry model. Accurate prediction of molar mass is necessary to determine the correct value of the speed of sound. The strength of the shock wave was found to be important in creating post pressure increasing the reaction rate through intermediate reactions deciding either a strong or weak combustion in the research work of Diegelmann [170]. The coupling and decoupling between transverse shockwave and reaction zone were observed in the evolution of transverse detonation. By ignoring the endothermic reactions when using a simplistic chemical model,

the flow profile created by the transverse detonation and strong transverse wave structure may lead to unrealistic values.

[1] J. H. Lee and M. I. Radulescu, "On the hydrodynamic thickness of cellular detonations," *Combustion, Explosion and Shock Waves,* vol. 41, no. 6, pp. 745-765, 2005.

[2] J. H. Lee, The Detonation Phenomenon, New York: Cambridge University Press, 2008.

[3] W. Fickett and D. C. William, Detonation, Berkeley: University of California Press, 1979.

[4] V. N. Gamezo, D. Desbordes and E. S. Oran, "Formation and evolution of two-dimensional cellular detonations," *Combustion and Flame,* pp. 154-165, 1999.

[5] J. H. Lee, "Initiation of gaseous detonation," *Annual Review of Physical Chemistry,* vol. 28, no. 1, pp. 75-104, 1977.

[6] J. M. Powers, "Review of multiscale modeling of detonation," *Journal of Propulsion and Power,* vol. 22, no. 6, pp. 1217-1229, 2006.

[7] F. K. Lu and E. M. Braun, "Rotating detonation wave propulsion: experimental challenges, modeling, and engine concepts," *Journal of Propulsion and Power,* vol. 30, no. 5, pp. 1125-1142., 2014.

[8] C. Li and K. Kailasanath, "Detonation diffraction in pulse detonation engines," in *36th AIAA/ASME/SAE/ASEE Joint Propulsion Conference and Exhibit*, Las Vegas, 2000.

[9] M. Radulescu and J. Lee, "The failure mechanism of gaseous detonations: experiments in porous wall tubes," *Combustion and Flame*, vol. 131, no. 1, pp. 29-46, 2002.

[10] C. A. Eckett, "Numerical and analytical studies of the dynamics of gaseous detonations," PhD dissertation, California Institute of Technology, Pasadena, 2001.

[11] H. D. Ng, "The effect of chemical reaction kinetics on the structure of gaseous detonations.," McGill University, Quebec, 2005.

[12] J. M. Austin, "The role of instability in gaseous detonation," Caltech, Passadena,California, 2003.

[13] J. E. Shepherd, I. O. Moen, S. B. Murray and P. A. Thibault, "Analyses of the cellular structure of detonations.," *In Symposium (International) on Combustion,Elsevier.,* Vols. 21, No. 1, no. 1, pp. 1649-1658, 1988.

[14] A. V. Trotsyuk, P. A. Fomin and A. A. Vasil'ev, " Numerical study of cellular detonation structures of methane mixtures.," *Journal of Loss Prevention in the Process Industries,* vol. 36, pp. 394-403, 2015.

[15] J. J. Erpenbeck, " Stability of idealized one-reaction detonations," *The Physics of Fluids,* vol. 7, no. 5, pp. 684-696, 1964.

[16] M. Short and G. J. Sharpe, "Pulsating instability of detonations with a two-step chain-branching reaction model: theory and numerics," *Combustion Theory and Modelling,* vol. 7, no. 2, pp. 401-416, 2003.

[17] M. I. Radulescu, "The propagation and failure mechanism of gaseous detonations: experiments in porous-walled tubes," Doctoral dissertation, McGill University Libraries, Quebec, 2003.

[18] F. Sharpe and S. A. E. G. Sharpe, "Two-dimensional numerical simulations of idealized detonations," *Proceedings of the Royal Society of London. Series A: Mathematical, Physical and Engineering Sciences*, vol. 456, pp. 2081-2100, 2000.

[19] M. I. Radulescu, G. I. Sharpe and D. Bradley, "A universal parameter quantifying explosion hazards, detonability and hot spot formation: χ number," in *ISFEH7 Proceedings of the Seventh International Seminar*, Leeds, UK, 2013.

[20] M. Short, A. K. Kapila and J. J. Quirk, " The chemical-gas dynamic mechanisms of pulsating detonation wave instability," *Philosophical Transactions of the Royal Society of London. Series A: Mathematical, Physical and Engineering Sciences* , vol. 357, no. 1764, 1999.

[21] V. P. Korobeinikov, "Gas dynamics of explosions," *Annual Review of Fluid Mechanics* , vol. 3, no. 1, pp. 317-346, 1971.

[22] K. Kailasanath and E. S. Oran, "Ignition of flamelets behind incident shock waves and the transition to detonation," *Combustion Science and Technology,*, vol. 34, no. 1-6, pp. 345-362, 1983.

[23] E. S. Oran, V. N. Gamezo and D. A. Kessler, "Deflagrations, detonations, and the deflagration-to-detonation transition in methane-air mixtures.," Naval Research Lab For Computational Physics And Fluid Dynamics, Washington DC, 2011.

[24] T. L. Jackson, A. K. Kapila and D. S. Stewart, "Evolution of a reaction center in an explosive material," *SIAM Journal on Applied Mathematics* , vol. 49, no. 2, pp. 432-458, 1989.

[25] A. Oppenheim and L. Zajac, "Dynamics of an explosive reaction center," *AIAA Journal*, vol. 9, no. 4, pp. 545-553, 1971.

[26] E. S. Oran and V. N. Gamezo, "Origins of the deflagration-to-detonation transition in gas-phase combustion," *Combustion and Flame* , vol. 148, no. 1-2, pp. 4-47, 2007.

[27] J. E. Shepherd, "Detonation in gases," *Proceedings of the Combustion Institute* , vol. 32, no. 1, pp. 83-98, 2009.

[28] V. N. Uskov and P. S. Mostovykh, "Triple configurations of traveling shock waves in inviscid gas flows," *Journal of applied mechanics and technical physics*, vol. 49, no. 3, pp. 347-353., 2008.

[29] J. D. Anderson, Modern Compressible Flow: With Historical Perspective, NewYork: (McGraw-Hill series, 1982.

[30] S. M. Lau-Chapdelaine and M. I. Radulescu, "Viscous solution of the triple-shock reflection problem.," *Shock Waves*, vol. 26, no. 5, pp. 551-560, 2016.

[31] D. Schwer and K. Kailasanath, "Numerical investigation of the physics of rotating-detonation-engines," *Proceedings of the Combustion Institute*, vol. 33, no. 2, pp. 2195-2202, (2011). .

[32] H. K. Versteeg and W. Malalasekera, An introduction to computational fluid dynamics: the finite volume method, England: Pearson education, 2007.

[33] P. K. Kundu and I. M. Cohen, Fluid mechanics. 2004, ondon 199: Elsevier Acad. Press, L, 2008.

[34] J. L. Ziegler, "Simulations of compressible, diffusive, reactive flows with detailed chemistry using a high-order hybrid WENO-CD scheme," Caltech, Passadena, 2012.

[35] E. S. Oran, J. W. Weber Jr, E. I. Stefaniw, M. H. Lefebvre and J. D. Anderson Jr, "A numerical study of a two-dimensional H2-O2-Ar detonation using a detailed chemical reaction model," *Combustion and Flame* , pp. 147-163., 1998.

[36] G. Ben-Dor, Shock wave reflection phenomena, vol. 2, Shock wave reflection phenomena : Springer, 2007.

[37] X. Y. Hu, B. C. Khoo, D. L. Zhang and Z. L. Jiang, "The cellular structure of a two-dimensional H 2/O2/Ar detonation wave," *Combustion Theory and Modelling,* vol. 8, no. 2, pp. 339-359, 2004.

[38] R. Deiterding, "Parallel adaptive simulation of multi-dimensional detonation structures," Von der Fakult¨at f¨ur Mathematik, Naturwissenschaften und Informatik, 2003.

[39] D. A. Kessler, V. N. Gamezo and E. S. Oran, "Multilevel detonation cell structures in methane-air mixtures," *Proceedings of the Combustion Institute,* vol. 33, no. 2, pp. 2211-2218, 2011.

[40] V. N. Gamezo, A. A. Vasil'ev, A. M. Khokhlov and E. S. Oran, "Fine cellular structures produced by marginal detonations," *Proceedings of the Combustion Institute,* vol. 28, no. 1, pp. 611-617, 2000.

[41] M. I. Radulescu, "A detonation paradox: Why inviscid detonation simulations predict the incorrect trend for the role of instability in gaseous cellular detonations?," *Combustion and Flame,* vol. 195, pp. 151-162, 2018.

[42] E. S. Oran, T. R. Young, J. P. Boris, J. M. Picone and D. H. Edwards, "A study of detonation structure: The formation ofunreacted gas pockets," *Combustion Institute,* vol. 19, no. 1, pp. 573-582, 1982.

[43] B. D. Taylor, D. A. Kessler, V. N. Gamezo and E. S. Oran, " Numerical simulations of hydrogen detonations with detailed chemical kinetics," *Proceedings of the combustion Institute,* vol. 34, no. 2, pp. 2009-2016, 2013.

[44] M. I. Radulescu, G. J. Sharpe, C. K. Law and J. H. S. Lee, " The hydrodynamic structure of unstable cellular detonations," *Journal of Fluid Mechanics,* vol. 580, pp. 31-81, 2007.

[45] Z. Liang, S. Browne, D. R. and J. E. Shepherd, " Detonation front structure and the competition for radicals.," *Proceedings of the Combustion Institute,* pp. 2445-2453, 2007.

[46] B. M. Maxwell, "Turbulent combustion modelling of fast-flames and detonations using compressible LEM-LES," University of Ottawa, Ottawa, 2016.

[47] J. M. Austin, F. Pintgen and J. E. Shepherd, "Reaction zones in highly unstable detonations," *Proceedings of the Combustion Institute,* pp. 1849-1857, 2005.

[48] V. N. Gamezo, A. M. Khokhlov and E. S. Oran, "Secondary detonation cells in systems with high activation energy," in *Proceedings of the 17th ICDERS*, 1999.

[49] V. N. Gamezo, D. Desbordes and E. S. Oran, " Two-dimensional reactive flow dynamics in cellular detonation waves.," *Shock Waves,* vol. 9, no. 1, pp. 11-17, 1999.

[50] P. Hwang, R. Fedkiw, B. Merriman, T. Aslam, A. Karagozian and S. Osher, "Numerical resolution of pulsating detonation waves," *Combustion Theory and Modelling,* vol. 4, no. 3, pp. 217-240, 2006.

[51] C. A. Eckett, J. J. Quirk and J. E. Shepherd, "The role of unsteadiness in direct initiation of gaseous detonations," *Journal of Fluid Mechanics,* vol. 421, pp. 147-183, 2000.

[52] R. R. Bhattacharjee, S. S. M. Lau-Chapdelaine, G. Maines, L. Maley and M. I. Radulescu, "Detonation re-initiation mechanism following the Mach reflection of a quenched detonation.," *Proceedings of the Combustion Institute,* vol. 34, no. 2, pp. 1893-1901, 2013.

[53] M. Dormal, J. C. Libouton and P. J. Van Tiggelen, "Etude experimentale des parametres a l'interieur d'une maille de detonation," *Explosifs,* vol. 36, no. 1, p. 63, 1983.

[54] J.-C. Libouton, M. Dormal and P. J. Van Tiggelen, "Reinitiation process at the end of the detonation cell," *Gasdynamics of detonations and explosions,* pp. 358-369, 1981.

[55] M. H. Lefebvre, "Contribution a L'etude Numerique des Detonations, Modelisation de la Structure Cellulaire et Role de la Cinetique Chimique," Universite Catholique de Louvain, Belgium., 1992.

[56] M. H. Lefebvre and E. S. Oran, "Analysis of the shock structures in a regular detonation," *Shock Waves,* vol. 4, no. 5, pp. 277-283, 1995.

[57] S. Gallier, F. Le Palud, F. Pintgen, R. Mével and J. E. Shepherd, "Detonation wave diffraction in H2–O2–Ar mixtures," *Proceedings of the Combustion Institute,* vol. 36, no. 2, pp. 2781-2789, 2017.

[58] C. B. Kiyanda and A. J. Higgins, "Photographic investigation into the mechanism of combustion in irregular detonation waves."," *Shock Waves* , vol. 23, no. 2, pp. 115-130, 2013.

[59] C. B. Kiyanda, "Photographic study of the structure of irregular detonation waves," McGill University, 2005.

[60] M. I. Radulescu, G. J. Sharpe, J. H. S. Lee, C. B. Kiyanda, A. J. Higgins and R. K. Hanson, "The ignition mechanism in irregular structure gaseous detonations," *Proceedings of the Combustion Institute,* vol. 30, no. 2, pp. 1859-1867, 2005.

[61] J. Lee, "The propagation mechanism of cellular detonation," in *Shock Waves. Springer*, Berlin, 2005.

[62] R. R. Bhattacharjee, "Experimental investigation of detonation re-initiation mechanisms following a Mach reflection of a quenched detonation," University of Ottawa, Canada, 2013.

[63] S. S. M. Lau-Chapdelaine, "Numerical simulations of detonation re-initiation behind an obstacle," University of Ottawa , Ontario, 2013.

[64] Y. Mahmoudi, N. Karimi, R. Deiterding and S. Emami, "Hydrodynamic instabilities in gaseous detonations: comparison of Euler, Navier–Stokes, and large-eddy simulation," *Journal of Propulsion and Power,* vol. 30, no. 2, pp. 384-396, 2014.

[65] B. Maxwell, R. Bhattacharjee, S. Lau-Chapdelaine, S. Falle, G. Sharpe and M. Radulescu, "Influence of Turbulent Fluctuations on the Structure of Irregular Detonation

Propagation," in *Proceedings of Combustion Institute - Canadian Section*, Waterloo, 2016.

[66] C. B. Kiyanda, C. B. Morgan, G. H. Nikiforakis and H. D. Ng, "High resolution GPU-based flow simulation of the gaseous methane-oxygen detonation structure," *Journal of Visualization* , pp. 273-276., 2015.

[67] P. Mcmurtry, "ME 7960: Turbulence," The University of Utah, Salt Lake City, 2001.

[68] E. Garnier, N. Adams and P. Sagaut, Large eddy simulation for compressible flows, Springer Science & Business Media, 2009.

[69] H. Tennekes and J. L. Lumley, A first course in turbulence., MIT press, 1972.

[70] B. V. Voytsekhovskiy, V. V. Mitrofanov and M. E. Topchiyan, "The structure of a detonation front in gases," FOREIGN TECHNOLOGY DIV WRIGHT-PATTERSON AFB OH. (No. FTD-MT-64-527), Ohio, 1955.

[71] C. K. Law, Combustion physics, Cambridge university press, 2010.

[72] R. Deiterding, "Detonation simulation with the AMROC framework," Forschung und wissenschaftliches Rechnen: Beiträge zum Heinz-Billing-Preis, Rechnen, 2003 .

[73] T. Poinsot and D. Veynante, Theoretical and numerical combustion, RT Edwards, Inc, 2005.

[74] F. A. Williams, Combustion Theory: the fundamental theory of chemical reacting flow systems, Addison-Wesley, 1965.

[75] S. Browne, J. Ziegler and J. Shepherd, " Numerical solution methods for shock and detonation jump conditions. ,," Energy Conservation, Caltech, Passadena, 2004.

[76] T. E. Hull, W. H. Enright and K. R. Jackson, "User's guide for DVERK: A subroutine for solving non-stiff ODE's," University of Toronto. Department of Computer Science , Toronto, 1976.

[77] R. J. LeVeque, Finite volume methods for hyperbolic problems, Cambridge university press, 2002., 2002.

[78] E. F. Toro, Riemann solvers and numerical methods for fluid dynamics: a practical introduction, Springer Science & Business Media, 2013.

[79] T. J. Chung, Computational fluid dynamics, Cambridge university press, 2010.

[80] I. Danaila, P. Joly, S. Kaber and M. Postel, An introduction to scientific computing: Twelve computational projects solved with MATLAB, Springer Science & Business Media, 2007.

[81] C. W. Shu, "High-order finite difference and finite volume WENO schemes and discontinuous Galerkin methods for CFD," *International Journal of Computational Fluid Dynamics*, vol. 17, no. 2, pp. 107-118, 2003.

[82] D. J. I. P. Hill, "Hybrid tuned center-difference-WENO method for large eddy simulations in the presence of strong shocks.," *Journal of Computational Physics*, vol. 194, no. 2, pp. 435-450, 2004.

[83] C. Pantano, R. Deiterding, D. J. Hill and D. I. Pullin, "A low numerical dissipation patch-based adaptive mesh refinement method for large-eddy simulation of compressible flows," *Journal of Computational Physics,* vol. 221, no. 1, pp. 63-87, 2007.

[84] J. L. Ziegler, R. Deiterding, S. J. E. and D. I. Pullin, "An adaptive high-order hybrid scheme for compressive, viscous flows with detailed chemistry," *Journal of Computational Physics* , vol. 230, no. 20, pp. 7598-7630., 2011.

[85] C. A. Gilkeson, V. V. Toropov, H. M. Thompson, M. C. T. Wilson, N. A. Foxley and P. H. Gaskell, "Dealing with numerical noise in CFD-based design optimization," *Computers & Fluids,* vol. 94, pp. 84-97, 2014.

[86] S. U. Schöffel and F. Ebert, "Numerical analyses concerning the spatial dynamics of an initially plane gaseous ZND detonation," *Progress in Astronautics and Aeronautics* , vol. 114, pp. 3-31, 1988.

[87] I. A. Zaev and I. V. Prokopovich, " Global mechanism of methane autoignition: Approach and algorithm.," *Russian Journal of Physical Chemistry B,* vol. 8, no. 4, pp. 467-474., 2014.

[88] M. I. Radulescu, W. Wang, M. Saif, M. Levin and A. Pekalski, "On chapman jouguet deflagrations," in *In Proceedings of 25th International Colloquium on the Dynamics of Explosions and Reactive Systems*, Leeds, UK, 2015.

[89] E. S. Oran, J. P. Boris, T. Young, M. Flanigan, T. Burks and M. Picone, "Numerical simulations of detonations in hydrogen-air and methane-air mixtures," *In Symposium (International) on Combustion. Elsevier,* vol. 18, no. 1, pp. 1641-1649, 1981.

[90] C. Wang, X. Dong and C. W. Shu, " Parallel adaptive mesh refinement method based on WENO finite difference scheme for the simulation of multi-dimensional detonation," *Journal of Computational Physics,* vol. 298, pp. 161-175, 2015.

[91] M. J. Berger and P. Colella, "Local adaptive mesh refinement for shock hydrodynamics," *Journal of computational Physics,* vol. 82, no. 1, pp. 64-84, 1989.

[92] A. Dubey, A. Almgren, J. Bell, M. Berzins, S. Brandt, G. Bryan and P. Colella, "A survey of high level frameworks in block-structured adaptive mesh refinement packages," *Journal of Parallel and Distributed Computing* , vol. 74, no. 12, pp. 3217-3227, 2014.

[93] J. Bell, M. Berger, J. Saltzman and M. Welcome, "Three-dimensional adaptive mesh refinement for hyperbolic conservation laws," *SIAM Journal on Scientific Computing,* vol. 15, no. 1, pp. 127-138, 1994.

[94] I. Celik, L. J. G. Hu and C. Shaffer, "Limitations of Richardson extrapolation and some possible remedies," *Journal of Fluids Engineering,* vol. 127, no. 4, pp. 795-805, 2005 .

[95] F. Stern, R. V. Wilson, H. W. Coleman and E. G. Paterson, "Verification and validation of CFD simulations," No. IIHR-407, Iowa Institute of Hydraulic Research, Iowa City, 1999.

[96] M. Parashar and X. Li, "Grace: Grid adaptive computational engine for parallel structured amr applications," *Advanced Computational Infrastructures for Parallel and Distributed Adaptive Applications* , vol. 66, p. 249, 2010.

[97] M. Parashar and J. C. Browne, "On partitioning dynamic adaptive grid hierarchies.," *Proceedings of the Twenty-Ninth Hawaii International Conference in System Sciences, IEEE,* vol. 1, pp. 604-613, 1996.

[98] I. Glassman and R. A. Yetter, Combustion, California: Academic press, 2014., 2008.

[99] W. L. Oberkampf and T. G. Trucano, "Verification and validation benchmarks," *Nuclear engineering and Design,* vol. 238, no. 3, pp. 716-743., 2008.

[100] J. Levandosky, "Math 220A Partial Differential Equations of Applied Mathematics-Conservation Laws," Stanford University, California, 2002.

[101] A. C. Berkenbosch, Capturing detonation waves for the reactive Euler equations.\, Æneas, 1995.

[102] J. Franke, C. Hirsch, A. Jensen, H. Krüs, M. Schatzmann, P. Westbury, S. Miles, J. Wisse and N. Wright, "Recommendations on the use of CFD in wind engineering," *In Cost action ,* vol. 14, no. C1, 2004.

[103] J. A. Greenough and W. J. Rider, "A quantitative comparison of numerical methods for the compressible Euler equations: fifth-order WENO and piecewise-linear Godunov.," *Journal of Computational Physics ,* vol. 196, no. 1, pp. 259-281., 2004.

[104] C. J. Roy, "Grid convergence error analysis for mixed-order numerical schemes," *AIAA journal,* vol. 41, no. 4, pp. 595-604, 2003 .

[105] H. M. Glaz, P. Colella, I. I. Glass and R. L. Deschambault, "A numerical study of oblique shock-wave reflections with experimental comparisons," *Proceedings of the Royal Society of London. A. Mathematical and Physical Sciences,* vol. 398, no. 1814, pp. 117-140, 1985.

[106] P. Mach, "Bifurcating Mach Shock Reflections with Application to Detonation Structure," Doctoral dissertation, University of Ottawa, Ontario, 2011.

[107] A. Kasimov, " Theory of instability and nonlinear evolution of self-sustained detonation waves," Doctoral dissertation, University of Illinois at Urbana-Champaign, Urbana, 2004.

[108] M. Saif, W. Wang, A. Pekalski, M. Levin and M. Radulescu, "Chapman–Jouguet deflagrations and their transition to detonation," *Proceedings of the Combustion Institute,* vol. 36, no. 2, pp. 2771-2779, 2017.

[109] R. B. Gilbert and R. A. Strelow, "Theory of detonation initiation behind reflected shock waves," *AIAA Journal,* vol. 4, no. 10, pp. 1777-1783, 1966.

[110] W. Cai, W. Oh and Y. Zhu, "Direct numerical calculations of a neutral stability curve for one-dimensional detonations," *SIAM Journal on Scientific Computing ,* vol. 17, no. 5, pp. 814-829., (1996). .

[111] H. I. Lee and D. S. Stewart, "Calculation of linear detonation instability: one-dimensional instability of plane detonation," *Journal of Fluid Mechanics,* vol. 216, pp. 103-132, 1990.

[112] J. D. Regele, "Effects of inertial confinement on the ignition of diffusion-free unreacted pockets.," *In 24th International Colloquium on the Dynamics of Explosions and Reactive Systems (ICDERS), Taipei Taiwan ,* vol. 28, pp. 1-6, 2013.

[113] R. A. Strehlow, "Gas pase detonations: recent developments," *Combustion and Flame ,* vol. 12, no. 2, pp. 81-101, 1968.

[114] R. A. Strehlow, "Nature of transverse waves in detonations," *Astronautica Acta,* vol. 14, no. 5, p. 539, 1969.

[115] R. Strehlow and A. Crooker, "The structure of marginal detonation waves," *Acta Astronautica,* vol. 1, no. 3-4, pp. 303-315, 1974.

[116] S. Taki and T. Fujiwara, "Numerical simulation of triple shock behavior of gaseous detonation," *In Symposium (International) on Combustion,Elsevier,* vol. 18, no. 1, pp. 1671-1681, 1981.

[117] D. N. Williams, L. Bauwens and E. S. Oran, "Detailed structure and propagation of three-dimensional detonations," *In Symposium (International) on Combustion,Elsevier,* vol. 26, no. 2, pp. 2991-2998, 1996.

[118] M. Hanana and M. H. Lefebvre, "Pressure profiles in detonation cells with rectangular and diagonal structures," *Shock Waves,* vol. 11, no. 2, pp. 77-88, 2001.

[119] H. S. Dou, H. M. Tsai, B. C. Khoo and J. Qiu, " Simulations of detonation wave propagation in rectangular ducts using a three-dimensional WENO scheme," *Combustion and Flame,* vol. 154, no. 4, pp. 644-659, 2008.

[120] R. A. Strehlow, "Detonation structure and gross properties," *Combustion Science and Technology,* vol. 4, no. 1, pp. 65-71, 1971.

[121] J. W. Weber Jr, "Physical and numerical aspects of two-dimensional detonation simulations including detailed chemical kinetics on a massively parallel connection machine," University of Maryland, College Park, 1994.

[122] C. K. Westbrook, "Chemical kinetics of hydrocarbon oxidation in gaseous detonations.","*Combustion and Flame* , pp. 191-210, 1982.

[123] M. H. Lefebvre, E. S. Oran and K. Kailasanath, "Computations of detonation structure: the influence of model input parameters," (No. NRL/MR/4404-92-6961). Naval Research Lab, Washington DC, 1992.

[124] S. Kao and J. E. Shepherd, "Numerical solution methods for control volume explosions and ZND detonation structure,Galcit report fm(2006)(7)," Caltech , Passadena, 2008.

[125] M. I. Radulescu, H. D. Ng, J. H. Lee and B. Varatharajan, "The effect of argon dilution on the stability of acetylene/oxygen detonations," *Proceedings of the Combustion Institute,* vol. 29, no. 2, pp. 2825-2831, 2002.

[126] T. Geßner and D. Kröner, "Dynamic mesh adaption for supersonic reactive flow," *Freistühler H., Warnecke G. (eds) Hyperbolic Problems: Theory, Numerics, Applications. International Series of Numerical Mathematics,* vol. 140, pp. 415-424, 2001.

[127] H. D. Ng, C. B. Kiyanda, G. H. Morgan and N. Nikiforakis, "The influence of high-frequency instabilities on the direct initiation of two dimensional gaseous detonations," in *In 25th International Colloquium on the Dynamics of Explosions and Reactive* , Leeds,UK, 2015.

[128] G. J. Sharpe, "Transverse waves in numerical simulations of cellular detonations," *Journal of Fluid Mechanics,* vol. 447, pp. 31-51, 2001.

[129] J. A. Fay, "Two-dimensional gaseous detonations: Velocity deficit," *The Physics of Fluids* , vol. 2, no. 3, pp. 283-289., 1959.

[130] N. Manson, "Propagation of Detonations and Deflagrations in the Melanges Gaseaux," in *Compt. Makes. Acad. Sci. 222 , 46.*, Paris, 1947.

[131] B. T. Chu, "On the Stability of Systems Containing a Heat Source," The RAYLEIGa Criterion. NACA AM, 56., 1956.

[132] G. Emanuel, "Vorticity in unsteady, viscous, reacting flow and downstream of a curved shock," *AIAA journal,* vol. 45, no. 8, pp. 2097-2099, 2007.

[133] F. Pintgen, C. A. Eckett, J. M. Austin and J. E. Shepherd, "Direct observations of reaction zone structure in propagating detonations," *Combustion and Flame,* vol. 133, no. 3, pp. 211-229, 2003.

[134] F. Reinbacher, "Hotspot characterization and detonation initiation in thermally stratified reactive mixtures," MS Thesis, Iowa State University, Ames, 2018.

[135] D. R. Kassoy, "The response of a compressible gas to extremely rapid transient, spatially resolved energy addition: an asymptotic formulation," *Journal of Engineering Mathematics,* vol. 68, no. 3-4, pp. 249-262, 2010.

[136] M. D. Kurtz, "Acoustic timescale characterization of hot spot detonability.," MS Thesis, Iowa State University, Ames, 2014.

[137] B. Zhang, H. Liu, B. Yan and H. D. Ng, " Experimental study of detonation limits in methane-oxygen mixtures: Determining tube scale and initial pressure effects," *Fuel, Elsevier,* vol. 259, no. 116220., 2020.

[138] M. Kaneshige and d. J. E. Shepherd, "Detonation database," Caltech, Passadena, 1997.

[139] Y. Mahmoudi and K. Mazaheri, "High resolution numerical simulation of the structure of 2-D gaseous detonations," *Proceedings of the Combustion Institute,* vol. 33, no. 2, pp. 2187-2194., 2011.

[140] B. G. Franzelli, "Impact of the chemical description on direct numerical simulations and large eddy simulations of turbulent combustion in industrial aero-engines," France, Ph.D. Dissertation 2011.

[141] W. L. Martinez and A. R. Martinez, Computational statistics handbook with MATLAB, Boca Raton: CRC press, 2007.

[142] J. Ahrens, B. Geveci and C. Law, "Paraview: An end-user tool for large data visualization.The visualization handbook," LA-UR-03-1560, Los Alamos National Laboratory, New Mexico, 2005.

[143] V. I. Manzhalei, "Fine structure of the leading front of a gas detonation," *Combustion, Explosion and Shock Waves* , vol. 13, no. 3, pp. 402-404., 1977.

[144] J. C. Chao, " Critical deflagration waves that lead to the onset of detonation," PhD Dissertation, McGill University, Montreal, 2007.

[145] A. K. Oppenheim, Introduction to Gasdynamics of Explosions, NewYork: Course Held at the Department of Hydro-and Gas-Dynamics, September 1970 (Vol. 48). Springer., 2014.

[146] S. Patankar, Numerical heat transfer and fluid flow, NewYork: Taylor & Francis, 1980.

[147] C. W. Shu, "Essentially non-oscillatory and weighted essentially non-oscillatory schemes for hyperbolic conservation laws," in *Advanced Numerical Approximation of Nonlinear Hyperbolic Equations* , Berlin, Heidelberg, Springer, 1998, pp. 325-432.

[148] J. VonNeumann and R. D. Richtmyer, " A method for the numerical calculation of hydrodynamic shocks," *Journal of applied physics* , vol. 21, no. 3, pp. 232-237, 1950.

[149] K. Mazaheri, Y. Mahmoudi and M. I. Radulescu, "Diffusion and hydrodynamic instabilities in gaseous detonations," *Combustion and Flame,* vol. 159, no. 6, pp. 2138-2154, 2012.

[150] B. M. Maxwell, R. R. Bhattacharjee, S. S. Lau-Chapdelaine, S. A. Falle, G. J. Sharpe and M. I. Radulescu, "Influence of turbulent fluctuations on detonation propagation," *Journal of Fluid Mechanics,* vol. 818, pp. 646-696, 2017.

[151] M. Arienti and J. E. Shepherd, "The role of diffusion at shear layer in irregular detonations," in *42th Joint Meeting of the US Sections of the Combustion Institute*, Philadelphia, 2005.

[152] S. Singh, J. Powers and S. Paolucci, "Detonation solutions from reactive Navier-Stokes equations.," in *In 37th Aerospace Sciences Meeting and Exhibit (p. 966).*, Reno, 1999.

[153] K. Mazaheri, Y. Mahmoudi and M. I. Radulescu, "Diffusion in gaseous detonations," in *Proceedings of the 23rd International Colloquium on the Dynamics of Explosions and Reactive Systems,* Irvine, 2011.

[154] B. Costa and W. S. Don, "High order hybrid central—WENO finite difference scheme for conservation laws," *Journal of Computational and Applied Mathematics,* vol. 204, no. 2, pp. 209-218, 2007 .

[155] L. Massa, J. M. Austin and T. L. Jackson, "Triple-point shear layers in gaseous detonation waves," *Journal of Fluid Mechanics,* vol. 586, pp. 205-248, 2007.

[156] L. Bates, D. Bradley, I. Gorbatenko and A. S. Tomlin, "Computation of methane/air ignition delay and excitation times, using comprehensive and reduced chemical mechanisms and their relevance in engine autoignition," *Combustion and Flame,* vol. 185, pp. 105-116, 2017.

[157] M. Liberman, C. Wang, C. Qian and J. Liu, "Influence of chemical kinetics on spontaneous waves and detonation initiation in highly reactive and low reactive mixtures.," *Combustion Theory and Modelling* , vol. 23, no. 3, pp. 467-495, 2019.

[158] A. Frassoldati, A. Cuoci, T. Faravelli, E. Ranzi, C. Candusso and D. Tolazzi, "Simplified kinetic schemes for oxy-fuel combustion," in *1st international conference on sustainable fossil fuels for future energy,* 2009.

[159] Z. He, X. B. Li, L. M. Liu and W. Zhu, "The intrinsic mechanism of methane oxidation under explosion condition: A combined ReaxFF and DFT study," *Elsevier Fuel,* vol. 124, pp. 85-90, 2014.

[160] K. Chenoweth, A. Van Duin and W. Goddard, "ReaxFF reactive force field for molecular dynamics simulations of hydrocarbon oxidation," *The Journal of Physical Chemistry A,* vol. 112, no. 5, pp. 1040-1053, 2008.

[161] T. Nakamura, "Computational Analysis of Zel'dovich-von Neumann-Doering (ZND) Detonation," Texas A & M University, College Station, 2010.

[162] K. N. Roberts, "Analysis and Design of a Hypersonic Scramjet Engine with a starting Mach number of 4.00," The University of Texas at Arlington, 2008.

[163] S. R. Turns, An introduction to combustion, New York: McGraw-hill, 1996.

[164] S. C. Li and F. A. Williams, "Reaction mechanisms for methane ignition.," in *ASME Turbo Expo 2000: Power for Land, Sea, and Air* , 2000.

[165] J. M. Simmie, "Detailed chemical kinetic models for the combustion of hydrocarbon fuels," *Progress in energy and combustion science* , vol. 29, no. 6, pp. 599-634, 2003.

[166] M. Frenklach, H. Wang, C. Yu, M. Goldenberg, C. Bowman, R. Hanson, D. Davidson, E. Chang, G. Smith and D. Golden, "Gri-mech-1.2, an optimized detailed chemical reaction mechanism for methane combustion," Gas Research Institute, 1995.

[167] D. G. Goodwin, H. K. Moffat and R. L. Speth, "Cantera: an object-oriented software toolkit for chemical kinetics," *Thermodynamics, and Transport Processes,* vol. 103, 2017.

[168] C. T. Bowman, M. Frenklach, W. R. Gardiner and G. Smith, " The GRI 3.0 chemical kinetic mechanism.," University of California, Berkeley, 1999.

[169] C. Wang, C. W. Shu, W. Han and J. Ning, "High resolution WENO simulation of 3D detonation waves," *Combustion and Flame,* vol. 160, no. 2, pp. 447-462, 2013.

[170] F. Diegelmann, S. Hickel and N. A. Adams, "Shock Mach number influence on reaction wave types and mixing in reactive shock–bubble interaction," *Combustion and Flame,* vol. 174, pp. 85-99, 2016.

[171] E. Oran, "Shock-driven nonequilibrium turbulence and high-speed deflagrations," in *44th AIAA Aerospace Sciences Meeting and Exhibit*, Reno, 2006.

[172] A. M. Khokhlov, E. S. Oran and G. O. Thomas, "Numerical simulation of deflagration-to-detonation transition: the role of shock–flame interactions in turbulent flames," *Combustion and Flame,* vol. 117, no. 1-2, pp. 323-339, 199.

[173] S. Dorofeev, A. Bezmelnitsin, V. Sidorov, J. Yankin and I. Matsukov, " Turbulent jet initiation of detonation in hydrogen-air mixtures," *Shock Waves,* vol. 6, no. 2, pp. 73-78, 1996.

[174] E. A. Lundstrom and A. K. Oppenheim, "On the influence of non-steadiness on the thickness of the detonation wave," *Proceedings of Royal Society of London,* vol. A 310, no. 1503, pp. 463-478, 1969.

[175] D. H. Edwards, A. T. Jones and D. E. Phillips, "The location of the Chapman-Jouguet surface in a multiheaded detonation wave," *Journal of Physics D: Applied Physics,* vol. 9, no. 9, p. 1331, 1976.

[176] S. Browne, Z. Liang and J. E. Shepherd, "Detailed and simplified chemical reaction mechanisms for detonation simulation," in *Fall 2005 Western States Section of the Combustion Institute*, 2005.

[177] F. Genin, " Study of compressible turbulent flows in supersonic environment by large-eddy simulation.," Georgia Institute of Technology, 2009.

[178] H. N. Nagarajan, "Direct numerical simulation of interaction of detonation wave with homogeneous isotropic turbulence.," The University of Texas at Arlington, Arlington, 2009.

[179] J. H. Lee, "Dynamic parameters of gaseous detonations," *Annual review of fluid mechanics,* pp. 311-336, 1984.

[180] D. H. Porter, A. Pouquet and P. R. Woodward, " A numerical study of supersonic turbulence.," *Theoretical and Computational Fluid Dynamics,* pp. 13-49, 1992.

[181] J. Yiguang, A. Shimano and O. Inoue, "Vorticity generation and flame distortion induced by shock flame interaction," *Symposium (International) on Combustion. Vol. 27. No. 1. Elsevier, ,* 1998..

[182] A. Trotsyuk, "Numerical modelling of continuous spin detonation in rich methane-oxygen mixture," *Journal of Physics: IOP Publishing,* vol. 754, no. 5, p. 052006, 2016.

[183] P. A. Fomin, Trotsyuk.A.V. and Vasil'ev.A.A, "Reduced detonation kinetics and detonation structure in one-and multi-fuel gaseous mixtures," *Journal of Physics: IOP Publishing,* vol. 894, no. 1, 2017.

[184] M. T. Parra-Santos, F. Castro-Ruiz and C. a Mendez-Bueno, "Numerical simulation of the deflagration to detonation transition," *Combustion, Explosion and Shock Waves ,* vol. 41, no. 2, pp. 215-222, 2005.

[185] F. Virot, B. Khasainov, D. Desbordes and H. N. Presles, "Spinning detonation: Experiments and simulations," in *21st International Colloquium on the Dynamics of Explosions and Reactive Systems,* 2007.

[186] M. I. Radulescu and B. M. Maxwell, "The mechanism of detonation attenuation by a porous medium and its subsequent re-initiation," *Journal of Fluid Mechanics,* vol. 667, pp. 96-134, 2011.

[187] B. Maxwell, M. Radulescu, S. Falle and G. Sharpe, "Reaction Rate Closure for Turbulent Detonation Propagation through CLEM-LES," in *25th International Colloquium on the Dynamics of Explosions and Reactive Systems,* Leeds, UK, 2015 .

[188] A. C. McIntosh, "Deflagration fronts and compressibility," *Philosophical Transactions of the Royal Society of London. Series A: Mathematical, Physical and Engineering Sciences,* vol. 357, no. 1764, pp. 3523-3538, 1999.

[189] L. M. Cohen and A. K. Oppenheim, "Effects of size and dilution on dynamic properties of exothermic centers," *Combustion and Flame,* vol. 25, pp. 207-211, 207-211.

[190] I. B. Zeldovich, S. M. Kogarko and N. N. Simonov, "An experimental investigation of spherical detonation of gases," *Soviet Phys. Tech. Phys.,* vol. 1, pp. 1689-1713, 1956.

[191] J. H. S. Lee and A. J. Higgins, "Comments on criteria for direct initiation of detonation," *Philosophical Transactions of the Royal Society of London Series A: Mathematical, Physical and Engineering Sciences, ,* vol. 357, no. 1764, pp. 3503-3521, 1999.

[192] M. Kaneshige and S. J. E, "Detonation database," GAL, Caltech, Pasadena, 1997.

[193] F. Diegelmann, S. Hickel and N. A. Adams, "Three-dimensional reacting shock–bubble interaction," *Combustion and Flame,* vol. 181, pp. 300-314, 2017.

Biographical Statement

Nandakumar Vijayakumar earned his Bachelor of Engineering degree in Aeronautical Engineering from Hindustan University, India in 2012. During his senior year, he was a research intern at the aerodynamics and propulsion unit of Hindustan Aeronautics Limited, India, where his research study focused on computational fluid dynamics and heat transfer simulation of a single-engine helicopter propulsion system. He was inspired by his rocket propulsion professor; Dr. K. Ramamurthi (IIT Madras) which led him to pursue his Master of Science at the University of Texas, Arlington. Due to his interest in high speed gas dynamics and detonation propulsion, he joined the Aerodynamic Research Center and began his research on hypersonic vehicles. The combustion summer school experience at Princeton University, New Jersey in 2015 instilled his interest in detonation physics which led to this research. During his time as a Ph.D. student, he had received several scholarships and a fellowship from the UTA graduate school. He also spent a semester at ANSYS, San Diego as a combustion CFD intern. He is an active member of the AIAA High Speed Air Breathing Propulsion Technical Committee. His research interests are combustion, CFD, high performance computation, aerodynamics, and propulsion.